# EVALUATION OF MULTIFUNCTIONAL PROPERTIES OF GRAPHENE BASED CEMENT COMPOSITES

SARDAR KASHIF UR REHMAN

FACULTY OF ENGINEERING
UNIVERSITY OF MALAYA
KUALA LUMPUR

2018

# EVALUATION OF MULTIFUNCTIONAL PROPERTIES OF GRAPHENE BASED CEMENT COMPOSITES

SARDAR KASHIF UR REHMAN

THESIS SUBMITTED IN FULFILMENT OF THE REQUIREMENTS FOR THE DEGREE OF DOCTOR OF PHILOSOPHY

FACULTY OF ENGINEERING
UNIVERSITY OF MALAYA
KUALA LUMPUR

2018

## UNIVERSITY OF MALAYA
## ORIGINAL LITERARY WORK DECLARATION

Name of Candidate: Sardar Kashif Ur Rehman,

Registration/Matric No: KHA140023

Name of Degree: Doctor of Philosophy (PhD)

Title of Research Report: Evaluation of multifunctional properties of graphene based cement composites.

Field of Study: Structural Engineering & Materials

I do solemnly and sincerely declare that:

(1) I am the sole author/writer of this Work;
(2) This Work is original;
(3) Any use of any work in which copyright exists was done by way of fair dealing and for permitted purposes and any excerpt or extract from, or reference to or reproduction of any copyright work has been disclosed expressly and sufficiently and the title of the Work and its authorship have been acknowledged in this Work;
(4) I do not have any actual knowledge nor do I ought reasonably to know that the making of this work constitutes an infringement of any copyright work;
(5) I hereby assign all and every rights in the copyright to this Work to the University of Malaya ("UM"), who henceforth shall be owner of the copyright in this Work and that any reproduction or use in any form or by any means whatsoever is prohibited without the written consent of UM having been first had and obtained;
(6) I am fully aware that if in the course of making this Work I have infringed any copyright whether intentionally or otherwise, I may be subject to legal action or any other action as may be determined by UM.

Candidate's Signature _________________________ Date: ____________

Subscribed and solemnly declared before,

Witness's Signature _________________________ Date: ____________

Name:

Designation:

# EVALUATION OF MULTIFUNCTIONAL PROPERTIES OF GRAPHENE BASED CEMENT COMPOSITES

## ABSTRACT

Nanomaterials are being used in the construction industry to improve the microstructural, mechanical and electrical properties of the building material. These nanomaterials are incorporated to overcome the shortcomings of conventional construction materials. Graphene is one of the nanomaterials that has been widely focused due to its extraordinary properties such as huge specific surface area, high intrinsic strength and high electrical transport properties. Nowadays, graphene was found to have a potential to enhance the properties of cement composite. This study evaluates the multifunctional properties of graphene-cement composites (GCC), aiming at the micro-analytical characterization, rheological behavior, mechanical and piezo-resistive properties. In this research, three types of graphene flakes based on surface area and lateral flake thickness were used. Firstly, dispersion efficiency of graphene was examined by UV-vis spectroscopy. Then, GCC were characterized by using Thermogravimetric Analysis (TGA), Fourier Transform Infrared (FTIR) Spectrometry, X-ray Diffraction (XRD) and Field Emission Scanning Electron Microscopy (FESEM). Afterwards, the rheological properties of fresh cement paste with various graphene types, graphene content, shear rate cycles, resting time and geometrical conditions were investigated. The rheological data were fitted by the Bingham model, Modified Bingham model, Herschel-Bulkley model and Casson model to estimate the flow properties of GCC. The effectiveness of these rheological models was expressed by the standard error. Mechanical properties were investigated for graphene cement mortar. Electrical properties of graphene were employed to evaluate the damage-sensing characteristics of GCC. Finally, the practical application of GCC was evaluated by testing the full length reinforced concrete (RC) beam. Various damage levels were induced in RC beam to monitor the response of GCC. Experimental results concluded that 40 min magnetic stirring in combination with 3 min ultrasonication gave the optimum results. Moreover, graphene with the high surface area and less thickness have stable and uniform dispersion. From TGA and XRD results, it was found that more hydration occurred due to graphene. FESEM images showed that graphene flakes with high surface area successfully provide the hindrance to the propagation of cracks; moreover, hydrated cement products grow in an ordered way. Rheological results showed that yield stress and plastic viscosity increased by the addition of graphene flakes with higher flake thickness and more resting time while these values decreased for higher shear rate cycle. Concentric cylinders estimated lower yield stress and standard error as compared to parallel plates. Moreover, non-linear models i.e. Herschel-Bulkley and Modified Bingham were found as best fitted models. In comparison to control sample, the GCC with more flake thickness showed a 30.5% increase in load carrying capacity and 113.5% increase in overall failure strain. It was found that electrical resistivity value for high surface area flakes reduced by 67.8% at the maximum compressive load, and hence GCC can be used to detect the damages in concrete. Graphene cement composite determined the electrical resistivity against various damage levels in an accurate manner in RC beam. In conclusion, GCC has better improved properties and it can successfully predict the response against cracks propagation. The outcome of this study is as a precursory development for smart composites to be utilized as construction materials as well as to monitor the structural health of the concrete structures.

**Keywords:** graphene cement composite, micro-analytical characterization, rheological behaviour, piezo-resistive properties, self-sensing

# MENILAI CIRI-CIRI PELBAGAI FUNGSI BAGI KOMPOSIT SIMEN BERASASKAN GRAFIN

## ABSTRAK

Bahan nano digunakan dalam industri pembinaan untuk meningkatkan sifat mikrostruktur, mekanikal dan elektrik bahan binaan. Bahan nano ini dicampur untuk mengatasi kekurangan bahan binaan konvensional. Grafin adalah salah satu bahan nanomaterial yang telah banyak digunakan kerana sifat luar biasanya seperti kawasan permukaan spesifik yang besar, kekuatan intrinsik yang tinggi dan sifat pengangkutan elektrik yang tinggi. Pada masa kini, grafin didapati mempunyai potensi untuk menambah baik sifat komposit simen. Kajian ini menilai ciri-ciri pelbagai fungsi komposit grafin-simen (*GCC*), yang bertujuan untuk pencirian mikro-analitik, sifat rheologi, sifat mekanik dan piezo-resistif. Dalam kajian ini, tiga jenis serpihan grafin berdasarkan kawasan permukaan dan ketebalan serpihan sisi digunakan. Pertama sekali, kecekapan taburan serpihan grafin telah diperiksa oleh spektroskopi *UV-vis*. Kemudian, *GCC* dicirikan dengan menggunakan Analisis Permeteran Gaviti Haba (*TGA*), *Fourier Transform* Spektrometri Inframerah (*FTIR*), Pembelanan Sinar-X (*XRD*) dan Medan Pancaran Mikroskop Pengimbasan Elektron (*FESEM*). Selepas itu, sifat rheologi pes simen segar dengan pelbagai jenis grafin, kandungan grafin, kitaran kadar ricih, masa rehat dan keadaan geometri telah disiasat. Data rheologi dipadankan dengan model *Bingham*, model modifikasi *Bingham*, model *Herschel-Bulkley* dan model *Casson* untuk menganggarkan sifat aliran *GCC*. Keberkesanan model rheologi ini dinyatakan dengan ralat piawai. Ciri-ciri mekanikal telah dikaji untuk mortar simen grafin. Sifat-sifat elektrik grafin telah digunakan untuk menilai ciri-ciri kesan deria-kerosakan *GCC*. Akhirnya, aplikasi praktikal *GCC* telah dinilai dengan menguji rasuk konkrit bertetulang bersaiz penuh (*RC*). Pelbagai tahap kerosakan teraruh di dalam rasuk RC untuk memantau tindak balas *GCC*. Keputusan eksperimen menyimpulkan bahawa pengaduk magnetik 40 min dalam kombinasi dengan *ultrasonication* 3 min memberikan hasil yang optimum. Selain itu, grafin dengan kawasan permukaan yang tinggi dan kurang ketebalan mempunyai penyebaran yang stabil dan seragam. Dari hasil *TGA* dan *XRD*, didapati penghidratan yang lebih banyak berlaku disebabkan penggabungan grafin. Imej *FESEM* menunjukkan bahawa serpihan grafin dengan permukaan permukaan yang tinggi berjaya memberikan penghalang kepada penyebaran keretakan; selain itu, produk simen terhidrat tumbuh dengan cara yang lebih teratur. Keputusan rheologi menunjukkan bahawa tekanan alah dan kelikatan plastik meningkat dengan penambahan serpihan grafin dengan lebih ketebalan serpihan dan masa rehat manakala nilai-nilai ini berkurangan untuk kitaran kadar ricih yang lebih tinggi. Silinder konsentrik menganggarkan tegasan alah dan ralat piawai yang lebih rendah berbanding dengan plat selari. Lebih-lebih lagi, model bukan linear iaitu *Herschel-Bulkley* dan Modifikasi *Bingham* didapati sebagai model yang paling sesuai. Sebagai perbandingan kepada sampel kawalan, *GCC* dengan ketebalan serpihan yang lebih tinggi menunjukkan peningkatan 30.5% dalam kapasiti menanggung beban dan peningkatan 113.5% dalam keseluruhan kegagalan terikan. Didapati bahawa nilai rintangan elektrik untuk serpihan kawasan permukaan tinggi berkurang sebanyak 67.8% pada beban mampatan maksimum, dan oleh itu *GCC* boleh digunakan untuk mengesan kerosakan dalam konkrit. Komposit simen grafin telah menentukan resistensi elektrik terhadap pelbagai tahap kerosakan secara tepat dalam rasuk *RC*. Sebagai rumusan, *GCC* mempunyai ciri-ciri yang lebih baik dan ia dapat meramal dengan berkesan tindak balas terhadap perambatan retakan. Hasil daripada kajian ini adalah sebagai prapenanda pembangunan bagi komposit pintar yang boleh digunakan sebagai bahan binaan disamping dapat juga memantau kondisi struktur bagi struktur konkrit.

**Kata kunci:** komposit simen grafin, pencirian mikro-analitik, tingkah laku rheologi, sifat-sifat piezo-resistif, swaderia.

# ACKNOWLEDGEMENTS

First of all, I would like to express my gratitude to the Almighty Allah who has created the whole universe, taught by pen and taught man that he knew not. I would like to extend my gratefulness to my supervisors Associate Prof. Dr. Zainah Binti Ibrahim, Professor Dr. Mohammed Jameel as well as Assistant Professor Dr. Shazim Ali Memon (Pakistan) for their continuous support of my PhD study and research, for their patience, enthusiasm, motivation and immense knowledge. I am especially grateful to my beloved Parents, family and friends who have encouraged and supported me with continuous help throughout the study.

Finally, I would like to acknowledge gratefully the University of Malaya for providing me with the financial support from Fundamental Research Grant Scheme, Ministry of Education, Malaysia (FRGS – Project No. FP028/2013A) and Postgraduate Research Fund (PPP – Project No. PG217–2014B) to accomplish this work. I gratefully acknowledge the privileges and opportunities offered by the University of Malaya. I also express my gratitude to the staff of this institute as well as a University that helped directly or indirectly to carry out my research work.

# TABLE OF CONTENT

# LIST OF FIGURES

# LIST OF TABLES

# LIST OF SYMBOLS AND ABBREVIATIONS

0D : Zero-dimensional

1D : One-dimensional

2D : Two-dimensional

$\Omega$ : Ohm

$\rho$ : Resistivity ohm-cm

$\rho_o$ : Electrical resistivity at the start of the test

$\rho_t$ : Electrical resistivity at the given time during the test

AC : Alternating current

AE : Acoustic emission

AFt : Ettringite

ASTM : American society for testing and materials

$C_2S$ : Belite

$C_3S$ : Alite

$C_4AF$ : Tetra calcium aluminate ferrite

$CaCO_3$ : Calcium carbonate

$Ca(OH)_2$ : Calcium hydroxide;

CB : Carbon black

CFRC : Carbon fibre reinforced cement composites

CH : Calcium hydroxide; Portlandite

CNCs : Cement mortar nanocomposites

CNTs : Carbon nanotubes

C-O : Carbon-Oxygen

C-OH : Carbon-hydroxide

$CO_2$ : Carbon dioxide

| | | |
|---|---|---|
| CSH | : | Calcium Silicate Hydrate |
| DC | : | Direct Current |
| DTA | : | Differential thermal analysis |
| DTG | | Differential thermal gravimetric |
| EDS | | Energy-dispersive X-ray Spectrometer |
| EDX | : | Energy-dispersive X-ray |
| ER | : | Electrical resistivity |
| FCR | : | Fractional change in resistance |
| FESEM | : | Field emission scanning electron microscopy |
| FGN | : | Functionalized graphene nanoplatelets |
| FRC | : | Fiber reinforced concrete |
| FTIR | : | Fourier transform infrared spectroscopy |
| GC | : | Graphene cement |
| GCC | : | Graphene cement composites |
| GPa | : | Giga Pascal = $10^9$ Pa |
| GNDs | : | Graphene and its derivatives |
| GNP | : | Graphene nanoplatelet |
| GO | : | Graphene oxide |
| GONPs | : | Graphene oxide nanoplatelets |
| GPR | : | Ground penetrating radar |
| HB | : | Herschel–Bulkley |
| H-O-H | : | Hydrogen-oxygen-hydrogen |
| I | : | Electric current |
| ICDD | : | International Centre for Diffraction Data |
| IE | : | Impact echo |
| IR | : | Impulse response |

|  |  |  |
|---|---|---|
| ITZ | : | Interfacial transition zone |
| KBr | : | Potassium bromide |
| kHz | : | Kilo Hartz |
| MC | : | Methylcellulose |
| MW | : | Molecular weight |
| MWCNTs | : | Multiwall carbon nanotubes |
| n | : | Power rate index |
| n-$Al_2O_3$ | : | Nano alumina |
| n-$Fe_2O_3$ | : | Nano-iron |
| n-$SiO_2$ | : | Nano-silica |
| n-$TiO_2$ | : | Nano-titania |
| NaDDBS | : | Sodium dedecylbenzenesulfonate |
| NCL | : | Normalized compressive loading |
| NDT | : | Non-destructive tests |
| OPC | : | Ordinary Portland Cement |
| P | : | Compressive loading at the given time during the test |
| $P_{max}$ | : | Maximum compressive loading throughout the whole test |
| PCC | : | Plain cement concrete |
| PCNT | : | Plain CNTs |
| PEG | : | Polyethylene Glycol |
| PGO | : | Pristine graphene oxide |
| RGO | : | Reduced graphite oxide |
| rGO | : | Reduced graphene oxide |
| $\Delta R$ | : | Change in resistance |
| R | : | Electrical resistance |
| $R_0$ | : | Initial resistance |

| | | |
|---|---|---|
| $\Delta R/R_0$ | : | Fractional variations of resistance |
| RC | : | Reinforced concrete |
| S | : | Spacing |
| SEM | : | Scanning electron microscope |
| SHM | : | Structural health monitoring |
| Si-O | : | Silicon-oxygen |
| SP | : | Superplasticizer |
| SPCNT | : | Functionalized carbon nanotubes |
| SRC | : | Sulphate Resistant Cement |
| SWCNT | : | Single walled carbon nanotube |
| TPa | : | Tera Pascal = $10^{12}$ Pa |
| TGA | : | Thermogravimetric analysis |
| Triton X-100 | : | *t*-octylphenol decaethylene glycol ether |
| UV-vis | : | Ultraviolet-visible |
| V | : | Voltage |
| w/c | : | Water-cement ratio |
| WRA | : | Water reducing agent |
| XRD | : | X-ray Diffraction |

# CHAPTER 1: INTRODUCTION

## 1.1 Background of Study

In civil engineering, almost every discipline encourages the use of cement-based material to accommodate the ever-increasing demands for structural needs due to the rise in population. The cementitious materials are mainly used to construct facility structures such as bridges, houses, dams etc. to meet the needs of the escalating population. Concrete is one of the major construction materials which has extensively used and thoroughly studied (Barcelo et al., 2014). Concrete has many credentials which include but not limited to (1) simple production process (2) rapid placement in any shape (3) low development cost and (4) high compressive strength which outshined it in the construction industry (Neville & Brooks, 1987). However, degradation, brittleness, porosity, low tensile strength, cracks formation and poor resistance to propagation of cracks are major drawbacks for hardened concrete (Birchall et al., 1981; Chuah et al., 2014; Gopalakrishnan et al., 2011; Raki et al., 2010; Tyson, 2010).

In addition, consistency, homogeneity, workability and fluidity are the primary elements that significantly based on the mixing and placing of fresh concrete. A little inadequacy in these parameters will lead to segregation, bleeding, laitance and cracking of the concrete (Zhang et al., 2016). Furthermore, the uneven growth of hydration products formed a complex heterogeneous microstructure that becomes denser over time. However, this complex structure becomes less dense due to interaction with aggregates and thus, reduced the bond between cement matrix and subsequently create a platform for the propagation of cracks (Raki et al., 2010). As a result, building structures constructed with these cementitious materials will deteriorate over time due to the factors such as materials ageing, overloading, excessive use, and environmental conditions (Chong et al., 2003). Cement composite which overrules the above-mentioned shortcomings and integrated with functional applications, such as self-monitoring is the need of this era. Therefore, with the advancement and application of new technologies, demands on the innovative, smart and stronger cement composite becomes more intense.

In order to overcome these limitations, many attempts were being carried out to further enhance the performance of cementitious material by incorporating fibers to manipulate the properties of the cementitious composite (Juárez et al., 2007; Shah & Ouyang, 1991; Topçu & Canbaz, 2007; Wang et al., 2012). Typical fibres lengths lie in the range of 3.5-100 mm and diameters in the range of 0.1-1 mm. Since the 1960s, research works on Fiber Reinforced Concrete (FRC) began in earnest and currently, FRC is being used commonly for special applications. Although FRC increased the flexural strength, fracture toughness and had the capability of replacing large cracks with a dense network of microcracks, however, the fibres still fail to put a halt to the crack initiation at the nanoscale (Chuah et al., 2014).

Over the last decade, nanotechnology had been seen as one of the most promising technology to be incorporated in cement-based materials. Nanoengineered cementitious composite means the methods of manipulating the structure at nanometre scale in order to fabricate a new kind of tailored multifunctional cementitious composite. Several researchers investigated the influence of various engineered nanomaterials on cement composite (Konsta et al., 2010; Ormsby et al., 2011; Shang et al., 2015). Nanoengineered cementitious composites have excellent mechanical properties and durability including other novel properties such as low electrical resistivity, high ductility, self-crack control and most importantly the capability of self-sensing (Sanchez & Sobolev, 2010). These cement composites are not only mechanically strong but also brings out its potential functionalities i.e. stops the initiation of crack at a nanoscale level, which overcomes the limitation of FRC. As a matter of fact, nanotechnology has made a paradigm shift in the cement-based reinforcing behaviour from macroscopic level to nanoscopic level. In reality, nano-engineered cementitious composites provided the solution strategies to overcome the problems faced by the ordinary building materials.

Graphene is one of the nanomaterials that has been widely focused. Graphene possesses some amazing and extraordinary properties such as huge specific surface area (2630 $m^2g^{-1}$), high intrinsic strength (130 GPa), firm Young's modulus (~1.0 TPa) and high electrical transport properties (Lee et al., 2008). Therefore, incorporation of graphene in cement composite will alter the microstructural, mechanical, rheological characteristics and electrical properties of the composite. The rheological properties of the cement paste are directly related to the workability, flowability and consistency of the concrete. Most of the recent researches were focused on the rolled sheets of graphene and its derivatives (GNDs) i.e. carbon nanotubes (CNTs) and graphene oxide (GO) (Shang et al., 2015; Wang et al., 2017; Wang et al., 2016). However, the rheological properties of graphene cement paste remained unexplored and rarely reported. Therefore, an in-depth knowledge of the connection of graphene and rheology of cement paste is still to be discovered. It is known that the cement based composite reinforced with conducting fillers i.e. carbon nanotubes and graphene can observe its own strain by monitoring the changes in the electrical resistivity values (Chung, 2002). These conducting filler significantly reduce the electrical resistivity values of the cement composite. Self-sensing ability is related to the breaking of conducting fibres i.e. when cracks are initiating in the cement based composite consequently, enhancing the electrical resistivity of the overall sample. The electrical properties of the graphene cement composites (GCC) are important and can be used to monitor the damage in a concrete structure for the purpose of maintaining safe, reliable and sustainable civil infrastructure.

Most of the existing researches were focused on the graphene oxide and carbon nanotubes based cement composites and less emphasize was given to the graphene based cement composites. Furthermore, it has been found that current studies were engrossed in the mechanical properties such as compressive strength, flexural strength and tensile strength of GCC. However, some other important material properties e.g. microstructural characterization, rheological behaviour, cracks bridging and damage memorizing of graphene cement composite are yet to be explored to get maximum benefits attributed from this composite in civil engineering.

Therefore, in this study, characterization of graphene cement composite was explored by using micro-analytical analysis. Crack bridging phenomena were observed using microscopic images. Flow properties were determined using rheological mathematical models. Self-sensing and piezoresistive characteristics were discovered using electrical properties and; damage-memorization was studied by applying controlled damages to the specimen.

## 1.2 Problem Statement

Ordinary cement based construction materials have porosity, brittleness, low tensile strength, poor resistance to crack formation and propagation (Neville & Brooks, 1987). Due to this civil infrastructure begins to deteriorate once they are built and used. Maintaining safe and reliable civil infrastructures for daily use is important for the well-being of humankind. Operation and maintenance of build structures become more complex with the increased age. With progress in nanotechnology, the idea of manufacturing innovative, smart and strong cement composite came into existence i.e. graphene cement composites (GCC). Recent advances in nanomaterials have led to new possibilities in health monitoring techniques. Before application of GCC in a civil industry few research questions arise:

- Will GCC possess superior characteristics and overcome the deficiencies encountered by the ordinary cement based building materials?
- Will the flow properties of GCC remain same as plain cement?
- Is it possible that graphene flakes modify the electrical resistivity of the cementitious material and introduce the strain sensing functional property in GCC?
- Can real-time damage monitoring be easily possible by using these GCC specimens?
- Will damage memorization characteristics be present in GCC smart specimens?
- Is this demand to develop the novel smart material with self-sensing characteristics really evolved from construction industry?

In order to provide answers to the above-mentioned questions, there will be a need to explore the properties of GCC in the laboratory. A comprehensive research study is required to investigate the influence of graphene on the micro-analytical, mechanical, rheological and self-sensing characteristics of the composite material.

## 1.3 Research Objectives

This study is conducted to evaluate the multifunctional properties of graphene based cement composites. Moreover, development of strong composite materials which possess sensing capabilities. This research tried to quantify the techniques for damage memorization by incorporating the graphene cement composite in concrete structures. In order to achieve the above aims, the specific research objectives are planned as follows:

(1) To determine the dispersion efficiency and micro-analytical characteristics of graphene based cement composites.

(2) To evaluate the rheological properties, compressive and flexural strengths of the graphene based cement composites.

(3) To investigate the piezoresistivity and self-sensing properties of graphene based cement composites.

(4) To evaluate the potential application of graphene based cement composite for structural health monitoring of concrete structures.

## 1.4 Scope and Limitation of Study

This underlying objective of this research is to evaluate the multifunctional properties of graphene based cement composites. Therefore, the scope and limitations of this study are defined as:

1. Only three different types of graphene based on surface area and lateral flake thickness were used to investigate the characteristics of graphene based cement composite. Dispersion efficiency of graphene in aqueous solution is studied using Ultraviolet-visible (UV-vis) spectroscopy only.
2. Characterization of graphene cement composite is performed using only Thermogravimetric Analysis (TGA), Fourier Transform Infrared (FTIR) Spectrometry, X-ray Diffraction (XRD) Spectroscopy, Field Emission Scanning Electron Microscopy (FESEM) images and Energy-Dispersive X-ray (EDX) analysis.
3. Rheological properties were investigated for the graphene cement paste using Bingham, Modified Bingham, Herschel–Bulkley (HB) and Casson models. Flow properties were inspected for all samples using smooth parallel plates. In addition,

the different content of graphene, different shear rate cycles, resting time and test geometries were considered as only factors affecting the rheology of cement paste.

4. Graphene cement mortar was only used to investigate the compressive strength and flexural strength of the composite. Fresh and hardened properties of cement paste and mortar are measured according to American Society for Testing and Materials (ASTM) standards.
5. Piezoresistive properties of graphene cement paste were only investigated for graphene cement composite. The potential application of graphene cement composite embedded in the reinforced concrete beam was investigated.

## 1.5 Significance of Study

This research is performed to explore the multifunctional properties of graphene based cement composite in civil engineering. It was found that a very few researches have been done using graphene nanomaterial. Morphology and microstructural characterization have been reported rarely in literature for graphene based cement composite. Effect of surface area, lateral size and flake thickness of graphene flakes on cement composite have not been examined. The rheological properties of graphene cement composite have not been investigated as yet. Effect of shear rate range, resting time, superplasticizer and different test geometries on the rheology of graphene cement composite have not been explored. Therefore, in this study microstructural, rheological and mechanical properties of GCC were determined. Furthermore, Piezoresistive characteristics of GCC were investigated for various sizes of graphene flakes. Smart sensors using graphene based cement composites were developed which possess the damage-sensing characteristics and can significantly detect the propagation of cracks. This sensor is compatible with the concrete and can easily embed in concrete structures for the lifetime of the structural member. It will provide the real-time damage sensing characteristics as well as damage memorizing capability. The development cost of this smart sensor is very minimal hence, it will provide the economical solution for the health monitoring of concrete structures.

## 1.6 Outline of Thesis

This thesis consists of five chapters. These chapters are arranged in such a manner that it provides an easiness for the reader to not only understand the goals and scope of the research but also provides complete understanding about the method employed along with materials used to accomplish the research objectives. A brief description of each chapter is provided as under.

The introductory chapter, i.e. chapter 1 discusses the weaknesses of concrete material along with techniques used to overcome these weaknesses. Introduction of advanced nanotechnology in the civil engineering field is also discussed. It mentions the importance of the health monitoring of concrete structures and highlights the necessity of self-sensing cementitious material as well. Research question and problem statement are given in this chapter. Lastly, research objectives and the significance are also included in this chapter.

Literature review i.e. chapter 2 comprises of extensively reviewed academic writings pertains to the research title. Information regarding the application of nanotechnology and nanomaterials in civil engineering field has been presented in this chapter. Dispersion efficiency and its dependence on several parameters have also been provided along with microscale characteristics of nanomaterial-based cement composite. Moreover, flow characteristics of GNDs based cement composite and various mathematical models used to estimate the logical parameters are also presented. Mechanical properties followed by electrical and piezoresistivity properties of nanomaterial-based cement composite was given. Lastly, GNDs based cement composite sensors and their potential application are described.

Methods and procedures used to conduct this research have been explained in chapter 3. Materials, different equipment and procedure used in preparing GCC are described. Specimen preparation for the micro-scale characterization, rheological, mechanical and electrical properties of the composite material are presented. Moreover, experimental test protocols and testing standards are given as well. Design mixes and mix proportions are explained using tabular information. Lastly, the experimental setup for the potential application of GCC in concrete structures is described.

An in-depth analysis of the obtained results is presented in chapter 4 of this dissertation. This chapter is designed from the sequence of experimental work. Experimental and analytical analysis of the GCC has been presented. Effects of graphene flakes on the microstructural properties of the hydrated cement products have been explored. Flow properties of the nanomaterial-based cement composite have been calculated. Electrical and piezoresistivity characteristics of composite material have been observed. Practical application of the nanomaterial-based composite on the concrete reinforced beam and concrete-filled steel tubes has been discussed. All the presented results have been explained and discussed in this chapter.

Overall findings of the experimental work have been summarized in chapter 5. A correlation has been drawn between the obtained results and objectives of this research. The outcomes of the research study have been presented and recommendations for possible future work have been mentioned in this chapter.

# CHAPTER 2: LITERATURE REVIEW

## 2.1 Introduction

This chapter provides an overview of other related studies, their mode of approach and outcomes. The literature has been reviewed through a sound collection of related Ph.D. and Master thesis, journal articles, reports, conference papers, internet sources and books. Moreover, a substantial amount of relevant information has been collected through personal contact via emails, researchgate and at various forums with the key researchers around the world in this research area.

## 2.2 Nanoengineered Materials

Construction industry plays a key role in economic development of any country. Nowadays, concrete is the most widely used construction material (20-35 billion tons annually) (Barcelo et al., 2014) in the world and its use is increasing day by day because of its various beneficial properties such as high strength, durability and resistance to fire (Kodur & Sultan, 2003). However, its low tensile strength and brittleness are the major drawback of concrete (Birchall et al., 1981). In order to overcome the shortcomings of the construction field, researchers used different materials and techniques (Bessaies et al., 2016; Flatt & Houst, 2001; Hanehara & Yamada, 1999; Zhang et al., 2010). Chemical admixtures (Bessaies et al., 2016; Flatt & Houst, 2001; Hanehara & Yamada, 1999; Zhang et al., 2010) and supplementary cementitious material (Lothenbach et al., 2011; Richardson & Groves, 1997; Shi & Qian, 2000) and fibers, (Chung, 2001; Dawood & Ramli, 2011; Juárez et al., 2007; Topçu & Canbaz, 2007) were used to delay the development of micro-cracks and improve tensile strength. Size of these fillers diminished from the macro-scale to micro and now nanoscale. With advancement in nanotechnology now nano size cracks (pores with diameter < 20 nm) can control before developing micro size cracks (Konsta et al., 2010). There have been many recent studies on newly produced nanomaterials such as nanosilica, nanotitanium oxide, nanoiron oxide, carbon nanotubes and graphene oxide sheets (Abrishami & Zahabi, 2016; Cao et al., 2016; Chuah et al., 2014; Gong et al., 2014; Li et al., 2017). These newly developed engineered nanomaterials are classified according to their morphology: zero-dimensional (0D) nanoparticles (spherical shape and low aspect ratio) i.e. nanosilica, nano-alumina and nano-iron, one-dimensional (1D) fibers (straight and high aspect ratio) i.e. carbon fibers and CNTs; and two-dimensional (2D) sheets i.e. graphene and graphene oxide (Chuah et al., 2014). Figure 2.1 shows the schematic diagrams of these nanomaterials. These engineered materials are used in construction industry to overcome its weaknesses. Addition of these nanomaterials not only enhance their mechanical properties but also improves their electrical, thermal and electromagnetic properties as well (Sun et al., 2013).

(a) Wrapped honeycomb structure of zero-dimensional graphene

(b) Rolled honeycomb structure forms of one-dimensional graphene

(c) Single planar structure of two-dimensional graphene

(d) Stacked honeycomb structure of three-dimensional graphite

**Figure 2.1: Various structural forms of graphene (Kuilla et al., 2010).**

### 2.2.1 Zero-Dimensional Nanoparticles

Application of zero-dimensional nanoparticles in concrete and mortar are well explained by Sanchez &Sobolev (2010). Figure 2.1 (a) presents the wrapped honeycomb structure and schematic diagrams of zero-dimensional graphene nanoparticle. 143% increment in elastic modulus of mortar was noted by incorporating 5% of nano- alumina (n-$Al_2O_3$) by Li et al. (2006). Nano-alumina also move-down the porosity and move-up the density degree of the interfacial transition zone (ITZ). It was due to filling ability of nano-alumina in pores of loose structure around fine aggregate during calcium silicate hydrate (CSH) gel formation. However, the very limited effect was seen on compressive strength and no novel properties have been reported. Effect of Nano-iron (n-$Fe_2O_3$) in the mortar was explored by (Li et al., 2004a; Li et al., 2004b). Nano-iron enhanced not only the mechanical properties of the mortar but also electrical properties. 45% volume resistance of cement mortar decreases with 5% n-$Fe_2O_3$ as compared to that of the plain cement mortar (Li et al., 2004a). Li et al. (2004a) found that n-$Fe_2O_3$ did not decrease the electrical resistivity of mortar cubes and made them more durable mortar/structures. However, fractional variations of the resistance ($\Delta R/R_0$) versus stress (in stress direction) was sharp with more percentage of nanoparticles which makes it more sensitive to monitor its own compressive stress. Such sensing capabilities are invaluable for real-time, structural health monitoring and for the construction of smart structures (which don't use embedded or attached sensors) (Sanchez & Sobolev, 2010). Nano-$Fe_2O_3$ is a type of semiconducting material that absorbs energy, and the energy gap of nanoparticles is narrowed down when a compressive force is applied to the mortar specimen, which makes the electrons of nanoparticles transit easily to enhance the electrical conductivity of nanoparticles (Li et al., 2004a).

Li et al. (2006b) performed his study on the abrasion resistance of concrete by using nano-titania (n-$TiO_2$) and nano-silica (n-$SiO_2$). Around 90% abrasion resistance was enhanced by incorporating 5% binder content of n-$TiO_2$ and n-$SiO_2$. Authors determined that abrasion resistance, compressive strength and flexural strength of nanoparticles based concrete was increased as compared to plain concrete, however, with increasing percentage of nanoparticles degradation in compressive and flexural strength was observed. It was due to the presence of more micro-cracks and less workability in concrete (Li et al., 2006b). Senff et al. (2009) and Jo et al. (2007) used n-$SiO_2$ in a cement matrix. Nano-silica has a low aspect ratio (particle form), with average particle diameter 40 nm (Jo et al., 2007) and with a specific surface area of 300 $m^2/g$ (Senff et al., 2009). This huge surface area greatly affects the cement hydration, workability and flow of concrete. By containing 2.5 % nano-silica in mortars reduction of 32.8% in the spread diameter was observed as compared to plain mortar (Senff et al., 2009). Zero-dimensional nanoparticles lack the ability to arrest micro-cracks due to low aspect ratio, uniform mixing and weak zones formation in concrete increases especially when used in large amount.

### 2.2.2 One-Dimensional Nanoparticles

When compared to zero-dimensional nanoparticles, spherical shape one-dimensional nanofibers have high aspect ratio i.e. carbon nanotubes. Single wall carbon nanotubes have normally diameter in the range from 1-3 nm whereas, multi-walled carbon nanotubes have diameter of 5-50 nm (Agrawal et al., 2007). Length of these nanotubes varies from micrometre to centimetres, which form aspect ratio more than 1000 also multi-walled carbon nanotubes (MWCNTs) possessed surface area around 400 $m^2/g$ (Han et al., 2015). Han et al. (2015) in his review paper mentioned that CNTs have high elastic modulus 1TPa, tensile strength 10-60 GPa and 50-500 GPa for single and multi-walled respectively and electrical resistance 5-50 μΩcm. With these amazing properties, when CNTs were mixed with cement, it enhanced the properties of cementitious materials (Konsta et al., 2010). Konsta et al. (2010) noted the 25% increase in flexural strength of CNT-cement composite. Li et al. (2005) found the increase in compressive strength by 19%, flexural strength by 25% and 64% lower porosity by addition of 0.5% functionalized CNTs. Moreover, pores with size more than 50 nm diameter were 82% less as compared to plain cement concrete. Nevertheless, the problem with CNTs is non-uniform dispersion and weak bonding between CNTs and the cement mix. CNTs are produced in entanglements consisting of few hundred individual CNTs due to strong Van der Waals forces between particles cause formation of agglomeration and bundles in the composite. These agglomerate leads to the formation of defects and limits the modification effect (Ma et al., 2010). That’s why, even after decades of research on CNTs its full potential as reinforcement has been severely limited (Ma et al., 2010). Lv et al. (2013a), Cwirzen et al. (2009) and Cwirzen (2010) found the decline in mechanical properties of composite due to non-uniform dispersion, worst workability, higher inhomogeneity and porosity. At the higher concentration of carbon nanotubes, water demand of the paste increased and a higher concentration of the superplasticizer is required due to the high surface area and wrapping of CNTs with superplasticizer (Kowald & Trettin, 2004). Besides this, another problem which limits the use of CNTs is a weak bond between the CNTs and cement matrix. In a research conducted by Cwirzen et al. (2009), even by using surfactants and achieving uniform dispersion in the mix, no major effect was recorded on mechanical properties of the composite mix in contrast with pure cement mix. It was most probably due to the very low bond strength of the CNT-cement matrix, and nanotubes were easily pulled out in fractured cement paste specimens. It was suggested by Cwirzen et al. (2009) that functionalization, use of surfactants, superplasticizer, polymers and polar impurities should provide chemical bonding with cement beside the uniform dispersion. These nanotubes are considered as graphene sheets rolled into a tube shape. Rolled honeycomb structure forms one-dimensional graphene i.e. carbon nanotubes are given in Figure 2.1 (b).

### 2.2.3 Two-Dimensional Nanoparticles

In contrast to CNTs, graphene and graphene oxide are the two-dimension sheet-like structure and have large surface area. GO has a thickness of single atomic layer while lateral dimension up to tens of micrometres, which provide large surface area and high aspect ratio (Kim et al., 2010). It has been observed by the researchers that by incorporating GO, polymer properties i.e. electrical, thermal and gas barrier remarkably enhanced (Kim et al., 2010; Ramanathan et al., 2008). Furthermore, Lv et al. (2013a) reported that a rise in tensile strength by 78.6%, flexure strength by 60.7% and compressive strength by 38.9 % with 0.03% dosage of GO with 29.75% oxygen content in cement mortar. At the microscopic level, they observed the flower-like crystals, which benefits enhanced toughness. Pan et al. (2015) used 0.05% GO by weight of cement in the mix design. 41.7 % reduced workability was found in mini-slump test, due to the large surface area of GO, same as slump reported for the workability of CNT-cement paste (Collins et al., 2012) i.e. workability reduced to 48.9% by addition of 2% of CNT with water to cement ratio of 0.5. GO is the antecedent of graphene with a mixture of carboxyl, epoxy and/or hydroxyl functionalities (Wilson et al., 2009). Furthermore, the interatomic spacing in GO is, to an accuracy of better than 0.5%, identical to that of graphene (Wilson et al., 2009). Extensive research has been conducted on GO-based cement composites by the researchers, however, very less focus is given to graphene cement composite.

In 2004, Novoselov et al. (2004) extracted single atom thick crystallites from bulk graphite. They pulled graphene layer from graphite and transferred them onto thin silicon dioxide on a silicon wafer in a process called Scotch Tape technique (Novoselov et al., 2004). This method can achieve the thickness of graphene up to 0.00001 inches as stated by Zhang et al. (2005). In 2010, Geim and Novoselov received Nobel Prize in Physics for their research on graphene. Graphene is the thinnest material of the earth (Ferrari et al., 2006; Lee et al., 2008). It is a plane ribbon of $sp^2$ interacted carbon which is tightly confined into a honeycomb lattice. Boehm et al. (1962) made a conclusion that the graphene is one of the allotropes of carbon with two-dimensional properties. Graphene has a single planar sheet of $sp^2$ and densely packed in a honeycomb. The honeycomb pattern of graphene is looked similar with another allotrope of carbon (Kuilla et al., 2010). The structural relationship between graphene and various other forms are shown in Figure 2.1. Figure 2.1 (c) shows that graphene is arranged in a single planar sheet and Figure 2.1 (d) presents the stacked honeycomb structure forms of three-dimensional graphite. Each atom has four bonds, one σ-bond with each of its three neighbours and one π-bond that is oriented out of the lace. Graphene's hexagonal can be regarded as two interleaving triangular lattices. As mention before, graphene's stability is due to its high packed carbon atoms and $sp^2$ orbital hybridization- a combination of orbitals s, px and py that constitute the σ-bond and pz the π-bond. The reason for the presence of electrical properties of graphene is the half-filled band that permits free-moving electrons. The π-bonds hybridize together to form the π-band and π*-band which responsible for the electrical properties of graphene (Cooper et al., 2012).

Recently, this 2D flat sheet of carbon has conquered huge amount of interest in the scientific community. Because it possesses some amazing and extraordinary properties such as huge specific surface area (2630 $m^2\ g^{-1}$) (Zhu et al., 2010), high intrinsic strength (130 GPa) (Lee et al., 2008), sensitivity to detect single gas molecule (Katsnelson et al., 2009), firm Young's module (~1.0 TPa) (Geim & Novoselov, 2007; Lee et al., 2009; Mak et al., 2010) and high thermal conductivity (~5000 $Wm^{-1}K^{-1}$) (Balandin et al., 2008; Lin et al., 2010). These unique and tremendous characteristics of graphene opened a new window for a wide range of applications. The large exposed surface area of graphene sheets have strong capability to form a strong physical and chemical bond with cement matrix. Rafiee et al. (2010) mentioned that unzipping the multi-walled carbon nanotubes into graphene sheets results in significant improvement because of an extraordinary increase in interfacial area and geometry of graphene sheets as compared to multi-walled carbon nanotubes. Rafiee et al. (2010) also found that 30% increment in Young's modulus and 22% rise in ultimate tensile strength of graphene-composite against the same amount of multi-walled carbon nanotubes composite. Conversely, graphene has a very high production cost and also have difficulties in the dispersion. Therefore, application of graphene is restricted and limited in civil infrastructure especially like bridges, dams and buildings due to low scale production (Alkhateb et al., 2013). Actually, graphene sheets are naturally available and only required to exfoliate them from the graphite (Segal, 2009). Exfoliation of graphite into graphene can be obtained by using chemical and mechanical techniques (Novoselov et al., 2012). For the mass scale production of graphene, the optimum method will be chemical oxidation and reduction of graphite (Aunkor et al., 2015). This method is considered as faster, easier, scalable, economic, facile and dynamic as compared to other methods (Aunkor et al., 2015). Keeping in view the importance of uniform dispersion of nanomaterials, next section discusses as to how we would achieve the full benefits of uniformly dispersed graphene in civil engineering.

## 2.3 Dispersion of Nanoparticles

Dispersion is the major challenge involved in fabricating cementitious nanocomposite because van de Waals force causes agglomeration of the nanoparticles (Grobert, 2007). Dispersion of nanomaterials in aqueous solution is an important step and significantly alters the hardened properties (Ubertini et al., 2014). In aqueous solution, nanomaterials tend to precipitate or float on the surface. Graphene is hydrophobic in nature and it formed the agglomerates in aqueous solution and caused non-uniform dispersion (Munz et al., 2015). According to Hamann & Clemens (1973), a poor dispersion will lead to the formation of a defect in the composite matrix and limit the effect of the nanoparticles. Most of the research on the dispersion of graphene and graphite nanoparticles was focused on surface modification, such as oxidation, or inclusion of other nanoparticles in the suspension. Geng et al. (2009) oxidized the graphene nanoplatelets (GNPs) to make graphene oxide, then reduced these graphene oxidized particles, and dispersed them in water. Li et al. (2014) also wrote that the oxygen containing functional groups on the graphene oxide could lead to stable dispersions due to electrostatic repulsion between the oxidized graphene oxide particles. As noted by Peyvandi et al. (2013) covalent surface modification, including oxidation, damages the atomic structure of the graphene flakes and can reduce the strength. Other methods of dispersion are needed to preserve the structure of the graphene flakes. This field is yet to be explored as minimal research on the dispersion of non-covalently modified GNPs in water has been reported. Therefore, to improve the dispersion of graphene flakes keeping the atomic structure safe in the cement matrix, different techniques and the effect of different type of solvent has been reviewed in this section.

### 2.3.1 Dispersion Using Dispersant

As graphene flakes are hydrophobic and tend to form coagulation in the aqueous solution, therefore, numerous researchers used different dispersants to obtain stable suspension. Stankovich et al. (2006) reduced graphite oxide (RGO) flakes in the presence of polysodium styrenesulfonate. These polysodium styrenesulfonate coated graphite nanoparticles, which consisted of multiple layers of graphene, remained in suspension.

Lu et al. (2010) used polyelectrolytes as dispersal aids with GNPs in water. Lu et al. (2010) wrote that this method of dispersal preserves the structure of the GNPs and allows the full exploitation of the properties of these nanoparticles. Shah et al. (2009) studied the dispersion of carbon black (CB) in the presence of five dispersants including *t*-octylphenol decaethylene glycol ether (Triton X-100, MW = 647), sodium dedecylbenzenesulfonate (NaDDBS, MW = 348.47), Tween 80, Dispex G40 and Dispex N40. They concluded that optimum dispersant was Triton X-100 as it showed the highest absorption peak in UV-vis absorption spectra as shown in Figure 2.2. Triton X-100 is a surfactant molecule containing an aliphatic chain and a short hydrophilic PEG unit. Binding of surfactant molecules to the surface of carbon nanomaterial is mostly driven by hydrophobic interactions.

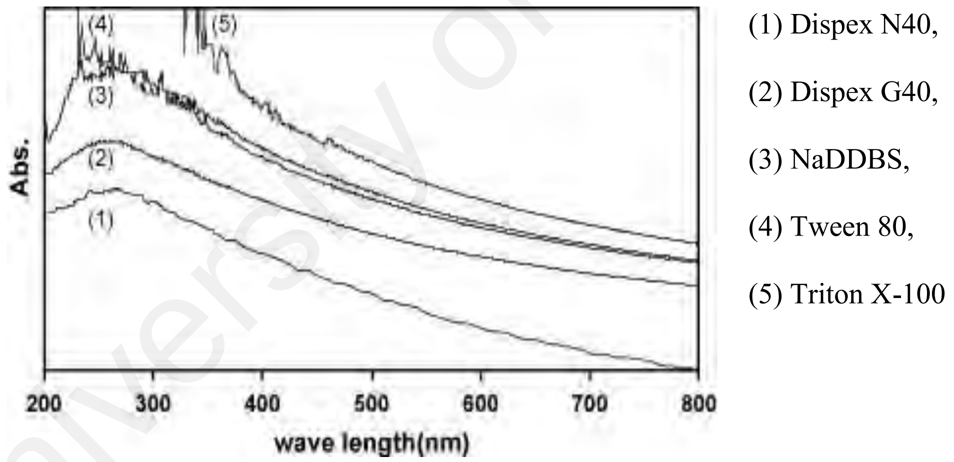

**Figure 2.2: UV–vis absorption spectra of different kinds of dispersant (Shah et al., 2009).**

Sixuan (2012), used the acetone, Gum Arabic and Darex Super 20 solvent as a dispersant for graphite flakes in water solution. The stability and homogeneity of graphite suspensions with respect to time using various dispersing agents were tested by visual inspection. Figure 2.3, presents the dispersion of graphite flakes in different dispersants. Stability of graphite flakes were assessed by observing the colour of the solution. Usually, the dispersant and distilled water are colourless and after inducing the graphene the colour changed to black. Based on Figure 2.3, the graphite flakes in Darex Super 20 and Gum Arabic showed the good stability and colour of the solution remained unchanged after 30 min of mixing. However, in acetone and water solution the graphite deposited at the bottom of the test tube. Gum Arabic is a natural polysaccharide and available in the form of white powder. It is extremely soluble in the water. For Gum Arabic, its weak acidity made it reactive in the alkaline cementitious environment, which resulted in the generation of excess water during mixing. It brought watery mixture with light graphite nanoparticles floating on top. Besides, Darex Super 20 is the naphthalene sulfonate based high water-reducing superplasticizer and exhibited a good stability dispersant with minimal alteration on the fresh mixture. Therefore, Sixuan (2012) concluded that Darex Super 20 is the best dispersant for the graphite flakes in cement matrix.

(a) 5 min (b) 30 min

**Figure 2.3: Stability test for graphite suspension in various dispersant of liquid (Sixuan, 2012).**

In 2014, Wotring (2014) investigated the dispersion behaviour of GNP in water with high range water reducing admixture. Water-cement (w/c) ratio was kept as 0.5, graphene dosage was 0.1% by weight of cement paste and AdvaCast 575 polycarboxylates based high range water reducing admixture in the range of 0-10 times the weight of graphene flakes. According to Wotring (2014), the water reducing agent (WRA) was able to maintain the stability of graphene in the solvent. When the dosage of water reducing agent increased, the stability also increased. By visual observations, it was found that the WRA to GNP ratio of 3% was stable until 7 days as shown in Figure 2.4 (Wotring, 2014). While good stability was observed after 24 hours for other ratios of WRA to GNP.

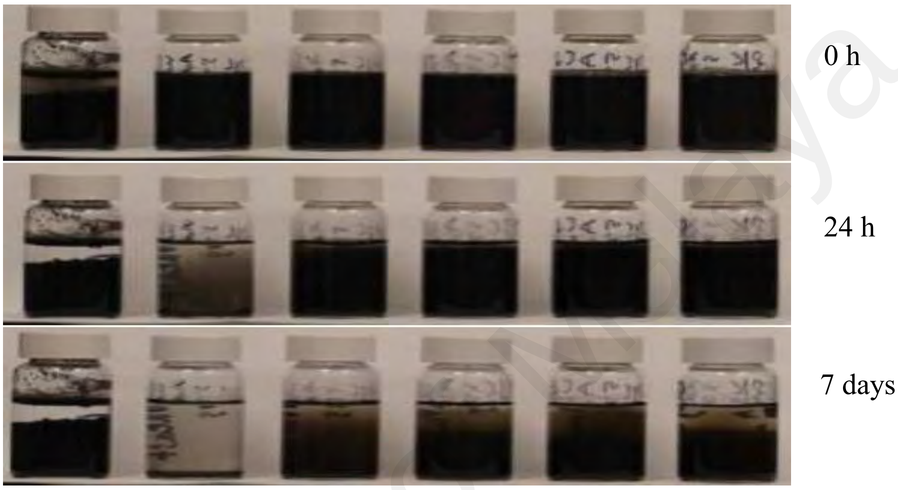

From left to right, the vials have WRA/GNP ratios of 0, 1, 1.5, 2, 2.5 and 3

**Figure 2.4: Effect of the presence of water reducing agent to the dispersion of graphene sedimentation. (Wotring, 2014).**

Recently, Silva et al. (2017) used the analytical grade isopropanol alcohol blended with the expanded graphite structures in a 1-1 ratio. Authors found that the combination of multilayer graphene sheets and isopropanol produced the excellent dispersion. Han et al. (2017) used the polycarboxylate superplasticizer (Sike ViscoCrete 3301E) to disperse multi layered graphene in aqueous solution and found that the graphene flakes did not form agglomerations.

Dispersion mechanism for dispersant and graphene flakes was explained by Sixuan (2012). Sixuan (2012) stated that the organic molecules in the dispersant are negatively-charged and absorbed mainly at the interface of water and graphite. The graphite surface initially possessed the residual charges on their surfaces. When these graphite nanoparticles were mixed with liquid solution, they formed the flocculated structures. The flocculation of the graphite particles occurred due to the electrostatics interactions exerted by the adjacent graphite particles of the opposite charges as seen in Figure 2.5 (a). After that, the dispersant was used to neutralize these residual charges and made the entire surface to carry the same charges. Lastly, the particles of graphite flakes remained fully dispersed in the suspension of the liquid due to the repulsion of the graphite nanoparticles as seen in Figure 2.5 (b) (Sixuan, 2012).

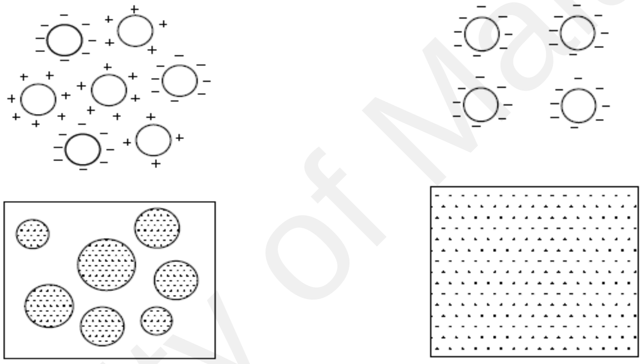

(a) Flocculated graphite flakes (b) Uniformly dispersed graphite

**Figure 2.5: Schematic diagrams of dispersion action for graphite nanoparticles (Sixuan, 2012).**

### 2.3.2 Dispersion using Ultrasonication

The sonication is the act of applying energy to agitate particles in a sample. The ultrasonication is referred to the waves having frequency more than 20 kHz. The primary part of a sonication device is the ultrasonic electric generator. This device creates a signal (usually around 20 kHz) that powers a transducer and it converts the electric signal to mechanical vibrations. These vibrations are further amplified by the sonicator and passed to the probe (Sixuan, 2012). The sonication probe transmits the vibrations to the solution. The rapid movement of the probe creates cavitation effect. Cavitation occurs when the vibrations create a series of microscopic bubbles in the solution, pockets of space wedged between the molecules that form and collapse continuously under the weight of the solution. Constant formation and collapse of thousands of these bubbles create the powerful waves of vibration that pass through the solution and break apart the particles (Li et al., 2007). The energy that had been delivered to the graphene flakes respectively lead to the wreckage of the interlayer π-bond. Hence, exfoliated graphene flakes can be attained with higher aspect ratio, decreased thickness and improved mobility of particles as shown in Figure 2.6. The maximum size of the bubble being produced in liquid is dependent on the frequency of ultrasonication. A low-frequency ultrasonication will generate large size bubbles and vice versa. Higher energy forces are being produced upon the collapse of the large-sized bubbles in the solution (Sixuan, 2012).

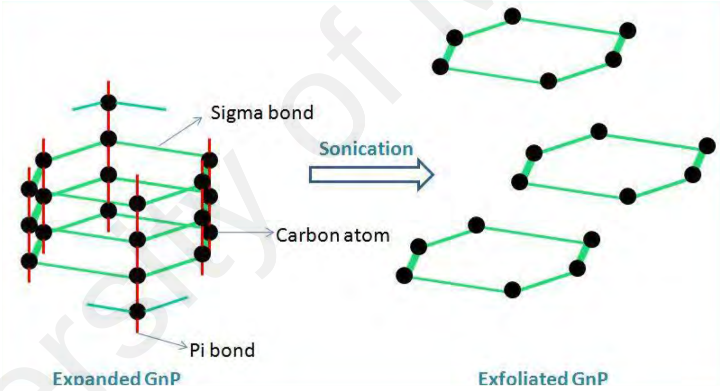

**Figure 2.6: Mechanism of graphene dispersant after ultrasonication (Sixuan, 2012).**

In 2014, Mehrali et al. (2014) sonicated graphene flakes in distilled water with a high-powered probe sonicator. The graphene flakes remained stable in suspension for 600 hours. Han et al. (2017) used the ultrasonication for 1 hour to achieve the uniform dispersion. Silva et al. (2017) employed the analytical grade isopropanol alcohol blended with the expanded graphite structures in 1-1 ratio and solution was further ultra-sonicated for 2 hours and achieve the excellent dispersion.

### 2.3.3 Assessment of Dispersion Efficiency Using UV-vis Spectrometry

Ultraviolet-visible spectroscopy (UV-vis) refers to absorption or reflectance spectroscopy in the ultraviolet-visible spectral region. Jiang et al. (2003) used the UV-vis measurements for the quantitative characterization of the colloidal stability of CNTs dispersion. In UV-vis spectral range carbon nanomaterials showed the absorption characteristics and it is attributed to the electronic transitions between the bonding and anti-bonding π orbital. (Liu & Horrocks, 2002). Jäger et al. (1999) stated that the σ–σ* transitions are anticipated in the ultraviolet range of 60–100 nm, meanwhile the π–π* transitions observed in 180–280 nm range. Due to this reason application of UV-vis spectroscopy has been utilized tremendously by the researchers for rGO as shown in Table 2.1. Wang et al. (2016) used graphene flakes in cement composite with water to cement ratio of 0.35, GNP-cement ratio of 0.05% by weight of cement with different concentration of dispersant Methylcellulose (MC) ranging from 0.2 g/L to 1.0 g/L. It was noted in Figure 2.7 that for different mixes the highest peak of GNP-suspension was found at 260 nm wavelength in UV-vis spectra. Similarly, an absorption peak at 270 nm was observed in the UV-vis absorption spectrum of graphene, which is generally regarded as the excitation of the π-plasmon of the graphitic structure (Aunkor et al., 2015). Moreover, Aunkor et al. (2015) state that the absorption peak value depends on the concentration of dispersed graphene sheets. Shah et al. (2009) studied the dispersion of carbon black using UV-vis spectroscopy and determined the increase in UV-vis absorption related to the surface area of nanomaterials (Figure 2.8). They used four types of carbon black with the varying surface area and determined the highest dispersion values for CB having highest surface area. Chen et al. (2011), Thakur & Karak (2012), Lei et al. (2011), Li et al. (2013), and Xu et al. (2010) reported the absorbance peaks for rGO near 271 nm using UV-vis spectroscopy as shown in Table 2.1.

**Table 2.1: UV-vis absorbance peak (C=C bonds) of reduced graphene oxide (rGO) at different reduction methods reported in previous literature.**

| **π-π* transition of rGO** | **References** |
|---|---|
| 275 nm | Lei et al., 2011 |
| 273 nm | Li et al., 2013 |
| 273 nm | Lei et al., 2011 |
| 272 nm | Mei & Ouyang, 2011 |
| 271 nm | Xu et al., 2010 |
| 271 nm | Wang et al., 2011 |
| 270.9 nm | Thakur & Karak, 2012 |
| 270 nm | Chen et al., 2011 |
| 269 nm | Khai et al., 2013 |
| 269 nm | Peng et al., 2012 |
| 269 nm | Tran et al., 2014 |
| 267 nm | Bose et al., 2012 |
| 266 nm | Pham et al., 2012 |
| 265 nm | Gurunathan et al., 2013 |
| 264 nm | Zhang et al., 2010 |
| 263 nm | Khanra et al., 2012 |
| 261 nm | Zhu et al., 2010 |
| 260 nm | Liu et al., 2011 |

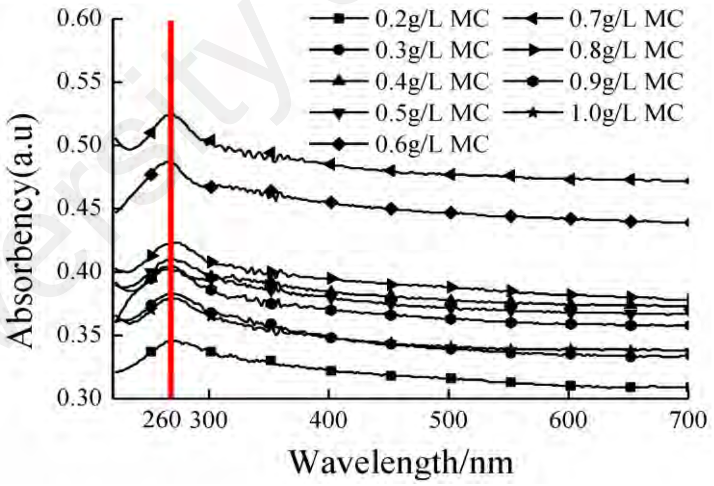

**Figure 2.7: UV-Vis spectroscopy absorbance spectra of GNP suspension with different methylcellulose (MC) concentrations (Wang et al., 2016).**

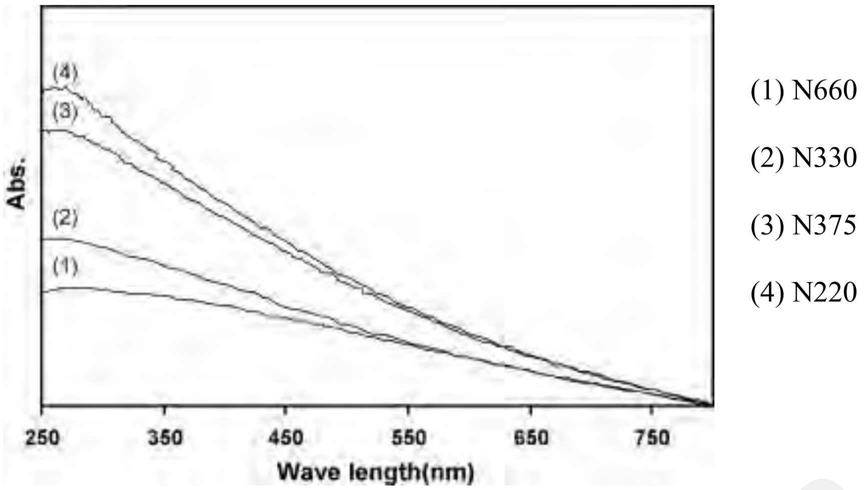

**Figure 2.8: UV–vis absorption spectra of different types of CB dispersed in water (Shah et al., 2009) .**

Therefore, it is concluded from the literature of dispersion section that ultra-sonication technique provides the uniform dispersion to graphene flakes. Furthermore, the use of dispersant i.e. polycarboxylate based high range water reducing admixture will help in exfoliation of graphene flakes. Additionally, UV-vis spectroscopy method is widely accepted to monitor and assess the dispersion of nanomaterials in aqueous solution. A detailed discussion on the uniform and stable dispersion efficiency and mechanism of graphene flakes has been provided in section 2.3. Afterwards, it was mixed with cement matrix to form the smart materials i.e. graphene based cement composite. In next section, the influence of nanomaterials on the microstructure of cement composite will be critically reviewed.

## 2.4 Characterization of Graphene Cement Composites

Characterization refers to the procedures by which a material's properties and structure are explored and measured. It is an essential process in materials science without which scientific understanding about the materials cannot be established. The microstructure is a descriptor to define the characteristics of the materials. The microstructure of cement composites has great influence on the physical and mechanical properties of the hardened concrete structure. Any alteration in the microstructure will describe the new characteristics of materials. Therefore, it is important to investigate the characteristics of the nanomaterial based cement composite. The characteristics of nanomaterials based cement composite were explored by (a) Thermogravimetric analysis (TGA); (b) Infrared spectroscopic analysis; (c) X-ray diffractometric (XRD) analysis; and (d) Morphological analysis.

### 2.4.1 Thermogravimetric Analysis (TGA)

Thermal analysis is a technique that measures the change in the properties of materials as a function of temperature and these changes are called thermal events (Leng, 2009). Thermogravimetric analysis is mainly used to examine the decomposition of materials by monitoring mass change with temperature with a constant rate of heating and as a function of time. TGA was used to determine the behaviour of construction materials at elevated temperature (Alarcon et al., 2005; Midgley, 1978). In the analysis, TGA curves are able to provide a quantitative measurement of mass change in materials associated with thermal degradation. According to available literature, few reactions occur due to heating of the hardened cement materials (a) 180-300 $^{O}$C bonded water loss from CSH and carboaluminate hydrate, (b) 430-480 $^{O}$C dehydroxylation of portlandite (calcium hydroxide) and (c) 600-780 $^{O}$C decarbonation of calcium carbonate (Bernal et al., 2016; Karim et al., 2016; Khoury, 1992; Nonnet et al., 1999; Ortego et al., 1989; Xu et al., 2015; Zhou & Glasser, 2001). A typical TGA curve for cement composite at 28-day age is presented in Figure 2.9. Important regions were marked in Figure 2.9 and weight loss corresponding to these regions are marked as 1, 2 and 3. Point 1, 2 and 3 are in the region from 180-300 $^{O}$C, 430-480 $^{O}$C and 600-780 $^{O}$C respectively. Gravimetric changes due to decomposition of $Ca(OH)_2$ and $CaCO_3$ are indicated by the regions 2 and 3 marked in TGA plot. The presence of $CaCO_3$ is also ascribed from the conversion of hydrated lime due to carbonation. Region 2 is attributed to the removal of $H_2O$ from the $Ca(OH)_2$ while region 3 corresponds to the removal of $CO_2$ from the $CaCO_3$. Law of conversion of mass calculations was used to determine the amount of calcium hydroxide (CH) from the mass changes of TGA plot (Murugan et al., 2016). Chemical reactions are assumed as

$$Ca(OH)_2 \rightarrow CaO + H_2 \qquad (2.1)$$

$$CaCO_3 \rightarrow CaO + CO_2 \qquad (2.2)$$

$$Ca(OH)_2 + CO_2 \rightarrow CaCO_3 + H_2O \qquad (2.3)$$

The molecular mass ratio was used to measure the amount of CH. Values from Equation 2.1 and Equation 2.3 were added to estimate the total amount of CH (Murugan et al., 2016).

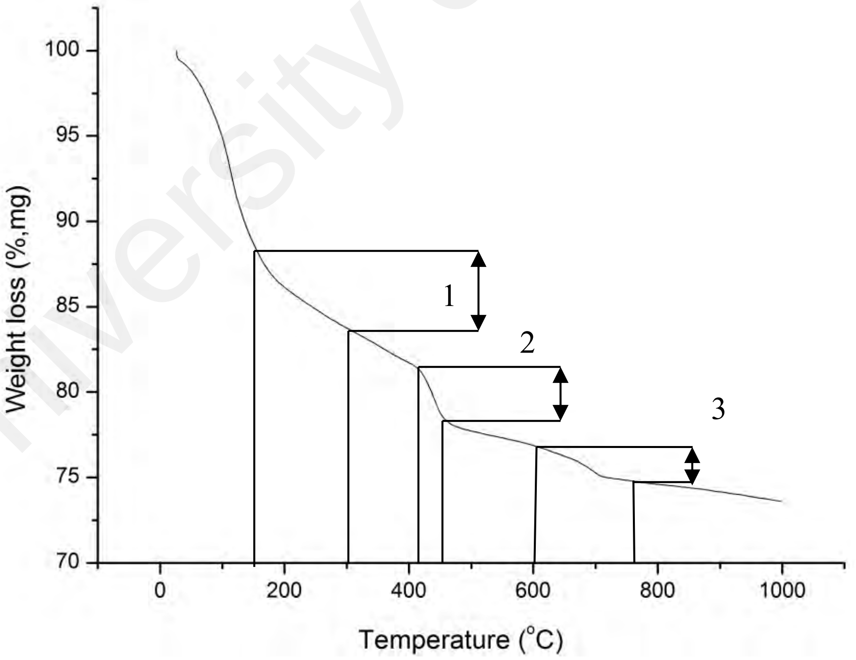

**Figure 2.9: TGA curve of the cement paste (Kakali et al., 2000).**

Murugan et al. (2016), performed experimental work by using reduced graphene oxide (rGO), n-$Al_2O_3$ and n-$SiO_2$ in cement composite. Reduced graphene oxide, nano-alumina, and nano-silica were added 0.02, 0.20 and 4.0 % by weight of cement respectively. The TGA curves of the cement paste with different nanocomposites and the control paste cured for 28 days are shown in Figure 2.10. It was noted that potential quantity of portlandite was approximately same in rGO and n-$Al_2O_3$ pastes in contrast with the control matrix. However, in the case of n-$SiO_2$, less amount of portlandite was recorded due to the pozzolanic reactivity which caused rapid conversion of CH to CSH products.

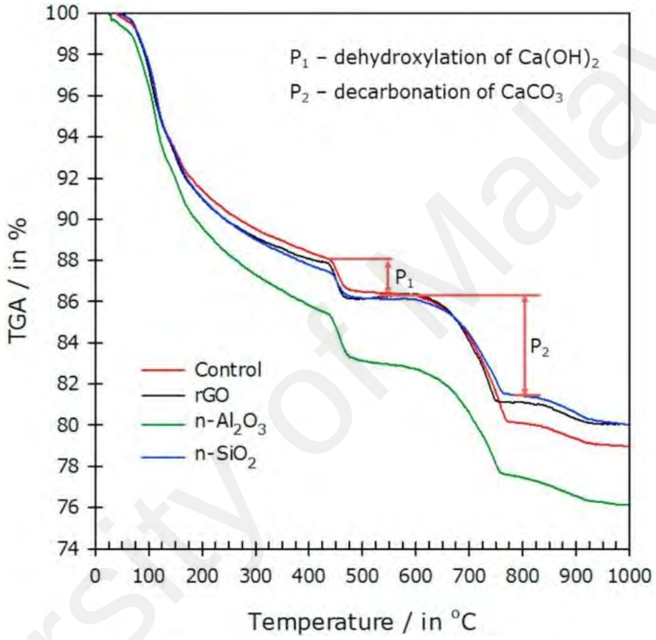

**Figure 2.10: TGA curves of the different pastes cured for 28 days (Murugan et al., 2016).**

Effects of pristine graphene oxide (PGO) and graphene oxide flakes (GONPs) (produced from ball-milling) were investigated by Sharma & Kothiyal (2016). Sharma & Kothiyal (2016) used 0.10% and 0.125% of PGO and GONPs in mix design with water cement ratio of 0.45. Figure 2.11 presents the TGA curves for control sample, 0.125% of PGO-cement mortar nanocomposites (PGO-CNCs) and GONPs-CNCs obtained after 90 days of curing. The weight loss corresponding to CH in control mix, 0.125PGO-CNC and 0.125GONP-CNC were calculated to be 12.7%, 10.8% and 5.3% respectively. The final weight loss in TGA curve for graphene oxide based cement mortar was slightly more as compared to control mix due to the inherent thermal conductive properties of graphene oxide as shown in Figure 2.11 (Sharma & Kothiyal, 2016).

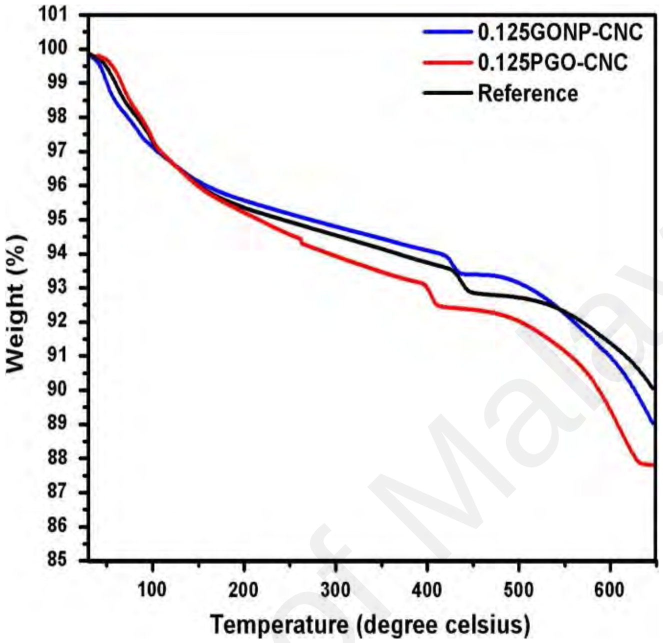

**Figure 2.11: TGA curves of different samples after 90 days of curing (Sharma & Kothiyal, 2016)**.

Wang et al. (2016) observed the variation in TGA curve after addition of graphene to the cement paste. Figure 2.12 showed the TGA curve for plain cement and GNP-cement composite at 7-day and 28-day after casting as investigated by Wang et al. (2016). According to Wang et al. (2016), the curves of two samples had a similar trend at various ages, however, the graphene flakes accelerated the hydration process of cement. At 7-day, the contents of hydrated cement products i.e. CSH and $Ca(OH)_2$ in GNP-cement composite was higher than the plain cement phase. After 28 days of curing, the content of both samples was nearly equal. Therefore, it was concluded that GNPs enhanced the hydrated cement products at an early age.

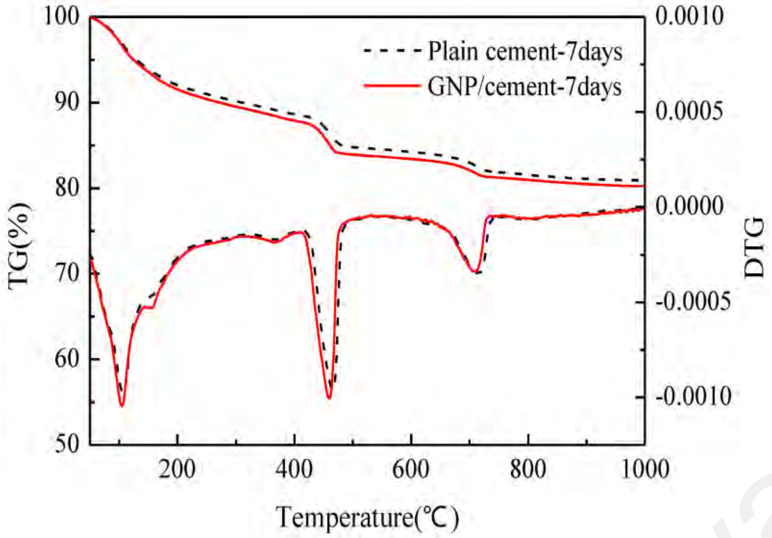

(a) 7- days

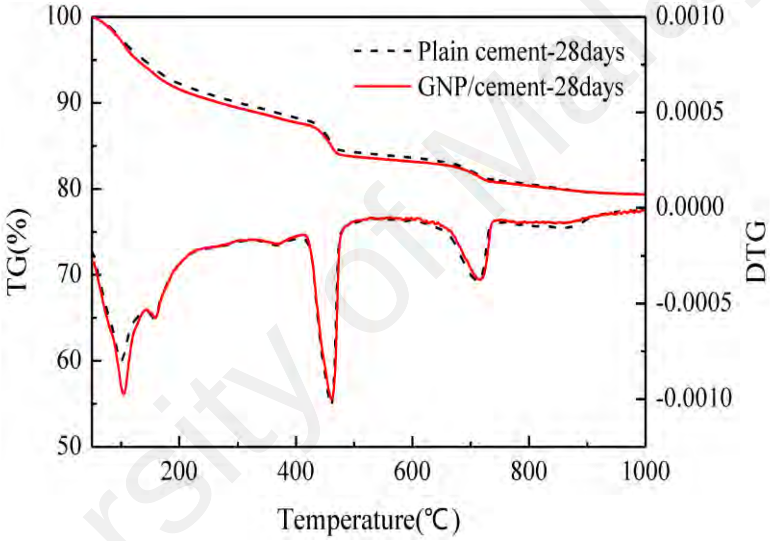

(b) 28-days

**Figure 2.12: TGA curves of plain and GNP-cement composite at various ages (Wang et al., 2016).**

### 2.4.2 Infrared Spectroscopic Analysis

Vibrational spectroscopy is a technique to analyse the structure of molecules by examining the interaction between electromagnetic radiation and nuclear vibrations in molecules. According to Leng (2009), vibrational spectroscopy used electromagnetic waves with longer wavelengths, in the order of $10^{-7}$ m. Vibrational spectroscopy detects the molecular vibrations by the absorption of infrared light or by the inelastic scattering of light by a molecule (Leng, 2009). FTIR is an infrared spectroscopy in which the Fourier transform method is used to obtain infrared spectrum in a whole range of wavenumbers. It provides the useful information about the possible chemical and physical interaction (Mollah et al., 2000). FTIR spectra of 28-day cement paste and graphene are given in Figure 2.13. The spectrum of a control sample (Figure 2.13 (a)) showed peaks at 3375 $cm^{-1}$ (H-O-H stretching of CSH), 1014 $cm^{-1}$ (Si-O asymmetric stretching vibrations of CSH), 460 $cm^{-1}$ (Si-O in-plane vibration of CSH), 690 $cm^{-1}$ (Si-O out of plane vibration of CSH), 1410 $cm^{-1}$, 874 $cm^{-1}$ and 712 $cm^{-1}$(C-O stretching of $CO_3^{-2}$), 1630 $cm^{-1}$ and 3430 $cm^{-1}$ (H-O-H stretching of ettringite), 695 $cm^{-1}$ (S-O bending vibration of $SO_4^{-2}$), 2299 $cm^{-1}$ and 2075 $cm^{-1}$ (C=O, C=C, O=O) (Bensted & Varma, 1974; Horgnies et al., 2013; Mollah et al., 2000; Ortego et al., 1989). In graphene spectra (Figure 2.13 (b)) besides these peaks two further peaks were present at 1570 $cm^{-1}$ ($sp^2$ hybridized C=C), 2918 $cm^{-1}$ and 2850 $cm^{-1}$ (symmetric and asymmetric stretching vibration of $-CH_2$) point out the $sp^2$ network (Naeimi & Golestanzadeh, 2015). According to Mollah et al. (2000), FTIR spectra can be divided into three regions; a) water region (>1600 $cm^{-1}$), the sulphate region (1100-1150 $cm^{-1}$), and the material region (<1000 $cm^{-1}$). Spectral data varies by the incorporation of different nanomaterials and analyses of these changes will yield the useful information. Shifting of these bands implies the stronger bonding, formation of hydrated products and polymerization in hydrated products (Mollah et al., 2000; Smith, 2011). Variation in the absorbance intensities provides the information about the quantity of material (Smith, 2011).

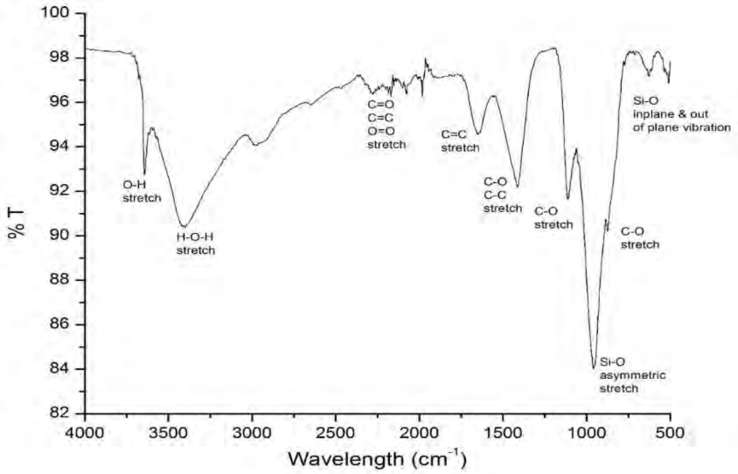

(a) Control sample (28-day cement paste)

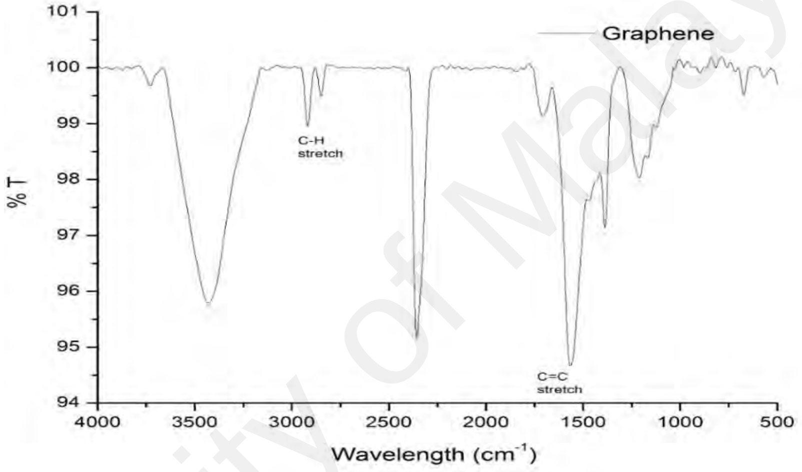

(b) Pure Graphene flakes

**Figure 2.13: FTIR spectra of control sample (plain cement paste) (Li et al., 2005) and graphene (Aunkor et al., 2015).**

Li et al. (2005) employed FTIR analysis on three different mixes of cement paste i.e. plain cement paste, untreated carbon fibres cement paste and surface treated with carboxylic carbon nanotubes-cement paste. Water-cement ratio was kept as 0.45 and carbon nanotubes and carbon fibres were added 2% by weight of cement. In Figure 2.14 four FTIR spectra were given, three spectra were associated with cement pastes and one related to treated carbon nanotubes. Plain cement paste spectra served as a reference for other mixes as given in Figure 2.14 (d). It was noted that untreated carbon fibre cement paste spectra were similar to plain cement paste as shown in Figure 2.14 (c). Hence, no chemical interaction and new phase formation were recorded. As surface treatment of carbon nanotubes involved chemical interaction. Therefore, in Figure 2.14 (a) spectra displayed the peaks at 1733 $cm^{-1}$ and 1118 $cm^{-1}$ corresponds to C=O stretching of carboxylic acid and C-OH stretch of hydroxyl. These peaks confirmed that various oxygen containing groups attached to the surface of CNTs. When these surface treated carbon nanotubes were added to cement paste chemical interaction took place as shown in Figure 2.14 (b). A positive shift in a spectral peak at 1756 $cm^{-1}$ by 22 $cm^{-1}$ indicated the possible existence of carboxylate and disappearance of a peak at 3643 $cm^{-1}$ specified the chemical interaction between hydrated cement products with oxygen groups of carboxylic acid attached with carbon nanotubes. Also, the variation in spectral shape in CSH region indicates the variation in CSH phases due to functionalization of carbon nanotubes.

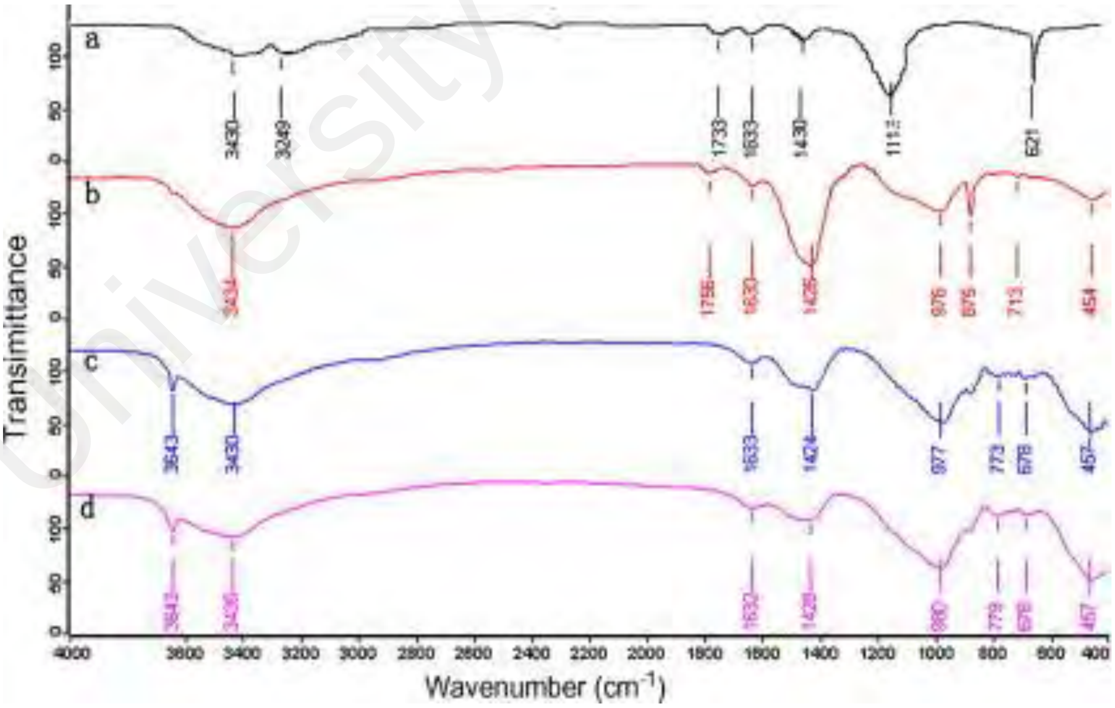

(a) carboxylic carbon nanotubes ; (b) carboxylic carbon nanotubes-cement paste ;
(c) carbon fibres cement paste ; (d) plain cement paste

**Figure 2.14: Typical FTIR spectra of 90-day cement matrix composites (Li et al., 2005).**

The influence of rGO, n-$Al_2O_3$ and n-$SiO_2$ in cement composite was investigated by Murugan et al. (2016). Figure 2.15 presents the IR spectra of these cement pastes. Authors did not notice any major difference in IR spectra's. In these spectra's, free water peak was found at ~1645 $cm^{-1}$ attributed to O-H bend, ettringite peak at ~1118 $cm^{-1}$ due to S-O stretch, silicates peaks at ~ 950 $cm^{-1}$ due to Si-O asymmetric stretch in all cement pastes after 28-days of curing. Calcite peaks which are indicative of carbonation were recorded at ~1414 $cm^{-1}$ and ~874 $cm^{-1}$ attributed to C-O stretch and C-O bend vibration respectively in all mixes.

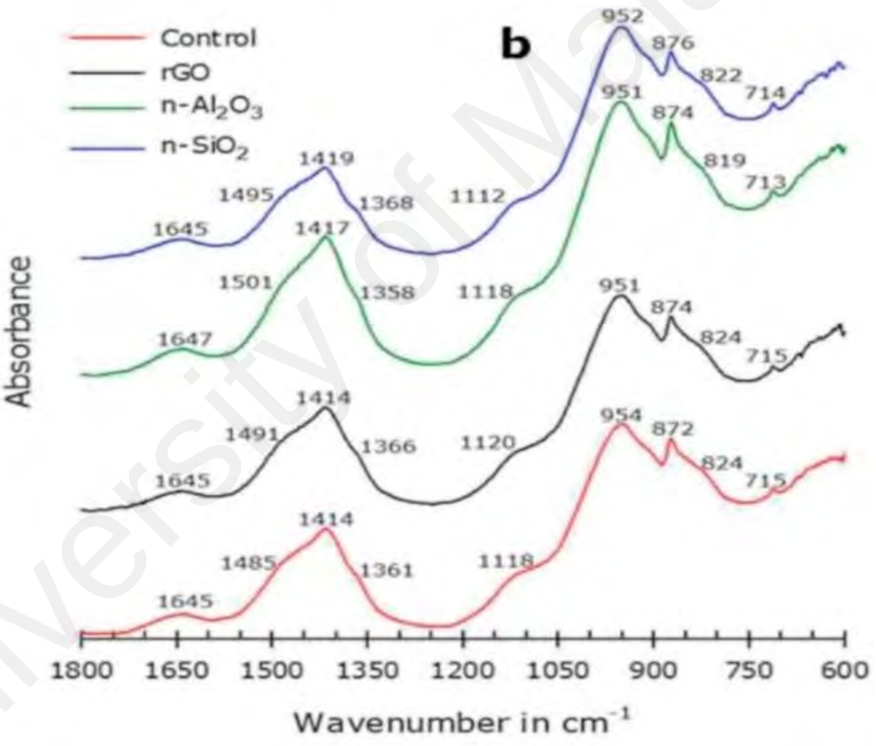

**Figure 2.15: FTIR spectra of the different pastes cured for 28 days (Murugan et al., 2016).**

Early age hydration process and influence of superplasticizer (SP) i.e. sodium lignosulfonate on cement paste was examined using infrared spectroscopic by Mollah et al. (2000). Specimens were studied immediately in the range of 2 min to 24 hours after preparation. Water to cement ratio was maintained at 0.4 and SP dosage by 1% of cement weight. When hydration process started for cement then, infrared spectral data altered as observed in Figure 2.16. Mollah et al. (2000) determined that due to hydration reaction of cement paste few peaks appeared in water region i.e. > 1600 cm$^{-1}$. In air cured specimen (Figure 2.16 (c)) hydrogen-bonded OH species (O-H–O-H) were found at 3405 cm$^{-1}$, while OH band from $Ca(OH)_2$ was seen at 3645 cm$^{-1}$. Argon cured cement specimen (Figure 2.16 (d)) had the same peak pattern as an air cured specimen. In SP added hydrated cement specimen additional peak appeared due to surface-bonded OH groups at 3610 cm$^{-1}$. Authors found that these bands mostly disappeared with the progress in hydration duration when analysed after 2 min to 24 hours. They also found the shift in bending vibrational band by 40 cm$^{-1}$ units at 1,630 cm$^{-1}$ peak in the presence of SP. The shifting of the H-O-H bending vibration indicates greater restriction and stronger bonding between the host structure and water molecules. In sulphate region (1100-1150 cm$^{-1}$) spectral peaks gradually shifted to the strong sulphate band due to the formation of ettringite. The shifting of Si-O asymmetric stretching ($\nu_3$), Si-O out-of-plane bending vibration ($\nu_4$) and in-plane bending vibrations ($\nu_2$) indicate polymerization of the silicate.

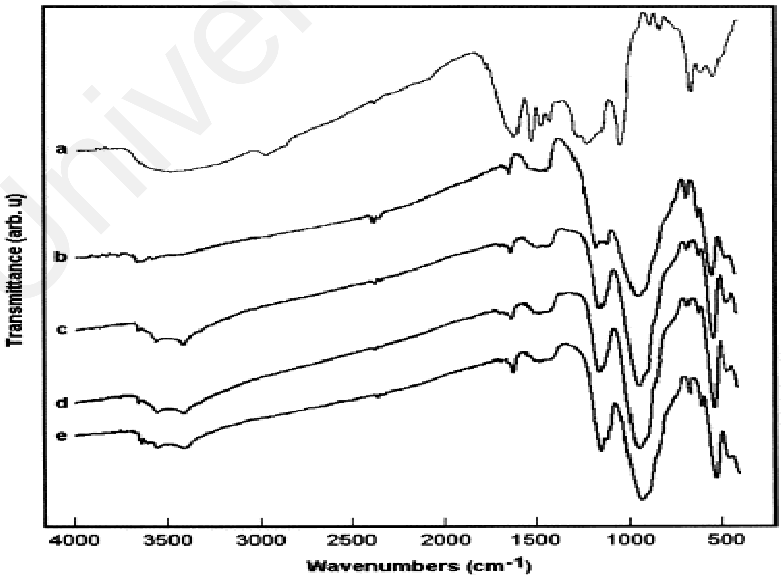

(a) pure dry sodium lignosulfonate

(b) dry cement

(c) hydrated cement prepared in the air

(d) hydrated cement prepared in argon

(e) SP-added hydrated cement prepared in air.

**Figure 2.16: FTIR spectra of different samples after 2 min of preparation (Mollah et al., 2000).**

### 2.4.3 X-ray Diffractometric Analysis

X-ray diffractometer was discovered in 1912 and widely used for determining the crystalline structure of materials (Leng, 2009). It identifies the chemical compounds from the crystalline structure, meaning that various mixtures having same crystalline structure but different chemical formulas could be identified. The XRD pattern of control sample at 28-day age is given in Figure 2.17. These XRD patterns and interpretation of corresponding crystalline phases were used to evaluate the hydration reactions (Jadhav & Debnath, 2011). The hexagonal platy crystal of calcium hydroxide (CH) was found in control sample at 18.3°, 28.9°, 34.5°, 47.1°, 50.8° and 54.3° (Trezza, 2007). It was known that the amount of CH can be used as an indicator to determine the degree of hydration (Trezza, 2007). Due to amorphous nature of CSH gel, its detection in XRD spectra is limited (Sharma & Kothiyal, 2016). Therefore, the presence of unhydrated cement contents i.e. alite ($C_3S$) and belite ($C_2S$) can be used as an indicator for estimating the amount of produced CSH gel. The peaks of $C_3S$ were observed at 29.4°, 32.2°, and 51.8° (Jadhav & Debnath, 2011). The peaks of $C_2S$ were observed in control sample at 32.6° and 41.1°. Besides that, the other hydration products such as ettringite were observed at 15.7 ° and 23.0 ° which can use determined the rate of hydration of cement.

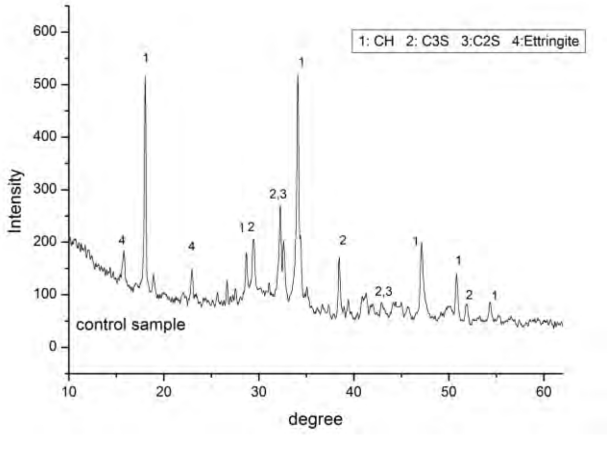

**Figure 2.17: Analysis of XRD for control sample (Wang et al., 2016).**

Wang et al. (2016) investigated the influence of graphene flakes in cement composite keeping water to cement ratio constant of 0.35 and graphene to cement ratio of 0.05%. XRD patterns of control sample and cement paste with graphene flakes at age of 7 and 28 days after casting were given in Figure 2.18. Authors observed that no new phases were found after the incorporation of graphene in the cement mix. Hence, the type and structure of final hydration products remained same. However, the XRD spectra characterize the degree of hydration process. Peak intensities of hydrated cement products i.e. calcium hydroxide and ettringite (AFt) were higher in graphene cement composite as compared to plain cement. The intensity of unhydrated cement content i.e. alite ($C_3S$) was also found lower in graphene cement composite. The authors conclude that graphene flakes accelerated the hydration process of cement paste, especially at an early age. Nevertheless, final hydration products in type and structure remained unaffected.

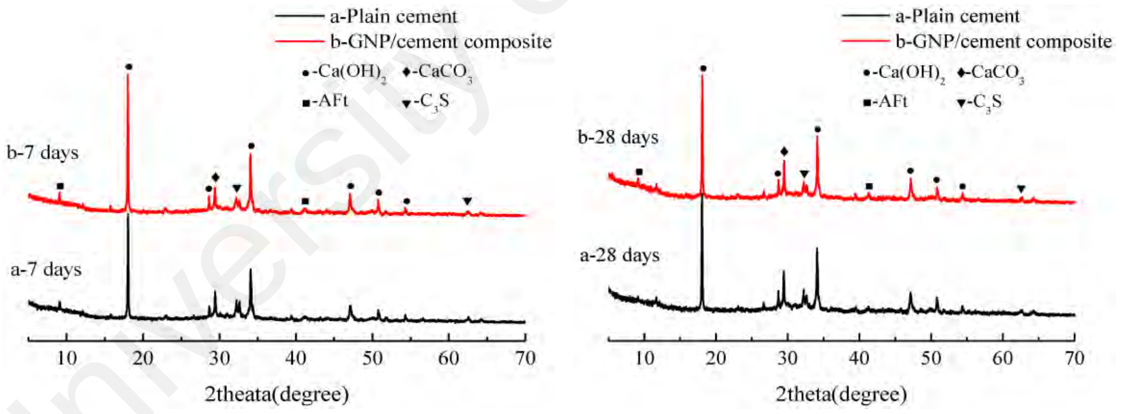

(a) 7-day (b) 28-day

**Figure 2.18: X-ray diffraction (XRD) patterns of plain cement paste and GNP-cement composite (Wang et al., 2016).**

Influence of various nanomaterials i.e. nanosilica, nano alumina and reduced graphene oxide in cement composite was investigated by Murugan et al. (2016). XRD spectra of these cement composites were given in Figure 2.19. Murugan et al. (2016) observed that the XRD spectra of nanomaterials based cement composite were similar to the plain cement and no major differences were seen in the diffraction patterns of the different pastes. Hence, it indicates that mineralogical composition remained same. Yet, the intensities of these products varied which suggest that quantity of these products varied after the incorporation of nanomaterials.

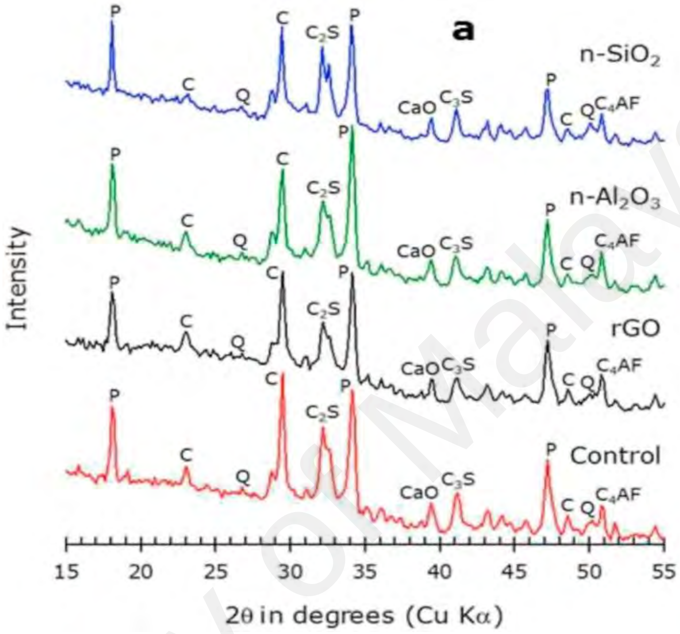

**Figure 2.19: XRD pattern of the different pastes cured for 28 days (Murugan et al., 2016).**

The XRD patterns for control mix, 0.125 PGO-CNC and 0.125 GONO-CNC after 90 days of curing were obtained by Sharma & Kothiyal (2016) and presented in Figure 2.20. The quantity of portlandite was found enhanced with the increase in the concentration of graphene oxide. Authors found that peaks of alite and belite were reduced significantly by incorporating the nanomaterial in the cement mix. Brittleness of composite mix was found less as compared to control sample due to the absence of Aft peak. Sharma & Kothiyal (2016) suggested that relative decrement of the $C_4AF$ (Tetra calcium aluminate ferrite) peak in composite mix indicates the higher hydration rates due to nanocomposites.

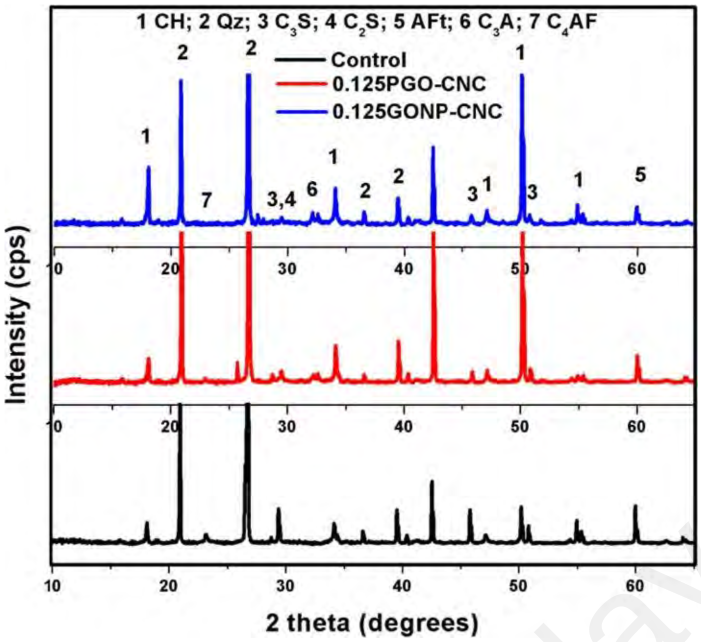

**Figure 2.20: X-ray diffractograms of different samples after 90 days of curing (Sharma & Kothiyal, 2016).**

Influence of functionalized graphene flakes on mortar composite was explored by Cao et al. (2016). Functionalized graphene flakes were added 0.02% by the mass fraction of cement in mix design (labelled as N2) keeping water to cement ratio 0.5 and sand to cement ratio 3.0. XRD patterns were recorded for the control sample (PO) and N2 sample at 3-day and 28-day after curing as shown in Figure 2.21.

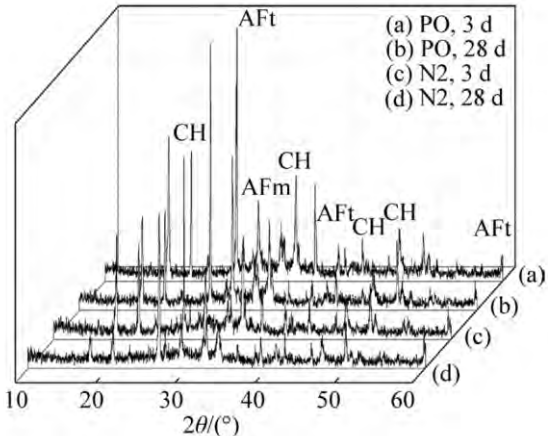

**Figure 2.21: XRD pattern of graphene cement composites at various curing age (Cao et al., 2016).**

Both XRD patterns were similar to each other and demonstrate that chemical composition of hydration products remained same, however, peak intensities of these patterns were varying. Hydrated cement peaks were found higher in the N2 mix as compared to PO. Therefore, Cao et al. (2016) concluded that functionalized graphene nanosheets have a significant role in promoting the growth of hydrated products.

### 2.4.4 Morphological analysis

Lastly, for microscale characterization, the focus was given on the morphological analysis. For this purpose, field emission scanning electron microscopy was incorporated which was used in material sciences to investigate molecular surface structures and their properties.

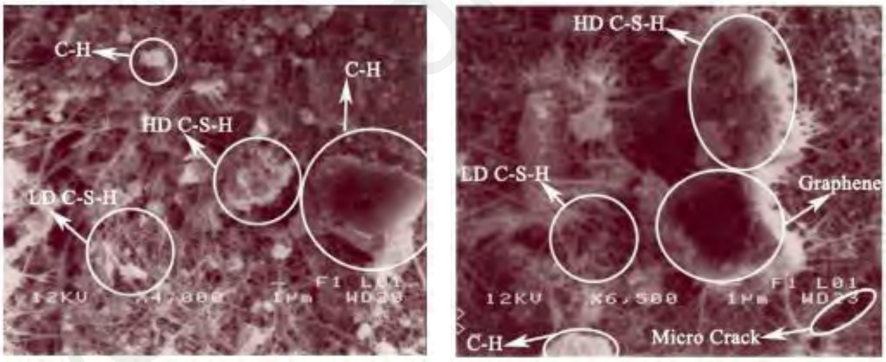

(a) x 4000 (b) x 6500

**Figure 2.22: SEM image of cement mixed with pristine graphene (Alkhateb et al., 2013).**

Alkhateb et al. (2013) used SEM images to locate the graphene in cement composite. Authors observed that high-density CSH was formed near pristine graphene flakes as shown in Figure 2.22. Therefore, they concluded that high interfacial strength is available between CSH and graphene flakes. Furthermore, microstructure and pattern of hydrated crystals of graphene oxide based cement composite were investigated by Lv et al. (2013a). Figure 2.23 showed the SEM images of fractured surfaces as found by Lv et al.

(2013a). Authors reported the disorderly stacked hydration products in plain cement paste (Figure 2.23 (a)). Whereas, increasing percentage of GO in cement composite resulted in the formation of flower-like crystals as shown in Figure 2.23 (b) and Figure 2.23 (c). These flower-like crystals became denser with the increase in graphene oxide percentage up to 0.03% (Figure 2.23 (d)). For 0.04% dosage of GO irregular polyhedral resembling shaped appeared for hydrated products (Figure 2.23 (e)) and for 0.05%, it became regular and complete polyhedral shapes (Figure 2.23 (f)). As per authors, these flower-like crystals enhanced the toughness while polyhedron like crystals contributed to compressive strength.

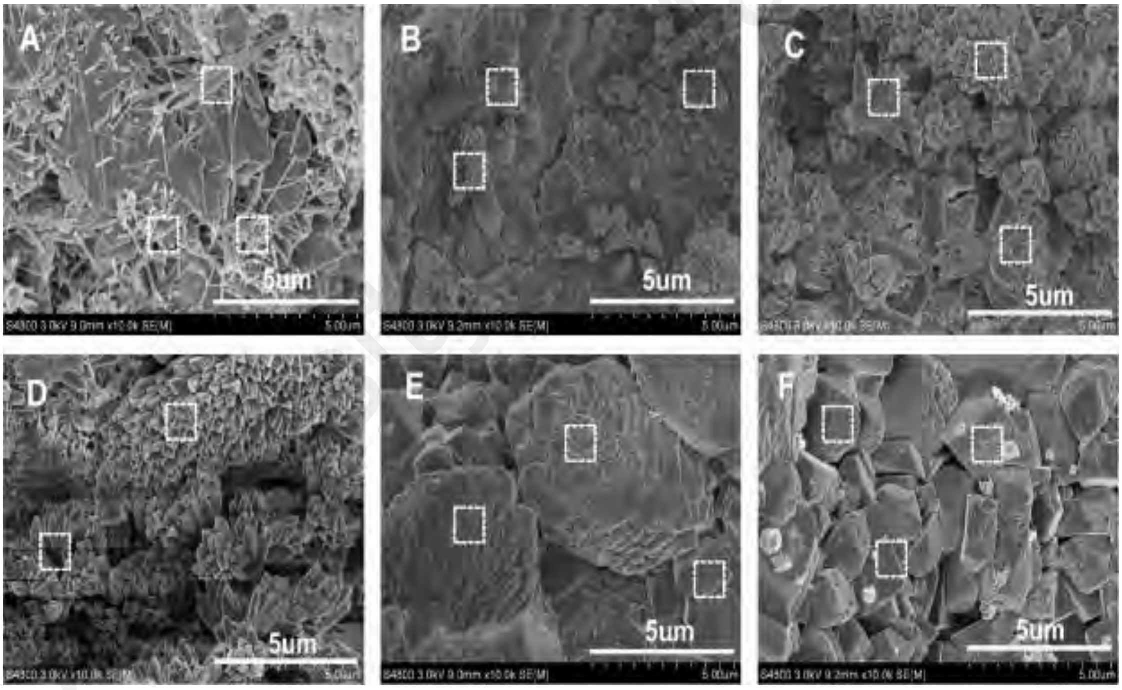

(A) no GO; (B) GO 0.01%; (C) 0.02%; (D) 0.03%; (E) 0.04%; and (F) 0.05%

**Figure 2.23: SEM images of cement composites at 28 days mixed with GO (Lv et al., 2013a).**

Lv et al. (2013a) concluded that GO regulated the cement hydration process and formed the regular flower-like and polyhedral like crystals. Furthermore, the effect of hydration time was also investigated for 0.03% of GO cement composite as shown in

Figure 2.24. GO encourage the formation of the flower-like structure after 1 day of casting and on 28-day these crystals became perfect and large flower-like shape as shown in Figure 2.24 (d). Therefore, it was confirmed that graphene oxide regulated the hydration crystals in flower-like shape and these shaped have a tendency to form massive and compact structure through the cross-linking of flower-like crystals.

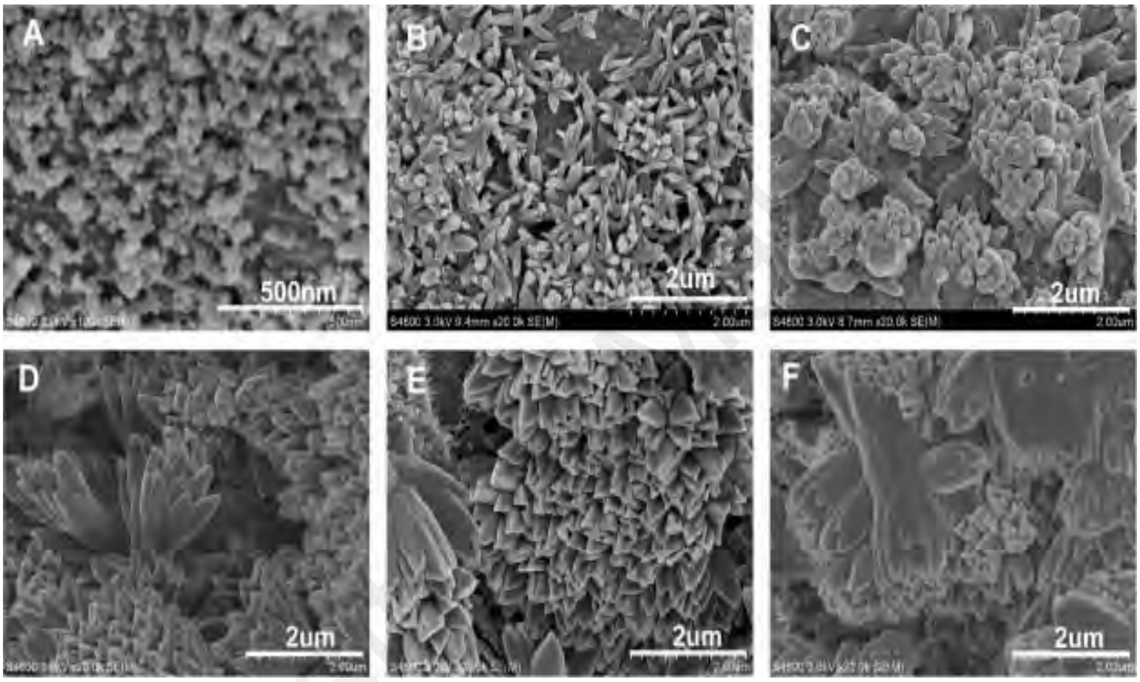

(A) 1 day; (B) 3 days; (C) 7 days; (D) 28 days; (E) 60 days; and (F) 90 days

**Figure 2.24: SEM images of cement hydration crystals with 0.03% GO with different hydration times (Lv et al., 2013a).**

Cui et al. (2017) determined that the chemical composition of flower-like crystal and polyhedral like hydrated crystal as reported in Lv et al. (2013a). They found that these are calcium carbonates, which are due to the carbonation of cementitious hydrates and not the product formed by cement hydration. Cui et al. (2017) anticipated that there might be a possible pitfall in sample preparation for scanning electron microscope (SEM) analysis by Lv et al. (2013a), which resulted in the formation of flower-like crystals. To prove this statement, Cui et al. (2017) performed experimental work using carbon nanotubes with –COOH functional group. They collected two samples for SEM analysis from the same mother cube using two methods. For method I, obtained sample was oven dried for 24 hours and then cooled down to room temperature for SEM analysis. For method II, obtained sample was placed in natural environment for 7 days. After that sample was oven dried and then cooled for SEM analysis. Figure 2.25 showed the SEM image and XRD pattern of the specimen obtained from method II. It was clearly distinguished that calcite peaks were prominent in Figure 2.25 (b). Thus, Cui et al. (2017) recommended further research on the regulation mechanism of graphene oxide on cement hydration as proposed by Lv et al. (2013a).

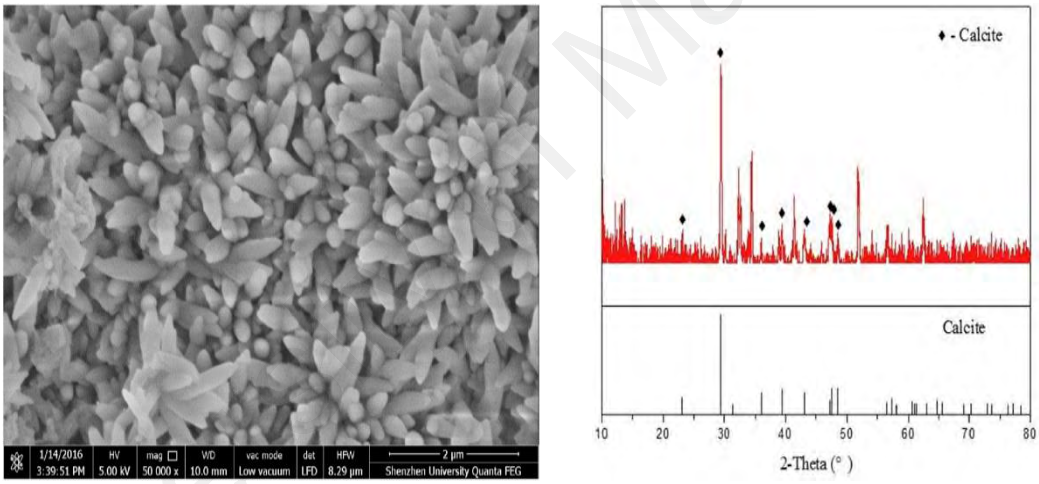

(a) SEM image

(b) XRD results

**Figure 2.25: Description of flow-like crystal of the surface of sample obtained by method II (Cui et al., 2017).**

Cao et al. (2016) stated that the structure of the hydrated cement products showed the disorderly formation of needle-shaped ettringite and hexagonal calcium hydroxide as shown in Figure 2.26 (a). After addition of functionalized graphene flakes (FGN) in mix design, the structure of hydrated cement products become more compact and less needle-shaped crystals were seen (Figure 2.26 (b)). When graphene percentage increased to 0.02%, it formed the polyhedron shape (Figure 2.26 (c)) and represents the compacted structure and certain space to absorb movement simultaneously. However, when the high content of graphene was used i.e.0.03% to 0.05%, the degree of hydration product decreased due to the attachment of hydrophilic groups on the surface of graphene flakes, which absorbed some part of the available water and prevented the full hydration process of cement pastes (Figure 2.26 (d)-(f)) (Cao et al., 2016).

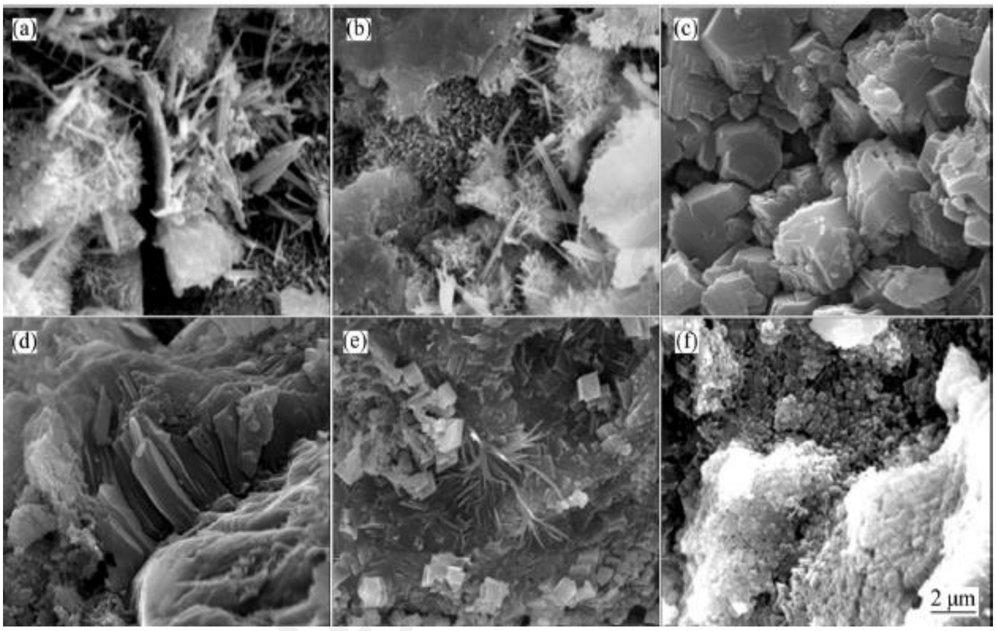

(a) No FGN; (b) 0.01% FGN; (c) 0.02% FGN; (d) 0.03% FGN; (e) 0.04% FGN; (f) 0.05% FGN

**Figure 2.26: The effect of functionalized graphene flakes (FGN) to the cement composites after 28 days of curing (Cao et al., 2016).**

A detailed literature review of micro-scale characterization of nanomaterial based cement composites has been done. It was found in the literature that, the microstructure characterization and hardened properties of cement based construction materials depend on the viscosity and fresh properties of cement. Therefore, flow properties of nanomaterial based cement composite are investigated in the next section.

## 2.5 Flow Properties of GNDs based Cement Paste

Concrete is the most widely used structural material and usually placed in the plastic form. Fluidity, homogeneity, consistency and workability are the key elements to be considered during the mixing and placing of the concrete. Any shortcoming in these properties will lead to bleeding, segregation, laitance and cracking of the concrete (Zhang, Yanrong et al., 2016). However, these properties greatly depend on the viscosity of concrete. Therefore, the rheological properties of concrete are utmost significant to achieve homogeneity and good workability. Rheology of cement paste has a strong influence on the overall fresh properties of the concrete (Ferraris, 1999). Usually, the flow properties of the cement paste are acquired by shear stress and shear rate. Later from the flow curves, viscosity and other flow parameters are calculated by using mathematical models. With the advancement in nanotechnology, research emphasis has been moved to the effect of nanomaterials on cement composite (Kawashima et al., 2013).

Numerous researchers studied the effect of various engineered nanomaterials on flow characteristics of the cement paste (Konsta et al., 2010; Ormsby et al., 2011; Shang et al., 2015; Wang et al., 2017; Wang et al., 2016). Ormsby et al. (2011) used the parallel plate geometry for rheological investigation and found that multi-walled carbon nanotubes (MWCNTs) meaningfully influenced the rheological behaviour of polymerizing cement. Konsta et al. (2010) used the long MWCNTs with the content of 0.16 % of water (by weight) and w/c = 0.5. MWCNTs were treated using with and without sonicated energy. They observed the shear thinning response of cement paste and at high shear stress (above 70 Pa) approximately constant viscosity independent of sonication energy. Shang et al. (2015) explored the rheological characteristics of GO and GO encapsulated silica fume based cement pastes using Bingham model. Graphene oxide reduces the fluidity of the cement paste by 36.2 % as compared to plain cement paste. They noted that the values of yield stress and plastic viscosity increased with the addition of graphene oxide. Wang et al. (2016) found that addition of graphene oxide in cement paste results in flocculation structures. These flocculated structures were depended on the content of GO and as a result, it enhanced the yield stress, plastic viscosity and area of the hysteresis loop of the flow curve. Wang et al. (2017) determined the influence of fly ash on flow properties of graphene oxide cement paste. They observed that for 0.01 % of GO and 20 % of fly ash (by weight), the yield stress and plastic viscosity of the cement paste decreased in comparison with control specimen by 85.81 % and 29.53% respectively. For cement specimen with 0.03 wt% of GO and 20 wt% of fly ash, the yield stress and plastic viscosity of the cement paste was lowered by 50.33% and 5.58% respectively (Figure 2.27).

Yahia & Khayat (2001) found that flow properties are greatly dependent on the mathematical model. Various researchers used different mathematical models to estimate the yield stress and plastic viscosity values. These mathematical models statistically determined the yield stress (shear stress at zero shear rate) and plastic viscosity (generalized viscosity for a range of shear rate) and also predict the specific trend of the flow. As, these mathematical models possess statistical errors (Nehdi & Rahman, 2004), therefore, one model cannot predict accurately the trend of the flow behaviour of cement paste (Yahia & Khayat, 2001). Therefore, some of the well-known and commonly used mathematical models for cement paste are discussed in next section.

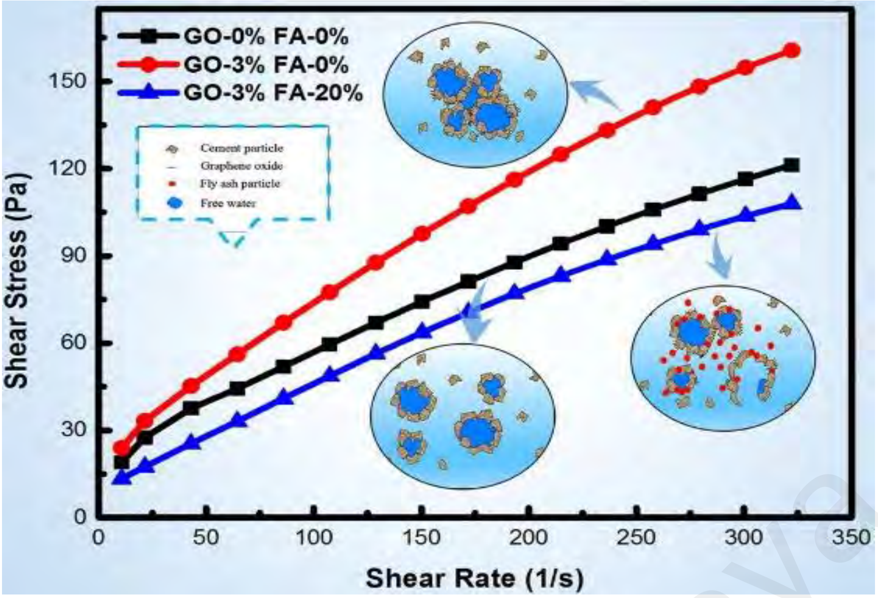

**Figure 2.27: Influence of fly ash on flow curves of graphene oxide cement paste (Wang et al., 2017).**

## 2.6 Rheological Models

The rheological properties of the cement paste are directly related to the workability, flowability and consistency of the concrete. Rheological models consider several factors which have the great influence on cement paste rheology and are necessary to be considered to achieve better and realistic approaches. Cement paste has the complex rheological behaviour as it depends on several parameters like water-cement ratio, chemical admixtures, shear rate and supplementary cementitious materials (Papo, 1988). Therefore, due to the influence of several factors in the rheological model for cement paste, the flow behaviour cannot predict with best fitting curves by using single model (Yahia & Khayat, 2001). The accuracy and efficiency of the mathematical model depend on absolutely fitting the experimental data. For that purpose, four rheological models have been selected from various standards and researchers (Nehdi & Rahman, 2004).

### 2.6.1 Bingham Model

Bingham (1922) proposed his model in 1919 with the title, “Bingham Model”. He was the pioneer to introduce the visco-plastic materials and class of non-Newtonian materials

(Mitsoulis, 2007). This model requires two parameters, the yield stress ($\tau_o$) and plastic viscosity (μp). Yield stress is the critical value of stress below which material does not flow (Mitsoulis, 2007) and plastic viscosity is the slope of the line in shear stress-shear rate curve. This model has the characteristics of the Newtonian equation and the only difference is the yield stress. Mathematical equations for both Newtonian and Bingham models are given in Equation (2.4) and Equation (2.5) respectively (Ferraris, 1999). Bingham model was widely used by researchers to determine the yield stress and plastic viscosity of the cement paste (Rao, 2014; Yahia & Khayat, 2001, 2003). Bingham mathematical equation is linear as given in Equation (2.5) (Bingham, 1922) and comparatively convenient to use for an analytical solution (Yahia & Khayat, 2003).

$$\tau = \mu p \ddot{\Upsilon} \qquad (2.4)$$

$$\tau = \tau_o + \mu p \ddot{\Upsilon} \qquad (2.5)$$

Where, $\tau$ = shear stress (Pa); $\tau_o$ = yield shear stress (Pa); $\mu_p$ = plastic viscosity (Pa.s) and $\ddot{\Upsilon}$ = shear rate ($s^{-1}$)

However, it fails to fit into the nonlinear portion of the flow curve at a low shear rate and cannot predict yield shear stress accurately especially for shear thickening behaviour (Yahia & Khayat, 2001). According to Feys et al. (2007) Bingham model underestimates the shear stress and for their reference mix, it results in the negative yield stress, which was physically impossible. Therefore, this model is not valid to describe the rheological properties, especially in nonlinear portion.

### 2.6.2 Herschel-Bulkley Model

To solve the problem of Bingham model, the nonlinear model can be used. Power equation was frequently used for the liquids to study the rheological behaviour (Ferraris, 1999). However, it is not valid for the visco-plastic materials. In 1926, Herschel-Bulkley

(HB) provides the relationship to determine the rheological properties of Bingham materials in nonlinear portion (Herschel & Bulkley, 1926). The Herschel-Bulkley equation is the upgraded form of the power model containing both yield stress and power equation. This model contains three parameters: yield shear stress '$\tau_o$', power index 'n' and consistency 'K'. Power index is an important parameter and estimates the degree of fluid for shear thinning and shear thickening. The mathematical representation of both power model and Herschel-Bulkley model is given in Equation (2.6) and Equation (2.7) respectively (Ferraris, 1999). This model is also known as yield power-law because it has the characteristics of both Bingham and Power models (Yahia & Khayat, 2003), therefore, it offers an advantage over the Bingham and Power-law models (Hemphill et al., 1993).

$$\tau = K\ddot{Y}n \qquad (2.6)$$

$$\tau = \tau o + K\ddot{Y}n \qquad (2.7)$$

Where, $\tau$ = shear stress (Pa); $\tau_o$ = yield shear stress (Pa); $\ddot{Y}$ = shear rate ($s^{-1}$); K = consistency ($Pa.s^n$) and n = power index or pseudoplastic index

The Herschel-Bulkley model can quantify the shear thickening behaviour of the cement paste. If the power index (n) value will be more than 1, the fluid will present the shear thickening behaviour, whereas, if the value is less than 1, the shear thinning behaviour will be found. As per the study conducted by Yahia & Khayat (2001) this model results in the lowest yield stress in shear thinning in contrast to other mathematical models on the same flow data. This discrepancy was due to mathematical formulation. Zero shear viscosity (inclination of flow data curve at zero shear rate), is always either zero or infinite based on power index value. For the shear thickening fluids (n > 1), zero shear velocity is zero and for shear thinning materials it is infinite. Thus, this model is not the best model to describe the non-linear behaviour of flow curve (Feys et al., 2007; Yahia & Khayat, 2001).

### 2.6.3 Modified Bingham Model

To overcome the deficiency of Herschel-Bulkley model, a linear term was added to the HB mathematical equation. This new model is called Modified Bingham model because the Bingham equation was modified and second order of the shear rate was used to fit the model in pseudo-plastic or shear thickening behaviour. As the modified Bingham model, contains the characteristics of Bingham model and Herschel-Bulkley model, therefore, it can provide a better description of the nonlinear behaviour (Feys et al., 2013). The mathematical expression of the modified Bingham model is given in Equation (2.8) (Yahia & Khayat, 2001).

$$\tau = \tau o + \mu p\ddot{\Upsilon} + c\ddot{\Upsilon}^2 \qquad (2.8)$$

Where, $\tau$ = shear stress (Pa); $\tau_o$ = yield shear stress (Pa); $\mu_p$ = plastic viscosity (Pa.s); $\ddot{\Upsilon}$ = shear rate ($s^{-1}$) and c = regression constant

Although this model has a limitation that fluid should not be highly-shear thickening, it can only be possible by keeping power index value less than 2 (Feys et al., 2013). Therefore, it restrained the response of the fluid to second order polynomial, which will limit its fitting to the flow data.

### 2.6.4 Casson Model

Casson (1959) proposed the equation to relate the shear stress and shear rate for the suspensions. Casson suggested a special structure for the suspension in fluid called “particles” which form flocculates of certain cohesive strength (Scott, 1966). The Casson model has two adjustable parameters as shown in Equation (2.9) and it can predict the viscosity at a very high shear rate (infinite shear rate) (Papo, 1988). However, this equation has a limitation in predicting the flow parameters for very concentrated suspensions (Papo, 1988). As per Scott (1966) observation, Casson equation fits very well to various types of fluid and is more appropriate to use as compared to Herschel-Bulkley equation, yet, it is difficult to explain in most cases.

$$\sqrt{\tau} = \sqrt{\tau_o} + \sqrt{\mu_p \ddot{\Upsilon}} \tag{2.9}$$

Where, $\tau$ = shear stress (Pa); $\tau_o$ = yield shear stress (Pa); $\ddot{\Upsilon}$ = shear rate ($s^{-1}$) and $\mu_p$ = plastic viscosity (Pa.s)

### 2.6.5 Standard error

The ability of an analytical model to accurately match the nonlinear regression at low shear rate will define its accuracy. As this ability is varying with each mathematical expression, therefore, the calculated rheological parameters especially yield stress values can offer different values for different models. Standard error for each rheological model has been determined using Equation (2.10) (Yahia & Khayat, 2001). It depends on the normalized standard deviation. Finally, a comparison has been drawn amongst the calculated values to determine the effective and best-fitted model.

$$Standard\ error = \frac{1000 * \left(\frac{\sum(measured\ value - calculated\ value)^2}{(number\ of\ data\ points - 2)}\right)^{1/2}}{(Maximum\ measured\ value - Minimum\ measured\ value)} \tag{2.10}$$

It was found that most of the existing researches were performed on the CNTs and graphene oxide. However, the rheological properties of graphene cement paste remained unexplored. Therefore, one of the objectives of this study is to investigate the flow properties of the graphene cement paste by using Bingham, Modified Bingham, Herschel-Bulkley and Casson models. The graphene flakes were utilized to measure the variation in the flow curves of the cement paste. After discussing and reviewing the various rheological models and influence of different nanomaterials on flow properties of cement paste, mechanical properties of graphene cement composite will be critically reviewed in next section from the available literature.

## 2.7 Mechanical Properties of Graphene Cement Composites

Consumption of cementitious building materials i.e. concrete is increasing every day because of its various beneficial properties such as high strength, durability and resistance to fire (Kodur & Sultan, 2003). Sixuan (2012) conducted a study on the mechanical properties of both cement paste and mortar by adding different concentrations of GNPs. The study revealed that there was no increment in compressive strength for the cement paste incorporated with 0.05% and 0.25% of GNPs. However, an increment of 20% in compressive strength mortar was observed for 0.50% of GNP cement mortar. As for the flexural strength, the maximum increment up to 82% was observed for the cement paste with 0.05% of GNP (Sixuan, 2012).The influence of graphene nanomaterials and its derivatives (GND) on mechanical properties of cement composites is presented in Table 2.2. Addition of nanomaterials significantly increased the mechanical properties of cement composites at both early and later stages. Li et al. (2017) suggested that due to the nucleation and filling effect of graphene oxide, GO can help to accelerate the hydration process at an early age. Yet, the complete mechanisms have not been described in the literature. For example, the compressive and flexural strength reported by Lv et al. (2013b) and Mokhtar et al. (2017) are considerably different. Both researchers used the same water to binder ratio, dosage of GO and similar curing conditions. Moreover, Wang et al. (2017) and Wang et al. (2016) used the same water to cement ratio and graphene oxide dosage, however, the difference for increase in compressive strength was found almost double to each other. Furthermore, increase in compressive strength reported by

Kothiyal et al. (2016) and Shang et al. (2015) is twice of the Sharma & Kothiyal (2016) and Li et al. (2017) respectively, under similar conditions. It is well known that the influencing factors on mechanical strength in the composite matrix are water/binder (w/b) ratio, type of nanomaterials, its dosage and curing duration of the specimen (Yang et al., 2017). Moreover, the effects of dispersion, agglomeration, size and functional groups attached with nanomaterials have considerable influence on mechanical properties (Yang et al., 2017). It was observed from Table 2.2 that the nanomaterials have more influence on the flexural strength of cement composite as compared to compressive strength. According to Sharma & Kothiyal (2015), the bridging and bonding effect of graphene oxide with cement matrix and denser microstructure of cement matrix are related factors contributing to flexural strength. Furthermore, use of dispersant, surface modification, reduction in size and thickness of graphene have been employed to improve the effectiveness of GND on mechanical properties of cement based materials (Abrishami & Zahabi, 2016; Lv et al., 2016; Sharma & Kothiyal, 2015). It is understood that the key factors controlling the porosity and the mechanical properties of cement based materials are more hydrated cement products, filling of pores and bonding between hydrated cement products and nanomaterial (Sharma & Kothiyal, 2015). Nevertheless, the tremendous increment in the mechanical properties have been recorded however, the role of GND has not been clearly defined in the literature. Actually, many explanations given by various researchers are controversial and sparks much debate.

**Table 2.2: The influence of graphene and its derivatives on mechanical properties of cement based materials modified from Yang et al. (2017).**

| Matrix | Type/dosage (wt.%) | w/b | Increase in Flexural strength (%)/age | Increase in Compressive strength (%)/age | Reference |
|---|---|---|---|---|---|
| Paste | GO/0.05 | 0.3 | 90.5/28 d | 52.4/3 d | (Wang et al., 2015) |
| Paste | GO/0.05 | 0.3 | 69.4/7 d | 66.4/7 d | (Lv et al., 2014b) |
| Paste | FGON/0.03 | 0.3 | 65.5/28 d | 51.3/28 d | (Lv et al., 2016)] |
| Paste | GO/0.03 | 0.3 | 55.0/28 d | 42.5/28 d | (Wang et al., 2017) |
| Paste | GO/0.02 | 0.3 | 84.5/28 d | 60.1/28 d | (Lv et al., 2013b) |
| Paste | GO/0.04 | 0.3 | 43.2/28 d | 28.6/28 d | (Lv et al., 2014a) |
| Paste | GNPs/0.15 | 0.3 | 27.5/28 d | 49.4/28 d | (Metaxa, 2016) |
| Paste | GO/0.02 | 0.3 | 41.0/28 d | 13.0/28 d | (Mokhtar et al., 2017) |
| Paste | rGO/0.02 | 0.3 | 70.0/7 d | 22.0/28 d | (Murugan et al., 2016) |
| Paste | GO/0.03 | 0.3 | 56.6/28 d | 18.8/28 d | (Wang et al., 2016) |
| Paste | GNPs/0.03 | 0.4 | 16.8/28 d | 1.3/28 d | (Wang et al., 2016) |
| Paste | GO-CNFs/0.05 | 0.4 | 25.0/28 d | 2.89/28 d | (Sun et al., 2017) |
| Paste | GO/0.04 | 0.4 | – | 15.1/28 d | (Shang et al., 2015) |
| Paste | GO/0.05 | 0.4 | 16.2/15 d | 11.0/15 d | (Lu et al., 2015) |
| Paste | GO/0.04 | 0.4 | 14.2/28 d | 37.0/28 d | (Li et al., 2017) |
| Paste | GO-CNT/0.05 | 0.4 | 24.1/15 d | 21.1/15 d | (Lu et al., 2015) |
| Paste | GO-CNT/0.06 | 0.4 | 16.7/28 d | 23.9/28 d | (Zhou, C et al., 2017) |
| Paste | GO/0.022 | 0.4 | 26.7/3 d | 27.6/3 d | (Zhao et al., 2016) |
| Paste | GO/0.03 | 0.5 | – | 40.0/28 d | (Gong et al., 2014) |
| Mortar | GO/0.03 | 0.4 | 70.7/3 d | 45.1/3 d | (Lv et al., 2013a) |
| Mortar | GO/0.05 | 0.4 | 106.4/14 d | 43.2/3 d | (Wang et al., 2015) |
| Mortar | GO/0.022 | 0.4 | 34.1/7 d | – | (Zhao et al., 2017a) |
| Mortar | GO/0.03 | 0.4 | 18.7/7 d | – | (Qian et al., 2015) |
| Mortar | GO/1.0 | 0.5 | – | 114.1/14 d | (Sharma & Kothiyal, 2015) |
| Mortar | GO/0.03 | 0.5 | – | 30.0/28 d | (Mohammed et al., 2016) |
| Mortar | GO/0.125 | 0.5 | – | 53.0/3 d | (Sharma & Kothiyal, 2016) |
| Mortar | GO/0.125 | 0.5 | – | 110.7/3 d | (Kothiyal et al., 2016) |
| Mortar | GO/0.02 | 0.5 | 36.7/3 d | – | (Zhao et al., 2017b) |
| Mortar | FGON/0.1 | 0.5 | 70.8/15 d | 39.0/15 d | (Abrishami & Zahabi, 2016) |
| Mortar | FGON/0.03 | 0.5 | 32.0/28 d | 20.3/28 d | (Cao et al., 2016) |
| Mortar | GNPs/0.8 | 0.5 | – | 87.5/28 d | (Rhee et al., 2016) |
| Mortar | GNPs/0.1 | 0.5 | – | 19.9/28 d | (Tong et al., 2016) |
| Mortar | GNPs/0.08 | 0.6 | – | 55.3/7 d | (Rhee et al., 2015) |
| Concrete | GO/0.1 | 0.5 | 4.0/3 d | 14.2/7 d | (Devasena & Karthikeyan, 2015) |

Note: CNT (carbon nanotube), FGON (functionalized graphene oxide nanosheets), GNPs (graphene flakes), CNFs (carbon nanofibers)

## 2.8 Electrical Properties of Composite Materials

The electrical properties of the cement composites are important and can be used to monitor the damage in a concrete structure. The cement based composite reinforced with conducting fillers can observe its own strain by monitoring the changes in the electrical resistivity values. This ability is related to the breaking of conducting fibers when cracks are initiating in the cement based composite consequently enhancing the resistivity of the overall sample. If cracks are opening up due to tensile or fracture loading then resistivity values will be positive while it will be negative when subjected to compressive loading. Piezo-resistive properties are the effect of a change in electrical resistance in specimen when it is subjected to mechanical strain (Zhao & Bai, 2015). For this purpose, electrical resistance of the cement composite is measured. By definition, the electrical resistance is the strength of a material in opposing the electrical current flowing through it. Based on Ohm's law given in Equation 2.11, the material's electrical resistance at a given constant temperature is equal to the amount of applied voltage divided by the amount of electrical current flowing through it. Mathematically it is expressed as:

$$R = \frac{V}{I} \qquad (2.11)$$

Where: R = electrical resistance of the material in ohms (Ω); V = applied voltage in volts (V); I = electrical current in amperes (A).

It should be noted that Equation 2.11 can only be used for direct current (DC) circuits but not for the alternating current (AC) circuits. Four-probe method is mostly used by researchers to investigate the electoral properties of cement composites. Four-probe method involves four electrical contact points in which voltage is measured through the inner two electrical contacts while the current is measured using outer two electrical contacts (Han et al., 2009). Four-probe method is better than the two-probe method due to the fact that, measured resistance does not include the contact resistance (Han et al., 2007).

According to Han et al. (2007), the space between the current pole and voltage pole is very important. However, its influence is marginal if space is more than 7.5 mm. The various researcher used different spacing in their experimental work. Li et al. (2007) used the spacing of 10 mm while Le et al. (2014) used 40 mm spacing between current and voltage measuring probes. Similarly, the distance between the two voltage measuring probes is not fixed and its value varies. Li et al. (2007) used the 40 mm gap between two measuring probes while Le et al. (2014) used 80 mm gap. As resistivity values remain unaffected provided that the spacing is above a threshold value (Han et al., 2007), therefore, in this research we used 40 mm spacing between the current measuring probe and voltage measuring probes and 60 mm between two voltage measuring probes. Electrical resistivity values were calculated by using Equation (2.12) for unequal spacing (Valdes, 1954).

$$\rho = \frac{V}{\mathrm{I}} \times 2\pi \times \frac{1}{\left(\frac{1}{\mathrm{S1}} + \frac{1}{\mathrm{S3}} - \frac{1}{\mathrm{S1+S2}} - \frac{1}{\mathrm{S2+S3}}\right)} \qquad (2.12)$$

Where “V” is the floating potential difference between inner two probes; “I” is current measured by outer two probes; "ρ" is the resistivity in ohm-cm and “S” is the spacing in cm and was calculated from current carrying probe to the voltage measuring probe. S1 = S3 = 40 cm and S2 = 60 cm.

### 2.8.1 Self-sensing Properties of Nanomaterials Based Cement Composites

Nanomaterials are gifted with the amazing characterises and their incorporation in cement composite brought these characteristics to cement composite as well. Self-sensing and damage memorizing capability of nanomaterial based cement composite are one of the characteristics which nanomaterials brought in cement composite. Various researchers used the piezoresistive characteristics of nanomaterials based cement composite for self-sensing prose (Chung, 2002; Li et al., 2007; Qu & Han, 2008). In the following section piezoresistive properties of nanomaterial based cement composite will be reviewed and critically analysed.

It has been reported by Li et al. (2004a) that cement mortar reinforced with nano-$Fe_2O_3$ have self-sensing properties which can monitor the produced stresses with the application of load. For this purpose, changes in the electrical resistance values of cement composite were recorded. It was found that using 10% of nano-$Fe_2O_3$ particles of 30nm size in mix design with water to binder ratio of 0.5 produce 40% fractional change in electrical resistance values, meanwhile, control specimen showed slight variation. Therefore, it was concluded that nano-$Fe_2O_3$ based cement mortar successfully monitored the produced stresses. According to Li et al. (2004a), this self-sensing property of the cement composite can be used for structural health monitoring (SHM) purposes without the need of any additionally attached or embedded sensors. It will further open the application of nanomaterials based cement composites for fabricating smart sensors (Li et al., 2004a). Li et al. (2007) conducted a research on the functionalization of CNTs using carboxyl. The effect of functionalization on the piezoresistive and electrical properties of the cement composite was observed. It was noted that the electrical resistance of cement composite with 0.5% of carboxyl functionalized CNTs (SPCNT) was 149 Ω.cm and for plain CNTs (PCNT) was 130 Ω.cm. Afterwards, the fractional change in electric resistivity for both types of cement composited was recorded against the cyclic compressive loading and presented in Figure 2.28. It was seen from the Figure 2.28 that both cement composites were capable of monitoring the applied compressive cyclic loading, however, SPCNT specimen showed better response as compared to PCNT.

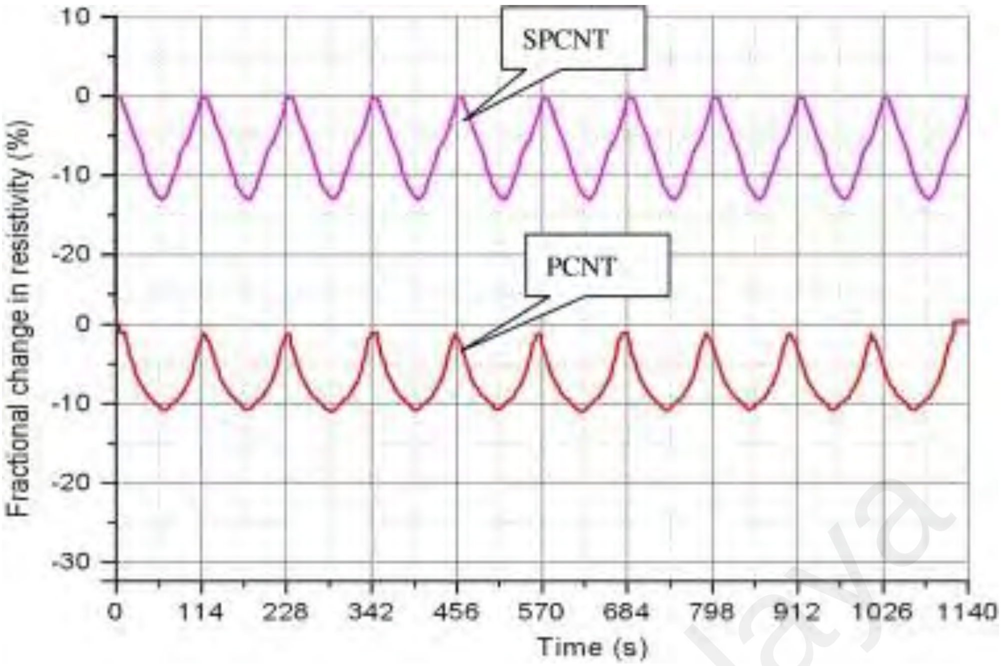

**Figure 2.28: The change in fractional resistivity against the time of the cyclic compressive stress (0-15kN) (Li et al., 2007).**

Yu & Kwon (2009) studied the piezoresistive behaviour of the CNT based cement composite and investigated its potential application as an embedded sensor in civil infrastructure. It was found that electrical resistance of CNT based cement composite was following the same trend as applied compressive loading (Figure 2.29). Yu & Kwon (2009) proposed that fabrication method needs to be further optimized and response of these composite materials must be investigated in concrete. Furthermore, they proposed that if these composite stress sensors were embedded in civil infrastructure e.g. pavements or bridges then due to their compatibility with concrete they will have a long service life with least maintenance.

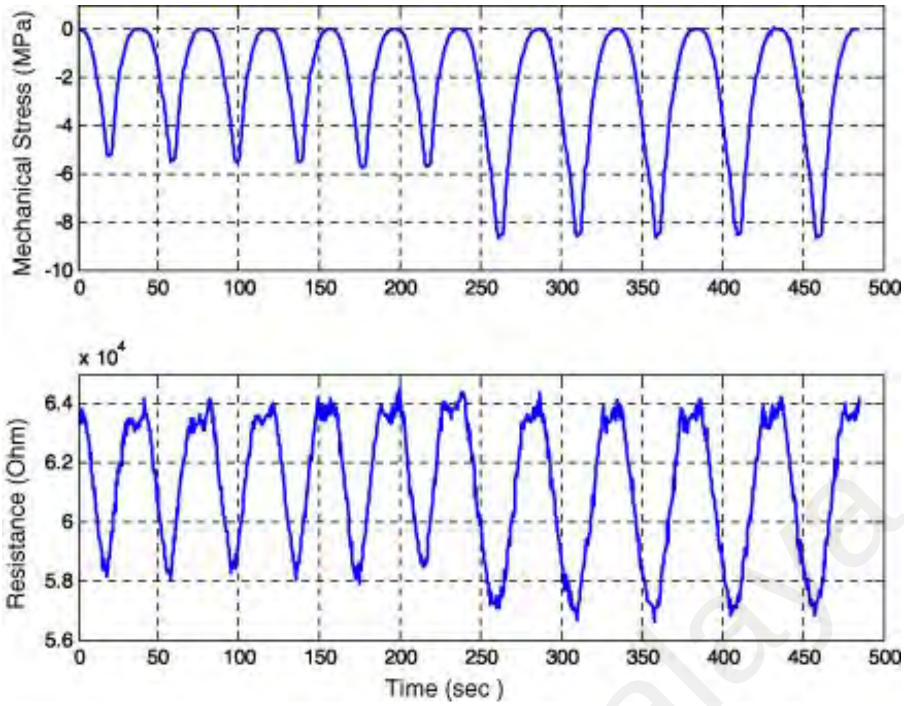

**Figure 2.29: The piezoresistivity behaviour of cement paste enhanced with 0.1% of carboxyl functionalized MWCNTs (Yu & Kwon, 2009).**

Sixuan (2012) examined the effect of crack depth on the GNP reinforced mortar with different shapes i.e. cube and prism. Furthermore, cube sample was labelled as TC307 cube and prism specimen was labelled as 3375 prism. The change in the electrical resistance of cement composite samples was recorded and it was revealed that specimens in both shapes (cubes and prism) responded to an increase in electrical resistance with increase in crack depth as seen in Figure 2.30. The change in electrical resistance for the TC307 cube showed a nearly linear trend up to the extent of relative crack depth value of 0.6 with 60% corresponding peak value of the change in electrical resistance. On the other hand, for the 3775 prism, initial decrease in the electrical resistance was observed. Afterwards, a slight increase in the change of electrical resistance was observed until the relative crack depth value becomes 0.4. It increased, until the change in electrical resistance reached to 30% at 0.85 relative crack depth value. Therefore, it was concluded that TC307 cube specimen determined better response as compared to 3375 prism.

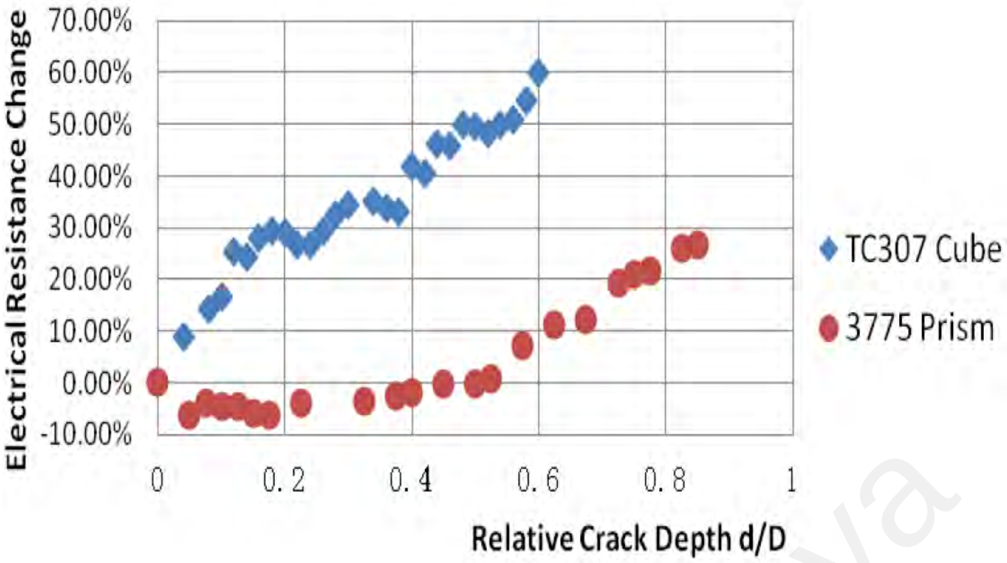

**Figure 2.30: The relationship between the relative crack depth and change in electrical resistance for the GNP reinforced cement mortar (Sixuan, 2012).**

The effect of different concentration of GNPs on the sensing behaviour of the cementitious composite was studied by Du et al. (2013). Authors found a decrement in the electrical resistivity of cement composites by adding 2.4% to 3.6% of GNPs. Le et al. (2014) investigated the electrical resistivity values of cement mortar with increasing content of graphene flakes. Furthermore, specimen was passed through two different environmental conditions, i.e. one specimen was air-dried for one year, and another specimen was oven-dried at 1-day after casting. The author's proposed a relationship between the electrical resistivity values of the specimen with increasing content of GNP as shown in Figure 2.31. It was found that electrical resistivity values decreased with the increase in GNP content. 2.4% of GNP was estimated as percolation threshold value for GNP-composite mortar (Le et al., 2014). The decrement of more than 1 order occurred between 2.4% and 3.6% of GNP content of cement mortar as shown in Figure 2.31 (b).

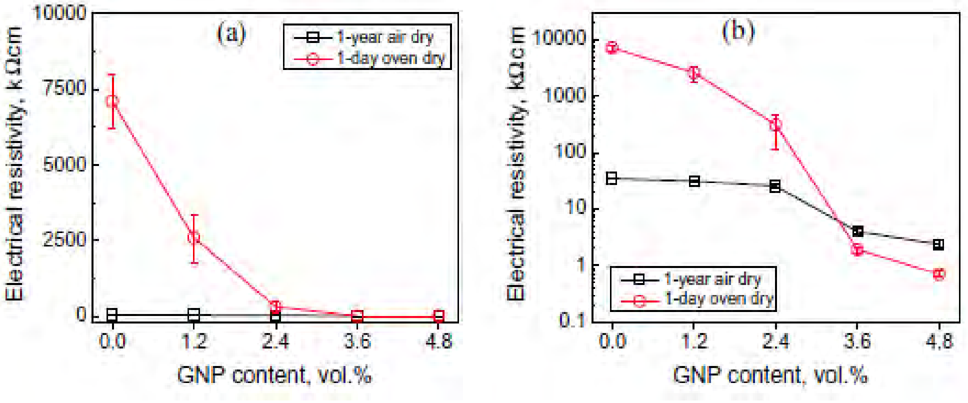

(a) linear scale (b) log scale

**Figure 2.31: The relationship between the electrical resistivity of the GNP cement mortar composite and its respective GNP content (Le et al., 2014).**

## 2.9 Industrial demand for self-sensing material

In this section, literature will be reviewed about the shortcoming of existing health monitoring methods, estimating the space and requirement of self-sensing smart materials in the construction industry. For this purpose, various Non-destructive test (NDT) methods were thoroughly reviewed which are applicable especially to concrete structures. Overall 17 NDT methods were studied and for analysis, they were classified into 5 major categories i.e. (1) audio-visual methods; (2) stress-wave methods; (3) Electromagnetic methods; (4) deterministic methods; and (5) Miscellaneous methods. Moreover, capabilities and limitation of some of the well-known NDT methods is given in Table 2.3.

## Table 2.3: Capabilities and limitations of Non-destructive test methods

| Test Name | Description | Applications/Capabilities | Limitations |
|---|---|---|---|
| Impact echo | Seismic or stress wave based method, | 1) Detect defects in concrete<br>2) Detect delamination in PCC and RC element<br>3) Detect wave reflectors<br>4) Surface opening cracks Characterization<br>5) Ducts detection<br>6) Voids detection<br>7) Concrete modulus of elasticity evaluation<br>8) Concrete compressive strength estimation<br>9) Grouting characterizations<br>10) Detect overlay debonding | 1) Asphalt concrete overlay detectable only with low temperature of asphalt concrete<br>2) Detection is possible for highly viscous material<br>3) Loosely bonded overlay to the deck is detectable only<br>4) Dense grids are required for the marking the boundaries of the delimited area.<br>5) Deck boundaries greatly affect the signals especially near the edges<br>6) Interference of boundary on signal is more prominent on limited dimensional elements like girders, piers etc. |
| Ultrasonic Pulse Velocity | Ultrasonic (acoustic) stress wave based method | 1) Measure depth of elements<br>2) Assess faults in concrete<br>3) Detect debonding of steel bars<br>4) Detect shallow cracking<br>5) Detect delamination<br>6) Detect material interface, specifically interfaces between concrete and air (e.g. grouting defects) and concrete and steel (reinforcement) (Afshari et al., 1996; Hevin et al., 1998; Krause et al., 2008; Taffe & Wiggenhauser, 2006)<br>7) Detect grouting defects | 1) Requires very close grid spacing<br>2) Time consuming method,<br>3) Data quality strongly depends upon the coupling of the sensor unit.<br>4) Difficult on rough surface to couple the sensor<br>5) Shallow defects may remain undetected<br>6) Some defects might remain undetected due to use of lower frequencies |
| Impulse response | Also known as transient dynamic or mechanical impedance method, extension of vibration test | 1) Detect cracks<br>2) Detect honeycombing or low density concrete<br>3) Detect voids<br>4) Detect delamination in concrete<br>5) Determine loss of support below rigid pavement<br>6) Determine load transfer at joints of concrete pavements<br>7) Detect debonding of overlays<br>8) Quality control and condition assessment of pavements and deep foundations,<br>9) Determine subgrade modulus<br>10) Used as screening tool for potential damage detection | 1) Reliable data interpretation is highly dependent on the selection of test points<br>2) Smaller defects may remain undetected<br>3) Automated apparatus is not available |

**Table 2.3: Continued**

| | | | |
|---|---|---|---|
| Acoustic emission | Transient elastic waves | 1) Real-time damage detection.<br>2) Remote monitoring<br>3) Applicable to both local and global monitoring.<br>4) Continuous monitoring without interrupting the traffic flow<br>5) Reliable analysis | 1) Background noise problem<br>2) Difficult to apply analysis to real structure<br>3) No standard procedure for all types of bridges |
| Ground Penetrating Radar | Use electromagnetic waves | 1) Able to determine the buried objects<br>2) Produce contour maps of subsurface features<br>3) Used for condition assessment of civil structures especially related to soil<br>4) Detect voids and anomalies<br>5) Evaluate thickness of members<br>6) Measure thickness of concrete cover<br>7) Determine rebar configuration<br>8) Detect delamination and its potential<br>9) Detect concrete deterioration<br>10) Sensitive to corrosive environment<br>11) Estimate concrete properties | 1) Inability to direct image<br>2) Unable to detect delamination in bridge decks, unless they are epoxy-impregnated or filled with water<br>3) Extreme cold conditions effect the GPR data<br>4) Completely frozen moisture will remain undetected<br>5) Frozen moisture influences the acquired signal<br>6) De-icing salts affect the dielectric constant<br>7) Unable to estimate mechanical properties of concrete like strength, modulus.<br>8) Unable to provide absolute information about the presence of corrosion, corrosion rate or rebar section loss<br>9) Expensive method as compared to other ones |
| Half-cell potential | Electrochemical method | 1) Determine active corrosion<br>2) Can be used at any time<br>3) Can be used in any climatic condition | 1) Minimum temperature must be higher than 2 degree Celsius (Elsener et al., 2003)<br>2) Influence of concrete cover depth is still unknown<br>3) Correcting data for depth is difficult<br>4) It is not used for moisture or salt content calculation.<br>5) Cannot take reading on the isolating layer (asphalt, coating and paint)<br>6) Measurements are often unreliable (concrete is wet, dense or polymer modified) |

**Table 2.3: Continued**

| | | | |
|---|---|---|---|
| Electrical Resistivity | Based on voltage and current measurement | 1) Detect moisture<br>2) Estimate about crack presence<br>3) Determine susceptibility of concrete towards corrosion<br>4) Identify regions susceptible to chloride penetration,<br>5) ER surveys can be used to map corrosion activity | 1) Provide raw data and interpretation is more challenging,<br>2) ER depends upon material properties like moisture content, salt content, porosity<br>3) It is very difficult to find out the contribution of specific one in overall results.<br>4) Automated measurement system for roads are not available in market<br>5) The surface has to be pre-wetted. |
| Infrared Thermography | Based on electromagnetic waves, in infrared region, emitting from the surface of the material related to temperature variation | 1) Detects cracks, delamination and concrete disintegration.<br>2) Detect Voids<br>3) Detect material changes<br>4) Detect change in density, thermal conductivity and specific heat capacity<br>5) Detect debonding<br>6) Detect cracks in concrete<br>7) Detect segregation in asphalt concrete | 1) Difficult to detect deep flaws<br>2) Do not give data about depth of crack<br>3) Surface irregularities, boundary condition and atmospheric temperature influence the results |
| Chain drag and Hammer sounding | Based on sound characteristics of the deck | 1) Detect delamination in concrete<br>2) Provide preliminary details for further testing<br>3) Provide contour maps regarding soundness of the surface | 1) Chain drag is not applicable to vertical surfaces<br>2) Depends upon hearing skills of the operator,<br>3) Unable to detect initial delamination<br>4) Ineffective on bridge decks with overlays |

As these well-known methods have their own limitations in the application and most importantly these methods provide the additional cost for health monitoring purposes. Therefore, it is required that smart sensors with self-sensing characteristics should be developed. These smart sensors are required to reduce the health monitoring cost and make construction projects financially economical. Furthermore, they should be compatible with the cement based building materials and also have the capability to use for the health monitoring purpose.

## 2.10 Research gap

An in-depth literature has been studied about the usage of nanomaterials in the civil engineering field as construction material. Following research gaps have been identified from the literature.

1) Nanoengineered material has been classified into three categories zero, one and two-dimensional nanomaterials. It was found that the nanomaterials have several issues needs to be resolved before its usage in construction industry e.g. zero-dimensional nanoparticles have deficiency in seizing the cracks at microscale due to low aspect ratio. For one-dimensional nanomaterials, weak bond formation and low bond strength between nanomaterials and hydrated cement products are major concerns. Two-dimensional nanomaterials have large surface area and high aspect ratio; however, high production cost is one of the obstacles.
2) Recently (last 3-4 years), an extensive research has been done on the graphene oxide based cement composite, whereas, less focus is given to graphene based cement composite. Further, non-uniform mixing of nanomaterial is the primary source of problem, which leads to the formation of weak zones. Most of the researches on dispersion of graphene and its derivatives were focused on surface modification, functionalization and oxidation process. However, these processes damaged the atomic structure of graphene. Therefore, other methods are indispensably required for dispersion of GNDs and preserving the atomic structure of graphene.
3) During micro-analytical analysis it was found that nanomaterials enhanced the hydrated products, however, the enhancement mechanism is not completely described as yet. Further research is required to study the regulating mechanism of graphene and its derivatives on hydrated cement crystals.

4) It was noted that the available literature on the rheological properties of graphene based cement composite is very rare. Flow properties of graphene cement composite and its dependence on various factors are missing in existing literature. Additionally, the variation of geometric flow with time, dispersing agent, shear rate and various types of graphene sheets is required to explore the real flow of cement paste in plastic state. Moreover, the best optimized rheological mathematical model needs to sort out, as a single rheological model cannot predict the flow behaviour of cement paste accurately. Thus, graphene cement composite demands further exploration to achieve maximum benefit from graphene.
5) Besides this, it was found that graphene and its derivatives enhanced the mechanical properties of cement composites and accelerate the hydration process at an early stage. Yet, the complete mechanism for accelerating the hydration reactions and enhancing overall mechanical properties has not been explained. Prominent differences in mechanical properties were found in experimental work conducted by various researchers in similar circumstances. Additionally, various explanations given by the researchers are controversial and sparked much debate.
6) During the literature review section, it was noted that spacing between current pole and voltage pole is required to be optimized in four-probe method. Piezoresistive properties of nanomaterials based cement composite can sweep the application of additionally attached sensors. The response of graphene and its derivatives in concrete is rarely reported. Furthermore, potential application of graphene based cement composite as an embedded smart sensor in the real concrete structure was seldom found in literature. Moreover, the suitability, industrial demand and compatibility of graphene cement smart sensors with the existing non-destructive health monitoring methods need to be determined.

In this research study dispersion efficiency of graphene, micro-analytical, rheological, hardened properties, piezoresistive properties and potential application of graphene based cement composite will be discussed. However, regulating mechanism of hydrated cement products and graphene will not be covered.

# CHAPTER 3: MATERIALS AND METHODS

## 3.1 Introduction

This chapter provides the information regarding materials, equipment, experimental methodology and various parameters that derived this research. The equipment handling protocols are also discussed. This chapter starts with details about research materials followed by the dispersion of nanomaterials in aqueous solution, preparation of specimens for investigation of physical and mechanical characteristics of graphene cement composites. Several spectroscopic and microscopic techniques are also explained which were used to evaluate the micro-analytical properties of the GCC.

## 3.2 Research Materials

The ordinary Portland cement (OPC) with the 28-day compressive strength of 48 MPa was used as a binder. The OPC was conforming to MS 522 Part 1 2003 (MS-522: Part 1, 2003) with a specific surface area and specific gravity of 0.351 $m^2/g$ and 3.14, respectively. The chemical composition of cement is given in Table 3.1. A third-generation polycarboxylate ether based superplasticizer Sika ViscoCrete (Sika ViscoCrete®-2055, brown liquid), was being used. This admixture is chloride free according to BS 5075 (BS EN 5075-1, 1985) and is compatible with all types of Portland cement including sulphate resistant cement (SRC). Local mining sand with fineness modulus of 2.89, specific gravity of 2.68, water absorption 0.51% and maximum grain size of 4.75 mm was used as fine aggregate. Meanwhile, graphene was purchased from Graphene Laboratories, Inc. USA. It is important to mention here that three different types of graphene were used. The difference was based on the average flake thickness, lateral size and specific surface area of graphene flakes. The detail properties of graphene were enlisted in Table 3.2. Detailed FESEM images of these graphene types are given in Figure 3.1. Normal tap water was used for the preparation of the mixes.

**Table 3.1: Chemical composition of cement.**

| Component | Content (%) |
|---|---|
| Calcium Oxide (CaO) | 63.40 |
| Silicon Dioxide ($SiO_2$) | 19.80 |
| Aluminium Oxide ($Al_2O_3$) | 5.10 |
| Iron Oxide ($Fe_2O_3$) | 3.10 |
| Magnesium Oxide (MgO) | 2.50 |
| Sulphur Trioxide ($SO_3$) | 2.40 |
| Potassium Oxide ($K_2O$) | 1.00 |
| Sodium Oxide ($Na_2O$) | 0.19 |

**Table 3.2: Properties of the graphene.**

| Parameters | G1 | G2 | G3 |
|---|---|---|---|
| Average flake thickness (nm) | 12 nm | 30 nm | 60 nm |
| Average particle (lateral) size (microns) | 1.5-10 | 5-25 | 3-7 |
| Specific surface area, SSA ($m^2/g$) | 80 | 60 | < 40 |
| Purity | 99.2% | 97% | 98.5% |
| Colour | Black | Black | Black |

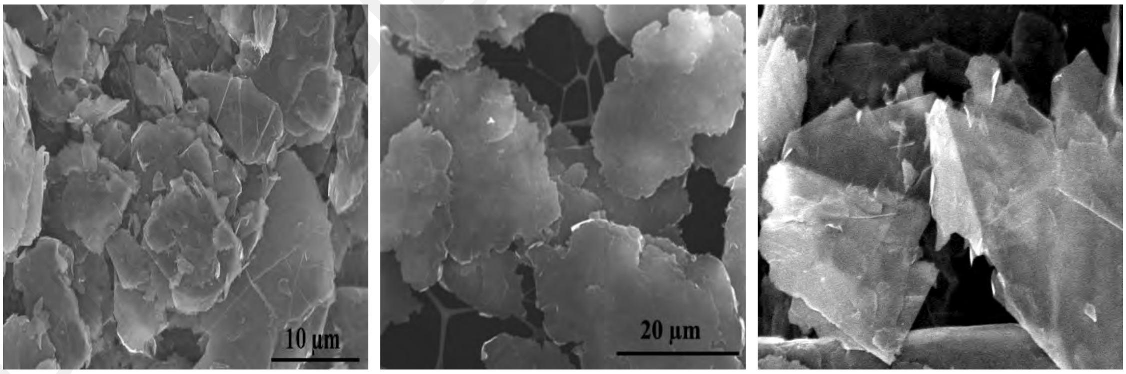

(a) G1 -12 nm (b) G2 - 30 nm (c) G3 - 60 nm

**Figure 3.1: FESEM images of the graphene obtained from Graphene Laboratories, Inc. USA.**

## 3.3 Experimental Methodology

### 3.3.1 Dispersion of Graphene

The Spectroquant® Pharo 300 UV-vis spectrophotometer with a wavelength range of 190 -1100 nm was used to determine the absorbance of the graphene flakes in aqueous solution with and without superplasticizer. The aqueous solution was obtained by mixing dry graphene with deionized water and then sonicated in Fisher Scientific™ Model 505 Sonic dismembrator. To keep the dispersion stable and uniform in solution magnetic stirring with various time duration was performed as well. FAVORIT Stirring Hotplate HS0707V2 was used for this purpose as shown in Figure 3.2 (a). Overall time for sonication was set as 3 min of ultrasonication followed by 40 min of the magnetic stirring. After that crystal cuvette, which was free from fingerprints and all sort of spot, was used to determine the absorbance spectrum. Deionized water was used as a reference in a spectrophotometer. Figure 3.2 shows the magnetic stirrer and Spectroquant® Pharo 300 UV-vis spectrophotometer apparatus used in this study.

(a) Magnetic stirrer FAVORIT Stirring Hotplate HS0707V2

(b) Spectroquant® Pharo 300 UV-vis spectrophotometer

**Figure 3.2: Equipment used for; (a) dispersion of graphene and (b) dispersion measurement.**

### 3.3.2 Preparation of Graphene Cement Composite

The GCC was prepared by mixing of ordinary Portland cement, standard sand, water, polycarboxylate superplasticizer and graphene. Table 3.3 shows the mix proportion of cement paste used to carry out for this research work. While Table 3.4 shows the mix design of GC mortar. It is important to mention here, that cement paste was utilized to determine the flow properties and self-sensing characteristics of GCC while mortar was used to investigate the hardened properties. For samples preparation, graphene (by weight of cement) was dispersed by sonication in deionized water for 3 minutes in the presence of superplasticizer to form a uniform mix. The obtained aqueous solution of graphene was then mixed with cement and sand for 5 minutes in spar mixer (SP-800A). Initially, the speed of the mixer was kept low for 2 minutes then static for 10 seconds and finally high for remaining time. Figure 3.3 shows the exfoliation of graphene sheets using ultrasonication and mixing of mortar in spar mixer. The workability of cement mortar was determined by ASTM C 1437-15 (ASTM C 1437, 2015). Figure 3.4 shows the apparatus used for measuring flow test of cement mortar and measurement of spread diameter.

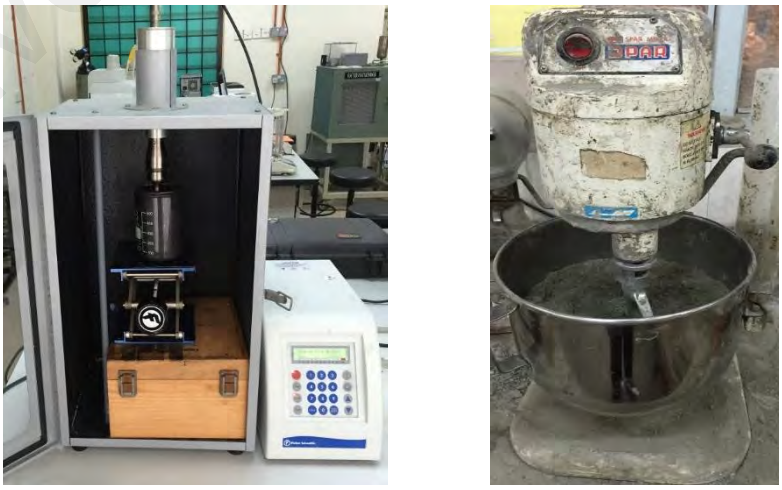

(a) Fisher Scientific™ Model 505 Sonic dismembrator

(b) Spar mixer (SP-800A)

**Figure 3.3: Equipment used for preparation of graphene-cement composite.**

(a) placement of graphene-cement composite in the mould

(b) measurement of spread diameter

Figure 3.4: Flow of hydraulic cement mortar.

Table 3.3: Mix proportions for graphene-cement paste.

| Mix Design | W/C ratio | Cement (C) (g) | Water (ml) | GNP (mg) | GNP/C (%) | SP/C (%) |
|---|---|---|---|---|---|---|
| M0 | 0.4 | 100 | 40 | 0 | 0 | 0 |
| M0S | 0.4 | 100 | 40 | 0 | 0 | 0.1 |
| G1M3<br>G2M3<br>G3M3 | 0.4 | 100 | 40 | 30 | 0.03 | 0 |
| G1M3S<br>G2M3S<br>G3M3S | 0.4 | 100 | 40 | 30 | 0.03 | 0.1 |
| G1M5<br>G2M5<br>G3M5 | 0.4 | 100 | 40 | 50 | 0.05 | 0 |
| G1M5S<br>G2M5S<br>G3M5S | 0.4 | 100 | 40 | 50 | 0.05 | 0.1 |
| G1M10<br>G2M10<br>G3M10 | 0.4 | 100 | 40 | 100 | 0.10 | 0 |
| G1M10S<br>G2M10S<br>G3M10S | 0.4 | 100 | 40 | 100 | 0.10 | 0.1 |

**Table 3.4: Mix proportions for graphene-cement mortar.**

| Mix Design | W/C ratio | Cement (C) (g) | Sand (g) | Water (ml) | GNP (mg) | GNP/C (%) | SP/C (%) |
|---|---|---|---|---|---|---|---|
| M0-M | 0.4 | 100 | 200 | 40 | 0 | 0 | 0.2 |
| G1M3-M<br>G2M3-M<br>G3M3-M | 0.4 | 100 | 200 | 40 | 30 | 0.03 | 0.2 |
| G1M5-M<br>G2M5-M<br>G3M5-M | 0.4 | 100 | 200 | 40 | 50 | 0.05 | 0.2 |
| G1M10-M<br>G2M10-M<br>G3M10-M | 0.4 | 100 | 200 | 40 | 100 | 0.10 | 0.2 |

### 3.3.3 Preparation of GCC for Micro-scale Characterization

For micro-scale characterization, small pieces were taken from hardened GCC paste specimens after 28-days of casting. Afterwards, these pieces were grounded into a fine powder using grinding machine. Figure 3.5 shows the grinding machine and powdered samples. These fine powder samples were further used for TGA, FTIR and XRD analysis.

(a) Grinding machine (b) Finely powdered sample packets

**Figure 3.5: Grinding process for remnant pieces of GCC**

### 3.3.3.1 Thermogravimetric Analysis

Thermogravimetric analysis (TGA) and differential thermal analysis (DTA) was used to determine the behaviour of graphene based cement composite at elevated temperature. TGA of the GCC was determined using NETZSCH STA 449 F3 *Jupiter*®. For this purpose, 40 mg sample was heated from 25 °C to 900 °C with a scanning rate of 10°C/min under nitrogen atmosphere condition. It determines the thermal stability of graphene-cement composite by measuring the weight loss with respect to heating under constant heating rate. NETZSCH STA 449 F3 *Jupiter*® runs under Proteus Software. It determines the mass changes in weight percentage and mg both with a readability range of 0.001 mg. It evaluates the mass-changes steps and determines the residual mass. It provides the differential thermogravimetric (DTG) curves i.e. 1st and 2nd derivative of the mass-change curve for an explanation of thermal results. Figure 3.6 shows the NETZSCH STA 449 F3 Jupiter® apparatus used in this experimental work.

**Figure 3.6: TGA apparatus NETZSCH STA 449 F3 *Jupiter*.**

### 3.3.3.2 FTIR Spectrometry

Fourier transform infrared (FTIR) spectrometry of GCC was evaluated by using Perkin Elmer FTIR-spectrum 400. The procedure for obtaining the FTIR spectra is as follows.

The crushed mortar sample and the Potassium bromide (KBr) were heated for 24 h at 105°C and then mixed in 1:1000 (powder: KBr) ratio in a controlled humidity environment. Next, the mixed sample was pressed at 10 ton for 1 minute using a Specac 15-Ton Manual Hydraulic Press. Finally, the obtained KBr pellet was placed in the sample container, and the infrared spectrum was obtained. Spectrum Analysis software was used to obtain the infrared spectrum. The spectrometer was operated with 4 $cm^{-1}$ resolution in the region of 400-4000 $cm^{-1}$. Figure 3.7 shows the FTIR apparatus attached to the computer.

**Figure 3.7: FTIR apparatus Perkin Elmer FTIR-spectrum 400 attached to computer system.**

### 3.3.3.3 XRD Analysis

X-ray diffraction was conducted on the grounded fine powder to see the mineralogical characteristics of the graphene-cement composite by using PANalytical-Empyrean X-ray diffractometer with Cu Kα radiation (1.5418 Å) operated at 45 kV and 40 mA and 2θ scan between 5° and 80°. Scan type was continuous and step time was 148.92 seconds, divergence slit was fixed type with slit size 0.0573° while receiving slit size was 0.10°. The measurement temperature was 25°C, scan axis was Gonio with 240 mm Goniometer radius. The diffraction pattern from International Centre for Diffraction Data (ICDD) was used to identify the chemical phases of the specimens by using “PANalytical X’Pert HighScore program. Figure 3.8 represents the PANalytical-Empyrean X-ray diffractometer, which has a perfect XRD platform to the characterization of materials, was used in this study.

Figure 3.8: PANalytical-Empyrean X-ray diffractometer.

### 3.3.3.4 FESEM Images

Later, from the remnant pieces of the cubes, small samples of size 1×1×0.5 cm were randomly picked and used for microstructural analysis. Surface morphology of graphene-cement composite was investigated by using Field Emission Scanning Electron Microscope (FE-SEM, Hitachi SU70 with semi-in-lens). FESEM can provide topographical and element information at a magnification of 10x to 800,000x. FESEM used a focused beam of a high-energy electron to generate a variety of signals at the surface of solid specimens. The signals that derive from electron-specimen interactions discovered information about the specimens. Moreover, it was equipped with Oxford Energy-dispersive X-ray (EDX) Spectrometer and used to identify the elemental composition of the specimens as shown in Figure 3.9. Samples were Gold/Palladium coated using the sputtering technique to enhance their conductivity prior to microscopic analysis.

**Figure 3.9: Hitachi SU70 Field emission scanning microscope (FESEM).**

### 3.3.4 Test Setup for Rheological Measurements

Rheological properties were characterized by using Rheometer MCR302 (Anton-Paar) as shown in Figure 3.10. The Rheoplus software was used to monitor and analyse the data points. To determine the rheological characteristics of the graphene-cement paste smooth parallel plates with the gap of 0.6 mm were used as shown in Figure 3.10 (b). GC paste was prepared according to the mix proportion of Table 3.5. Description of the specimens is given in Table 3.5. When material got ready it was poured on the plates immediately. Approximately 15 ml of GC paste was added on the plate having diameter 25 mm at a fixed temperature of 25 $^{O}$C. Initially, cement paste was held at rest and after 10 min then it was pre-sheared at a shear rate of 100 $s^{-1}$ for 60 seconds. This was done to re-homogenize the sample as cement paste has thixotropic character (Roussel et al., 2012). After 5 min, shear rate was applied from 0.6 $s^{-1}$ -200 $s^{-1}$ with 40 steps and then back from

200 $s^{-1}$ -0.6 $s^{-1}$. Downslope curve data was used for calculation of rheological parameters. Moreover, different content of graphene, different shear rate cycles, resting time, superplasticizer and test geometries were considered as the factors effecting the rheology of cement paste. To examine the influence of these variables on rheological properties only G1 type mix was used. Furthermore, the results of these variables were also determined by using concentric cylinder geometry. Smooth concentric cylinder with a gap thickness of 1.2 mm has been used. Figure 3.10 (c) shows the accessories for the concentric cylinder. The radius of the measuring cup (outer cylinder) and bob (inner cylinder) was 14.450 mm and 13.331 mm respectively. The active length of the bob was 120.2 mm and gap length was 40 mm. Bob (inner cylinder) rotates with variable rotational velocities to control the shear rate. Shear stress and shear rate were calculated from torque and applied rotational velocity. Cement paste samples were prepared according to the mix design of Table 3.3.

**Table 3.5: Description of rheological samples using parallel plates.**

| Mix Design | W/C ratio | Cement (g) | Water (ml) | GNP (mg) | GNP/cement (%) | Sher rate cycle range ($s^{-1}$) |
|---|---|---|---|---|---|---|
| M0 | 0.4 | 100 | 40 | 0 | 0 | 200-0.6 |
| G1M3<br>G2M3<br>G3M3 | 0.4 | 100 | 40 | 30 | 0.03 | 200-0.6 |
| G1M5<br>G2M5<br>G3M5 | 0.4 | 100 | 40 | 50 | 0.05 | 200-0.6 |
| G1M10<br>G2M10<br>G3M10 | 0.4 | 100 | 40 | 100 | 0.10 | 200-0.6 |

When the material was prepared, it was divided into three equal portions. The first portion was poured immediately while the second and third portion was poured after 30 min and 60 min later. Approximately 15 ml of graphene-cement paste was added at a fixed temperature of 25 $^{O}$C. Initially, cement paste was held at rest and after 10 min then it was pre-sheared at a shear rate of 100 $s^{-1}$ for 60 seconds. After 5 min, shear rate was applied from 0.6 $s^{-1}$ to 100 $s^{-1}$ and then back from 100 $s^{-1}$ to 0.06 $s^{-1}$ in 20 decreasing steps. Downslope curve data was used for calculation of rheological parameters. To examine the influence of shear rate cycle range on rheological properties only M0 and G1M3 mix were used. These samples were subjected to three different shear rate cycle range i.e. 100-0.6 $s^{-1}$, 200-06 $s^{-1}$ and 300-0.6 $s^{-1}$ with 20, 40 and 60 decreasing steps respectively. Three resting times, the time between sample preparation and casting were considered in this study to examine their effect on cement-paste rheology. For this purpose, only M0 and G1M3 mix were used. At different time interval, 0 min, 30 min and 60 min, samples were manually stirred for 15 seconds before measuring the rheological data. Influence of superplasticizer on rheological properties and different test geometries was studied on M0 and G1M3 mixes. The detail description of the graphene percentage, shear rate cycle range, resting time and superplasticizer of various samples for measuring rheological data is given in Table 3.6. Apparent viscosity, shear stress and a shear rate of graphene-cement paste with different proportions were measured by the rheometer. Yield stress and plastic viscosity of the graphene-cement paste was determined by using the Bingham, Modified Bingham, Herschel-Bulkley and Casson models. Besides this, results of the concentric cylinder geometry were compared to the parallel plate setup.

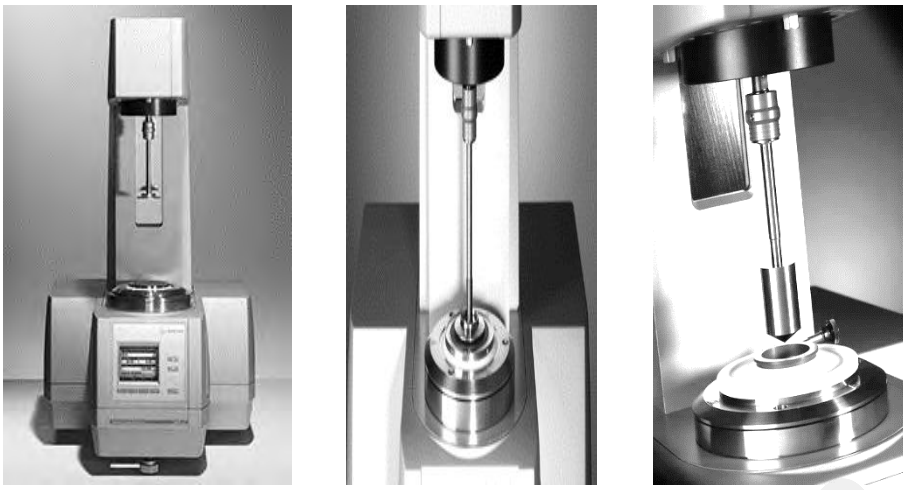

(a) Rheometer MCR302 Anton-Paar (b) Parallel plate setting (c) Concentric cylinder setting

**Figure 3.10: Experimental setup for rheological measurements.**

**Table 3.6: Description of rheological samples.**

| Sample | Sher rate cycle range ($s^{-1}$) | Resting time (min) |
|---|---|---|
| **Effect of graphene percentage** | | |
| M0 (Control) | 200-0.6 | 0 |
| G1M3 | 200-0.6 | 0 |
| G1M5 | 200-0.6 | 0 |
| G1M10 | 200-0.6 | 0 |
| **Effect of shear rate** | | |
| M0a | 100-0.6 | 0 |
| M0b | 200-0.6 | 0 |
| M0c | 300-0.6 | 0 |
| G1M3a | 100-0.6 | 0 |
| G1M3b | 200-0.6 | 0 |
| G1M3c | 300-0.6 | 0 |
| **Effect of resting time** | | |
| M0-0 | 200-0.6 | 0 |
| M0-30 | 200-0.6 | 30 |
| M0-60 | 200-0.6 | 60 |
| G1M3-0 | 200-0.6 | 0 |
| G1M3-30 | 200-0.6 | 30 |
| G1M3-60 | 200-0.6 | 60 |
| **Effect of SP** | | |
| M0 (Control) | 200-0.6 | 0 |
| M0S | 200-0.6 | 0 |
| G1M3 | 200-0.6 | 0 |
| G1M3S | 200-0.6 | 0 |

### 3.3.5 Mechanical Properties of Graphene Cement Composites

After the workability test, the mixture was poured into the moulds of dimensions 50 x 50 x 50 mm and 160 x 40 x 40 mm for compressive and flexural test respectively. Moulds were filled in three parts while vibrating table was used to remove the entrapped air. The moulds were removed after 24 hours and samples were cured in a curing tank at room temperature before testing. Mechanical properties i.e. compressive strength and flexural strength were determined at 1-day, 7-day and 28-day after casting, the specimens were being dried for approximately 5 hours. ASTM C109/C109M  was used for compressive strength test (ASTM C 109, 1999) and ASTM C348-14 was followed for the flexural strength test (ASTM C 348). Compressive strength and flexural strength tests were performed by using ELE International ADR-Auto V2.0 2000 36-4150/01. Experimental test setup for compressive strength test and flexural strength test is given in Figure 3.11. Moreover, a loading rate of 0.5 kN/s and 0.05 kN/s was being used for the compressive and the flexural strength tests respectively.

(a) ELE International ADR-Auto V2.0 2000 36-4150/01

(b) Compressive testing machine (c) Flexural testing machine

**Figure 3.11: Testing setup for graphene cement composite.**

### 3.3.6 Test Setup for Electrical Properties

To determine electrical properties, a prism was casted having dimensions of 160 x 40 x 40 mm. Four-stainless-steel wire meshes of 11 x 11 mm cross-section with an average thickness of 1.3 mm and dimensions of 40 x 70 mm were inserted in the samples to measure the electrical properties of GCC specimens as shown in Figure 3.12. The four-probe method was used to determine the piezoresistive properties of the GNP-cement composite specimens. The outer two wire meshes were positioned at 10 mm from the ends of the prism while the inner two wire meshes were positioned at 40 mm from the outer wire mesh.

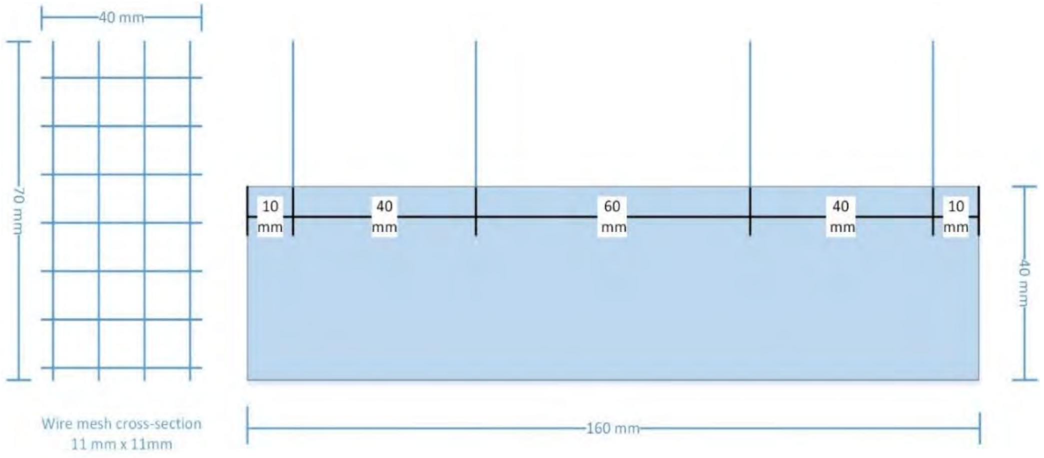

**Figure 3.12: Dimensions of the graphene-cement composite specimen with wire mesh details.**

Table 3.7 shows the mix proportions used for determining the piezoresistive properties of the graphene cement composites. The setup for measuring the electrical resistivity comprise of Instron 600 kN machine used for applying a compressive load, TDS-530 data logger to record the voltage measurements, a DC power supply, and 10-ohm resistance. Specimens were placed in Instron machine and a constant voltage of 15 V through DC power supply was applied to the samples. Figure 3.13 shows the schematic illustration of the electrical connection in circuit. Inner wire meshes were connected to the data logger and measures the voltage drop in V. Meanwhile, one of the outer wire meshes was connected to the negative terminal of the power supply and the remaining outer wire mesh was connected to the resistor followed by the connection to the second channel of the data logger and positive terminal of the power supply forming a series circuit as shown in Figure 3.13.

**Table 3.7: Mix proportions for cement paste.**

| Mix Design | W/C ratio | Cement (g) | Water (ml) | GNP (mg) | GNP/cement (%) |
|---|---|---|---|---|---|
| M0 | 0.4 | 100 | 40 | 0 | 0 |
| G1M3<br>G2M3<br>G3M3 | 0.4 | 100 | 40 | 30 | 0.03 |
| G1M5<br>G2M5<br>G3M5 | 0.4 | 100 | 40 | 50 | 0.05 |
| G1M10<br>G2M10<br>G3M10 | 0.4 | 100 | 40 | 100 | 0.10 |

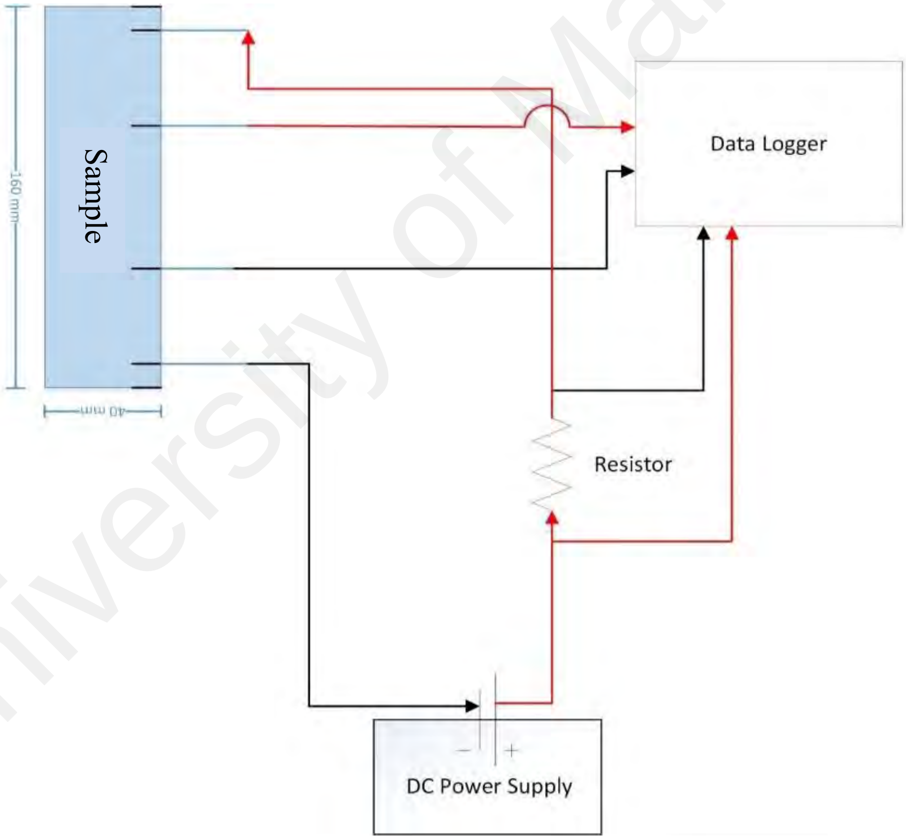

**Figure 3.13: Schematic illustration of the electrical connections.**

Furthermore, Figure 3.14 (a) shows the overall test setup for the measurement of electrical properties. The strain gauges were attached to the specimens to monitor the produced strain (Figure 3.14 (b)). TDS-530 data logger was recording all the measurements. The stress-strain curves were developed and compared to electrical properties of the GC specimens. Moreover, these curves were used to explore the characteristics of smart sensors and further used for SHM of concrete structures. Furthermore, to observe the sensing ability of the specimens, normalized compressive loading (NCL) values were calculated. It is the ratio between the applied loads to the maximum compressive load before specimen failure. For electrical resistance values, the fractional change in resistance (FCR) was used. Equations 3.1 and Equation 3.2 presents the calculation procedure for the NCL and FCR values.

$$\text{NCL} = \frac{P}{P_{max}} \quad (3.1)$$

$$\text{FCR} = \frac{\rho_t - \rho_o}{\rho_o} \text{ x } 100\% \quad (3.2)$$

Where: $\rho_t$ = electrical resistivity at the given time during the test; $\rho_o$ = electrical resistivity at the start of the test; P = compressive loading at the given time during the test; $P_{max}$ = maximum compressive loading for the specimen.

## 3.4 Practical Application of Graphene Cement Composite

The practical application of the graphene-cement composite specimen was investigated by testing the graphene-cement composite specimen in reinforced concrete beam and concrete-filled steel tube beam in the laboratory. Dai et al. (2014) explored the effect of percentage of graphene flakes on the strain and damage sensing of the composites. They found that with an increase in the percentage of graphene flakes in cement based composite, the fractional change in resistance values was also increasing. Therefore, based on the study of Dai et al. (2014), only M0 and G1M3 specimens were considered to explore the potential application of composite materials.

### 3.4.1 Reinforced Concrete (RC) Beam

A rectangular beam was casted having a cross-sectional dimension 200 x 300 (mm) and span length 3200 mm as shown in Figure 3.15. This RC beam was used for investigating the practical application of smart sensors based on GCC. Details and dimensions of GCC was already discussed in Figure 3.12. Moreover, Figure 3.15 (a) shows the placement of GC smart sensors in RC beam. Plain bar of 10 mm diameter was used as stirrups and main bars of 16 mm diameter were used as main tension reinforcement. The yield strength of the plain and main bars was ~ 394 MPa and 540 MPa respectively. Details of the reinforcement bars, stirrups and spacing are mentioned in Figure 3.15 (a). Figure 3.15 (b) shows the reinforced steel mesh prior to concrete casting. The strain gauge was attached to the main reinforcement bar to determine the strain values in steel. Later these values were compared to the readings of GC specimen. For the preparation of concrete beam, OPC, sand, coarse aggregate and water were used. The OPC was conforming to MS 522 Part 1 2003 (MS-522: Part 1, 2003) with a specific surface area and specific gravity of 0.351 $m^2/g$ and 3.14, respectively. The chemical composition of OPC is given in Table 3.1. Local mining sand with fineness modulus of 2.89, specific gravity of 2.68, water absorption 0.51% and maximum grain size of 4.75 mm was used as fine aggregate. Crushed granite aggregate of 20 mm maximum size was used as the coarse aggregate. The water-cement ratio (w/c) was kept constant as 0.5. Cement, sand and coarse aggregate were used in the ratio of 1:2:4.

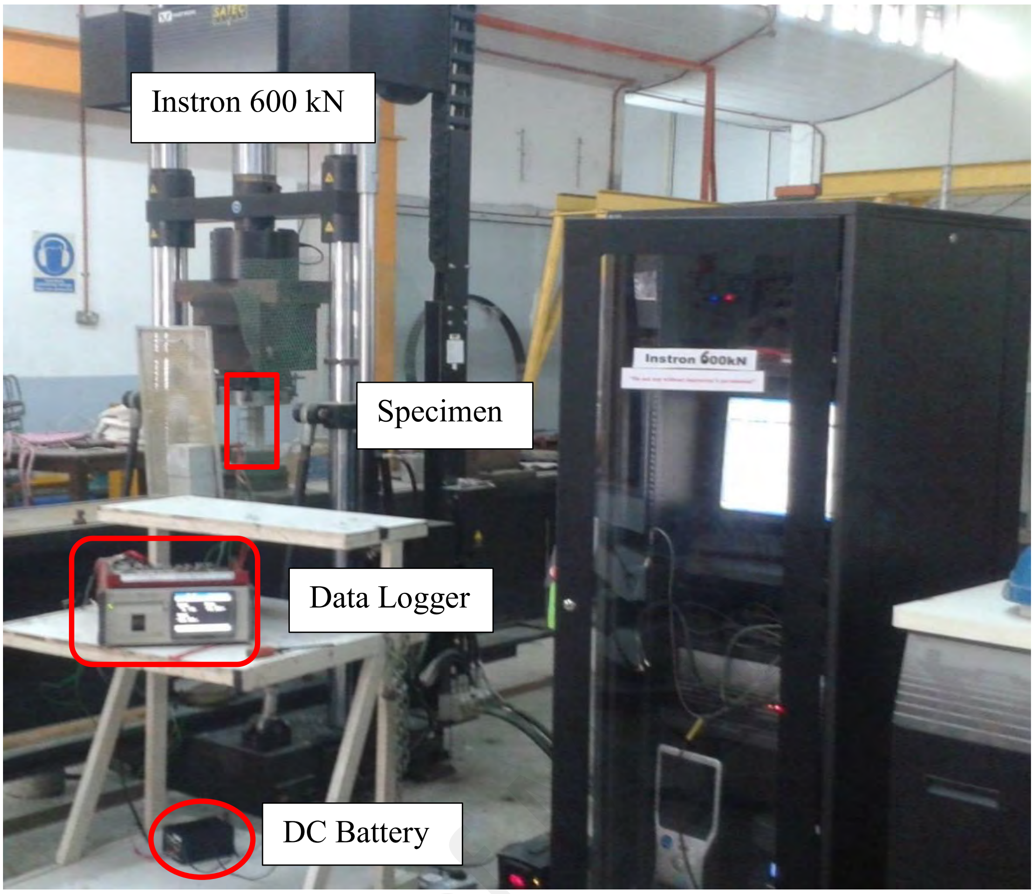

(a) The overall test set up for four-probe electrical properties testing

(b) placement of specimen with strain gauge into Instron 600 kN machine

(c) TDS-530 Datalogger

**Figure 3.14: Measurement of electrical properties.**

To determine the workability of concrete slump cone test was used as per BS EN 12350-2 (BS EN12350-2, 2009). Concrete was found workable with slump value of 35 mm. BS EN 12390-3 (BS EN 12390-3, 2000) was followed to calculate the compressive strength of concrete. Three cubes of 100 x 100 x 100 mm were tested after 28-day of casting and determined the average compressive strength of ~ 34 MPa.

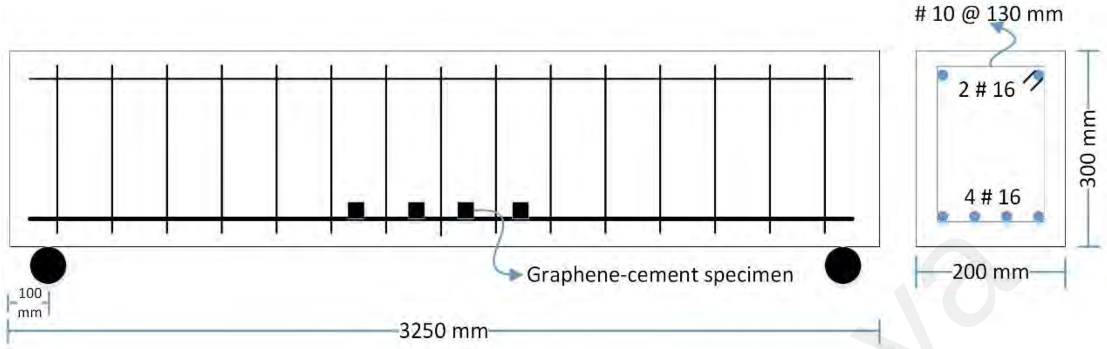

(a) Schematic layout of longitudinal and cross-sectional details of beam

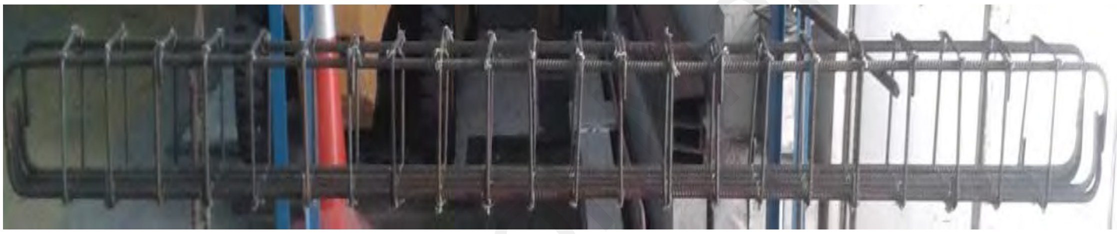

(b) reinforced steel cage

**Figure 3.15: Details of reinforced concrete beam.**

ASTM C469 (ASTM C 469, 2014) was used to determine the modulus of elasticity of concrete and its value was found 28.50 GPa. Figure 3.16 shows the sample placement and casting of concrete. GC specimens were placed in the middle-third portion of the concrete beam, in order to observe the propagation of the damages and cracks as shown in Figure 3.16 (a). Samples were tied with the main reinforcement to remain fix and unaffected due to vibration and casting of concrete. Spacing between GCC specimens was 300 mm. Portable vibrator was used to remove the entrapped air during concreting as shown in Figure 3.16 (b). It was used with extreme care so that the electrical connections remain in contact. Figure 3.16 (c) represents the casting of concrete in beam mould.

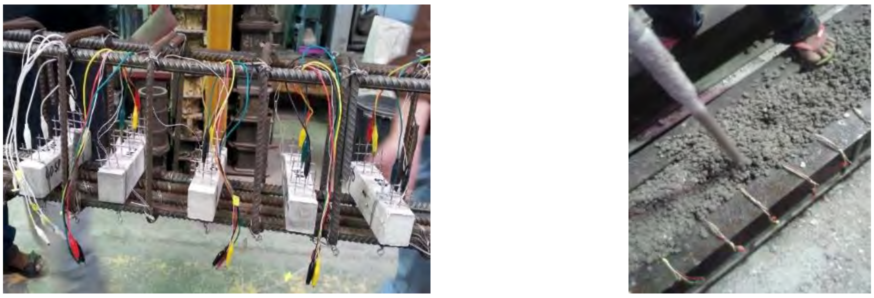

(a) Placement of sample on reinforced bars

(b) Use of vibrator to remove the entrapped air

(c) Casting of concrete in beam mould

**Figure 3.16: Sample placement and casting of the beam.**

After 28 days, this beam was subjected to flexural loading. Figure 3.17 (a) shows the test setup for the testing of the beam. Before testing all the electrical connections were checked. Two types of flexural loading were applied, one was from zero to failure stage and other one is profile loading. In profile loading, different damages were introduced in the beam by applying different loading. It determines the effectiveness of the GC smart sensor against various damages. Damage-sensing is better and realistic approach as compared to stress or strain sensing. Damage generation is irreversible upon unloading however, stresses are reversible upon unloading. Therefore, real-time and continuous monitoring is not required in case of damage-sensing. It is often called as damage memorization as well. Therefore, to check the effectiveness of graphene-cement specimen as damage-sensing instead of stress-sensing, the beam was subjected to profile loading. Damage levels from 1 to 5 were induced in the beam and response of the GC specimen was noted. Loading protocols and damage levels are given in Table 3.8. Profile loading was applied to the beam, a 15 kN/min loading rate was used for increase loading cycle and then at maximum load, it was held for 2 min and then finally reduced back to zero loads with 25 kN/min loading rate. Experimental setup for reinforced beam testing is given in 3.17 (a). Four-point loading was applied to the beam. Electric power was applied through the 15 V DC battery and TDS-530 data logger was used to record the data. Figure 3.17 (b) shows the electrical connection setup attached with the graphene-cement sample and battery. The parallel circuit was used to monitor the electrical resistivity values from the pure cement specimen and graphene-cement composite specimen. As the beam was subjected to flexural loading, therefore, flexural cracks were developed in the middle-third region of the beam as shown in Figure 3.17 (c). Due to this reason, graphene-cement specimens were placed within the middle-third portion of the RC beam. Figure 3.17 (c) showed the propagation of cracks and failure of the beam.

**Table 3.8: Description of loading protocols and damage levels.**

| **Damage Level** | **Deficiency Level** | **Crack length** | **Loading (kN)** | **Design loading (%)** |
|---|---|---|---|---|
| 0 | None | None / 1 µm | 0-40 | 20 |
| 1 | Marginal | Partial / 100 µm | 0-80 | 40 |
| 2 | Moderate | Some/ ≤ 1mm | 0-120 | 60 |
| 3 | Severe | Fair amount / ≤10 mm | 0-160 | 80 |
| 4 | Severe | Large amount / ≤100 mm | 0-200 | 100 |
| 5 | Failed | Large / ≤1m | 0-Fail (227) | >100 |

(a) Overall test set up for testing of reinforced concrete (RC) beam.

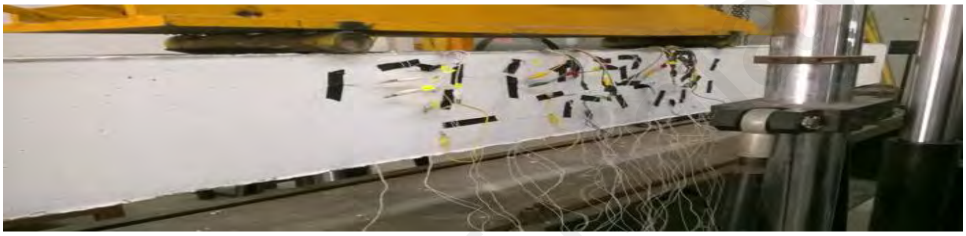

(b) Electrical connections for RC beam enlarge view of the marked area in (a).

(c) Failure of the beam under flexural loading.

**Figure 3.17: Description of test setup in the laboratory.**

# CHAPTER 4: RESULTS AND DISCUSSIONS

## 4.1 Introduction

This chapter focuses on the presentation and analysis of the experimental results. The data obtained throughout the investigation are interpreted and explained. This chapter consists of nine sections and several subsections. The outcomes of the results are discussed technically and elaborately.

## 4.2 Dispersion Efficiency of Graphene

Ultraviolet-visible (UV-vis) spectrometric measurements were used to determine the stability of dispersed graphene in aqueous solution. As graphene flakes absorbed light in aqueous solution therefore, absorbance peak values can represent the concentration of suspended graphene flakes in solution. Deionized water was used as a reference for determining the dispersion efficiency of graphene flakes. It is known that graphene is hydrophobic in nature and its hydrophobicity depends on the thickness of graphene layers (Munz et al., 2015). Moreover, it formed the flocculated structures in aqueous solution. Hence, it is important to study the dispersion efficiency of graphene in water. Figure 4.1 shows the absorbed spectra for the graphene solution. It was noted that the highest absorbance peak appeared at 271 nm, which represents the $\pi$ -$\pi$* transition of carbon bond.

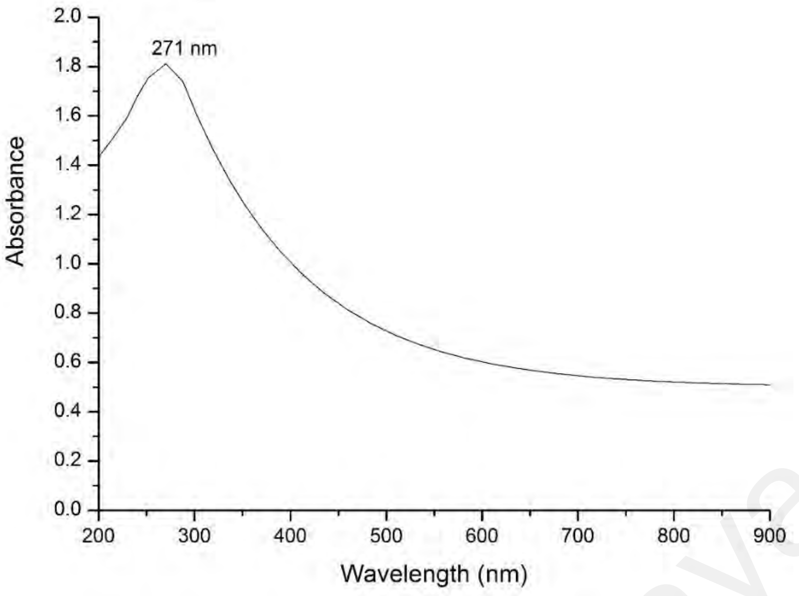

**Figure 4.1: Absorbance spectra of graphene in aqueous solution.**

### 4.2.1 Effect of Graphene Type on Dispersion Efficiency

The absorbance values for different types of graphene at a wavelength of 271 nm are given in Figure 4.2. The graphene flakes were dispersed in aqueous solution using ultrasonication. It was found that absorbance values were decreasing for all graphene types with the passage of time. Overall peak drop from 0-120 min after ultrasonication for G1 type graphene was recorded as 18%, however, for G2 and G3 type it was 57% and 56% respectively. It was noted that maximum absorbance value was observed for G1 type, while minimum for G2. According to Munz et al. (2015), the hydrophobicity of graphene is dependent upon the thickness of the graphene layers and it increases with the layers of graphene sheets. Therefore, the possible reason for absorbance values may be attributed to the high surface area and less flake thickness. However, for G2 type graphene, flake thickness is 2.5 times more than G1, which will make agglomeration easier and increase its sedimentation. Interestingly, from 30-120 min time interval absorbance peak drop value for G3 was approximately twice of the G2 and four-time of

G1. Main reason is the difference between average flake thickness and surface area. Average flake thickness is 5 times more than G1 and twice of G2, however, the surface area is half of G1 and two-thirds of G2. Therefore, it can be deduced from these results that surface area, flake thickness and average lateral flake size have a strong influence on the dispersion of graphene in aqueous solution. It may be concluded that graphene flakes with high surface area, less flake thickness and moderate lateral size have better dispersion.

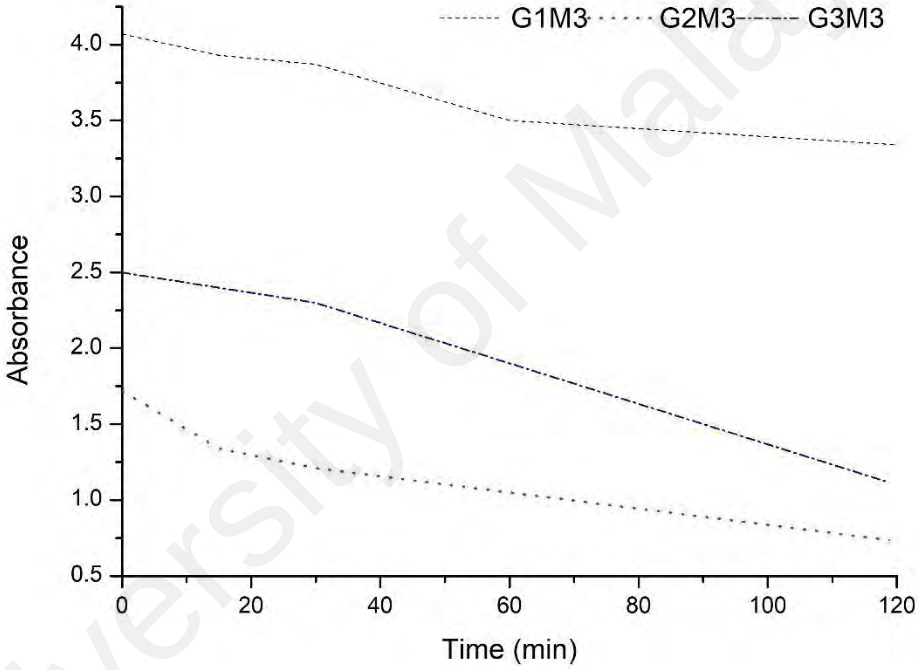

**Figure 4.2: Absorbance values for various graphene types at different time interval observed at 271 nm peak.**

### 4.2.2 Effect of Superplasticizer on Dispersion Efficiency

Superplasticizer (SP) plays an important role on the dispersion of nanomaterials. Influence of SP has been widely studied by the various researchers. As superplasticizer has an electromagnetic charge on it therefore, due to electrostatic repulsion it disperses the nanomaterials. Figures 4.3 represents the absorbance peak values for different graphene type at 271 nm with and without SP. SP greatly enhanced the dispersion of graphene flakes and higher absorbance peaks were recorded. Moreover, it was found that with the passage of time, SP significantly stops the sedimentation of graphene and make them stable for a long duration. However, for G3 type a continuous drop was observed in absorbance values and it may be attributed to the thick layer of graphene flakes which is in conformity of the findings of Munz et al. (2015). Munz et al. (2015) found that two-layer graphene is more hydrophobic than single-layer graphene. In general, it can be concluded that superplasticizer greatly influences the dispersion of graphene flakes and make them stable and uniformly spread in the aqueous solution over long duration.

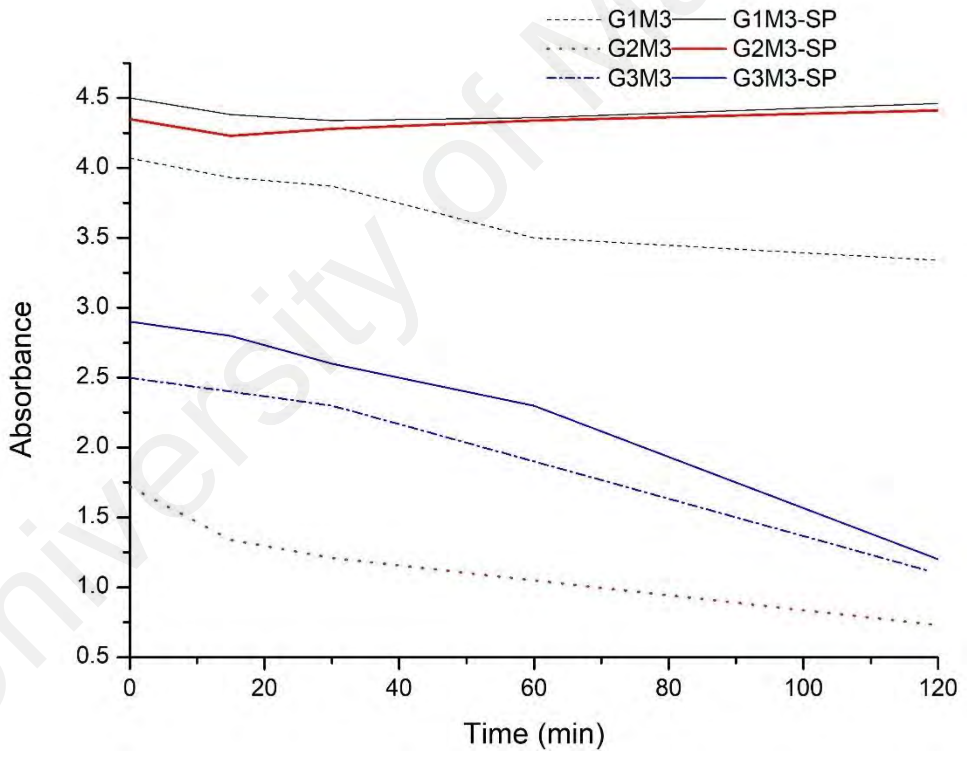

**Figure 4.3: Effect of superplasticizer on the absorbance values for various graphene types at different time interval observed at 271 nm peak.**

### 4.2.3 Effect of Magnetic Stirring on Dispersion Efficiency

As graphene is hydrophobic (Munz et al., 2015), therefore, it will form the agglomerates in aqueous solution as shown in Figure 4.4. The green circular line in Figure 4.4 shows the adhesion of graphene with the walls of beaker while, yellow circles marked various agglomerates. Materazzi et al. (2013) and Ubertini et al. (2014) used the magnetic stirring for the dispersion of nanomaterials in deionized water. Materazzi et al. (2013) performed the dispersion of nanomaterial with a magnetic stirrer, mechanical agitator and by sonication.

(a) Top view

(b) Side view

**Figure 4.4: Agglomeration of graphene in aqueous solution.**

Similarly, Ubertini et al. (2014) used 10 min of magnetic stirring, 60 min of sonication and 15 min of mechanical mixing for the preparation of carbon nanotube cement based sensor. Thus, in order to exfoliate graphene flakes further in aqueous solution, a combination of ultrasonication and magnetic stirring were used. In order to determine the optimum duration of magnetic stirring various stirring time was utilized. Figure 4.5 shows the variation of absorbance peaks value with different stirring time observed at 271 nm peak after 120 min of magnetic stirring. It was found from the Figure 4.5 that after magnetic stirring absorbance peaks increased. The optimum increase in absorbance peak was noted for all graphene types on 40 min of the stirring time. After this, a decrease in the absorbance values were recorded. According to Liu, CX &Choi (2012), high-speed stirring results in shearing forces which shorten the length of nanotubes. Magnetic stirring helps in dissolving the nanomaterials, however, make the dispersion less stable (Liu, CX & Choi, 2012). The possible reason for decrease in absorbance peaks is excessive magnetic stirring, which breaks the graphene flakes and reduce the surface area. Graphene flakes having high surface area shows more drop in absorbance values as compared to less surface area (Figure 4.5). Therefore, this drop is directly related to the surface area of graphene. In short, it is found that magnetic stirring of 40 min in combination with ultrasonication gave the optimum results.

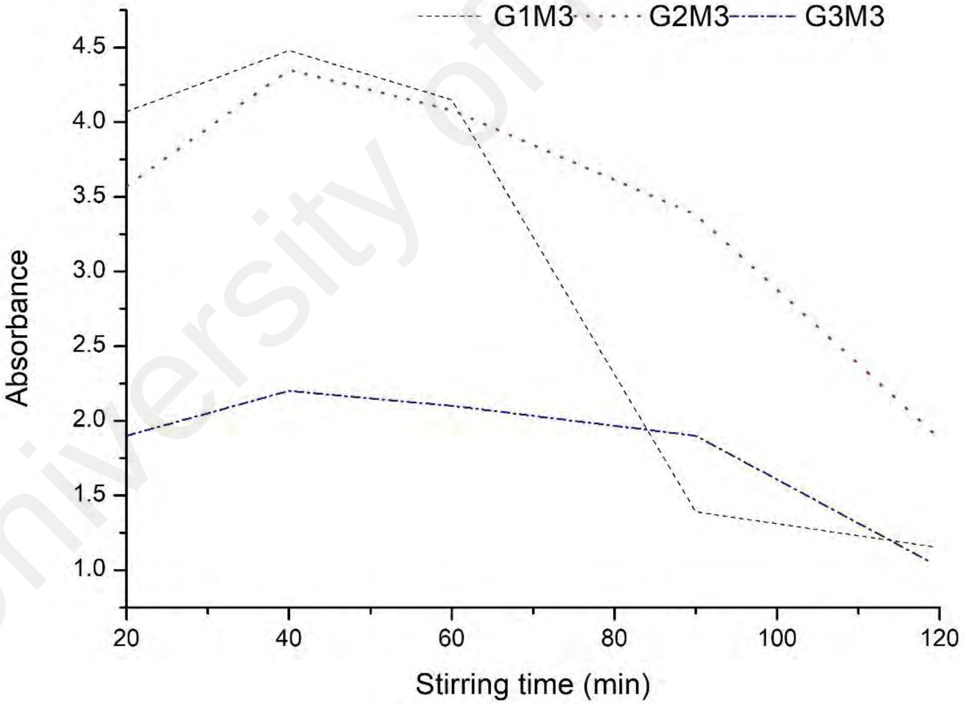

**Figure 4.5: Variation of absorbance peaks value of graphene types with different stirring time.**

Influence of magnetic stirring on graphene flakes in the presence of superplasticizer was investigated as well. Figure 4.6 presents the track of the absorbance peaks for different graphene types against magnetic stirring duration observed at 271 nm peak after 120 min of magnetic stirring. It was observed that due to superplasticizer the dispersion was more stable at high magnetic stirring duration. As the flake thickness was more for G3 type, therefore, at high magnetic stirring time these flakes broke, formed the agglomerates and made the overall dispersion less stable.

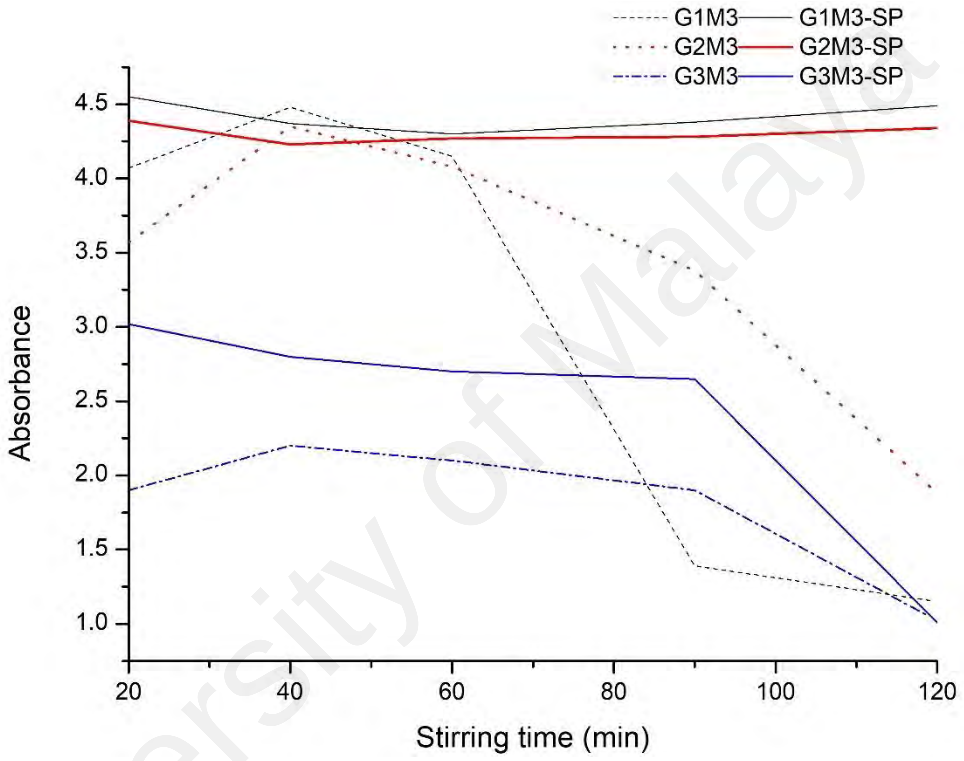

**Figure 4.6: Influence of superplasticizer on the absorbance peaks value of graphene types with different stirring time.**

In conclusion, graphene is hydrophobic in nature, however, hydrophobicity is dependent on the thickness, lateral size and surface area of graphene. Graphene flakes with the high surface area, less thickness and moderate lateral size provide better results. Additionally, magnetic stirring for 40 min in combination with ultrasonication gave the optimum results.

## 4.3 Micro-scale Characterization of Graphene Cement Composites

Microanalytical characterization of the graphene-cement composites were investigated using various techniques. Thermogravimetric analysis was used to investigate the thermal behaviour. Chemical interaction was examined using Fourier Transform Infrared spectrometer. X-ray Diffractometer was used to explore the crystalline structure and phase composition of GCC. Microstructure analysis of graphene-cement composite was done using field emission scanning electron microscope analysis. In this section, microanalytical characterization will be discussed in detail.

### 4.3.1 TGA/DTG Curves of Graphene Cement Composite

TGA/DTG curves for graphene-cement composite was obtained and presented in Figure 4.7. Table 4.1 shows the weight loss in the region 1, 2 and 3 as mention in Figure 2.9. TGA/DTG curves for G1, G2 and G3 types cement mixes were given in Figure 4.7 (a), (b) and (c) respectively. Each illustration highlights the influence of an increase in graphene content in the composite material. Percentage weight loss with respect to total weight loss in three regions were also determined. Moreover, approximate amount of calcium hydroxide was obtained using molecular mass ratio. The first derivative of the mass curve was also taken and plotted on the secondary axis in Figure 4.7. Overall 64 different samples were used to obtain the TGA/DTA data for various graphene cement composite mixes at different curing age time. It is important to mention here that, due to the limitation of measuring equipment and a huge number of specimens, some samples were not tested on the exact date. Testing of specimens was started with G1 type mix followed by G2, G3 type mixes and ended with control (M0) mix. Therefore, slight variation in results of G1 type and M0 was expected. Generally, the weight loss during 180-300 $^{o}$C range of cement composites was less for G1 type as compared to control sample. However, the weight loss for G2 and G3 was found more as compared to M0.

This weight loss is associated with the dehydration of bonded water from CSH, hence, it has higher hydration reaction degree. Increase in production of hydrated cement products i.e. CSH gel will fill up the micropores and enhance the mechanical properties. In region 2 weight loss is related to the dehydroxylation of portlandite. It gives the estimation of the presence of hydrated cement products. According to Trezza (2007), the amount of portlandite (CH) gives an indication of the degree of hydration reaction. It was noted that higher percentages of graphene yielded a higher amount of CH (Table 4.1). Few anomalies were observed for G1M3 mix and G3M5. These anomalies may be related to the delay of testing setup. Therefore, it is concluded that more hydrated cement products formed in graphene-cement composite material. Moreover, GCC are more packed, durable and more hydration occurred by incorporating graphene.

**Table 4.1: Weight loss obtained from TGA/DTG and calculation of CH for different percentage of graphene-cement composites.**

| **Sample / Temperature** | **Weight loss (%) / Weight loss with respect to total weight loss (%)** | | | | | | **Amount of CH using Molecular Mass ratio (%)** | | |
|---|---|---|---|---|---|---|---|---|---|
| | **180-300 $^{o}$C** | | **430-480 $^{o}$C** | | **600-780 $^{o}$C** | | **430-480 $^{o}$C** | **600-780 $^{o}$C** | **Total** |
| | (dehydration of bonded water) | | (dehydroxylation of portlandite) | | (decarbonation of calcium carbonate) | | | | |
| M0 | 3.17 | 39.7 | 2.60 | 32.5 | 2.22 | 27.8 | 10.68 | 3.74 | 14.42 |
| G1M3 | 2.58 | 28.7 | 1.35 | 15.0 | 5.05 | 56.2 | 5.54 | 8.486 | 14.03 |
| G1M5 | 3.01 | 38.3 | 2.91 | 37.0 | 1.94 | 24.7 | 11.96 | 3.26 | 15.22 |
| G1M10 | 3.00 | 36.3 | 3.38 | 40.9 | 1.89 | 22.9 | 13.91 | 3.17 | 17.08 |
| G2M3 | 3.10 | 40.2 | 2.66 | 34.5 | 1.95 | 25.3 | 10.95 | 3.28 | 14.23 |
| G2M5 | 3.15 | 40.1 | 2.66 | 33.9 | 2.04 | 26.0 | 10.93 | 3.43 | 14.36 |
| G2M10 | 3.29 | 39.5 | 2.90 | 34.8 | 2.14 | 25.7 | 11.93 | 3.60 | 15.53 |
| G3M3 | 3.60 | 43.4 | 2.93 | 35.3 | 1.76 | 21.2 | 12.03 | 2.96 | 14.98 |
| G3M5 | 2.53 | 36.8 | 1.98 | 28.8 | 2.36 | 34.4 | 8.13 | 3.97 | 12.09 |
| G3M10 | 3.29 | 41.9 | 2.68 | 34.1 | 1.88 | 23.9 | 11.03 | 3.16 | 14.19 |

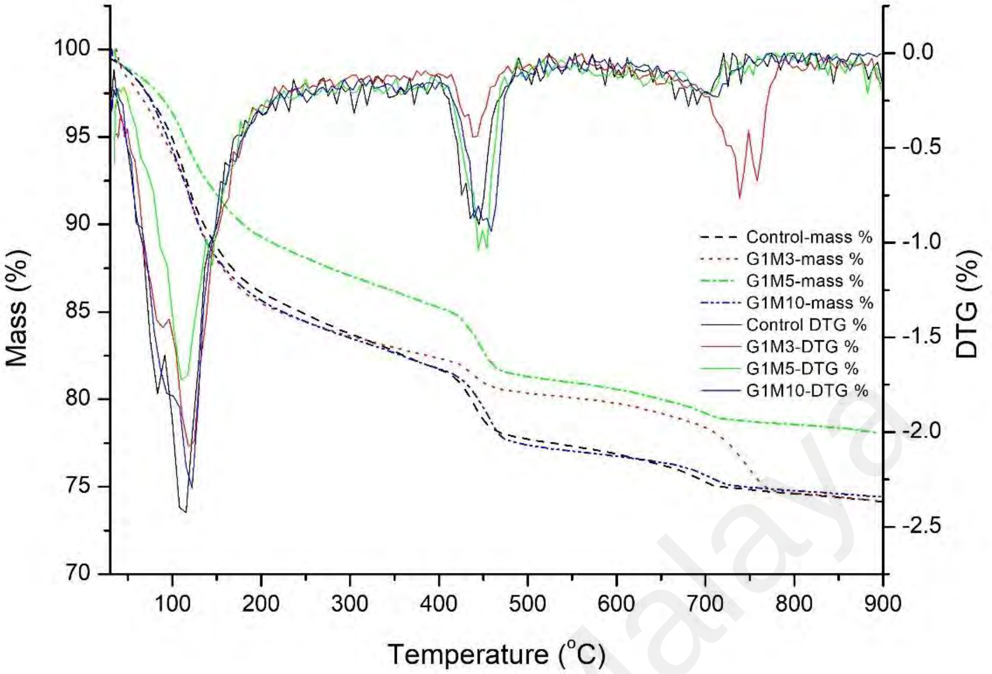

(a) G1-cement composites

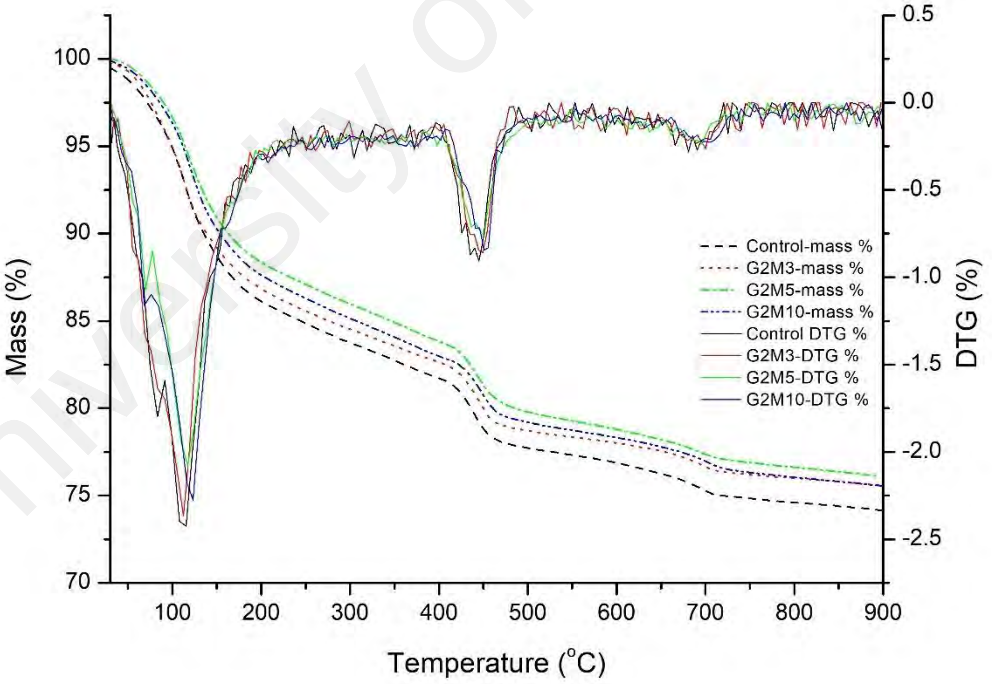

(b) G2-cement composites

**Figure 4.7: Continued**

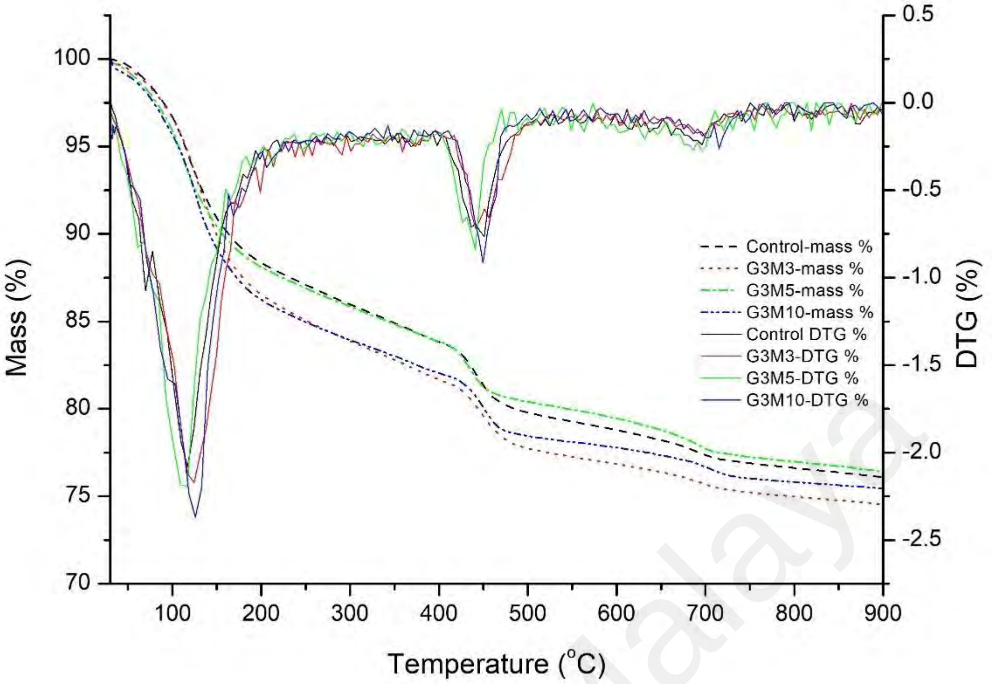

(c) G3-cement composites

**Figure 4.7: TGA/DTG curves for graphene cement composites.**

Table 4.1 is also used to study the influence of different types of graphene on cement composites with respect to weight loss obtains from TGA/DTG curves. TGA/DTG curves presented in Figure 4.7 may also be used further to investigate the effect of graphene surface area and sizes on elevated temperature. It was observed that weight loss corresponding to region 1 (water loss from the bonded water of CSH gel) was maximum for G3 type followed by G2 and G1. However, maximum percentage of calcium hydroxide was noted for G1 cement mixes followed by G2 and G3. Therefore, it is difficult to mention that's as to which graphene type yields more hydrated products than the other. However, it can be stated from observing the trend of TGA curves that graphene with more surface area produce more amount of CH whereas, graphene flakes with large lateral size and thickness will affect the amount of CSH gel. Thus, G2 type graphene is the optimum one and gave the best results. Later, in the mechanical properties section, it was found that G2 type cement mix obtains the maximum values for compressive and flexural strength. It was found that nanomaterials enhanced the mechanical properties at an early age more as compared to later age. For this purpose, samples were tested at 7 and 28 days after casting for thermogravimetric analysis. Table 4.2 shows the weight loss for region 1, 2 and 3 and the approximate amount of CH for cement composites at 7-day and 28-day. TGA/DTG curves for graphene type G1, G2 and G3 based cement composites were given in Figure 4.8 (a), (b) and (c). It was observed for G1 type cement composite that weight loss in region 1 for 28-day specimen was increased by 33% as compared to the 7-day specimen. In similar region increment of 9% and 17% were found for G2 and G3 type composites respectively. Generally, it was estimated that the amount of CH was increasing with curing age. In short, it can be concluded that hydrated cement products were increasing with increase in curing age, however, graphene flakes enhanced the growth of CSH gel in the cement composite.

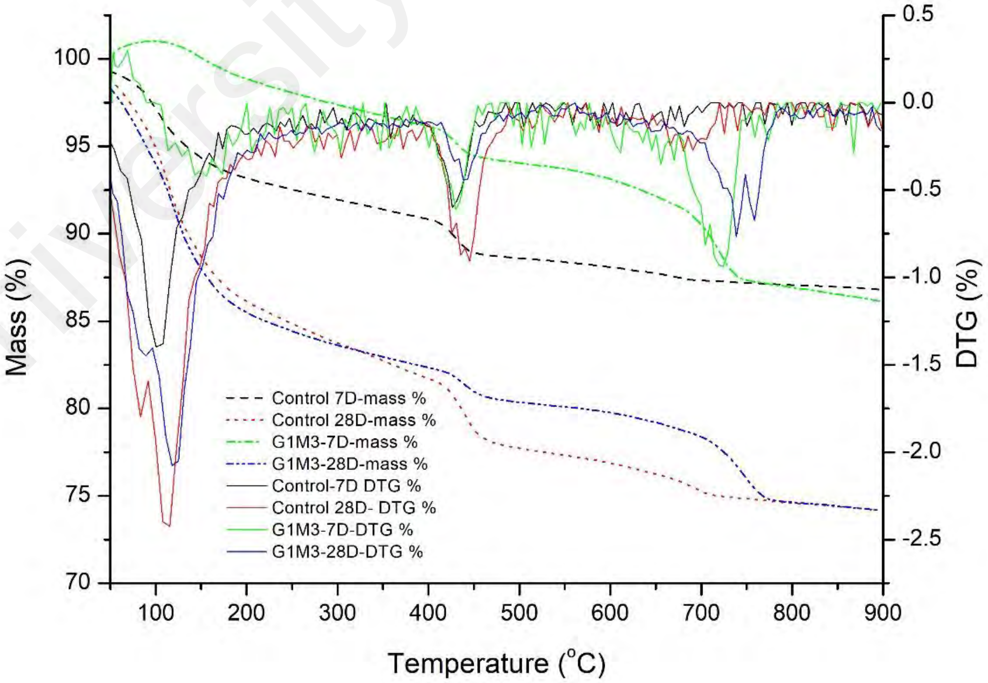

(a) G1-cement composites

**Figure 4.8: Continued**

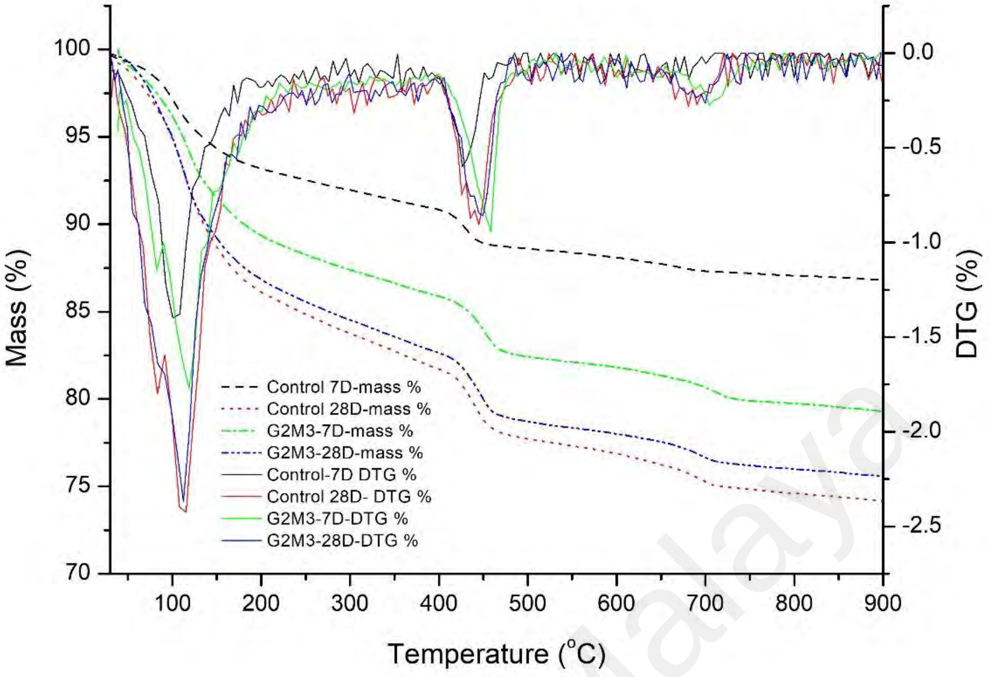

(b) G2-cement composites

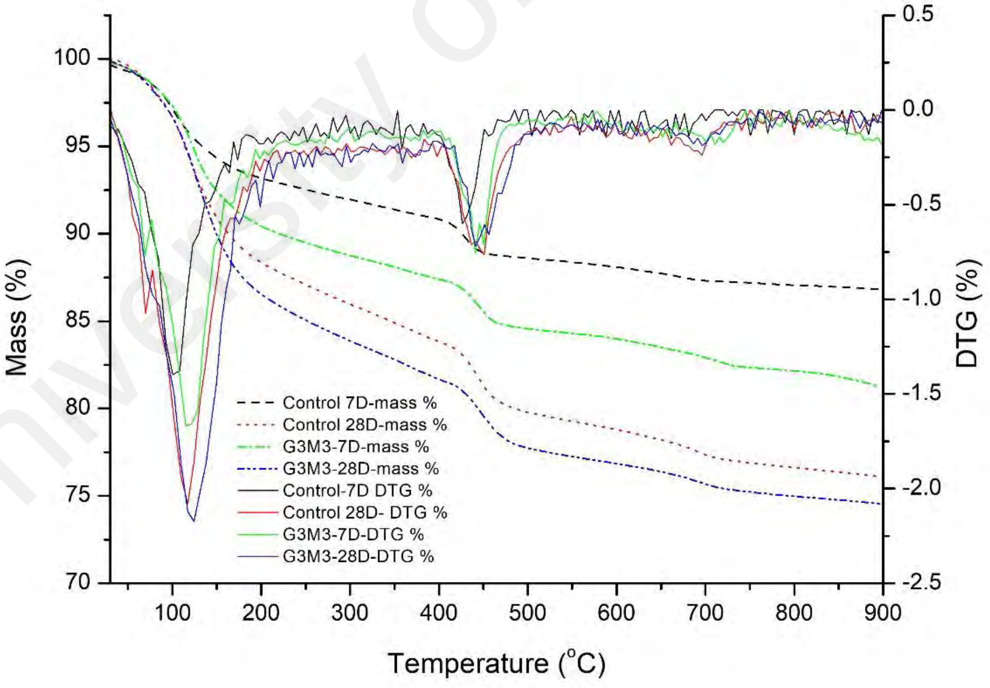

(c) G3-cement composites

**Figure 4.8: TGA/DTA curves for graphene cement composites at 7 and 28 days after casting.**

**Table 4.2: Weight loss obtained from TGA/DTA and calculation of CH for graphene cement composites at 7 and 28 days.**

| **Sample / Temperature** | **Weight loss (%) / Weight loss with respect to total weight loss (%)** | | | | | | **Amount of CH using Molecular Mass ratio (%)** | | |
|---|---|---|---|---|---|---|---|---|---|
| | **180-300 $^{o}$C** | | **430-480 $^{o}$C** | | **600-780 $^{o}$C** | | **430-480 $^{o}$C** | **600-780 $^{o}$C** | **Total** |
| | (dehydration of bonded water) | | (dehydroxylation of portlandite) | | (decarbonation of calcium carbonate) | | | | |
| M0-7D | 1.59 | 41.4 | 1.29 | 33.6 | 0.96 | 25.0 | 5.32 | 1.61 | 6.93 |
| M0-28D | 3.17 | 39.7 | 2.60 | 32.5 | 2.22 | 27.8 | 10.68 | 3.74 | 14.42 |
| G1M3-7D | 1.94 | 21.5 | 1.04 | 11.5 | 6.04 | 67.0 | 4.29 | 10.15 | 14.44 |
| G1M3-28D | 2.58 | 28.7 | 1.35 | 15.0 | 5.05 | 56.2 | 5.54 | 8.486 | 14.03 |
| G2M3-7D | 2.67 | 36.7 | 2.62 | 36.0 | 1.98 | 27.2 | 10.78 | 3.34 | 14.11 |
| G2M3-28D | 3.10 | 40.2 | 2.66 | 34.5 | 1.95 | 25.3 | 10.95 | 3.28 | 14.23 |
| G3M3-7D | 2.30 | 37.1 | 2.15 | 34.7 | 1.75 | 28.2 | 8.83 | 2.94 | 11.77 |
| G3M3-28D | 3.60 | 43.4 | 2.93 | 35.3 | 1.76 | 21.2 | 12.03 | 2.96 | 14.98 |

Lastly, the TGA/DTG curves were obtained for graphene-cement composite with superplasticizer (SP) and presented in Figure 4.9. Table 4.3 presents the weight loss and CH data obtained from these curves. It was noted that cement mixes with superplasticizers obtained more quantity of calcium hydroxide. CH is the most soluble of the hydration products, and thus is a weak link in cement and concrete from a durability point of view. Moreover, if the paste is exposed to fresh water, the CH will leach out (dissolve), increasing the porosity and thus making the paste more vulnerable to further leaching and chemical attack.

**Table 4.3: Weight loss obtained from TGA/DTA and calculation of CH for graphene-cement composites added with superplasticizer.**

| Sample / Temperature | Weight loss (%) / Weight loss with respect to total weight loss (%) | | | | | | Amount of CH using Molecular Mass ratio (%) | | |
|---|---|---|---|---|---|---|---|---|---|
| | 180-300 $^{o}$C (dehydration of bonded water) | | 430-480 $^{o}$C (dehydroxylation of portlandite) | | 600-780 $^{o}$C (decarbonation of calcium carbonate) | | 430-480 $^{o}$C | 600-780 $^{o}$C | Total |
| M0 | 3.17 | 39.7 | 2.60 | 32.5 | 2.22 | 27.8 | 10.68 | 3.74 | 14.42 |
| M0-SP | 0.94 | 14.7 | 2.62 | 41.1 | 2.82 | 44.2 | 10.77 | 4.74 | 15.50 |
| G1M3 | 2.58 | 28.7 | 1.35 | 15.0 | 5.05 | 56.2 | 5.54 | 8.486 | 14.03 |
| G1M3-SP | 2.61 | 28.0 | 1.28 | 13.7 | 5.43 | 58.3 | 5.27 | 9.13 | 14.40 |
| G2M3 | 3.10 | 40.2 | 2.66 | 34.5 | 1.95 | 25.3 | 10.95 | 3.28 | 14.23 |
| G2M3-SP | 3.11 | 40.1 | 2.71 | 34.9 | 1.94 | 25.0 | 11.12 | 3.26 | 14.38 |
| G3M3 | 3.60 | 43.4 | 2.93 | 35.3 | 1.76 | 21.2 | 12.03 | 2.96 | 14.98 |
| G3M3-SP | 2.43 | 39.8 | 1.83 | 30.0 | 1.84 | 30.2 | 7.51 | 3.09 | 10.59 |

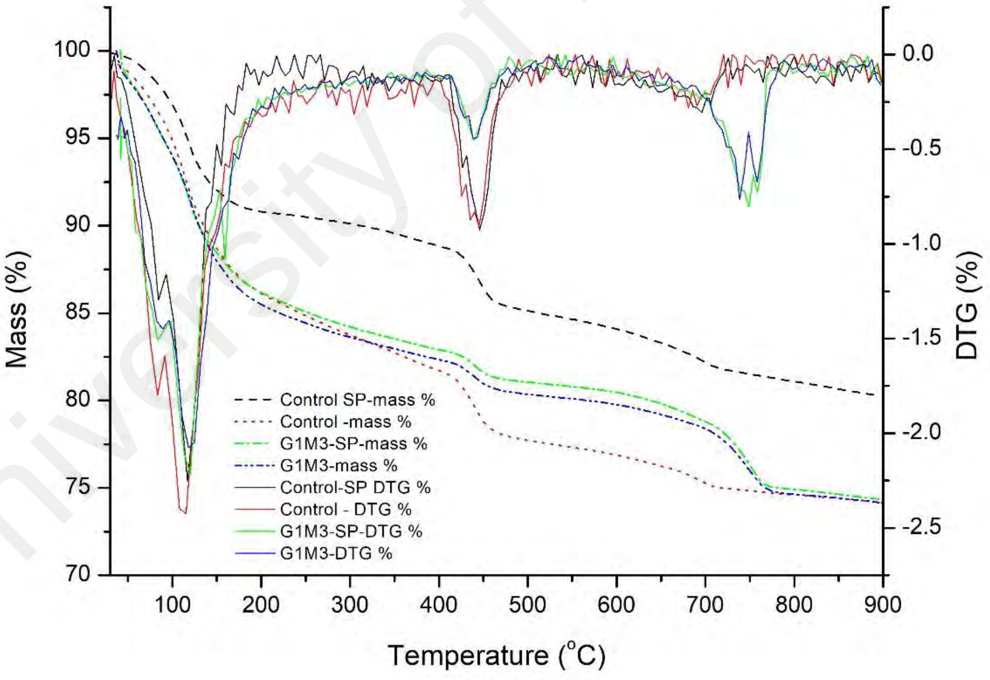

(a) G1-cement composites

**Figure 4.9: Continued**

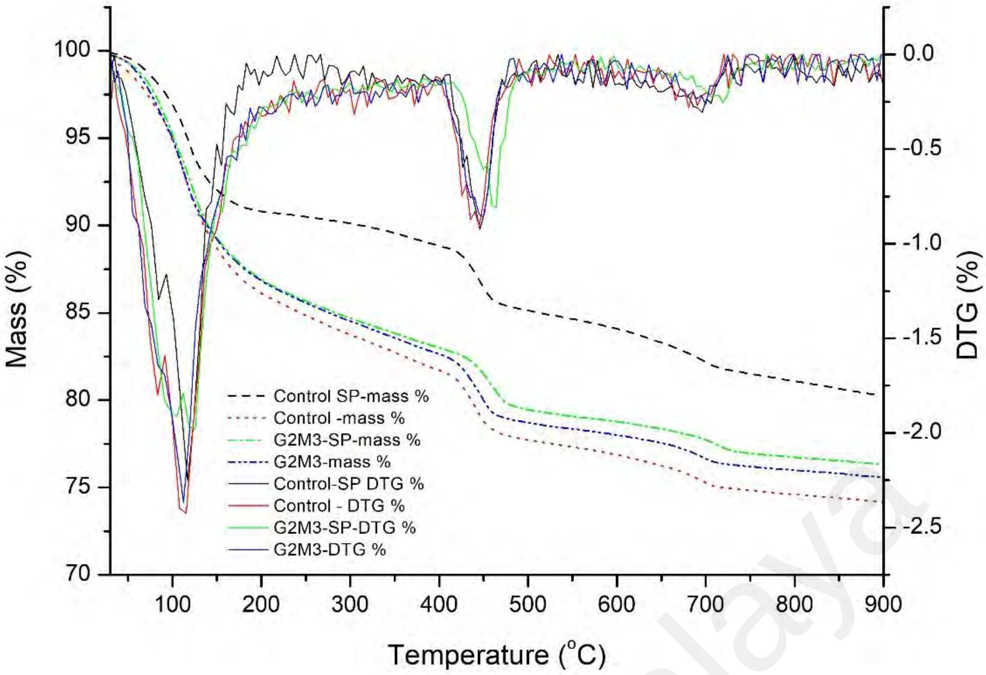

(b) G2-cement composites

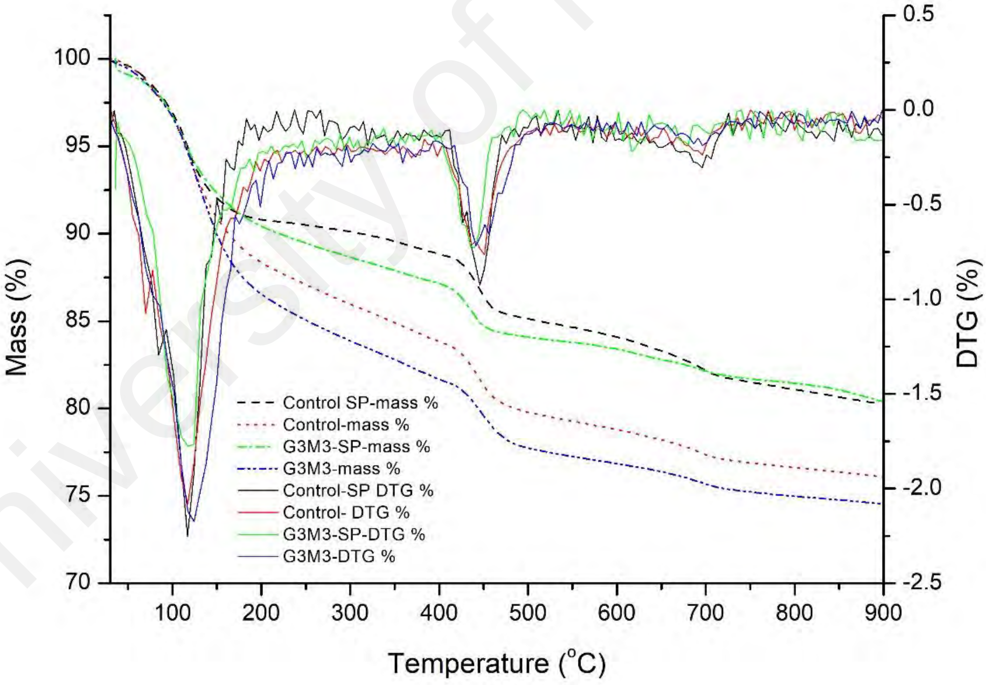

(c) G3-cement composites

**Figure 4.9: TGA/DTA curves for graphene cement composites added with superplasticizer.**

### 4.3.2 FTIR Analysis of Graphene Cement Composite

FTIR spectra of the various graphene-cement composites were obtained and presented in Figure 4.10. Spectra of G1 type cement composite is given in Figure 4.10 (a). It was observed that a new peak is located in the G1M3 mix at 2918 $cm^{-1}$, this peak was not present in control sample spectra as shown in Figure 2.13 and Figure 4.10. This peak was due to the graphene (Figure 2.13) and proposed a chemical interaction with the hydrated cement paste. However, this peak becomes more broad and smooth with increasing percentage of graphene. Few small peaks were found at 2045 $cm^{-1}$ (C=O stretch). Moreover, the peak at 1647 $cm^{-1}$ become broader indicating the chemical interaction. Similarly, the intensity of calcite peaks at 1428 $cm^{-1}$ and 875 $cm^{-1}$ (C-O stretch) was increased indicating the more hydrated products. Peaks due to Si-O asymmetric stretch at 956 $cm^{-1}$ became steeper and shifted to a high number. Water peaks at 3397 $cm^{-1}$ became broader. For G1M5 and G1M10 mixes the intensity of O-H stretch due to $Ca(OH)_2$ becomes more indicating the extra amount of hydrated cement products. Similarly, $sp^2$ hybridized peaks were noted in G2 mixes as well. Peaks at 1647 $cm^{-1}$ (C-O stretch) became broader, suggest the chemical interaction. Calcite peaks at 1416 $cm^{-1}$ and 873 $cm^{-1}$ were enhanced in intensities indicating more quantity. These calcite peaks were slightly shifted as compared to control sample indicating the chemical interaction and polymerization of hydrated products. In G3 mixes, the intensity of the peak at 3641 $cm^{-1}$ was increased along with the percentage of graphene (Mollah et al., 2000). It indicates, more quantity of hydrated cement product was formed due to the addition of graphene flakes. The H-O-H stretching of G3M3 and G3M5 mix shifted from 3397 $cm^{-1}$ to 3400 $cm^{-1}$ (Mollah et al., 2000), indicating that the bond is excited in H-O-H. As for G3M10 specimen, the peak at 3396 $cm^{-1}$ had higher intensity and broad as well. Similarly, the peak of G3 mixes at 2932 $cm^{-1}$ became broad and smooth. The peak of G3 mixes at 1647 $cm^{-1}$ showed more intensity as compared to control sample, indicating the high amount of ettringite. The peak of C-O was shifted from 1416 cm$^{-1}$ to 1419 cm$^{-1}$, suggests the formation of chemical interaction. The CSH peak in G3M3 and G3M10 mixes at 956 cm$^{-1}$ (Si-O asymmetric stretch) have more intensities and shifted from 956 cm$^{-1}$ to 955 cm$^{-1}$ (Horgnies et al., 2013). This showed that chemical interaction and high amount of polymerization of silicates occurred in the samples.

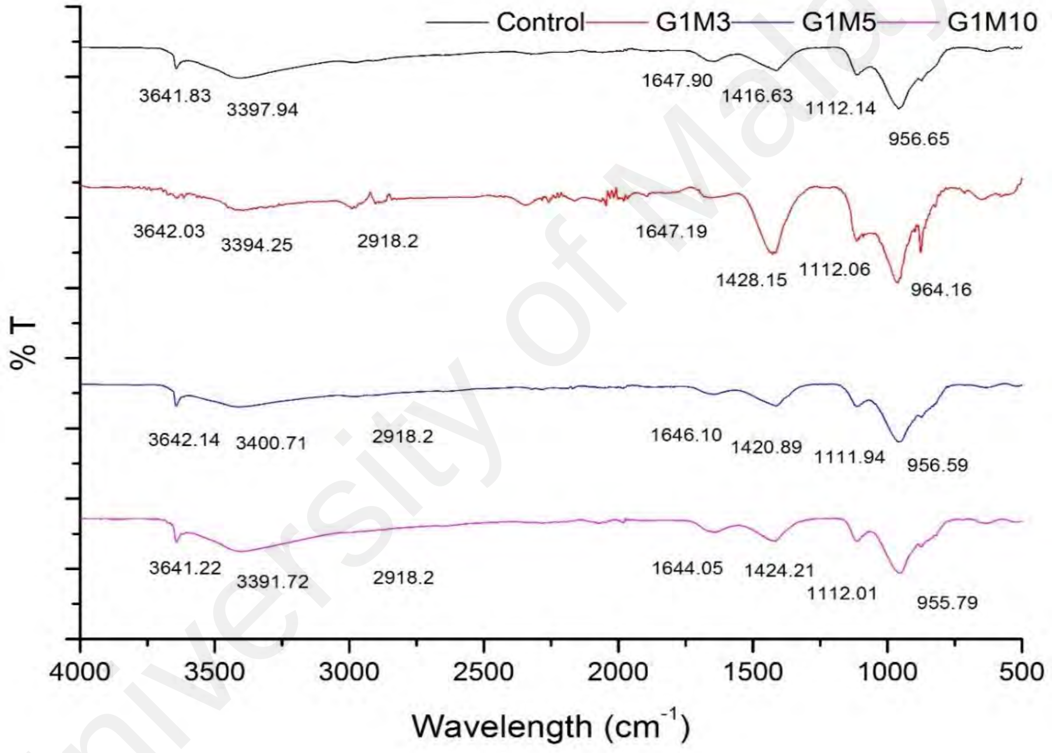

(a) G1

**Figure 4.10: Continue**

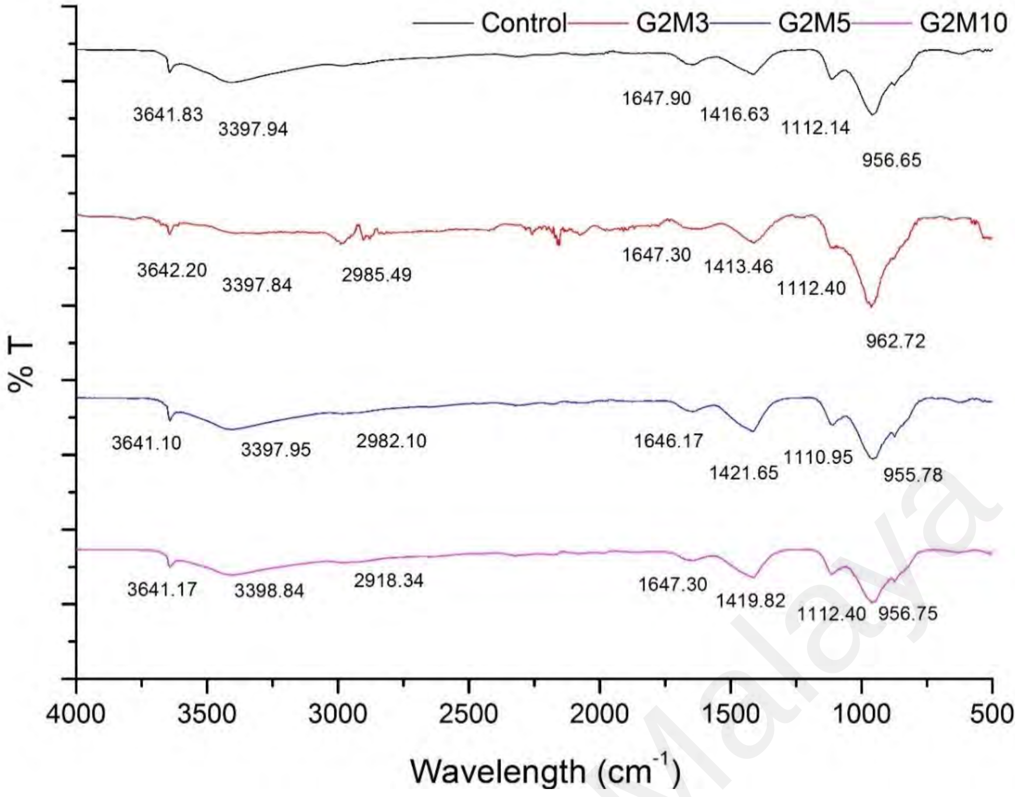

(b) G2

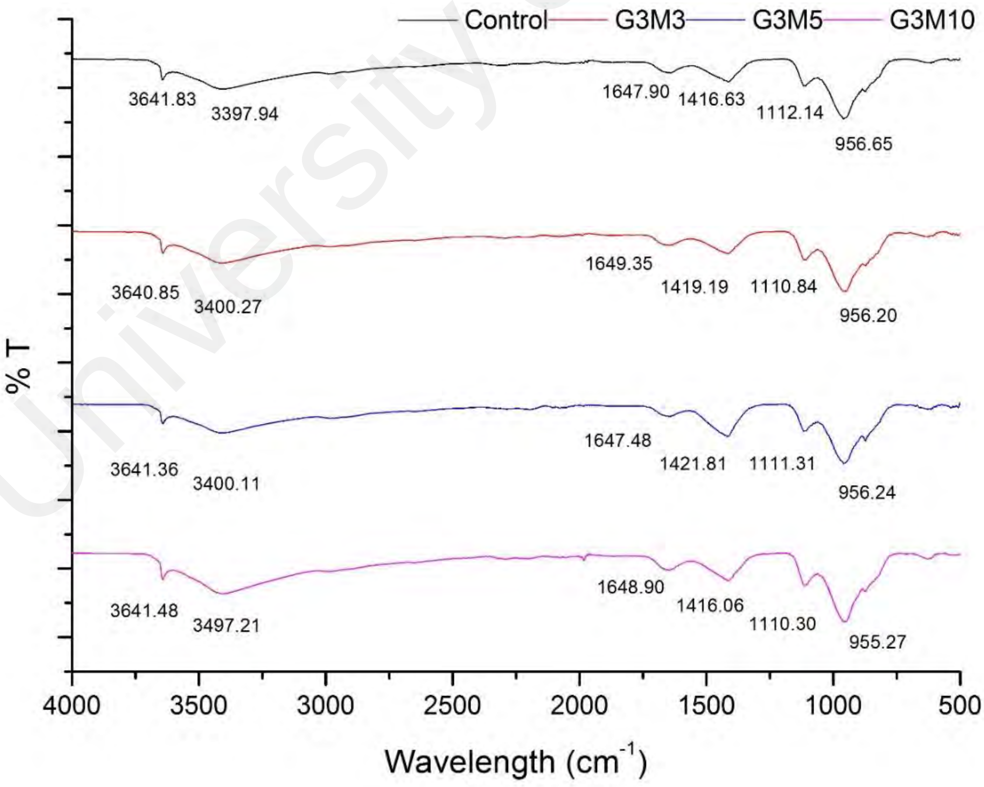

(c) G3

**Figure 4.10: FTIR spectra for graphene-cement composites.**

G1 and G2 type based cement mixes showed more peaks at 2918 cm$^{-1}$ and 2985 cm$^{-1}$ and broad peaks at 1647 cm$^{-1}$. It may be inferred that, graphene flakes with high surface area has more chemical interaction than the graphene having less surface area. The G1 type also showed steeper and high-intensity values for 1416 cm$^{-1}$ and 873 cm$^{-1}$ which are related to calcite peaks. It is also observed that, with high surface area, more hydrated products were formed. For M10 mixes C=C peaks mainly due to graphene were found smooth. It may be due to agglomeration of graphene due to a huge amount. However, the peak 1647 cm$^{-1}$ was broad and shifted indicating the chemical interaction with graphene flakes.

Effect of curing age was explored the dependence of the physical and chemical interaction between hydration time. For this purpose, samples were considered on 7, 28 and 90 days after hydration. FTIR spectra of control specimen and graphene cement composite are given in Figure 4.11. At 7-day the intensity of H-O-H stretch was low, however, at 28 days and 90 days is enhanced. The intensity of calcite peak increased with the passage of time. The peak at 1418 cm$^{-1}$ and 873 cm$^{-1}$ were increasing. The slight shift was also recorded. At 7-day 1420 cm$^{-1}$ then on 28-day it was 1416 cm$^{-1}$ and 90-day it was 1418 cm$^{-1}$. This shift indicates that hydration reaction is going on and hydrated products are forming. In case of the G1M3 mix for 7-day, a very sharp and high-intensity peak was present at 3395 cm$^{-1}$ as shown in Figure 4.11 (b). However, at 28-day its intensity reduced and it becomes broad. Graphene peaks appear at 2918 cm$^{-1}$ at 28-day suggesting the chemical interaction took place. Similarly, the intensity of calcite peak (1428 cm$^{-1}$ and 873 cm$^{-1}$) was observed more at 90-day as compared to 28-day. Sulphate peak was becoming smooth at 90-day. FTIR spectra of the G2M3 mix at 7, 28 and 90-day is shown in Figure 4.11 (c). As G2 type mix is having high surface area and flake thickness, therefore, more chemical interaction was noted at 7-day and 28-day spectra. Peak intensities were more at 2918 $cm^{-1}$ and 2985 $cm^{-1}$ and become smooth at 90-day. The intensity of calcite peak increased slightly but very less as compared to G1 type mix. Intensity and broadness of H-O-H stretch peak at 3397 $cm^{-1}$ were more at 90-day as compared to 7 and 28-day. Figure 4.11 (d) shows the spectra of the G3M3 mix at 7, 28 and 90-day of hydration. As the surface area of G3 type graphene is less, therefore, peak at 2918 $cm^{-1}$ and 2985 $cm^{-1}$ are disappeared. However, shift and broadness in a peak at 1649 $cm^{-1}$ suggest the chemical interaction. This chemical interaction is not strong enough as the shift move towards the lower wave number.

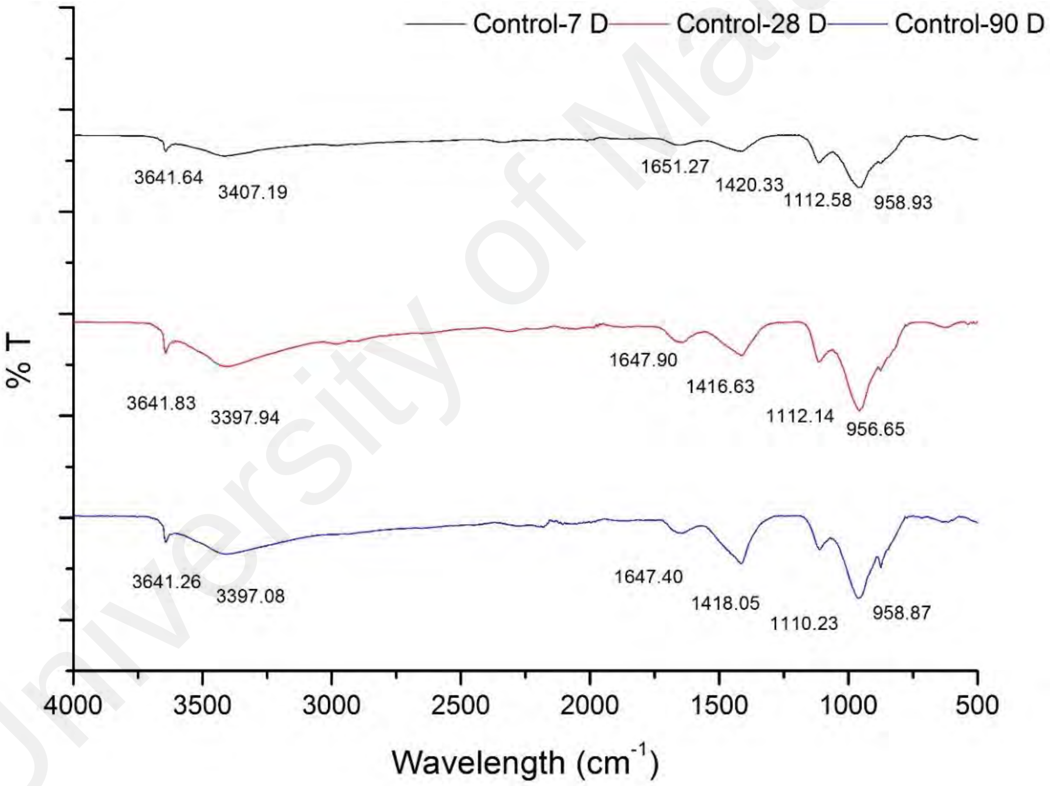

(a) M0 cement mix

**Figure 4.11: Continue**

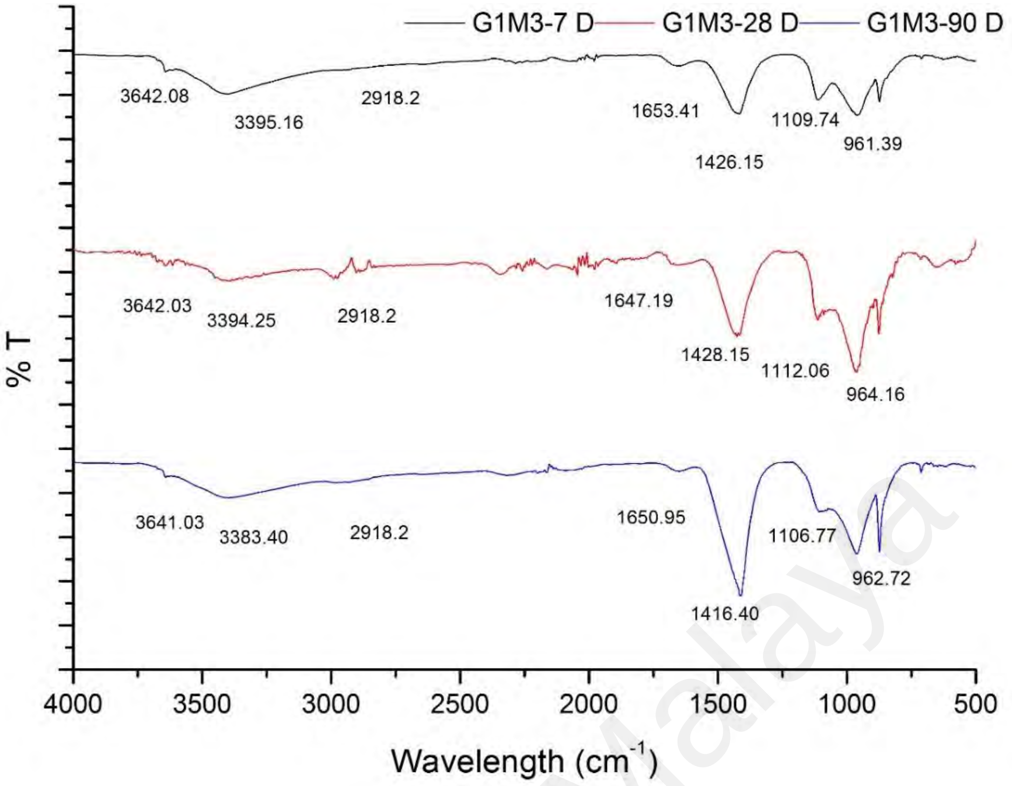

(b) G1-cement mix

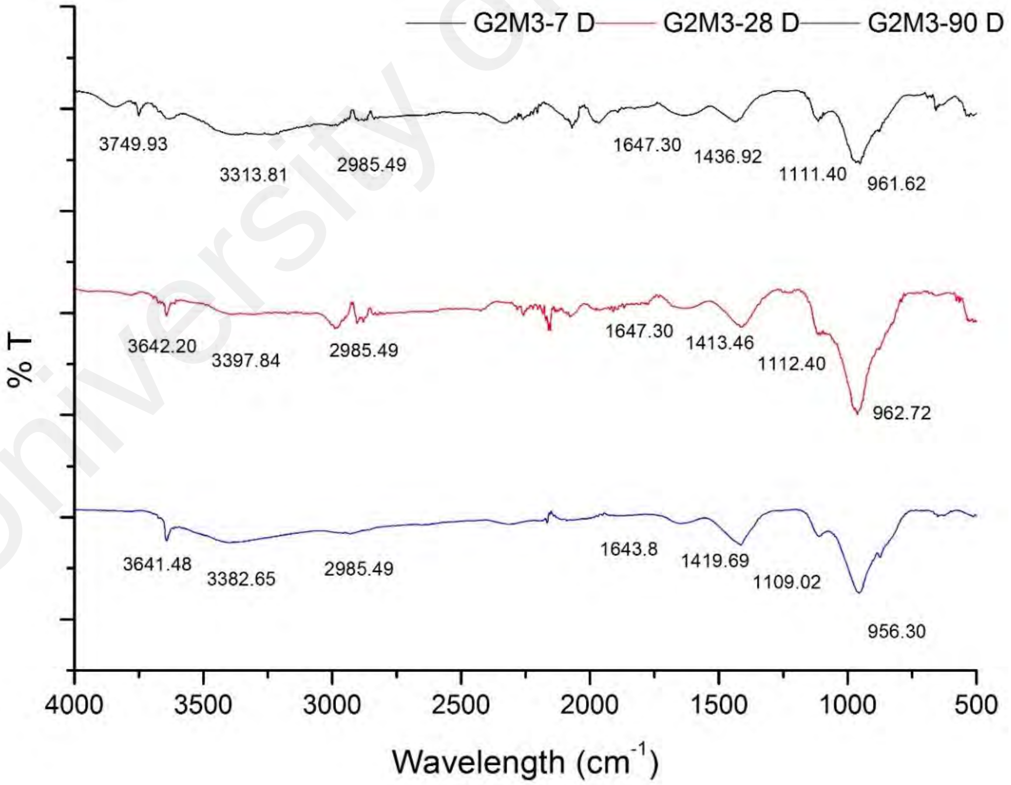

(b)  G2 cement mix

**Figure 4.11: Continue**

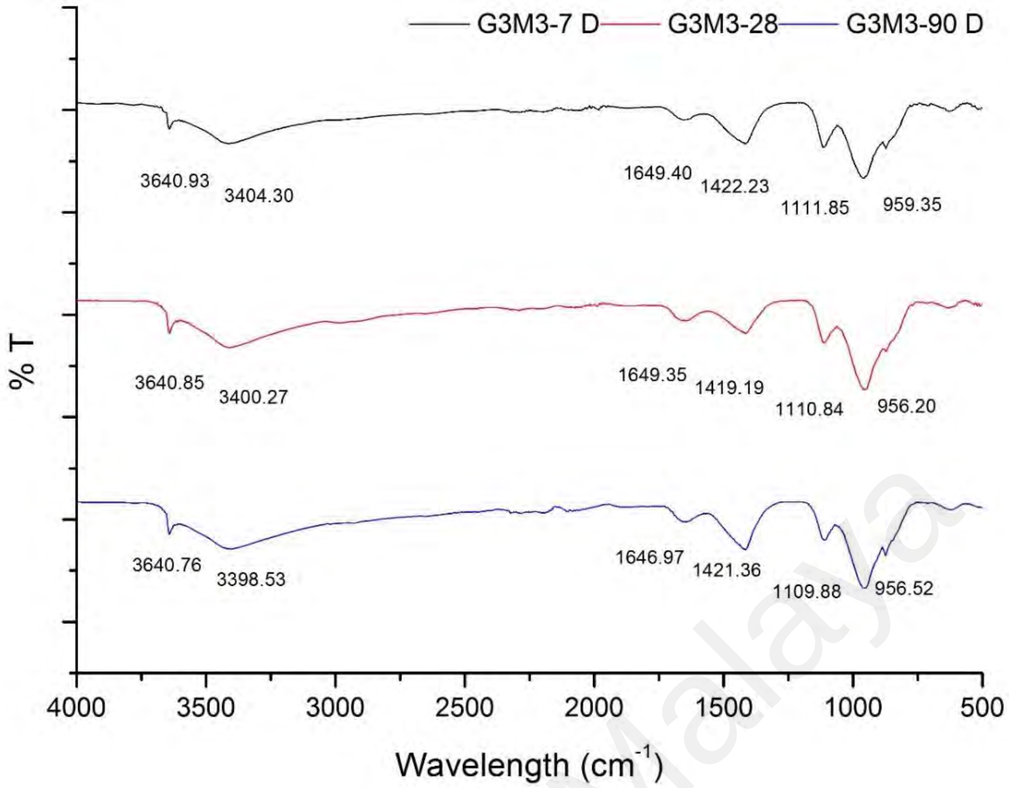

(d) G3 cement mix

**Figure 4.11: FTIR spectra for graphene-cement composites at 7, 28 and 90 days after casting.**

Influence of superplasticizer has also been investigated and presented in Figure 4.12. It was observed for control mix that SP-enhanced the intensity of the peaks and no distinguishable difference in the shift was found. It indicates that due to SP more hydration products formed, however, it didn't contribute to any chemical interaction. For G1M3 mixes with and without SP more broadness in the peaks was found (Figure 4.12 (a)). Peaks at 3394 cm$^{-1}$ and 3642 cm$^{-1}$ became broader. The peak at 1647 cm$^{-1}$ also become broader due to SP. It showed that SP did not contribute to the chemical interaction, however, due to SP chemical interaction of graphene with hydrated cement products became stronger. Similarly, for G2M3 mixes in Figure 4.12 (b) the intensity of O-H stretch peak at 3642 cm$^{-1}$ was more indicating more quantity of calcium hydroxide. Peaks at 2153 cm$^{-1}$ (C=O) becomes very smooth. Si-O peaks below 800 cm$^{-1}$ increased in intensity. Possible reason for increase in hydrated cement products is related to workability and presence of more amount of water for hydration of cement particles. Therefore, it can be concluded that due superplasticizer the growth of hydrated cement products becomes more. However, no chemical interaction was observed due to SP.

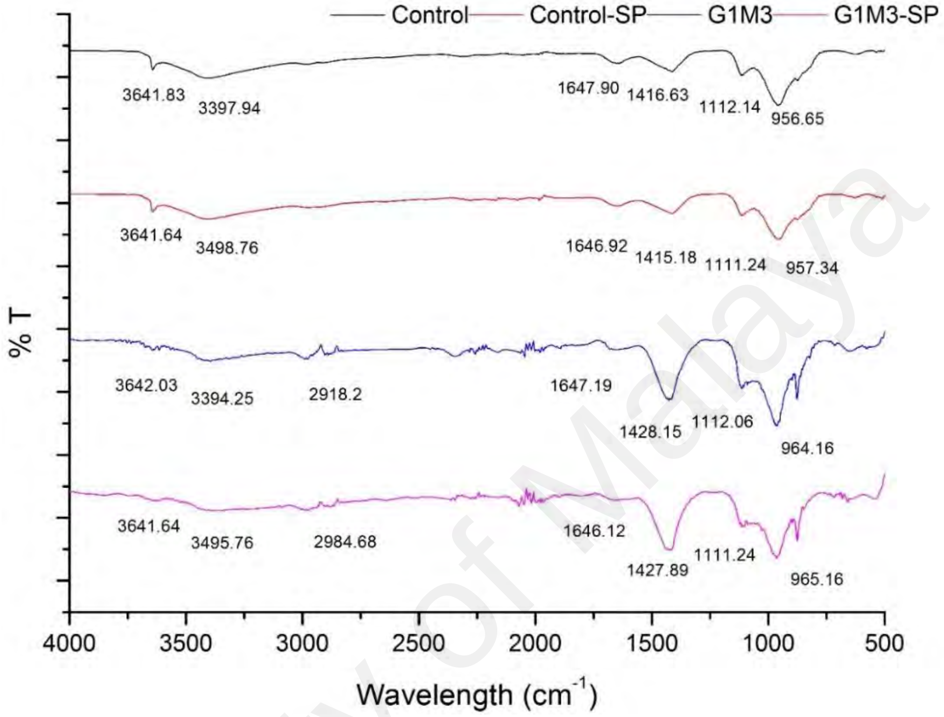

(a) G1-cement mix

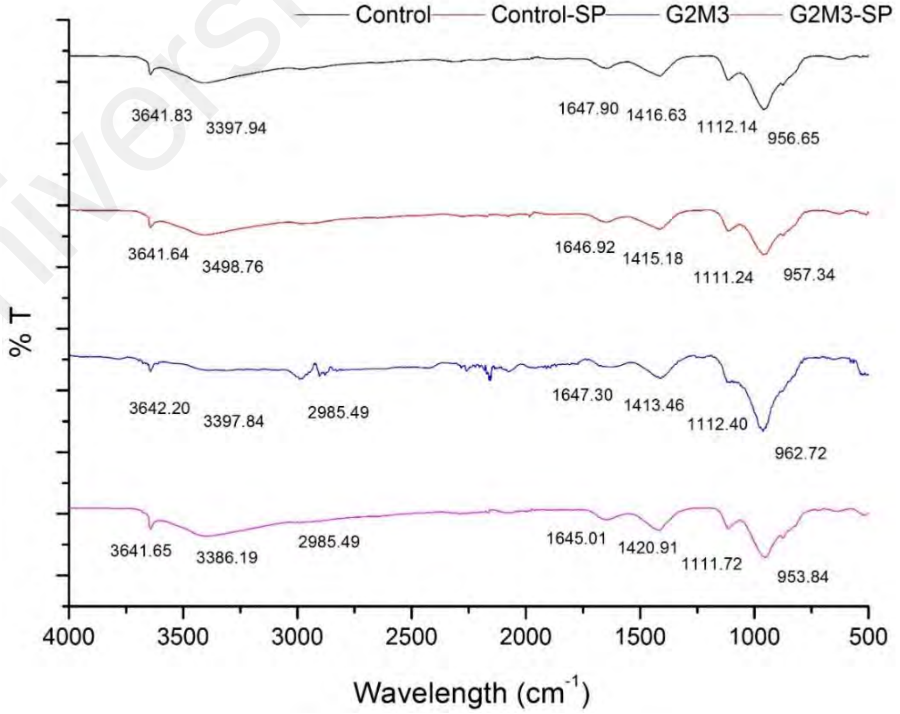

(b) G2-cement mix

**Figure 4.12: Continue**

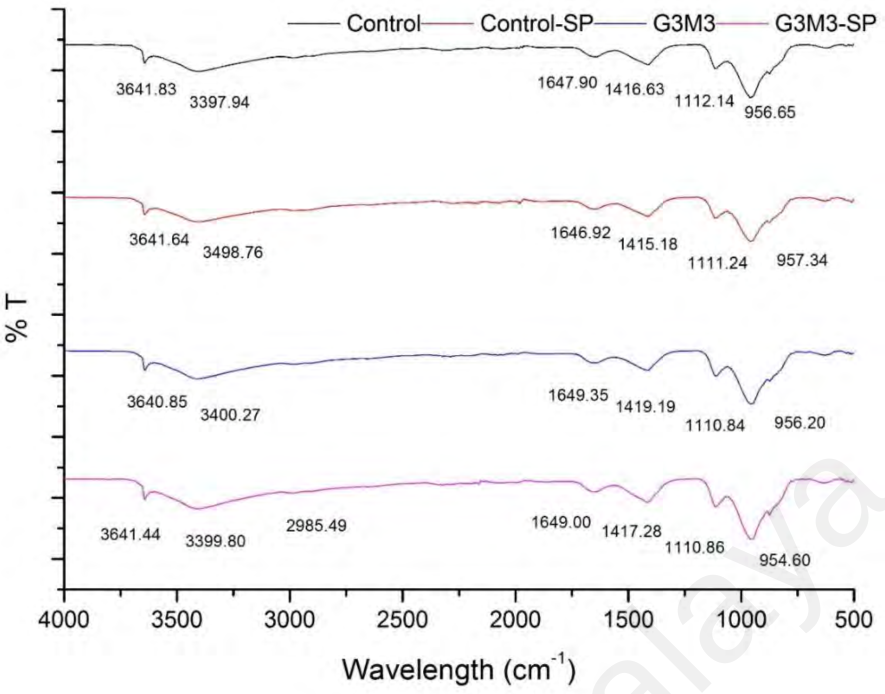

(c) G3-cement mix

**Figure 4.12: FTIR spectra for graphene cement composites added with superplasticizer.**

### 4.3.3 XRD Analysis of Graphene Cement Composites

XRD analysis of various graphene cement composite samples have been carried out and presented in Figure 4.13. The most prominent peak of calcium hydroxide CH was noted at 18.3° and 34.5°. XRD spectra of G1 type cement composite is given in Figure 4.13 (a). It was observed that peak of CH was increasing with the percentage of graphene. For G1M3 mix it was observed that alite ($C_3S$) peak is high. It is important to mention here that, when XRD spectra was obtained only for sample holder then sharp peak at 28.6° was recorded. Therefore, it may be said that peak in G1M3 sample at 28.6° is contributing from the sample holder. To further verify this, sample holder was replaced and no peak was found at 28.6° in G1M5 and G1M10 specimens. XRD spectra of G2 type cement mix is given in Figure 4.13 (b). It was observed that peak of hydrated cement content i.e. CH was increased with graphene content.

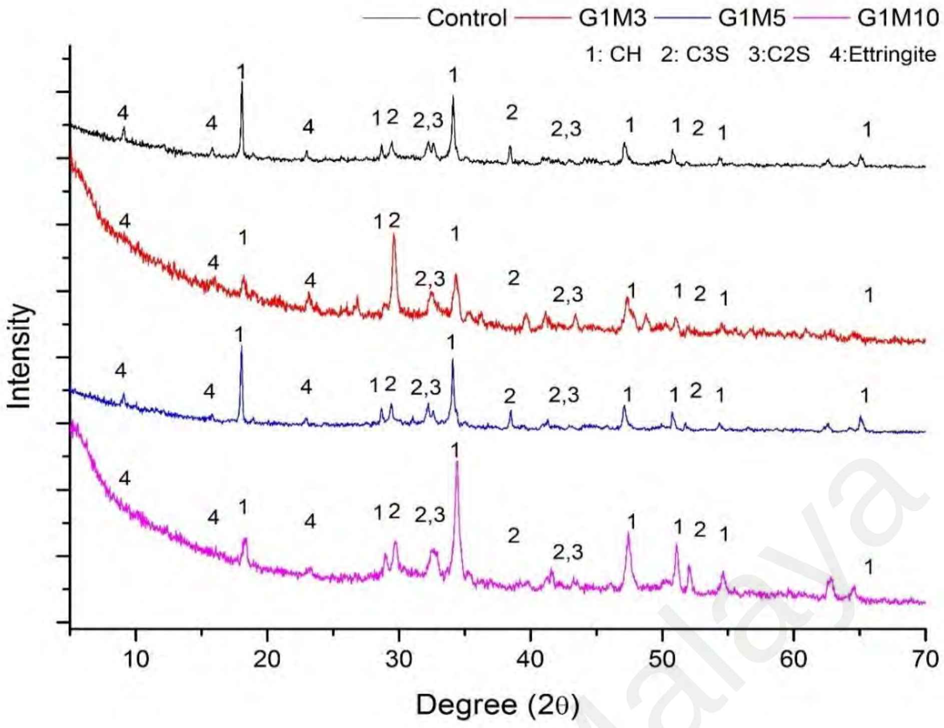

(a) G1-cement mix

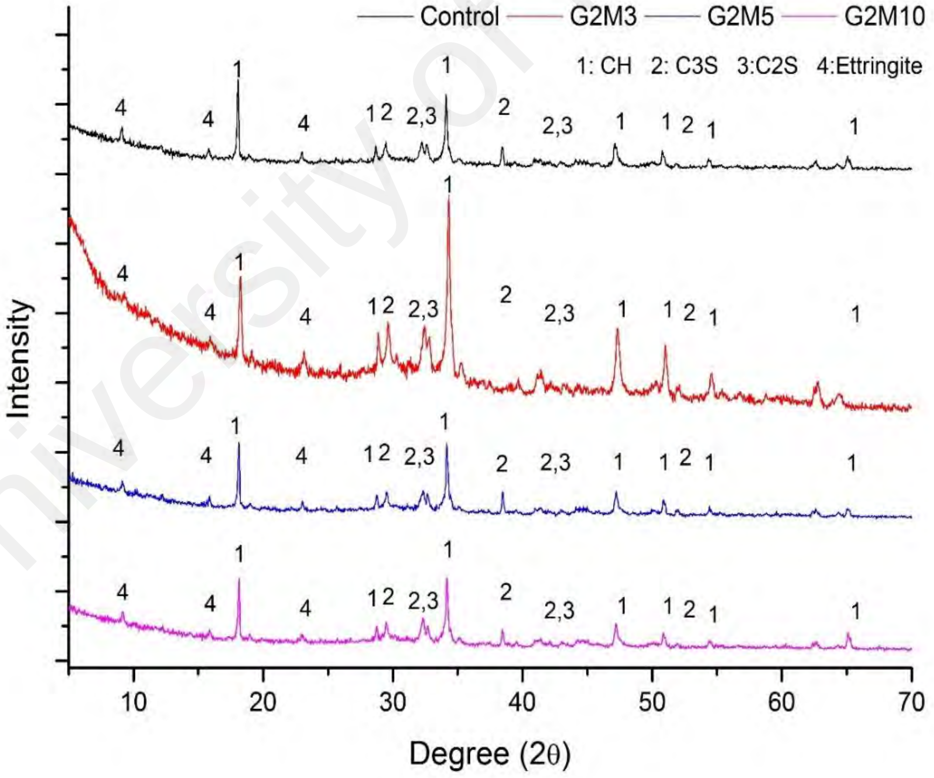

(b) G2-cement mix

**Figure 4.13: Continued**

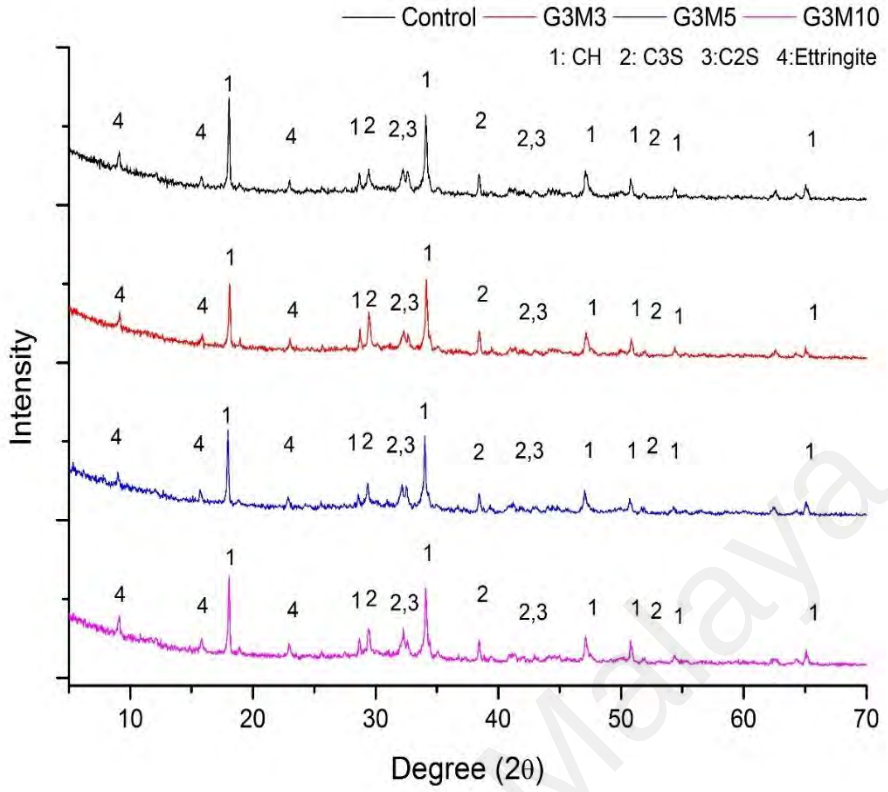

(c) G3- cement mix

**Figure 4.13: XRD spectra for graphene-cement composites.**

Unhydrated cement content i.e. alite ($C_3S$) and belite ($C_2S$) peaks were found for the G2M3 mix as well, however, these peaks reduced with an increase in graphene content. Ettringite peak was increasing by the addition of graphene in cement mix design. Moreover, Figure 4.13 (c) shows the XRD spectra of G3 type cement composite and increase in CH and ettringite peak was observed. Therefore, based on the XRD analysis, it may be inferred that more hydration was occurred by incorporation of graphene in cement mix design. In addition, Figure 4.13 was used to investigate the influence of graphene type on XRD spectra. For this purpose, a comparison among the M3, M5 and M10 mixes was done. M3 mixes includes the G1M3, G2M3 and G3M3 samples with similar conditions. It was determined that XRD spectra were similar, and no specific trend was recorded.

Furthermore, influence of curing age was investigated on XRD patterns. Figure 4.14 showed the XRD spectra of cement composite at 7, 28 and 90 days after sample casting. In spectra of M0 mix (Figure 4.14 (a)), it was recorded that at 7 day unhydrated cement content is more however, its intensities were reduced with curing time. It is noteworthy that, for G1M3 specimens same sample holder was used which enhanced the peak height at 28.6O. For G2 type cement composites, it was observed that unhydrated cement peaks reduced with the hydration time. Similarly, for G3 type cement mixes more alite and belite peaks were observed at 7-day after specimen preparations. However, with an increase in curing age the height of these peaks reduced.

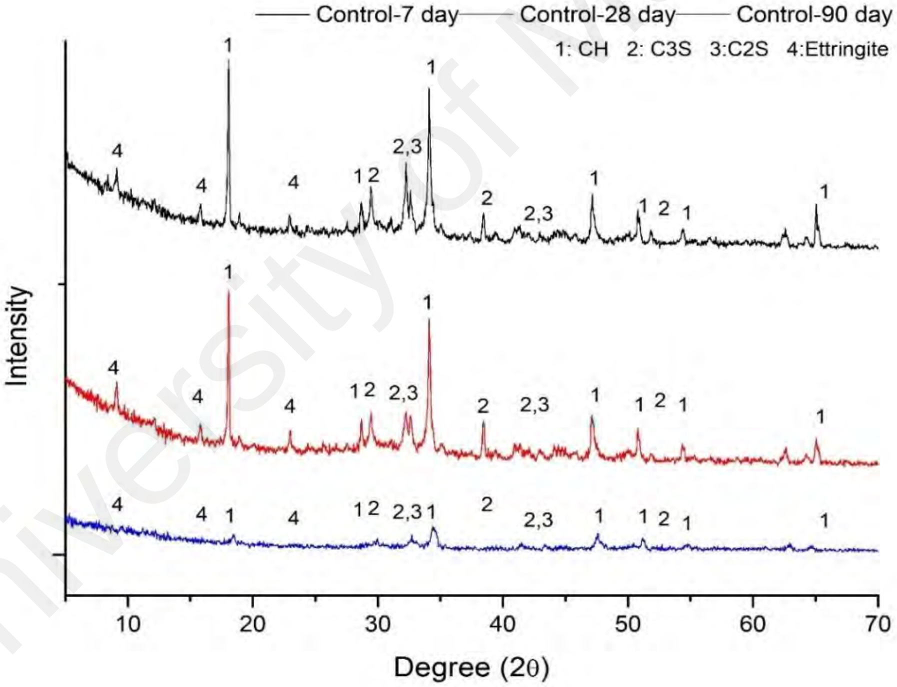

(a) M0 mix

**Figure 4.14: Continued**

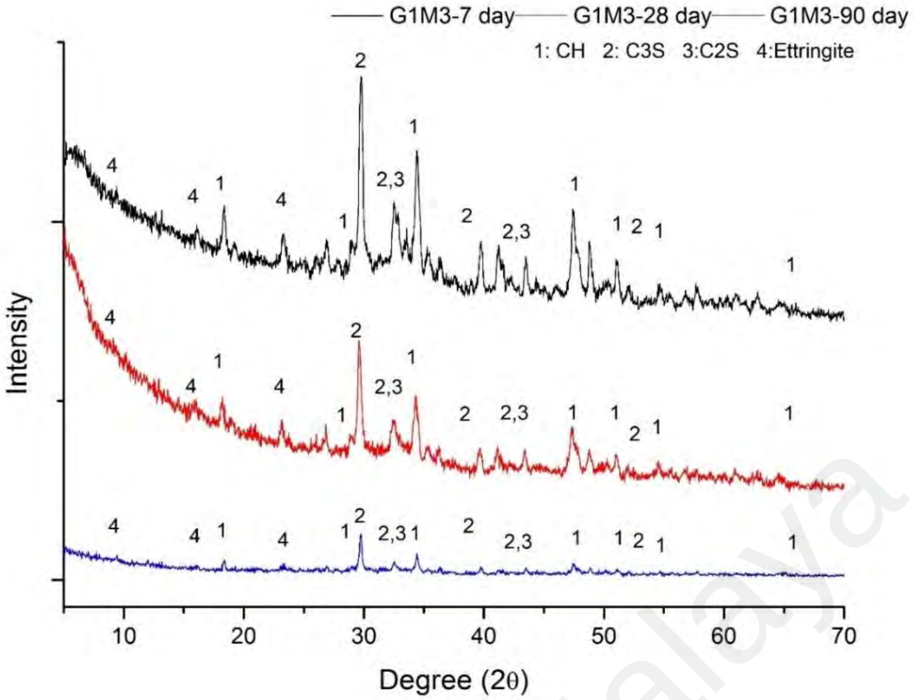

(b) G1M3 mix

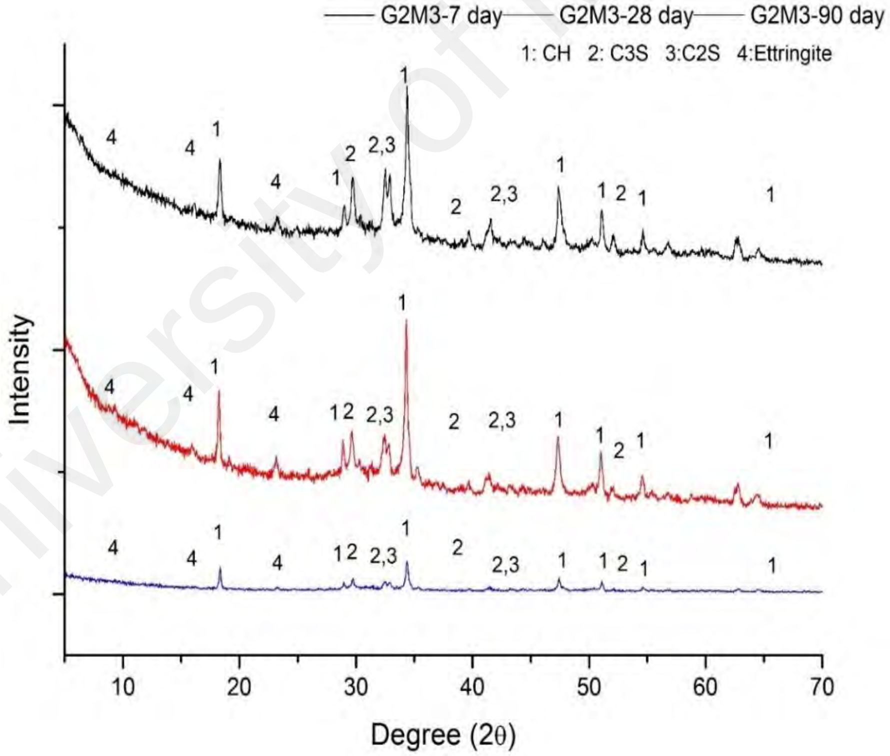

(c) G2M3 mix

**Figure 4.14: Continued**

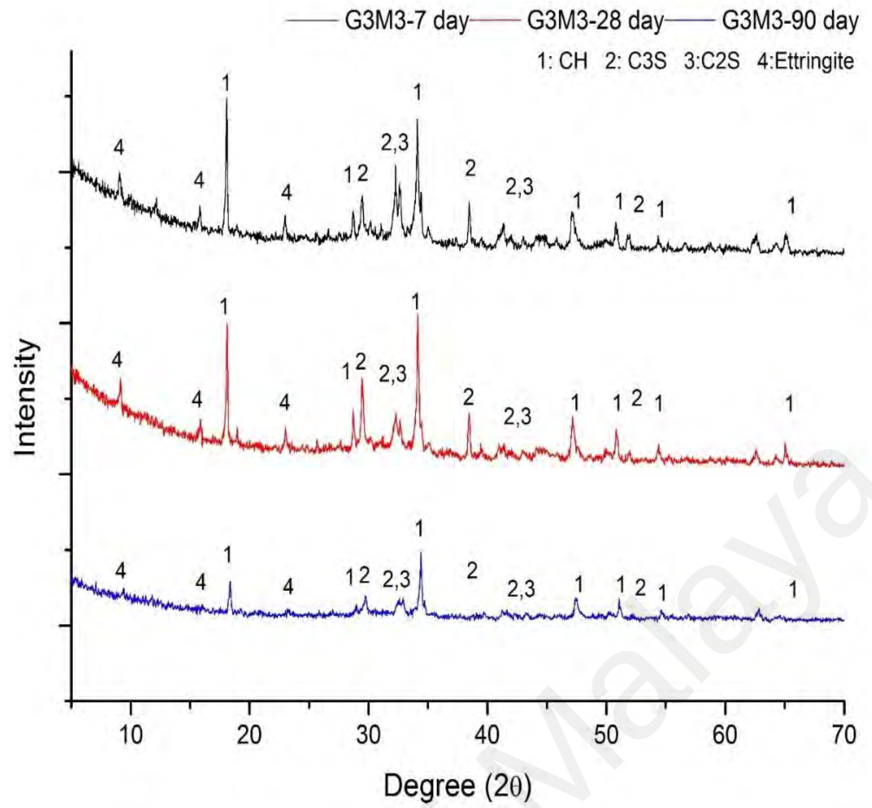

(d) G3M3 mix

**Figure 4.14: XRD spectra for cement composites at 7, 28 and 90 days after casting.**

Effect of superplasticizer (SP) on the crystalline structure was also investigated and presented in Figure 4.15. It was noted that ettringite peak was enhanced for control mix after addition of SP, whereas, peaks of CH remained same. As all G1M3 specimens for XRD analysis were prepared and tested in similar conditions, therefore, due to sample holder issue unhydrated cement content was found significant. Furthermore, due to the incorporation of SP in the mix CH peak was found high. For G2 type cement specimens alite and blite peaks were reduced however, the peak of CH was increased. Similar trend was noted for G3 type cement specimens.

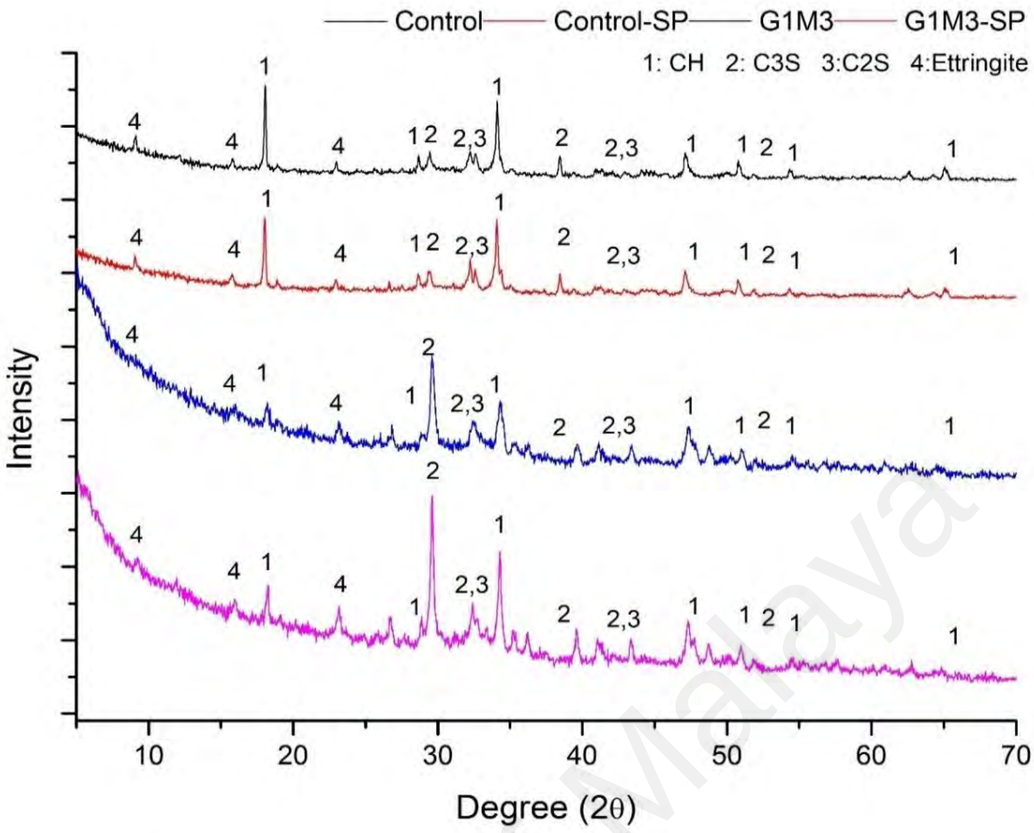

(a) G1M3 mix

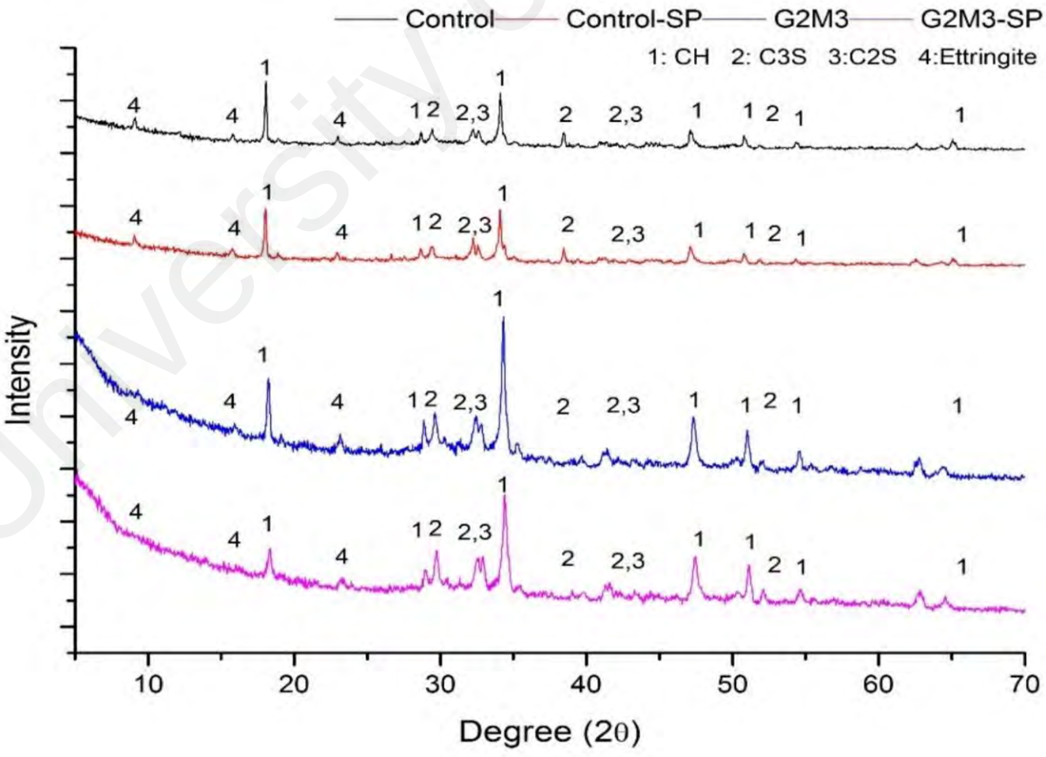

(b) G2M3 mix

**Figure 4.15: Continued**

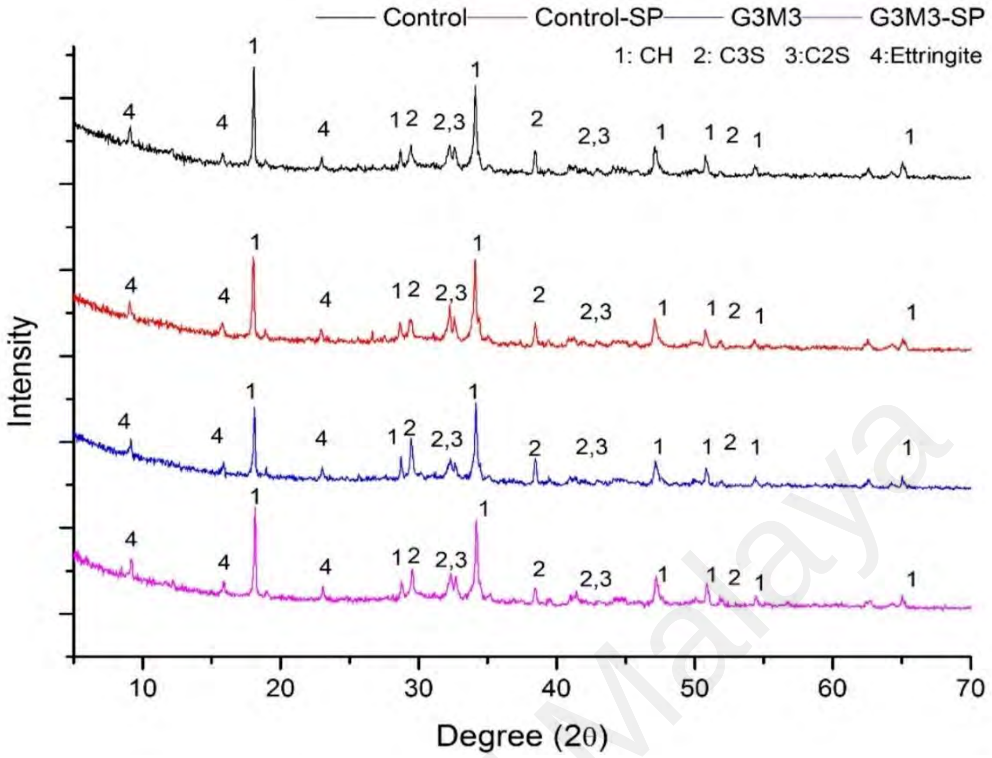

(c) G3M3 mix

**Figure 4.15: XRD spectra for graphene-cement composite added with superplasticizer.**

### 4.3.4 Morphology of Graphene Cement Composites

The morphology of the graphene-cement composite at 7th day and 28th day was investigated and presented in Figure 4.16. It can be seen in Figure 4.16 (a) and (e), that the hydrated cement products grow over the graphene flakes. Due to the ordered growth, hydrated crystals were compact and graphene fills up the pores which have great contribution in improving mechanical strength. Needle form of calcium silicate hydrate (CSH), hexagonal plates of portlandite and graphene flakes can be observed on 7-day FESEM image of G1M3 in Figure 4.16 (a). ESB or backscattered image was used to distinguish the carbon materials. It can be seen in Figure 4.16 (b) that graphene nanoparticle become completely black. EDX image was also employed to confirm the presence of graphene and hydrated cement products. Figure 4.16 (c) represents the EDX for the graphene sheets as indicated in Figure 4.16 (a). It can be seen clearly that carbon content was maximum in it, confirming the presence of graphene. EDX for the needle shape CSH was shown in Figure 4.16 (d) and location of the EDX point is marked in Figure 4.16 (b). Oxygen content was maximum in it followed by the silicon and carbon. Needle form of CSH transformed into honeycomb structure of CSH at 28 days as shown in Figure 4.16 (e). Backscattered image or ESB of Figure 4.16 (e) displayed that hydrated products grow over the graphene as shown in Figure 4.16 (f). EDX was also employed in Figure 4.16 (g) and Figure 4.16 (h) to confirm the presence of graphene and honeycombed CSH structure.

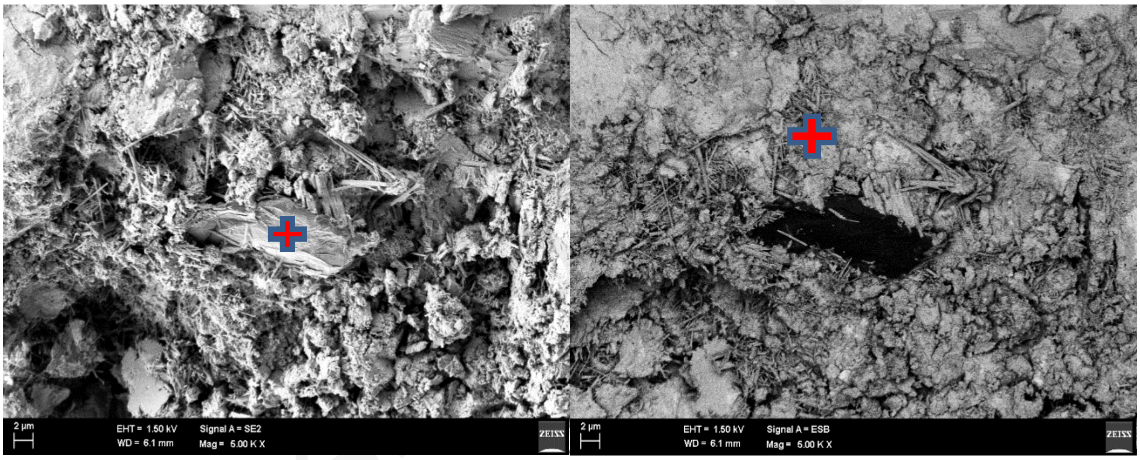

(a) FESEM image of G1M3 at 7 days

(b) ESB or backscattered image of (a)

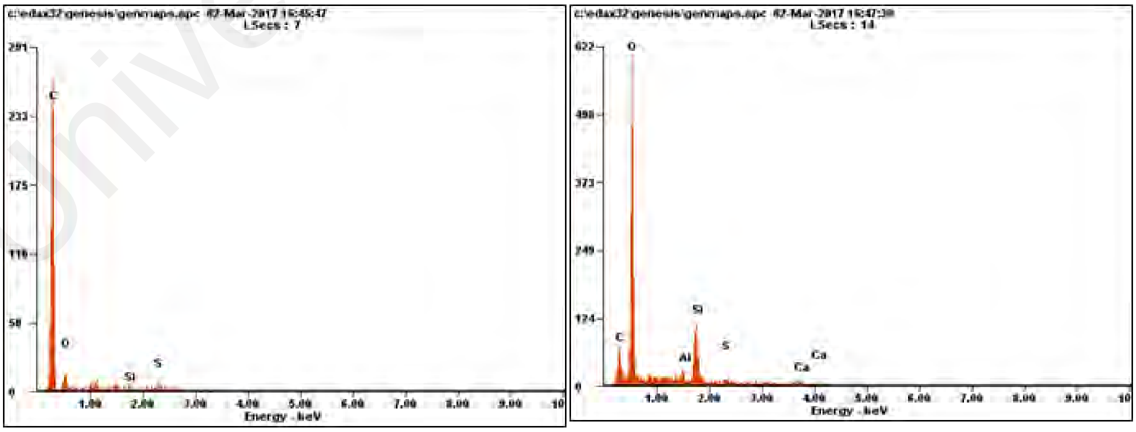

(c) EDX of graphene in G1M3 specimen on a point indicated in (a)

(d) EDX for the hydrated cement product at crosshair location in (b)

Figure 4.16: Continued

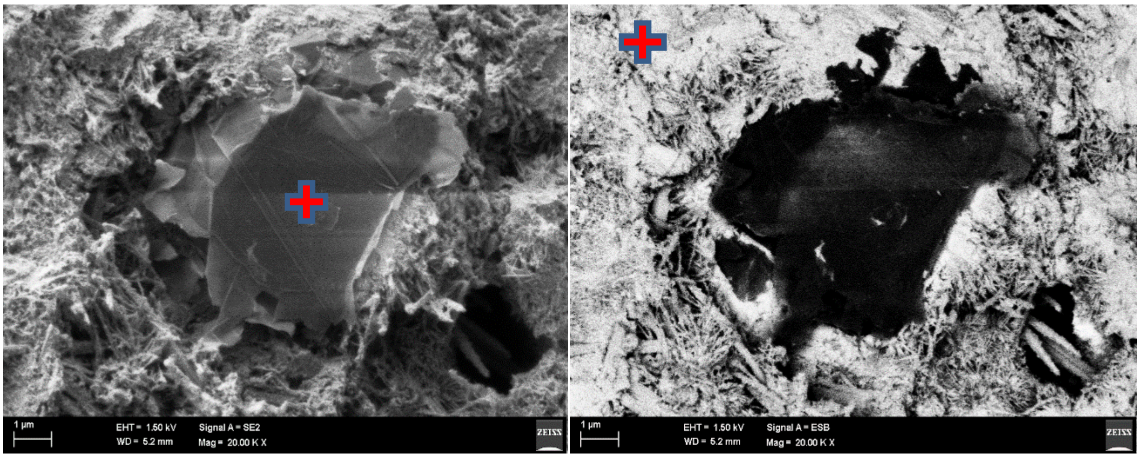

(e) FESEM image of G1M3 at 28 days (f) ESB or backscattered image of (e)

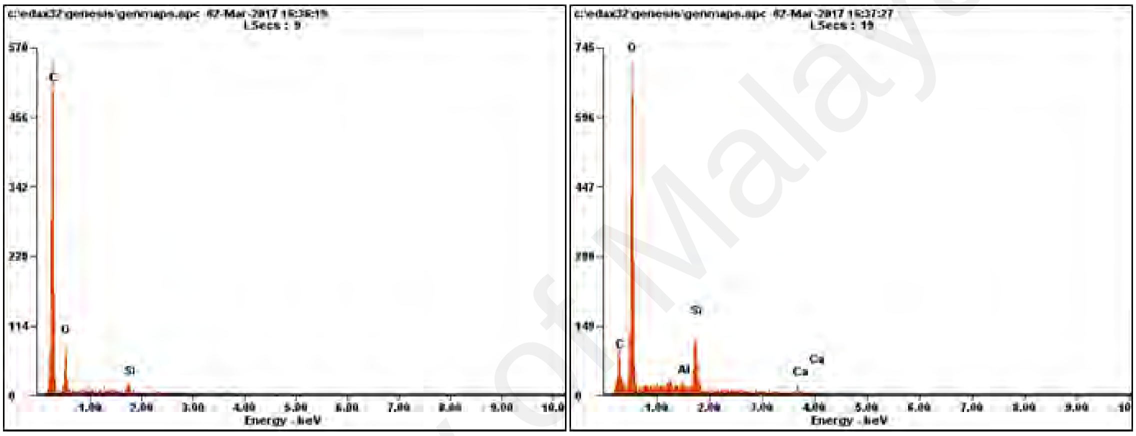

(g) EDX for the marked point in (e) (h) EDX at cross-hair location in (f)

**Figure 4.16: FESEM images of graphene-cement paste at 7 days and 28 days.**

Figure 4.17 shows the FESEM images for the G2M10 and G3M10 mixes. Similar to the G1M3 mix, it was noted that hydrated cement products formed on the graphene flakes. To identify the graphene and presence of pores ESB or backscattered image of Figure 4.17 (a) were used as given in Figure 4.17 (b). Figure 4.17 (c) and Figure 4.17 (d) provides the FESEM image and backscattered image of G3M10. CSH gel forms on each side of graphene flake. It was determined that hydrated cement products and graphene flakes successfully filled up the pores. Hence, based on above information, it can be determined that due to the addition of graphene, hydrated products grows in uniform and ordered way (Cao et al. (2016)), which significantly improves the compressive strength and mechanical properties.

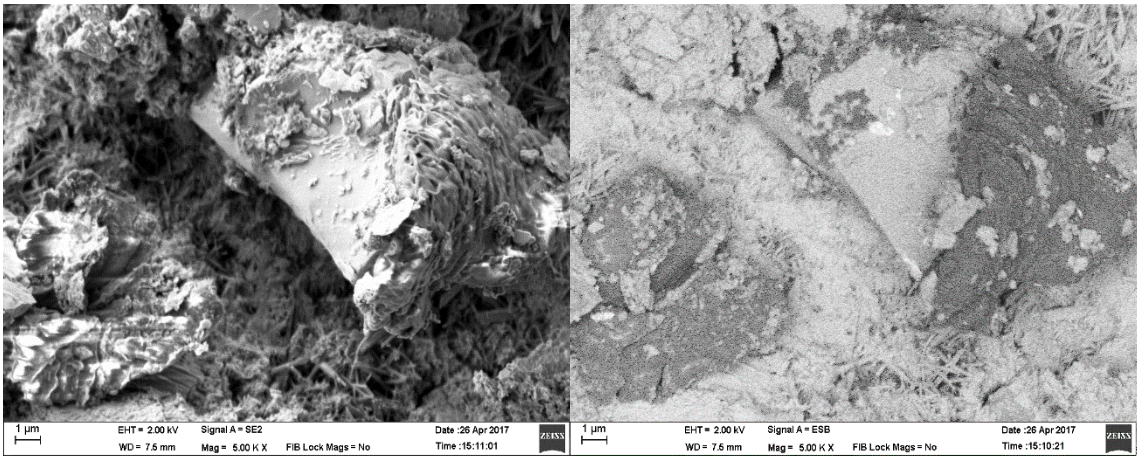

(a) FESEM image of G2M10 (b) ESB or backscattered image of (a)

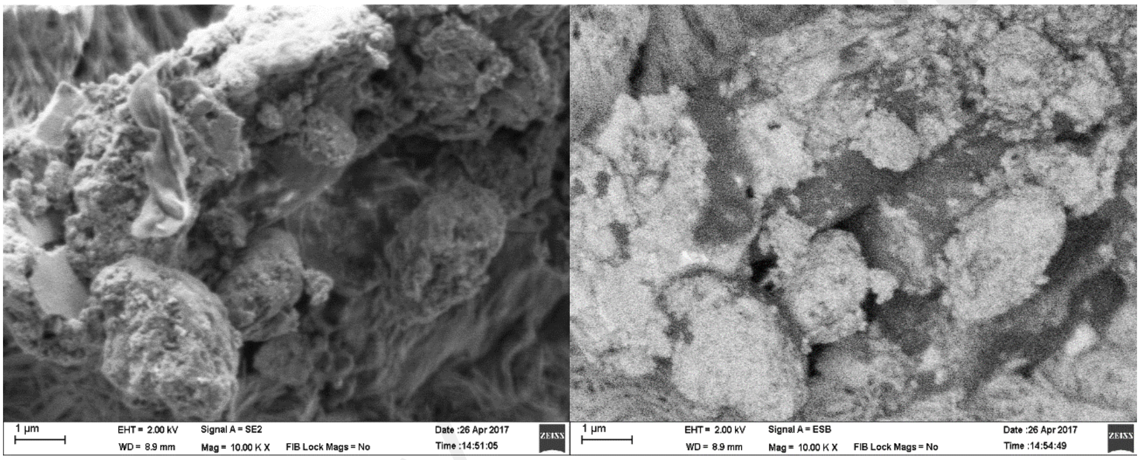

(c) FESEM image of G3M10 (d) ESB or backscattered image of (c)

**Figure 4.17: FESEM images of graphene-cement paste.**

## 4.4 Rheology of Graphene Cement Paste

As the cement based construction materials normally casted in plastic form and various properties e.g. workability, consistency and homogeneity depend on the viscosity of cement paste therefore, it is very important to consider the influence of graphene, its size, surface area and lateral dimension on the viscosity of cement paste. Hence, in this section rheological properties of the graphene-cement composite were explored. For this purpose, flow properties of the graphene-cement composite were calculated from flow curve which obtained from the shear stress and shear rate data. After this, using mathematical models, plastic viscosity, yield stress, and specific trend of the flow were determined. It is important to mention here that flow properties of graphene type G1 estimated by four rheological models has already been published.

### 4.4.1 Influence of Graphene on Yield Stress

Yield stress is an important parameter for determining the flow characteristics of any substance. According to Barnes & Walters (1985), yield stress concept is an idealization. In Bingham model, it is defined as the value of shear stress at zero shear rate. However, BS EN 5168-05 (2005) defines it, stress below which substance will be elastic solid and above the liquid. As it is a very important parameter therefore, yield stress values for graphene-cement composite paste were determined by using Bingham model, Modified Bingham model, Herschel–Bulkley (HB) model and Casson model. Table 4.4 showed the effects of addition of graphene to the yield stress. It was observed that with the addition of graphene, yield stress was increased. It was due to the high surface area and an average thickness of graphene flakes, which increased the overall water demand of the system. It was noted that yield stress values also enhanced with an increase in graphene content in the mix design. Maximum yield stress values were recorded for type G3. It was observed earlier in dispersion section that G3 type graphene flakes formed the agglomerates. These agglomerates entrapped some water molecules inside and as a result overall free available water content was reduced (Shan et al., 2015). Maximum yield stress values were found for G3M10 mix design. For G3M10 Herschel-Bulkley model, Bingham model, modified Bingham model and Casson model determined the 183%, 70%, 61% and 15% increase in yield stress value respectively as compared to M0 mix. Table 4.5 highlights the percentage change rate in yield stress values in contrast to control sample. Furthermore, variation of yield stress with mathematical model with respect to Bingham model is calculated as well and presented in Table 4.5. Casson model determined the lowest yield stress values as compared to other rheological models and modified Bingham model determined the highest yield stress values followed by Bingham and Herschel-Bulkley (HB) model. Therefore, it is concluded that yield stress values were increased due to the high surface area and average flake thickness of graphene.

**Table 4.4: Effect of graphene type on the yield stress values (Pa).**

| Sample | Bingham Model (BM) | Modified Bingham Model | Herschel-Bulkley (HB) Model | Casson Model |
|---|---|---|---|---|
| M0 | 1.53 | 1.76 | 1.22 | 0.52 |
| G1M3 | 1.67 | 1.79 | 1.3 | 0.62 |
| G1M5 | 1.84 | 1.89 | 1.48 | 0.79 |
| G1M10 | 1.9 | 1.93 | 1.53 | 0.8 |
| G2M3 | 1.46 | 1.56 | 1.44 | 0.7 |
| G2M5 | 1.56 | 1.81 | 1.44 | 0.7 |
| G2M10 | 1.59 | 2.61 | 1.78 | 0.86 |
| G3M3 | 1.98 | 2.39 | 2.26 | 0.53 |
| G3M5 | 2.3 | 2.6 | 2.88 | 0.54 |
| G3M10 | 2.6 | 2.83 | 3.45 | 0.6 |

**Table 4.5: Variation of yield stress values in terms of percentages.**

| Sample | Variation with mathematical models | | | | Variation with graphene content | | | |
|---|---|---|---|---|---|---|---|---|
| | Bingham Model (BM) | Modified Bingham Model | HB Model | Casson Model | Bingham Model (BM) | Modified Bingham Model | HB Model | Casson Model |
| M0 | 100 | 115 | 80 | 34 | 100 | 100 | 100 | 100 |
| G1M3 | 100 | 107 | 78 | 37 | 109 | 102 | 107 | 119 |
| G1M5 | 100 | 103 | 80 | 43 | 120 | 107 | 121 | 152 |
| G1M10 | 100 | 102 | 81 | 42 | 124 | 110 | 125 | 154 |
| G2M3 | 100 | 107 | 99 | 48 | 95 | 89 | 118 | 135 |
| G2M5 | 100 | 116 | 92 | 45 | 102 | 103 | 118 | 135 |
| G2M10 | 100 | 164 | 112 | 54 | 104 | 148 | 146 | 165 |
| G3M3 | 100 | 121 | 114 | 27 | 129 | 136 | 185 | 102 |
| G3M5 | 100 | 113 | 125 | 23 | 150 | 148 | 236 | 104 |
| G3M10 | 100 | 109 | 133 | 23 | 170 | 161 | 283 | 115 |

### 4.4.2 Influence of Graphene on Plastic Viscosity

Plastic viscosity is one of the important parameters which determines the resistance of the paste against the flow. It is described as the deformation of the cement due to external loading (Wang et al., 2016). In Bingham model, it is defined as the slope of the flow curve obtained from shear stress and shear rate data. Figure 4.18 presented the effect of the addition of graphene to the plastic viscosity. It was noted that plastic viscosity values significantly increased with the addition of graphene. This increment in plastic viscosity values is in correlation with the previous study conducted by Shan et al. (2015). Shan et al. (2015) determined the plastic viscosity values for graphene oxide. Table 4.6 describes the variation of plastic viscosity values with respect to graphene content and mathematical models. Approximately 50-107% increase in the plastic viscosity values were observed. These values were found in direct correlation with the percentage of graphene content in cement paste. Table 4.6 explains that Bingham model determined the maximum plastic viscosity values followed modified Bingham and Casson model. The plastic viscosity values for G3 were almost double of the M0. The maximum increase in plastic viscosity values of G3M10 mix was 84 %, 83 % and 107% as estimated by Bingham model, modified Bingham models and Casson model respectively. As the G3 type graphene flakes formed agglomerates structures which increase the resistance against the flow of cement paste.

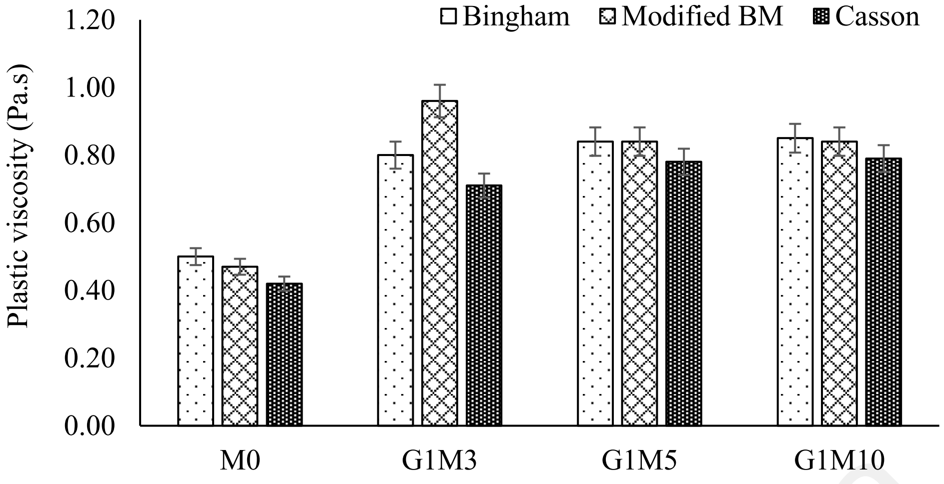

(a) G1-cement mix

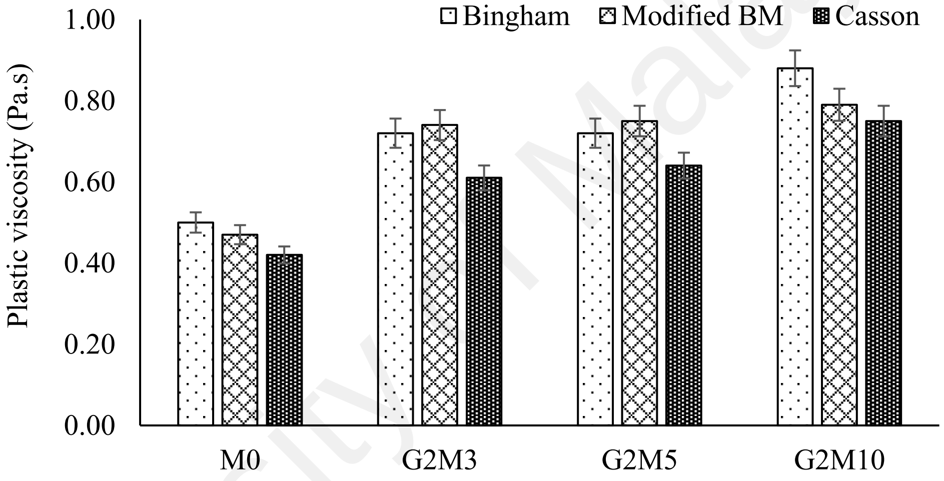

(b) G2-cement mix

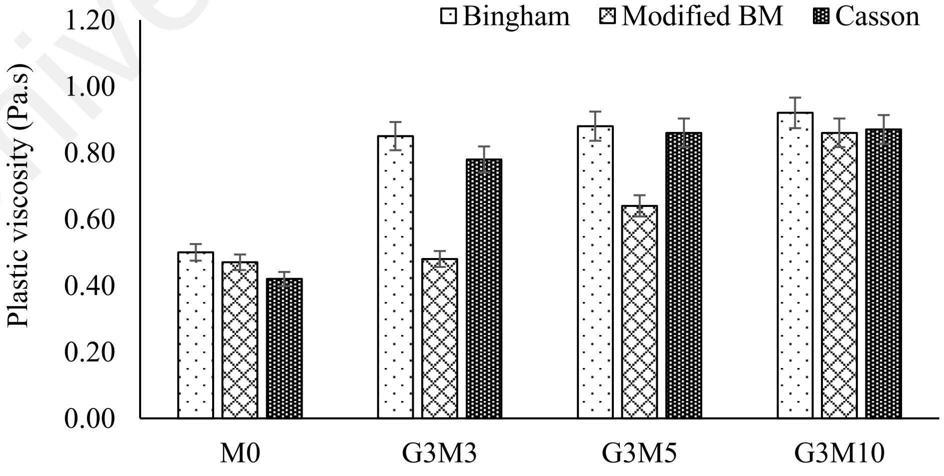

(c) G3-cement mix

**Figure 4.18: Effect of addition of graphene to the plastic viscosity of graphene-cement composite.**

**Table 4.6: Variation of plastic viscosity values in terms of percentages.**

| Sample | Variation with mathematical models | | | Variation with graphene content | | |
|---|---|---|---|---|---|---|
| | Bingham Model (BM) | Modified Bingham Model | Casson Model | Bingham Model (BM) | Modified Bingham Model | Casson Model |
| M0 | 100 | 94 | 84 | 100 | 100 | 100 |
| G1M3 | 100 | 120 | 89 | 160 | 204 | 169 |
| G1M5 | 100 | 100 | 93 | 168 | 179 | 186 |
| G1M10 | 100 | 99 | 93 | 170 | 179 | 188 |
| G2M3 | 100 | 103 | 85 | 144 | 157 | 145 |
| G2M5 | 100 | 104 | 89 | 144 | 160 | 152 |
| G2M10 | 100 | 90 | 85 | 176 | 168 | 179 |
| G3M3 | 100 | 56 | 92 | 170 | 102 | 186 |
| G3M5 | 100 | 73 | 98 | 176 | 136 | 205 |
| G3M10 | 100 | 93 | 95 | 184 | 183 | 207 |

Herschel-Bulkley (HB) model determined the viscosity trend using two parameters i.e. consistency (K) and power rate index (n). Table 4.7 showed the values estimated by HB model for consistency and rate index. Power rate index (n) is an important parameter and provide the information about shear deformation of the flow. If ‘n’ value is more than 1 then the flow has the shear thickening behaviour and for less than 1 it is shear thinning behaviour (Wang et al., 2016). However, the consistency (K) depends on ‘n’ and has no physical meaning and difficult to compare due to its dimension (Pa.s$^n$) (Vikan et al., 2007). Graphene cement paste behaves as shear thinning flow except for G3M10 mix (Table 4.7). It was deduced that graphene flake thickness had an important role on rheological properties and can alter the flow behaviour of cement paste. It was noted that power rate index was increasing with the addition and increase in the content of graphene. Similar behaviour was observed for the derivatives of graphene i.e. graphene-oxide based cement materials (Wang et al., 2016). Wang et al. (2016) used graphene-oxide based cement paste and found shear thinning behaviour at the high shear rate.

**Table 4.7: Effect of graphene to rate index and consistency.**

| Sample | Consistency, K | Power Rate index, n |
|---|---|---|
| M0 (Control) | 0.60 | 0.96 |
| G1M3 | 0.97 | 0.97 |
| G1M5 | 0.99 | 0.98 |
| G1M10 | 0.97 | 0.98 |
| G2M3 | 1.74 | 0.81 |
| G2M5 | 0.96 | 0.85 |
| G2M10 | 0.97 | 0.98 |
| G3M3 | 0.87 | 0.97 |
| G3M5 | 0.94 | 0.98 |
| G3M10 | 0.67 | 1.19 |

### 4.4.3 Standard Error Values

Efficiency and effectiveness of these mathematical models were estimated by using standard error values. Standard error values were calculated using Equation (2.7). Table 4.8 showed the standard error values for Bingham, modified Bingham, Herschel-Bulkley (HB) and Casson models. Best-fitting of flow data using these mathematical models to flow curves is given by the small value of standard error. Standard deviation and average values for each mathematical model is also calculated and presented in Table 4.8. Bingham model determined the lower standard error values as compared to other mathematical models. The standard deviation of Bingham model is less which indicates that all data points are closed to mean value, however, for Casson model the data points are staggered. Modified Bingham and Herschel-Bulkley models are both nonlinear models. Therefore, their standard deviation values are matching as well hence, both models determined similar standard error values. These models are good for shear thickening behaviour. Casson model determined the large values of standard error. According to (Papo, 1988) Casson model has a constraint to predict the flow parameter more accurately for concentrated suspension. Table 4.9 explained the variation of standard error values with respect to control sample and mathematical models. G1M10 mix shows very large values as compared to the other mixes. G2 and G3 type mix determined comparatively higher values as compared to G1 type (Table 4.9). It was due to the higher dosage of graphene content, more thickness of graphene flakes which caused the increase in agglomerates and flocculated structure.

**Table 4.8: Standard error of various model.**

| Sample | Bingham Model | Modified Bingham Model | HB Model | Casson Model |
|---|---|---|---|---|
| M0 | 74.4 | 74.5 | 74.4 | 73.6 |
| G1M3 | 34.3 | 89.0 | 70.5 | 82.9 |
| G1M5 | 30.7 | 30.6 | 45.1 | 57.3 |
| G1M10 | 223.6 | 233.3 | 261.6 | 283.1 |
| G2M3 | 79.2 | 87.2 | 79.6 | 77.2 |
| G2M5 | 160.8 | 153.0 | 158.6 | 161.9 |
| G2M10 | 97.9 | 104.4 | 99.7 | 92.1 |
| G3M3 | 74.4 | 91.2 | 99.4 | 96.1 |
| G3M5 | 71.5 | 99.8 | 98.3 | 85.4 |
| G3M10 | 65.9 | 199.3 | 85.0 | 185.3 |
| **Average** | 91.3 | 116.2 | 107.2 | 119.5 |
| **Standard deviation** | 58.7 | 61.1 | 61.7 | 70.3 |

**Table 4.9: Variation of standard error values of various models in terms of percentages.**

| Sample | Variation with mathematical models | | | | Variation with graphene content | | | |
|---|---|---|---|---|---|---|---|---|
| | Bingham Model (BM) | Modified Bingham Model | HB Model | Casson Model | Bingham Model (BM) | Modified Bingham Model | HB Model | Casson Model |
| M0 | 100 | 100.1 | 100.0 | 98.9 | 100.0 | 100.0 | 100.0 | 100.0 |
| G1M3 | 100 | 259.5 | 205.5 | 241.7 | 46.1 | 119.4 | 94.8 | 112.6 |
| G1M5 | 100 | 99.7 | 146.9 | 186.6 | 41.2 | 41.0 | 60.6 | 77.8 |
| G1M10 | 100 | 104.3 | 117.0 | 126.6 | 300.5 | 313.0 | 351.6 | 384.5 |
| G2M3 | 100 | 110.1 | 100.5 | 97.5 | 106.5 | 117.0 | 107.0 | 104.8 |
| G2M5 | 100 | 95.1 | 98.6 | 100.7 | 216.2 | 205.3 | 213.2 | 219.9 |
| G2M10 | 100 | 106.6 | 101.8 | 94.1 | 131.5 | 140.1 | 134.0 | 125.1 |
| G3M3 | 100 | 122.6 | 133.6 | 129.2 | 100.0 | 122.3 | 133.7 | 130.5 |
| G3M5 | 100 | 139.6 | 137.5 | 119.4 | 96.1 | 133.9 | 132.2 | 115.9 |
| G3M10 | 100 | 302.4 | 129.0 | 281.2 | 88.5 | 267.4 | 114.3 | 251.7 |

## 4.5 Dependence of Rheological Characteristics

Variation in rheological characteristics of both cement paste and graphene-cement paste was observed, which originates due to mixing composition of the paste, shear rate cycles, resting time and rheological models. The effect of mix composition mainly includes water to cement ratio, admixture, mixing and testing technique (Shaughnessy & Clark, 1988). As these parameters are already studied in detail (Nehdi & Rahman, 2004; Shaughnessy & Clark, 1988), therefore, all these factors were kept the constant and only effect of graphene/cement ratio, shear rate range, superplasticizer and resting time were investigated. As rheological methods determined the flow properties from statistical trials, therefore, several values can be obtained. However, in this study, best curve fitting and minimizing the standard error was considered in determining the rheological flow values. These results were further evaluated using concentric cylinder geometry as well. It is important to mention here that to determine the influence of different variables on rheological parameters only G1 type was considered. G1 type was selected based on the standard error values of Table 4.8. Moreover, G1 obtained the stable and uniform dispersion in aqueous solution. For shear rate range, superplasticizer and resting time only G1M3 mix was considered. This mix was selected due to more surface area and less content of graphene to obtain a true and realistic information of these variables on the rheology of graphene-cement paste.

### 4.5.1 Variables Effecting Yield Stress

Yield stress values were determined by Casson equation, Bingham method, Herschel-Bulkley (HB) model and Modified Bingham model. It was observed that yield stress values increase by the addition of graphene, shear rate range and resting time, however, decreased with the addition of superplasticizer. Generally, in concentric cylinders, Bingham model determined the highest yield stress values and HB model determined the lowest values. However, for the parallel plates, Modified Bingham model determined the highest yield stress values, followed by Bingham, HB and Casson model. It is important to mention here that; smooth parallel plates and concentric cylinders were used in this research study. Therefore, due to slippage effect and surface friction (Nehdi & Rahman, 2004), low yield stress values were found. Effect of graphene, shear rate range, resting time, superplasticizer and test geometry on yield stress were discussed as follows:

#### 4.5.1.1 Effect of Graphene Percentage on Yield Stress

It was observed in Table 4.10 that the yield stress values were increased by the incorporation of graphene to the cement matrix. By increasing percentage of graphene in the design mixture, the yield stress values were also increased for all the rheological models. This increase in yield stress values is in line with the available literature for the derivatives of graphene. Shan et al. (2015) performed the experimental work to study the effect of graphene oxide on rheological properties of cement paste. Yield stress values were found approximately four times of plain cement for 0.08 % of graphene oxide cement paste. Increase in yield stress values of graphene-cement paste might be due to the higher surface area of graphene. As explained earlier that graphene (G1) has about 80 times higher surface area compared to cement, therefore, it requires more amount of water to lubricate graphene flakes (Chuah et al., 2014). Besides that, it was noticed that negatively charged graphene flakes in water interact with each other by electrostatic interaction and formed flocculation structures. When this aqueous solution of graphene was mixed with cement then, the attractive forces become more prominent. These large agglomerates entrapped the water molecules, which will eventually reduce the content of free available water (Shan et al., 2015). Furthermore, Wang et al. (2016) also detected the flocculation structures with a higher dosage of graphene oxide in cement paste. Therefore, it can be concluded that by keeping the constant water to cement ratio in the mixture will increases the yield stress of the specimens. In addition, by increasing the amount of graphene in cement paste causes more flocculation, as a result, the yield stress values were significantly improved.

**Table 4.10: Effect of graphene percentage on yield stress values.**

| Sample | Bingham | Modified BM | HB | Casson | Bingham | Modified BM | HB | Casson |
|---|---|---|---|---|---|---|---|---|
| | Parallel Plate | | | | Concentric cylinders | | | |
| M0 | 1.53 | 1.76 | 1.22 | 0.52 | 0.91 | 1.21 | 0.13 | 0.58 |
| G1M3 | 1.67 | 1.79 | 1.30 | 0.62 | 2.42 | 0.98 | 0.42 | 1.48 |
| G1M5 | 1.84 | 1.89 | 1.48 | 0.79 | 2.23 | 0.99 | 0.34 | 1.34 |
| G1M10 | 1.90 | 1.93 | 1.53 | 0.80 | 2.43 | 1.00 | 0.40 | 1.51 |

### 4.5.1.2 Effect of Shear Rate Range on Yield Stress

The variation in shear rate is based on the delivering method of the concrete to the formwork i.e. by pumping or bucket. The shear rate of the cement paste in ordinary concrete during mixing and placing is generally found about 70 $s^{-1}$ (Ferraris, 1999). However, for high-performance concrete, cement paste bears more shear rate due to pumping, and researchers used higher shear rate range (Saak et al., 1999; Yahia & Khayat, 2003). Furthermore, Roussel (2006) reported that while concreting, cement paste bears the shear rate three to five times higher than that of the concrete. The concept of yield stress is a very important parameter, however, its value is directly related to the range of shear rate cycle (Barnes & Walters, 1985). Table 4.11 presents the yield stress values for three different shear rate range. The range of shear rate cycle from 100-0.6 $s^{-1}$, 200-0.6 $s^{-1}$ and 300-0.6 $s^{-1}$ has a significant effect on the yield stress values, and the increment was observed for both test geometries. Effect of shear rate range using parallel plate geometry has been published. Modified Bingham model determined the highest yield stress values and Casson model determine the lowest value. As the modified Bingham model has the characteristics of both Bingham and Herschel-Bulkley model thus, it fits more accurately to the flow data and its standard error value was also found the least amongst others. The yield stress values for the Casson equation was found lowest amongst other models, however, it precisely fits the flow data curve. Barnes & Walters (1985) performed the experimental investigation using Bingham model by considering three different shear rate ranges and determined the increase in yield stress values with high shear rate range cycle. In short, the effect of shear rate range on the yield stress is very beneficial for normal and high-performance concretes. Furthermore, this study also opens a new approach for the use of graphene-cement composite as a self-consolidating concrete.

**Table 4.11: Effect of shear rate range on yield stress values.**

| Sample | Bingham | Modified BM | HB | Casson | Bingham | Modified BM | HB | Casson |
|---|---|---|---|---|---|---|---|---|
| | Parallel Plate | | | | Concentric cylinders | | | |
| M0a | 1.46 | 1.46 | 1.17 | 0.45 | 0.30 | 0.30 | 0.04 | 0.39 |
| M0b | 1.53 | 1.76 | 1.22 | 0.52 | 0.91 | 1.21 | 0.13 | 0.58 |
| M0c | 1.60 | 1.83 | 1.27 | 0.55 | 3.76 | 0.98 | 0.42 | 1.67 |
| G1M3a | 1.51 | 1.61 | 1.21 | 0.50 | 0.76 | 0.99 | 0.06 | 0.98 |
| G1M3b | 1.67 | 1.79 | 1.30 | 0.62 | 2.42 | 0.98 | 0.42 | 1.48 |
| G1M3c | 1.74 | 1.86 | 1.34 | 0.64 | 8.31 | 0.99 | 1.60 | 3.069 |

### 4.5.1.3 Effect of Resting Time on Yield Stress

Generally, it was observed that with the passage of time, molecular structure may change in the cement paste due to chemical interaction, therefore, it is very important to consider the effect of resting time on the yield stress. Resting time is the time interval between sample preparation to casting. The results showed that the yield stress was increased with various resting time (Table 4.12). This increment in the yield stress may be attributed due to three factors; (a) thixotropic properties of cement (Wang et al., 2016); (b) hydration reaction of cement paste; and (c) presence of suspended particles (graphene). As cement paste has thixotropic properties (Wang et al., 2016) and structures change in the cement paste, therefore, high shear stress was observed at the same shear rate. It was also noted that for 60 min resting time more yield stress was recorded for mix G1M3 sample as compared to control mix (M0). This shows that graphene has a significant effect on yield stress. Thus, it can be summarized that with an increase in resting time of the mixtures the yield stress values also increased.

**Table 4.12: Effect of resting time on yield stress values.**

| Sample | Bingham | Modified BM | HB | Casson | Bingham | Modified BM | HB | Casson |
|---|---|---|---|---|---|---|---|---|
| | Parallel Plate | | | | Concentric cylinders | | | |
| M0-0 | 1.53 | 1.76 | 1.22 | 0.52 | 0.91 | 1.21 | 0.13 | 0.58 |
| M0-30 | 1.65 | 1.85 | 1.38 | 1.75 | 1.39 | 1.39 | 0.19 | 0.93 |
| M0-60 | 2.54 | 2.88 | 3.64 | 1.93 | 1.79 | 1.47 | 0.35 | 0.98 |
| G1M3-0 | 1.67 | 1.79 | 1.30 | 0.62 | 2.42 | 0.98 | 0.42 | 1.48 |
| G1M3-30 | 1.72 | 1.92 | 1.42 | 1.81 | 2.99 | 1.00 | 0.46 | 1.90 |
| G1M3-60 | 3.78 | 2.19 | 1.65 | 4.91 | 3.07 | 1.00 | 0.52 | 1.88 |

#### 4.5.1.4 Effect of Superplasticizer on Yield Stress

Several studies (Nehdi & Rahman, 2004; Wang et al., 2017; Wang et al., 2016) reported the effect of water reducing agent on the yield stress of the cement paste and considered a parameter to determine their interface with rheological models and test geometries. Wang et al. (2017) used the fly ash in graphene oxide cement paste and determined that yield stress values decrease. In this study, it was observed in Table 4.13 that with the addition of superplasticizer in the mixes, the yield stress was reduced for both mixes M0 and G1M3 in parallel plates and concentric cylinders. This reduction was might be due to the hydrophobic groups of poly-carboxylate superplasticizer, which, absorbed on the surface of cement particles and extend in an outwards direction. Due to the electrostatic repulsion flocculated structure destroyed as a result free water released which increases the fluidity and reduce the yield stress (Wang et al., 2016).

**Table 4.13: Effect of superplasticizer on yield stress values.**

| Sample | Modified BM | Bingham | HB | Casson | Modified BM | Bingham | HB | Casson |
|---|---|---|---|---|---|---|---|---|
| | Parallel Plate | | | | Concentric cylinders | | | |
| M0 | 1.76 | 1.53 | 1.22 | 0.52 | 1.21 | 0.91 | 0.13 | 0.58 |
| M0S | 1.33 | 1.24 | 1.17 | 0.36 | 0.47 | 0.73 | 0.65 | 0.42 |
| G1M3 | 1.79 | 1.67 | 1.30 | 0.62 | 0.98 | 2.42 | 0.42 | 1.48 |
| G1M3S | 0.89 | 0.58 | 0.67 | 0.51 | 0.99 | 0.62 | 0.04 | 0.82 |

### 4.5.1.5 Effect of Test Geometry on Yield Stress

It was noted that yield stress values were more in parallel plates as compared to the concentric cylinder. In parallel plates geometry, the surface area is more as compared to the concentric cylinder and particles sedimentation would be a key factor to increase the yield stress values (Nehdi & Rahman, 2004). Moreover, gap thickness is an important parameter which influences the yield stress values. Gap thickness in parallel plate is 0.6 mm whereas, 1.2 mm in concentric cylinder. Ferraris (1999) computed the gap in concrete by using the mathematical model developed by Garboczi & Bentz (1997) and found the average value of gap is between 0.16 to 0.22 mm. However, Concentric cylinders, normally estimate the rheological properties at large gap i.e. 6-7 times of estimated gap, therefore, it leads to measurement of the bulk values of cement paste and are not the correct values in accordance to concrete rheology (Ferraris, 1999). Hung et al. (2015) performed experimental work on asphalt rubber binder and measured its rheology with both concentric cylinder and parallel plates. They found no significant difference between two geometries. It was noticed that the authors used very large gap i.e. 2 mm in parallel plates, due to which, the difference with concentric cylinders vanishes. Therefore, it can be concluded that parallel plates are suitable for cement paste as it measures the rheological properties with the realistic approach (Ferraris, 1999).

### 4.5.2 Variables Effecting Viscosity

Plastic viscosity represents the deformation of cement pastes due to external loading (Wang et al., 2016). Plastic viscosities for the cement paste and graphene-cement composite were calculated by using concentric cylinders and parallel plates. The viscosities were computed from the flow curves proposed in Casson, Bingham and Modified Bingham Models. Generally, in parallel plates for control mix (M0), Bingham model predicted higher values of the plastic viscosities, followed by the Casson and Modified Bingham. Whereas, for sample G1M3, the Modified Bingham model estimated the highest plastic viscosities values which were about 26% and 17% higher than the Casson and Bingham models, respectively. Furthermore, in concentric cylinders, the modified Bingham method showed the highest plastic viscosities values for both M0 and G1M3 mixes, and Casson method estimated the lowest.

#### 4.5.2.1 Impact of Graphene Percentage on Viscosity

Incorporation of graphene in cement paste increases the plastic viscosities as shown in Table 4.14. Furthermore, the direct relationship between graphene and plastic viscosity was observed, as the amount of graphene increases the plastic viscosity was also increased. These results are in line with the study performed by Shan et al. (2015) on graphene oxide. They conducted the experimental work with a varying percentage of graphene oxide and found that the plastic viscosity values increased by 78 % with the addition of 0.04 % of graphene oxide in the plain cement mix. Increase in plastic viscosity values might be due to the large surface area of the graphene flakes. Since it requires more amount of water for lubricating the surface of graphene flakes which results in a dry mix of the graphene cement paste. Another reason may be that the incorporation of graphene in cement paste reduces the free available water which increases the frictional resistance between graphene and cement matrix which resulted in higher viscosities.

Therefore, it can be summarized that due to the large surface area of graphene sheets and reduction in free available water, overall plastic viscosity values increased. In addition, with the increase of graphene content, the deformation of the cement pastes become difficult due to external forces.

**Table 4.14: Effect of graphene on plastic viscosity values.**

| Sample | Bingham | Modified BM | Casson | Bingham | Modified BM | Casson |
|---|---|---|---|---|---|---|
| | Parallel plate | | | Concentric cylinder | | |
| M0 (Control) | 0.50 | 0.47 | 0.42 | 0.24 | 0.25 | 0.18 |
| G1M3 | 0.80 | 0.96 | 0.71 | 0.65 | 0.66 | 0.51 |
| G1M5 | 0.84 | 0.84 | 0.78 | 0.64 | 0.65 | 0.51 |
| G1M10 | 0.85 | 0.84 | 0.79 | 0.64 | 0.65 | 0.49 |

### 4.5.2.2 Impact of Shear Rate Range on Viscosity

Test results of shear rate range on plastic viscosity for various rheological models were determined and presented in Table 4.15. When samples were subjected to high shear rate cycle range, the apparent plastic viscosity was reduced and vice versa. Shan et al. (2015), reported that the apparent viscosities are dependent on the shear rate, at a low shear rate, apparent viscosities will be more and at a high shear rate, viscosities will be low. Shan et al. (2015) used the graphene oxide, silica fume and graphene oxide-silica fume in cement paste and found that for all mixes apparent viscosity decreases with the increase of shear rates. Furthermore, the addition of graphene produces the flocculated suspensions in the cement matrix, thus, with the increase in shear rate cycle range, those suspended particles were destroyed and resulted in lower apparent viscosity. Hence, due to high shear rate range deformation of cement pastes become easier under external forces.

**Table 4.15: Effect of shear rate range on plastic viscosity.**

| Sample | Bingham | Modified BM | Casson | Bingham | Modified BM | Casson |
|---|---|---|---|---|---|---|
| | Parallel plate | | | Concentric cylinder | | |
| M0a | 0.46 | 0.30 | 0.39 | 0.29 | 0.29 | 0.22 |
| M0b | 0.50 | 0.47 | 0.42 | 0.24 | 0.25 | 0.18 |
| M0c | 0.42 | 0.39 | 0.43 | 0.17 | 0.17 | 0.12 |
| G1M3a | 0.71 | 0.93 | 0.62 | 0.80 | 0.80 | 0.62 |
| G1M3b | 0.80 | 0.96 | 0.71 | 0.65 | 0.68 | 0.51 |
| G1M3c | 0.92 | 0.99 | 0.89 | 0.51 | 0.54 | 0.38 |

### 4.5.2.3 Impact of Resting Time on Viscosity

The resting time has a direct relationship to the plastic viscosity as well. Table 4.16 shows the values of plastic viscosity for both control mix and graphene cement mix. It was noted that plastic viscosity was increasing irrespective of the test geometry and mathematical model. It mainly involves two factors, the hydration of cement particles and the frictional resistance between cement and graphene flakes. Influence of hydration of cement particles and fractional resistance was dominant for the resting time of 60 min, in which plastic viscosity was very high. Cao et al. (2016) reported that the 30 min of resting time can be considered as a dormant period for the hydration of cement paste. Therefore, the major contribution for 30 min resting was given by the frictional resistance between the cement paste and graphene sheets. Hence, it can be summarized that due to increase in resting time, flow behaviour becomes difficult for the cement paste.

**Table 4.16: Effect of resting time on plastic viscosity.**

| Sample | Bingham | Modified BM | Casson | Bingham | Modified BM | Casson |
|---|---|---|---|---|---|---|
| | Parallel plate | | | Concentric cylinder | | |
| M0-0 | 0.50 | 0.47 | 0.42 | 0.24 | 0.25 | 0.18 |
| M0-30 | 0.90 | 0.48 | 0.86 | 0.31 | 0.31 | 0.23 |
| M0-60 | 1.47 | 0.87 | 1.19 | 0.12 | 0.12 | 0.11 |
| G1M3-0 | 0.80 | 0.96 | 0.71 | 0.65 | 0.66 | 0.51 |
| G1M3-30 | 0.91 | 0.96 | 0.89 | 0.75 | 0.77 | 0.58 |
| G1M3-60 | 1.46 | 0.99 | 1.20 | 0.83 | 0.84 | 0.65 |

#### 4.5.2.4 Impact of Superplasticizer on Viscosity

Table 4.17 shows the influence of superplasticizer on the plastic viscosities of the cement pastes. It was observed that with the addition of superplasticizer fluidity enhances. As superplasticizers and water reducing agents reduce the internal friction between the particles which dramatically alter the rheological characteristics of the cement paste (Ferraris, 1999). Therefore, the fluidity and workability of cement paste were greatly improved by incorporation of superplasticizer in the cement matrix.

**Table 4.17: Effect of superplasticizer on plastic viscosity.**

| Sample | Bingham | Modified BM | Casson | Bingham | Modified BM | Casson |
|---|---|---|---|---|---|---|
| | Parallel plate | | | Concentric cylinder | | |
| M0 (Control) | 0.50 | 0.47 | 0.42 | 0.24 | 0.25 | 0.18 |
| M0S | 0.31 | 0.21 | 0.28 | 0.22 | 0.20 | 0.17 |
| G1M3 | 0.80 | 0.96 | 0.71 | 0.65 | 0.66 | 0.51 |
| G1M3S | 0.46 | 0.47 | 0.40 | 0.42 | 0.41 | 0.30 |

#### 4.5.2.5 Impact of Test Geometry on Viscosity

Generally, parallel plates determined the higher values for the plastic viscosities as compared to the concentric cylinders. A possible reason may be the settlement of suspended particles. As parallel plates have the large surface area as compared to the concentric cylinders. Thus, suspended cement particles and graphene starts to settle down and provide great hindrance against the deformation of cement paste. Therefore, it can be concluded that the sedimentation or creaming will be a key factor in indicating the higher plastic viscosities for parallel plates (Barnes, 2000; Nehdi & Rahman, 2004).

### 4.5.3 Variables Effecting Consistency and Power Rate Index

The trend of the viscosity data was determined by considering Herschel-Bulkley (HB) model, which considers two factors such as consistency (K) and the power index (n). By considering these factors the relationship between viscosity trend and the shear rate can be determined (Nehdi & Rahman, 2004). It also provides the information about the shear deformation, i.e. shear thickening or shear thinning based on power index values ‘n’ (Wang et al., 2016). If $n > 1$ then fluid will be shear thickening and if $n < 1$ then shear thinning material. Generally, both consistency and rate index values were increased by the addition of graphene to the cement mix. The behaviour of the cement paste was found in shear thinning. Concentric cylinders showed higher values for the consistency (K) and lower values for the power rate index (n) as compared to the parallel plates.

#### 4.5.3.1 Effect of Graphene Percentage on Consistency and Power Rate Index

Consistency values were increased with the addition of graphene in the mix as shown in Table 4.18. It was noted that with an increase in the percentage of graphene in the cement paste, consistency and power index values increased for both parallel plates and concentric cylinders. However, these values were less than 1 predicting the shear thinning behaviour of the graphene cement paste. Wang et al. (2016) studied the shear deformation for graphene oxide in cement paste and found that cement paste curve can be divided into shear thinning and shear thickening stage based on the inflexion point. They suggested that cement paste with higher graphene oxide content shows the shear thinning effect at high shear rates. Govin et al. (2016) studied the effect of guar gum derivatives on the fresh state cement mortar. They found that power index ‘n’ values were less than 1, and paste was behaving as shear thinning material. Therefore, it can be said that incorporation of graphene results in more suspended structures in the paste, which makes it comparatively thicker to flow and enhance the resistance to flow.

**Table 4.18: Effect of graphene on consistency and rate index values calculated by HB model.**

| Sample | Consistency, K | Power rate index, n | Consistency, K | Power rate index, n |
|---|---|---|---|---|
| | Parallel Plate | | Concentric cylinders | |
| M0 (Control) | 0.60 | 0.96 | 0.59 | 0.82 |
| G1M3 | 0.97 | 0.97 | 1.49 | 0.81 |
| G1M5 | 0.99 | 0.98 | 1.45 | 0.84 |
| G1M10 | 0.97 | 0.98 | 1.53 | 0.83 |

#### 4.5.3.2 Effect of Shear Rate Range on Consistency and Power Rate Index

The increment in shear rate cycle range has no significant effect on the trend of viscosity data. Table 4.19 showed the values for consistency and power rate index for M0 and G1M3 mix and their dependence on the shear rate cycle range. Although, in parallel plates, the consistency values were initially increased and later they were decreased for both M0 and G1M3 mixes. Whereas, the consistency values were steadily decreased for the concentric cylinders. Consistency (K) has no physical meaning and difficult to compare because of its dimension (Pa.s$^n$) which is dependent on ‘n’ (Vikan et al., 2007). However, the rate index (n) values were initially increased and then decreased for both parallel plates and concentric cylinders. Therefore, it can be concluded that with the higher shear rate cycle range, the cement paste will observe more shear thinning behaviour. The flocculated structures will break down with the higher shear rate thus, cement paste becomes thinner.

**Table 4.19: Effect of shear rate range on consistency and rate index values.**

| Sample | Consistency, K | Power rate index, n | Consistency, K | Power rate index, n |
|---|---|---|---|---|
| | Parallel Plate | | Concentric cylinders | |
| M0a | 0.29 | 0.60 | 0.89 | 0.74 |
| M0b | 0.60 | 0.96 | 0.58 | 0.82 |
| M0c | 0.51 | 0.90 | 0.76 | 0.74 |
| G1M3a | 0.96 | 0.99 | 2.39 | 0.75 |
| G1M3b | 0.97 | 0.97 | 1.52 | 0.83 |
| G1M3c | 0.96 | 0.98 | 1.49 | 0.81 |

### 4.5.3.3 Effect of Resting Time on Consistency and Power Rate Index

It was observed that with an increase in resting time the behaviour of paste was closer to the shear thickening as shown in Table 4.20. For 60 min rest time samples, in parallel plate sample, the rate index 'n' was more than 1, indicating the shear thickening behaviour. Wallevik (2009) performed the experimental work to study the rheological properties of cement paste at 12 min, 42 min, 72 min and 102 min after initial mixing. They found that coagulation and links between two cement particles can be reversible and permanent. Initially, when cement particles come in contact with water, on the surface of cement particle membrane of gelatinous calcium silicate hydrates forms (Wallevik, 2009). When cement paste is mixed this membrane break and cement particles separated and start freely to move. However, with increase in rest time, this link and membrane become strong and difficult to break. Due to this reason, power rate index values increased in cement paste. Therefore, it can be concluded that with increase in resting time reversible coagulation and links between cement particles become irreversible, permanent and difficult to break which will result in high resistance to flow.

**Table 4.20: Effect of resting time on consistency and rate index values.**

| Sample | Consistency, K | Power rate index, n | Consistency, K | Power rate index, n |
|---|---|---|---|---|
| | Parallel Plate | | Concentric cylinders | |
| M0-0 | 0.60 | 0.96 | 0.58 | 0.82 |
| M0-30 | 0.96 | 0.98 | 0.88 | 0.80 |
| M0-60 | 0.22 | 1.21 | 0.47 | 0.72 |
| G1M3-0 | 0.97 | 0.97 | 1.52 | 0.83 |
| G1M3-30 | 0.92 | 0.99 | 1.88 | 0.82 |
| G1M3-60 | 0.99 | 1.10 | 1.94 | 0.83 |

### 4.5.3.4 Effect of Superplasticizer on Consistency and Power Rate Index

When water reducing agent was added to the mix, it enhanced the flowability of the paste. Therefore, it was observed in Table 4.21 that the consistency and rate index values were reduced by the addition of superplasticizer. It caused more shear thinning behaviour in all mix designs. Wallevik (2009) stated that van der Waals and electrostatic repulsive forces generate potential energy interaction between the cement particles. Due to this total potential energy interaction, cement particles become closer to each other and glued together in the form of coagulation. The superplasticizer absorbs on the surface of cement particles and changes the total potential energy in such a manner that dispersion becomes easier. Hence, it can be stated that superplasticizer greatly enhanced the flowability and reduce the internal friction between cement paste and graphene by lubricating them resulting in making the cement pastes thinner and easy to flow.

**Table 4.21: Effect of superplasticizer on consistency and rate index values.**

| Sample | Consistency, K | Power rate index, n | Consistency, K | Power rate index, n |
|---|---|---|---|---|
| | Parallel Plate | | Concentric cylinders | |
| M0 (Control) | 0.60 | 0.96 | 0.59 | 0.82 |
| M0S | 0.47 | 0.89 | 0.49 | 0.79 |
| G1M3 | 0.97 | 0.97 | 1.49 | 0.81 |
| G1M3S | 0.87 | 0.82 | 1.07 | 0.77 |

#### 4.5.3.5 Effect of Test Geometry on Consistency and Power Rate Index

Concentric cylinders showed higher values of the consistency and lower for rate index. The main reason might be that in concentric cylinders, inner and outer cylinders both have different diameter (cup and bob) which make their behaviour as non-linear, however, in parallel plates, both plates (upper and lower) have the same diameter and its results are linear (Hung et al., 2015). Another possible reason may be the gap between the parallel plates, which was small compared to the concentric cylinders. Hung et al. (2015) reported that an appropriate conversion factor is required for the concentric cylinders to obtain and convert the large gap to the small one equivalent to the parallel plate geometry. In brief, test geometry has a significant effect on the rheological properties.

### 4.5.4 Effectiveness of Rheological Mathematical Models

Standard error values for the various rheological models were calculated using Equation (2.7) and given in Table 4.22. A lower value of standard error represents the best-fitting of the mathematical model to the flow curve. It was observed that HB and Modified Bingham models showed the lower standard error, whereas, the Bingham and Casson models displayed higher values. M0c, M0a and G1M10 mixes showed the maximum standard error values for all mathematical models in the parallel plate. However, in concentric cylinders, M0S and M0-60 estimated the highest values for the standard error for all rheological models. Generally, the standard error values predicted by rheological models were found lower for the concentric cylinders compared to the parallel plates. Standard deviation values and average values are very less for concentric cylinders as compared to parallel plates. According to Hung et al. (2015), due to the same diameter of upper and lower parallel plates, results will be linear. In parallel plates, linear mathematical models i.e. modified Bingham and Bingham model estimated the lower standard error values in comparison to the Herschel-Bulkley and Casson models. As modified Bingham model have the characteristics of both Bingham and Herschel-Bulkley model (Feys et al., 2013) therefore, for parallel plates it predicted the flow behaviour more accurately. In concentric cylinders, nonlinearity is prominent due to the geometry of the apparatus. Hence Herschel-Bulkley model and Casson model estimated the lower standard error values. It can be concluded that, for parallel plates Modified Bingham, and for concentric cylinder Herschel-Bulkley, is the more appropriate models to predict the flow behaviour of the graphene based cement pastes

**Table 4.22: Values of standard error for various rheological models.**

| Sample | Bingham | Modified BM | HB | Casson |
|---|---|---|---|---|
| **Parallel plate** | | | | |
| M0 (Control) | 74.5 | 74.3 | 74.3 | 73.6 |
| M0S | 65.4 | 42.9 | 90.5 | 85.2 |
| M0a | 206.5 | 128.5 | 453.5 | 200.0 |
| M0b | 74.5 | 74.3 | 74.3 | 73.6 |
| M0c | 283.9 | 242.3 | 119.0 | 390.5 |
| M0-0 | 74.5 | 74.3 | 74.3 | 73.6 |
| M0-30 | 117.7 | 65.2 | 123.0 | 111.4 |
| M0-60 | 80.5 | 52.4 | 51.5 | 95.2 |
| G1M3 | 89.0 | 34.2 | 70.5 | 82.9 |
| G1M5 | 30.5 | 30.7 | 45.0 | 57.2 |
| G1M10 | 233.2 | 223.5 | 261.5 | 283.1 |
| G1M3S | 178.5 | 186.3 | 161.6 | 177.3 |
| G1M3a | 134.9 | 38.9 | 27.8 | 114.8 |
| G1M3b | 89.0 | 34.2 | 70.5 | 82.9 |
| G1M3c | 88.4 | 98.3 | 95.1 | 98.5 |
| G1M3-0 | 89.0 | 34.2 | 70.5 | 82.9 |
| G1M3-30 | 91.3 | 85.6 | 95.8 | 97.7 |
| G1M3-60 | 92.4 | 69.0 | 73.1 | 111.5 |
| **Average** | 116.3 | 88.3 | 112.9 | 127.3 |
| **Standard deviation** | 66.3 | 65.4 | 99.6 | 86.1 |

**Table 4.22: Continued**

| Sample | Bingham | Modified BM | HB | Casson |
|---|---|---|---|---|
| **Concentric cylinders** | | | | |
| M0 (Control) | 37.4 | 49.2 | 14.5 | 16.3 |
| M0S | 186.2 | 194.9 | 262.3 | 202.6 |
| M0a | 66.3 | 66.3 | 15.7 | 38.1 |
| M0b | 37.4 | 49.2 | 14.5 | 16.3 |
| M0c | 43.7 | 68.8 | 20.3 | 23.0 |
| M0-0 | 37.4 | 49.2 | 14.5 | 16.3 |
| M0-30 | 42.9 | 42.9 | 15.7 | 18.5 |
| M0-60 | 91.2 | 80.2 | 43.9 | 280.6 |
| G1M3 | 35.6 | 37.3 | 18.3 | 17.7 |
| G1M5 | 35.5 | 35.0 | 13.3 | 13.3 |
| G1M10 | 37.0 | 38.9 | 15.5 | 15.6 |
| G1M3S | 52.83 | 54.3 | 32.1 | 31.9 |
| G1M3a | 60.3 | 60.5 | 14.8 | 34.0 |
| G1M3b | 35.6 | 37.3 | 18.3 | 17.7 |
| G1M3c | 34.8 | 45.2 | 21.9 | 20.7 |
| G1M3-0 | 35.6 | 45.2 | 21.9 | 17.7 |
| G1M3-30 | 38.6 | 41.0 | 17.3 | 17.8 |
| G1M3-60 | 35.5 | 37.8 | 16.8 | 16.6 |
| **Average** | 52.4 | 57.4 | 32.9 | 45.3 |
| **Standard deviation** | 36.5 | 36.5 | 57.8 | 73.0 |

## 4.6 Mechanical Properties of Graphene Cement Composite Mortar

In this section mechanical properties of graphene-cement mortar were investigated. In common practice, cement mortar and concrete have been extensively used in construction industry. By the addition of coarse and fine aggregates in cement paste, the percentage content of graphene in the overall volume of concrete structure would be very small. Moreover, it was assumed that if the same percentage of graphene will be used then its effect will be very minute due to a small amount in comparison to the volume of the hardened structure. Additionally, the overall amount of graphene in the complete project will be quite expensive and make the project uneconomical. Thus, mechanical properties were obtained on the graphene-cement mortar only. For this purpose, the influence of 0.03%, 0.05% and 0.10% of graphene by weight of cement in a mortar was investigated.

### 4.6.1 Compressive Strength

Compressive stress values for the graphene cement mortar was observed at 1, 7 and 28 days after casting. Figure 4.19 shows the overall compressive stress values after the 28 days. Strength gain with the passage of time has been highlighted in Figure 4.19 (a). Figure 4.19 (b) presents the percentile strength gain at various days and its contribution for 28 days strength. Influence of different types of graphene and its content on the compressive strength of cement composites have been made in Table 4.23. It was noted that graphene significantly enhances the early age strength and contributed to the hydration reaction of cement (Wang et al., 2016). Minimum increase of 4% in compressive strength of 1-day was observed for the G3M3-M specimen and maximum of 79% was noted for G2M5-M specimen. Furthermore, percentage strength contribution to total strength for 1 day was also high for all graphene cement composites (Table 4.23). Strength gain between 8-28 days after casting was significantly dropped. Therefore, it can be stated that graphene has no direct effect on later age strength values. Overall 28-day compressive strength values were found increasing with the addition of graphene. The maximum increment of 18% was observed for the G2M5-M mix. The impact of the lateral size and thickness of graphene flakes is prominent for early age contribution whereas, surface area role is significant for later age strength as well (Table 4.23). High surface area helps in hydration reaction and hydrated cement product grows in an ordered way. Graphene acted as a heterogeneous nucleation site. The activation energy of hydration reactions decreased and the reaction rate increased, eventually it produced more hydrated cement products i.e. C-S-H and portlandite (Sedaghat, 2014).

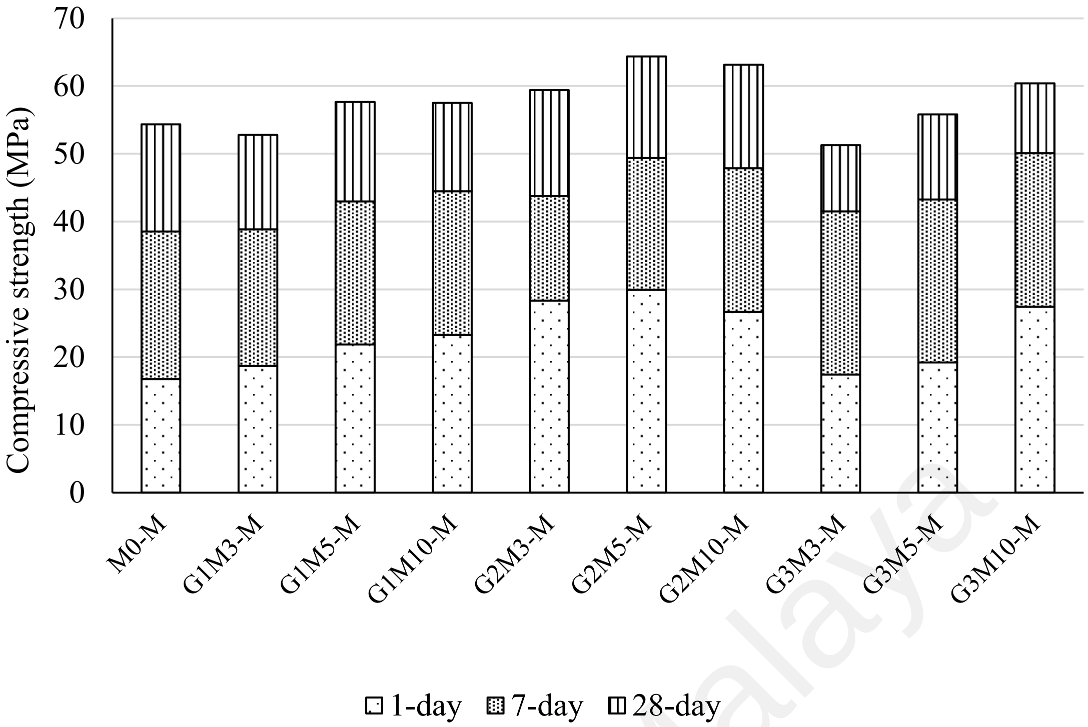

(a) Compressive strength values

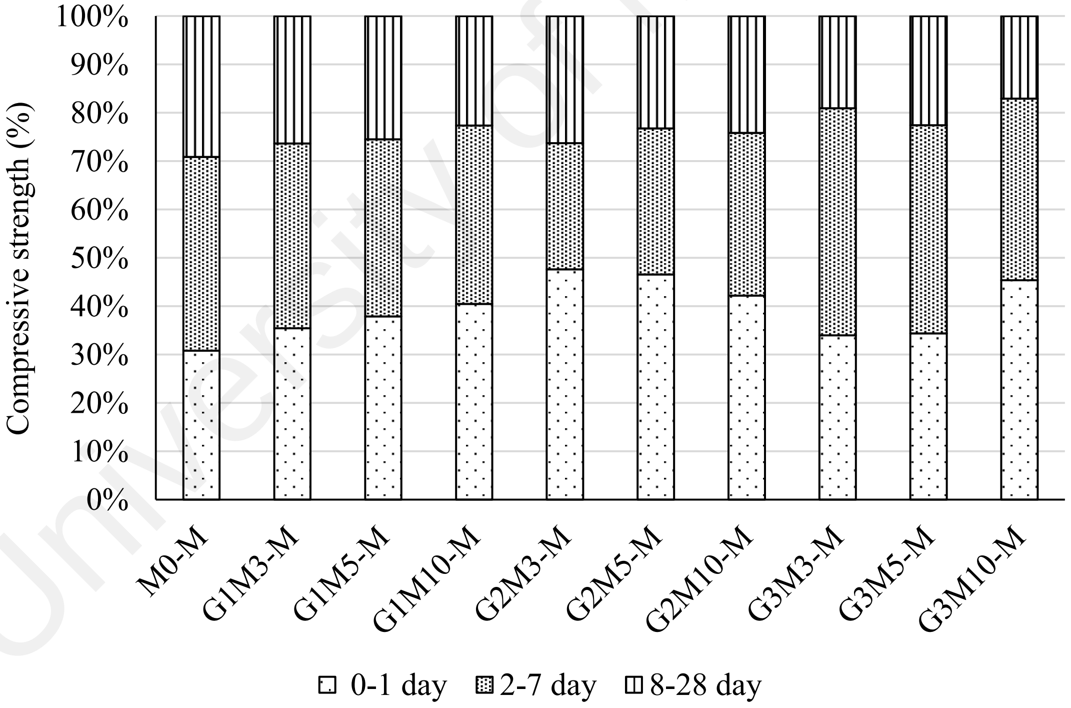

(b) Percentage gain in compressive strength

**Figure 4.19: Determination of compressive stress for graphene cement mortar.**

Moreover, two phenomena i.e. obstructing the propagation of flaws and crack bridging played an important role in strength contribution. These parameters depend upon the surface area and thickness of graphene flakes. Eventually, when cracks were developed and propagated, graphene flakes hold them together which results in higher strength. It further able to slow down the initiation of cracks and offers hindrance to the opening of the existing cracks (AlMuhit, 2015). G2 type graphene-cement composite specimens obtained the maximum values for compressive strength followed by G3 and G1 type as shown in Table 4.23. G2 type graphene flakes have more surface area than G3 type and more lateral size and thickness of graphene flakes than G1 type. Hence, it can be said that higher surface area, lateral size and thickness of graphene flakes contributed to the increase in compressive strength. Graphene content also plays a significant role in strength gain e.g. for M10 mixes, the highest compressive strength values were observed, which were 57.5, 63.14 and 60.41 MPa, for G1, G2 and G3 type respectively. When the amount of graphene content increased, more particle size reduced to the nanoscale level. The large surface area and surface energy of graphene flakes results in better absorption capability and chemical reactivity in comparison to other conventional materials. Therefore, large amount of graphene experienced higher compressive strength values.

**Table 4.23: Compressive strength values estimated for graphene cement mortar.**

| Sample | Strength Increment (MPa) / Percentage strength contribution to total strength (%) | | | | | | Total strength-28 Day | |
|---|---|---|---|---|---|---|---|---|
| | 0-1 Days | | 2-7 Days | | 8-28 Days | | Strength (MPa) | Percentage rate (%) |
| M0-M | 16.7 | 30.81 | 21.7 | 40.08 | 15.8 | 29.10 | 54.3 | 100.00 |
| G1M3-M | 18.7 | 35.43 | 20.2 | 38.23 | 13.9 | 26.34 | 52.7 | 97.09 |
| G1M5-M | 21.8 | 37.92 | 21.1 | 36.62 | 14.6 | 25.46 | 57.6 | 106.09 |
| G1M10-M | 23.2 | 40.49 | 21.2 | 36.87 | 13.0 | 22.64 | 57.5 | 105.78 |
| G2M3-M | 28.3 | 47.66 | 15.5 | 26.04 | 15.6 | 26.30 | 59.4 | 109.31 |
| G2M5-M | 29.9 | 46.54 | 19.4 | 30.23 | 14.9 | 23.23 | 64.3 | 118.38 |
| G2M10-M | 26.6 | 42.22 | 21.2 | 33.61 | 15.2 | 24.17 | 63.1 | 116.15 |
| G3M3-M | 17.4 | 33.98 | 24.1 | 46.95 | 9.7 | 19.08 | 51.2 | 94.32 |
| G3M5-M | 19.2 | 34.39 | 24.0 | 43.04 | 12.6 | 22.57 | 55.8 | 102.70 |
| G3M10-M | 27.4 | 45.41 | 22.6 | 37.51 | 10.3 | 17.08 | 60.4 | 111.13 |

### 4.6.2 Flexural Strength

Flexural strength values were determined for graphene cement mortar. These values were obtained on 7 and 28 days after casting. Flexural strength values were not recorded for 1-day as the values were undetectable and sample broke before any reading. The obtained values of flexural strength were presented in Figure 4.20. Generally, flexural strength values increased with the addition of graphene. By comparing the percentage of graphene, the highest flexural strength values were computed for M10 mixes of graphene. The flexural strength of M10 mix was increased by 20.9%, 38.1%, and 18.5% for G1, G2 and G3respectively as compare to the flexural strength of M0-M at 28-day of casting as shown in Table 4.24. These results support the findings of Pan et al. (2015) and Murugan et al. (2016). The authors found 15-33% enhancement in compressive strength and 41-59% in flexural strength by using 0.05% of GO (Pan et al., 2015). G2 type mortar mixes have the highest values of flexural strength. A similar trend was observed in a compressive strength test. Interestingly, it was noted that later age flexural strength was significantly enhanced by the addition of graphene. In flexural test tensile cracks formed and these cracks become wider with the application of external loading. Hence, crack bridging and hindrance to crack propagation by graphene flakes was more prominent. In short, it can be concluded that flexural strength development was based on the crack bridging action of graphene and compressive strength development was based on both hydrated products development and crack bridging action.

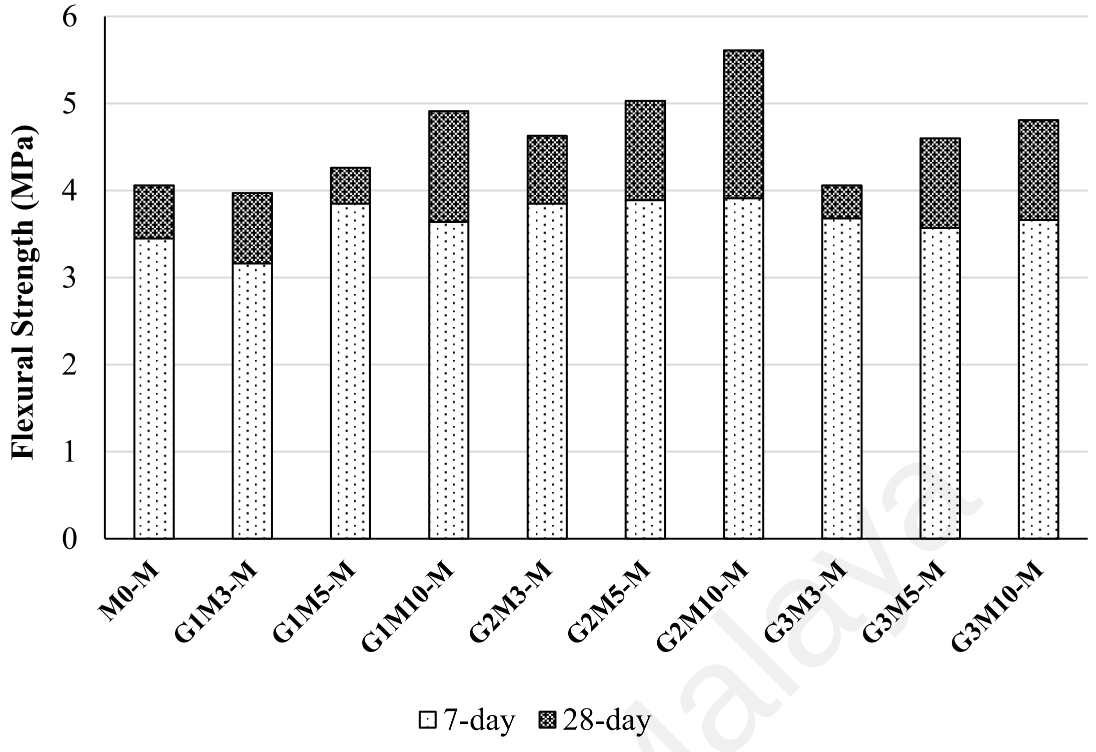

(a) Flexural strength values

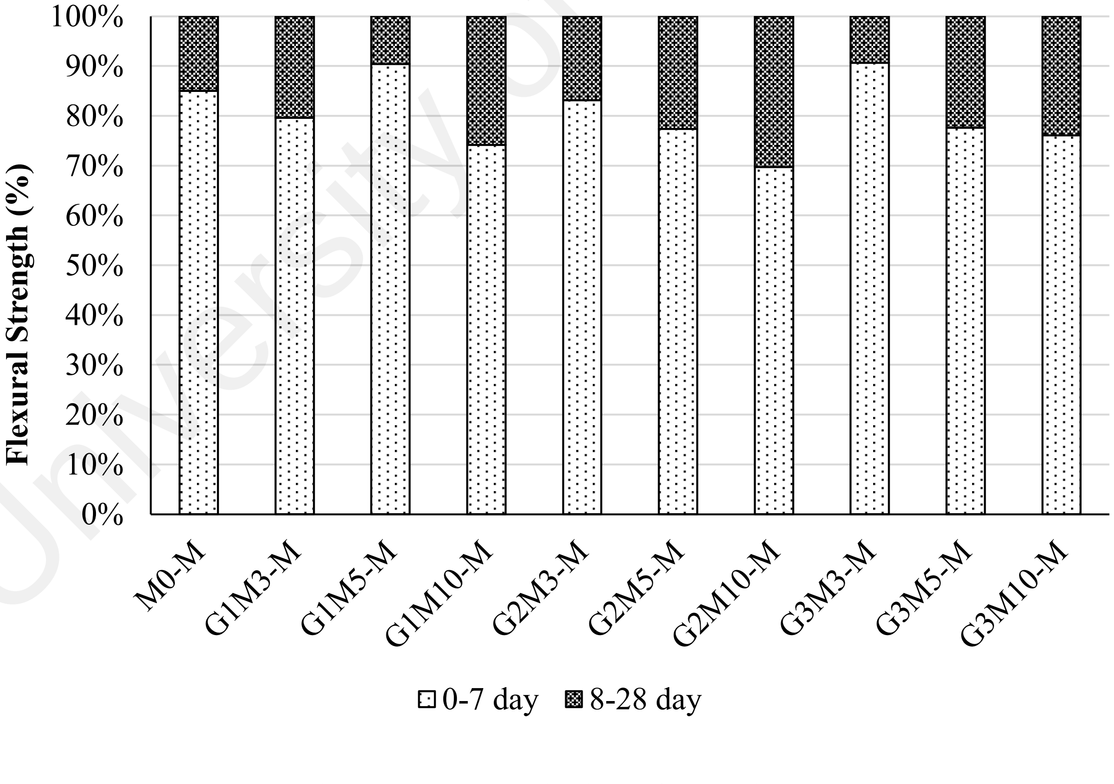

(b) Percentage gain in flexural strength

**Figure 4.20: Determination of flexural strength for graphene cement mortar.**

**Table 4.24: Flexural strength values estimated for graphene cement mortar.**

| Sample | Strength Increment (MPa) / Percentage strength contribution to total strength (%) | | | | Overall strength-28 Day | |
|---|---|---|---|---|---|---|
| | 0-7 Days | | 8-28 Days | | Strength (MPa) | Percentage rate (%) |
| M0-M | 3.4 | 84.98 | 0.6 | 15.02 | 4.1 | 100.00 |
| G1M3-M | 3.2 | 79.60 | 0.8 | 20.40 | 4.0 | 97.78 |
| G1M5-M | 3.8 | 90.38 | 0.4 | 9.62 | 4.3 | 104.93 |
| G1M10-M | 3.6 | 74.13 | 1.3 | 25.87 | 4.9 | 120.94 |
| G2M3-M | 3.8 | 83.15 | 0.8 | 16.85 | 4.6 | 114.04 |
| G2M5-M | 3.9 | 77.34 | 1.2 | 22.66 | 5.0 | 123.89 |
| G2M10-M | 3.9 | 69.70 | 1.7 | 30.30 | 5.6 | 138.18 |
| G3M3-M | 3.7 | 90.64 | 0.4 | 9.36 | 4.1 | 100.00 |
| G3M5-M | 3.6 | 77.61 | 1.0 | 22.39 | 4.6 | 113.30 |
| G3M10-M | 3.6 | 76.09 | 1.2 | 23.91 | 4.8 | 118.47 |

## 4.7 Properties of Graphene Cement Paste

In this section influence of graphene flakes on flow diameter, hardened density, stress-strain curve, hydrated cement products, generation and propagation of cracks of cement composite paste was investigated.

### 4.7.1 Workability

For workability, the flow diameter test was performed for the graphene-cement composite and its obtained values are presented in Table 4.25. The flow diameter values for graphene-cement composite were found lower as compared to mix M0. Pan et al. (2015) used 0.05% of graphene oxide in cement paste with w/c = 0.5 and observed the 41.7% reduction in the slump diameter. Similarly, for 2 % carbon nanotubes with w/c = 0.5 in cement paste 48.9% reduction in slump diameter were found (Collins et al., 2012). A possible reason for the reduction in flow diameter could be the large surface area of the graphene flakes which required more amount of water for lubrication and decrease the free available water. As G1 type was having the maximum surface area, therefore, the 9.3% reduction was noted in G1M10 mix. Spread diameter of the G1M3 mix was 5.4% lowered as compared to the M0 mix. As G3 type was having the lowest surface area thus, for the mix G3M10 only 6.2% reduction was recorded in contrast to M0. Another factor which may contribute to the reduction of flow diameter is the formation of agglomerates due to hydrophobic nature of graphene. However, due to a combination of ultrasonication and magnetic stirring dispersion technique, its effect was observed very minimally. It was also observed that increase in the percentage of graphene content caused more reduction in flow diameter of the graphene-cement composite. Therefore, it can be deduced that the overall workability of the cement paste was reduced by addition of graphene in the cement paste.

**Table 4.25: Flow diameter, maximum compressive load and corresponding resistivity values.**

| Sample | Flow diameter (mm) / Percentage rate (%) | Density (kg/m$^3$) / Percentage rate (%) | Maximum compressive load (kN) / Percentage rate (%) | Compressive strength (MPa) / Percentage rate (%) | Compressive strain at maximum compressive load (mm/mm) / Percentage rate (%) | Four probe resistivity at maximum compressive loading (kΩ-cm) / Percentage rate (%) |
|---|---|---|---|---|---|---|
| M0 | 225 / 100 | 2155.6 / 100 | 93.6 / 100 | 58.5 / 100 | 0.0086 / 100 | 69.8 / 100 |
| G1M3 | 213 / 94.6 | 2045 / 94.9 | 103.6 / 110.6 | 64.7 / 110.6 | 0.012 / 147.2 | 22.5 / 32.2 |
| G1M5 | 211 / 93.8 | 2150.7 / 99.8 | 109.2 / 116.7 | 68.3 / 116.7 | 0.014 / 170.1 | 28.3 / 40.5 |
| G1M10 | 204 / 90.7 | 2077.4 / 96.4 | 95.4 / 101.9 | 59.6 / 101.9 | 0.132 / 153.6 | 35.4 / 50.8 |
| G2M3 | 217 / 96.4 | 2053.7 / 95.3 | 92.4 / 98.8 | 57.8 / 98.8 | 0.0138 / 160 | 40.4 / 57.8 |
| G2M5 | 211 / 93.8 | 2151.9 / 99.8 | 122.2 / 130.6 | 76.4 / 130.6 | 0.015 / 173.4 | 64 / 91.7 |
| G2M10 | 209 / 92.9 | 2038.2 / 94.6 | 107.2 / 114.5 | 67 / 114.5 | 0.012 / 144.2 | 36.7 / 52.5 |
| G3M3 | 217 / 96.4 | 2110.4 / 97.9 | 114.9 / 122.7 | 71.8 / 122.7 | 0.018 / 213.5 | 49.8 / 71.3 |
| G3M5 | 210 / 93.3 | 2114.4 / 98.1 | 122.1 / 130.5 | 76.3 / 130.5 | 0.014 / 160.3 | 57.3 / 82.2 |
| G3M10 | 211 / 93.8 | 2104.8 / 97.6 | 110.8 / 118.4 | 69.3 / 118.4 | 0.0150 / 174 | 52.4 / 75.1 |

*Percentage rate is to be compared with M0 mix.

### 4.7.2 Hardened Density

The density of hardened graphene-cement composites was measured using BS EN 1015-10-1999 (BS EN 1015-10, 1999). A small drop in density values was observed with the increase in the percentage of graphene. A maximum of 5.4 % drop in density value was found for G2M10 mix as compared to M0 (Table 4.25). Pan et al. (2015) used the

0.05% of graphene oxide by weight of cement in design mix and found 1.86% reduction in density values, however, 19% increase in compressive strength as compared to plain cement mix. Similarly, Yakovlev et al. (2006) noted that density values reduced by 6.36% after the incorporation of 0.05% of carbon nanotubes in the cement mix with 70% increase in compressive strength. For M5 mixes of graphene, density values were very close to the M0 mix and have higher compressive strength values (Table 4.25). The possible reason for the increase in compressive strength and reduction in density was uniformity and better distributions of small pores. According to Pan et al. (2015) small and medium size pores (1-45 nm) significantly increase by incorporation of GO in the cement mix. Furthermore, gel pores (1-10 nm), which are composed of CSH gel pore system, increased by 109% (Gong et al., 2014). Pan et al. (2015) and Murugan et al. (2016) found that addition of GO promotes the hydration process (early stages hydration), achieve a high degree of hydration and yields more proportion of CSH gel. Gong et al. (2014) also reported that overall pore area was enhanced by 36% as compared to the plain cement. Therefore, it can be concluded that due to increase in pore area density values of the graphene-cement composite was reduced, however, increase in gel pore sizes, uniformity and discontinuity of pores influenced the mechanical properties.

### 4.7.3 Stress-Strain Curve

The stress-strain curves for the plain cement and graphene-cement composite were obtained after 28-day of casting and illustrated in Figure 4.21. The compressive strength of the graphene cement composite was increasing with the addition of graphene. Increase in compressive strength was attributed mainly to the more hydrated products. The maximum increase in compressive strength of 30% was found for G2M5 and G3M5 mix. As it can be seen in Figure 4.21 that graphene not only enhances the load carrying capacity of the cement paste but exhibited more ductile behaviour as compared to M0

(Table 4.25). The maximum increase in strain was 113.5 % observed for the G3M3 mix as compared to M0. The stress-strain curve for G1 type is given in Figure 4.21 (a). For G1M3 specimen with a small amount of graphene compressive stress was enhanced by 10.6% and the maximum strain was increased by approximately 47%. Compressive stress values for G1M10 and M0 were very close to each other, however, the ductility and compressive strain values were 53.6 % more as compared to M0. Figure 4.21 (b) shows the stress-strain curve for G2 type graphene. As the lateral size and thickness of this graphene flakes are more, therefore, it exhibits more ductile behaviour in the start. The maximum increase in a compressive strain of 73% was noted for G2M5 in contrast to control mix. For G2M10 mix due to more amount of graphene flakes agglomerates structures easily formed which reduce the ductility value. As average thickness of G3 flakes is twice of G2, hence it showed more ductile behaviour. G3M3 determined the maximum compressive strain values amongst all mixes. However, due to increase in agglomerate structures for G3M5 and G3M10 mixes a decrease in strain value was found. G3M10 mix exhibits the maximum compressive stress and strain values amongst the M10 mix. The results of this study were further compared to the available stress-strain curve of graphene-oxide based cement paste, which is derivative of graphene (Pan et al., 2015). Pan et al. (2015) studied the cement paste containing 0.05% of graphene oxide and reported significant improvement of about 19% in compressive strength compared to control specimen. They suggest that due to the presence of graphene oxide, propagation of micro-cracks was delayed and result as increased in strain capacity. In short, the increase in compressive strength and compressive strain may be attributed to the higher strength of graphene, increased hydrated product, template effect, and crack bridging by graphene flakes (Cao et al. (2016))

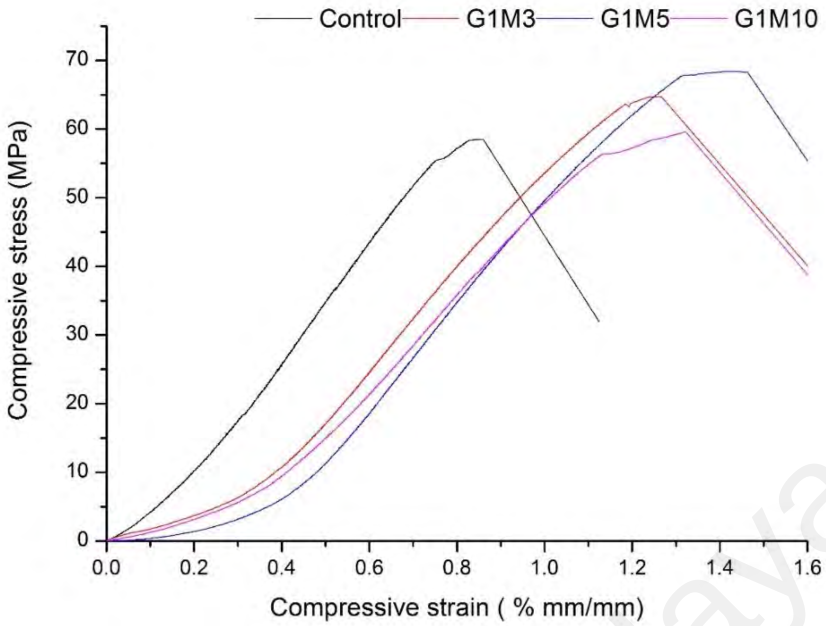

(a) G1-cement mix

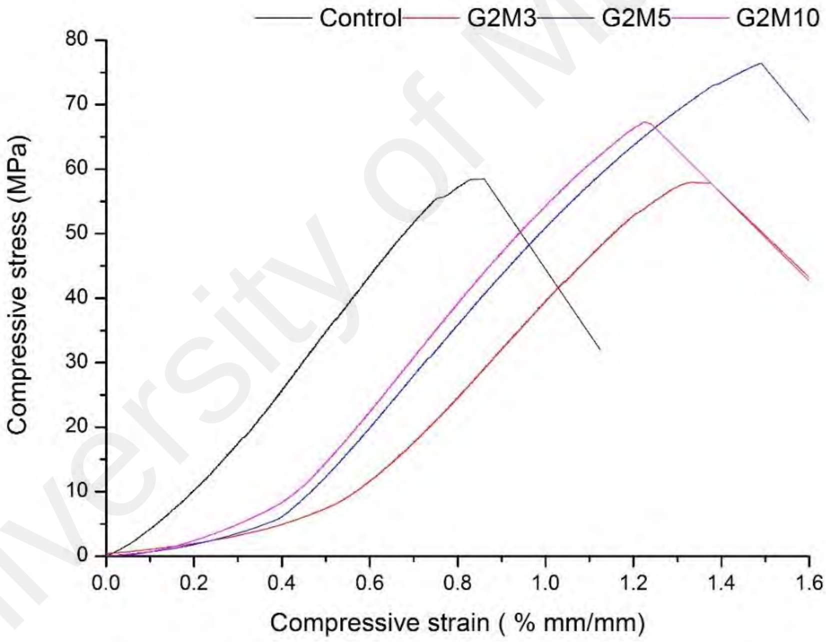

(b) G2-cement mix

**Figure 4.21: Continued**

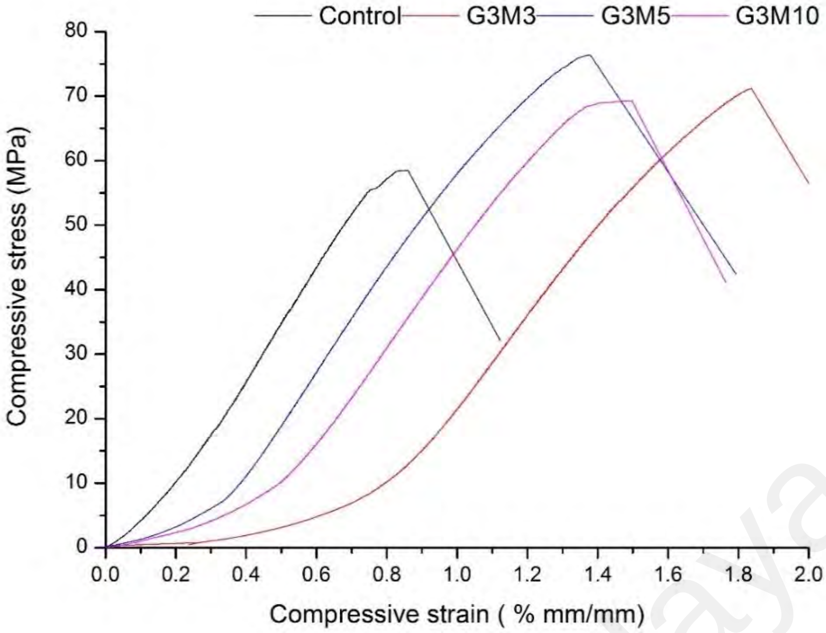

(c) G3-cement mix

**Figure 4.21: Effect of percentage of graphene on stress-strain curve of cement composite.**

Later on, a comparison has been drawn amongst the stress-strain curve of various graphene types. As G3 has more thickness of graphene flakes, therefore, it observed maximum compressive strain values. G3M3 mix has the maximum compressive stress and strain value as presented in Table 4.25. It was observed that M5 mixes (containing 0.05% of graphene) obtained the optimum increase in compressive strength of graphene-cement composites. For M10 mixes a drop in compressive strength was noted. It was due to an excessive amount of graphene content, which formed agglomerates in cement mixes. It leads further to the formation of voids and non-uniform distribution of graphene content in cement paste. Thus, it can be concluded that flake thickness and size play an important role for an increase in compressive strain and compressive stress of graphene cement composite.

### 4.7.4 Influence of Graphene on Growth of Cracks

Generation and growth of cracks for the M0 sample were identified using FESEM images as shown in Figure 4.22 (a). These are the nano size cracks which becomes later micro size cracks without any interference and play their role in failure mechanism of material. Graphene flakes successfully interrupt these cracks and stop their growth at nanoscale level and provide a great obstacle to the continuity of the cracks. As can be seen in Figure 4.22 (b) that the graphene is blocking the crack in G3M10 specimen. Furthermore, Figure 4.22 (c) and Figure 4.22 (d) explain this phenomenon more clearly that graphene flakes are holding the microcracks and preventing their further growth. Longitudinal growth of cracks is highlighted using green lines and location of graphene in red circles. Cracks were discontinued and deflected due to the presence of graphene flakes. The backscattered image was used to confirm the presence of graphene for G3M10 specimen in Figure 4.22 (d). Therefore, G3M10 sample shows the more ductile behaviour and enhanced compressive strain as compared to the mix M0. Similar phenomena were observed for G2 and G1 mixes in Figure 4.22 (e) and Figure 4.22 (f). Graphene flakes successfully provide the hindrance to the propagation of cracks. The thickness of graphene flakes plays an important role during the crack bridging phenomena. Pan et al. (2015) made the comparison of crack patterns for plain and graphene-oxide based cement composite. They found that in plain cement cracks were passing straight through the dense hydrated product. However, in graphene oxide cement paste cracks were fine and discontinued. Therefore, it can be summarized that graphene flakes deflected the crack pattern, make them fine, discontinue and provide hindrance in their growth, which resulted in enhancing the ductility and compressive strength of the graphene cement composite.

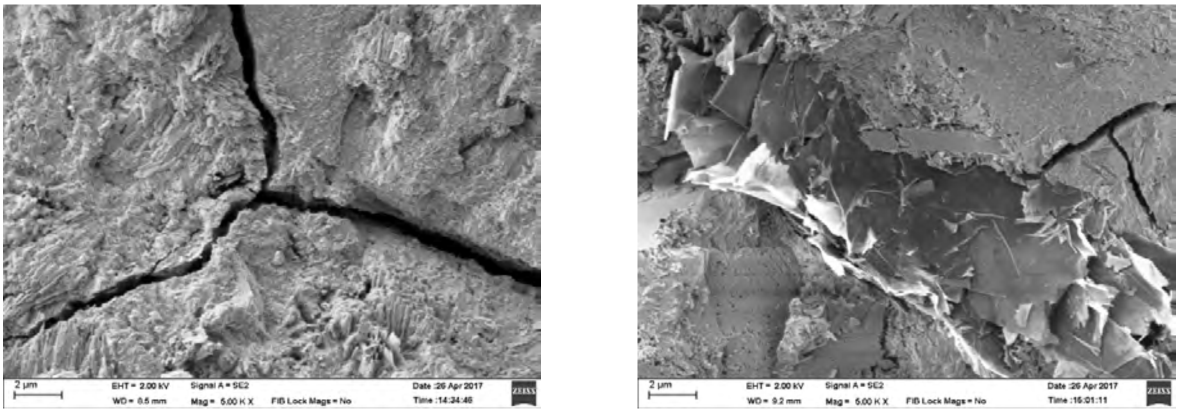

(a) Crack propagation in control specimen

(b) blockage of the cracks by graphene in G3M10

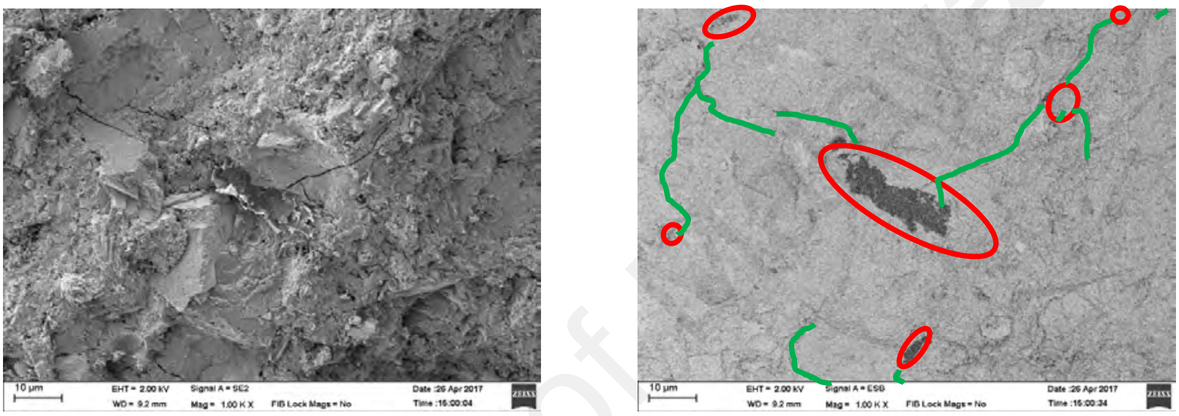

(c) crack bridging phenomena by graphene in G3M10

(d) backscattered electron image to identify the graphene in (c)

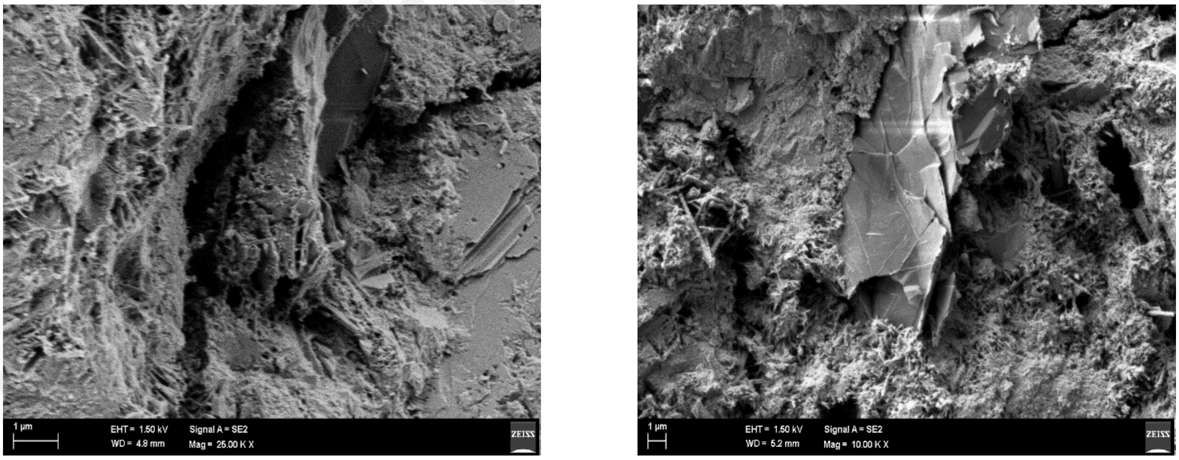

(e) blockage of the cracks by graphene in G2M3

(f) blockage of the cracks by graphene in G1M10

**Figure 4.22: Effect of graphene on propagation of cracks.**

## 4.8 Electrical Resistivity Values of Graphene Cement Composite

In this section, results related to the electrical properties of graphene cement composite will be discussed. Which is mainly based on the fractional change in resistance (FCR) of the specimens when being subjected to compressive loading. Furthermore, the comparison between different specimens' results will be made. Last but not least, the piezoresistive and conductive mechanism of the cementitious nanoparticles composite will also be discussed in the last part of this section. Piezoresistive properties of control specimen and graphene-cement composite samples were investigated by using the four-probe method. Electrical resistivity for unequal spacing between the probes was calculated by using Equation (2.12) and presented in Table 4.25. It was noted that the electrical resistivity value for G1M3 sample at maximum compressive load was 67.8 % less as compared to M0. Graphene-cement composites containing G1 type showed very small electrical resistivity values as compared to G2 and G3 type (Table 4.25). The overall reduction in electrical resistivity values for G1, G2 and G3 mixes at maximum compressive load were recorded as 60%, 33% and 24% respectively as compared to control mix. Therefore, it can be said that surface area of graphene plays an important role in investigating the piezoresistivity characteristics of graphene-cement composite mixes.

The relationship between the fractional change of resistance in percentage and the normalized compressive load were shown in Figure 4.23. Figure 4.23 (a) presents the response of G1 type cement mixes. Maximum FCR (%) values were observed for G1M5 and G1M3 specimens at maximum normalized compressive load and found 2.72 and 2.44 times of control specimen respectively. It can be noted that G1M3 mix determines the fractional change in resistance more rapidly, however, G1M5 mix determined the FCR values more precisely after 40% of applied maximum loading as compared to the G1M3 mix. Due to the more agglomerates, the response of G1M10 mix was less as compared to other mixes of G1 type. Figure 4.23 (b) and Figure 4.23 (c) showed the variation in FCR values as compared to normalized applied compressive loading for G2 and G3 type. It was observed that with increase in graphene content more agglomerates structures formed which results in less sensitivity of the composite material. As the surface area of graphene flakes was reducing the electrical resistivity response is becoming closer to the plain cement mix. Average thickness and lateral sizes of graphene flakes have a very small role in conducting the electricity values. Therefore, it can be said that piezoresistive properties are related to the dispersion, uniform mixing and surface area of graphene flakes.

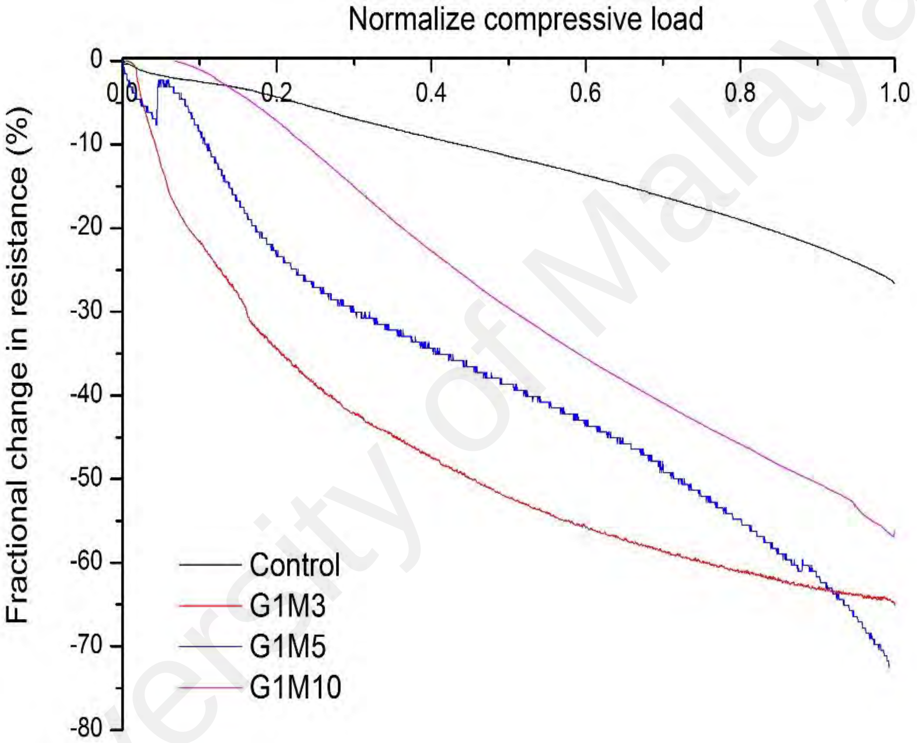

(a) G1-cement mix

**Figure 4.23: Continued**

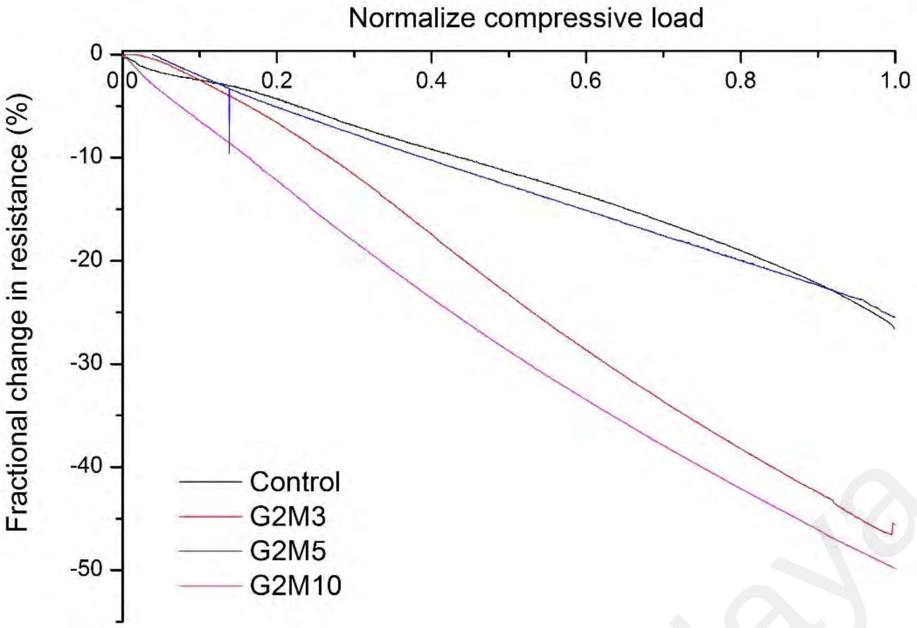

(b) G2-cement mix

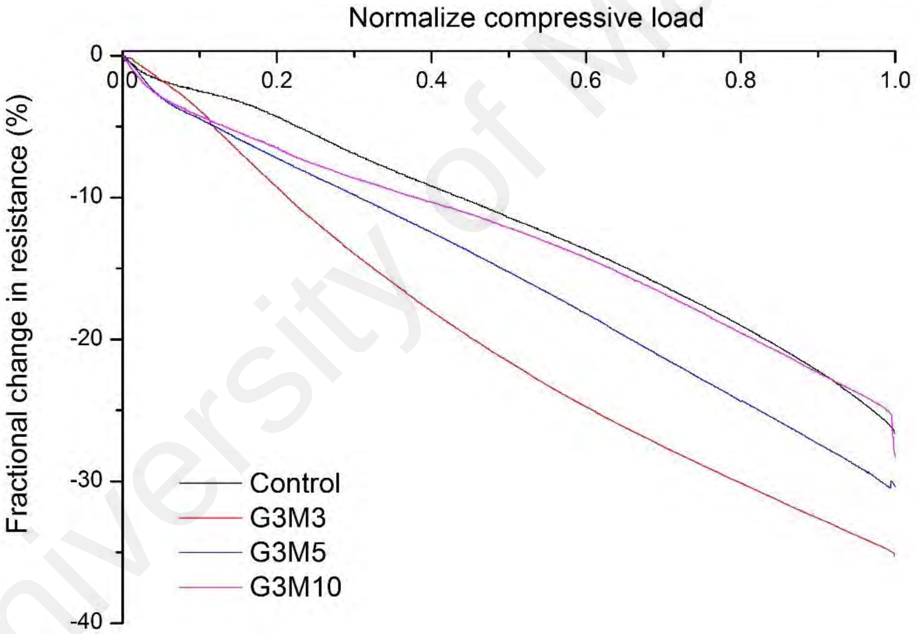

(c) G3-cement mix

**Figure 4.23: Fractional change in electrical resistance against the normalized compressive loading in graphene-cement composite.**

Figure 4.24 shows the effect of various graphene type on piezoresistive characteristics of cement composites. As the surface area of G2 and G3 was less, therefore, the maximum FCR values against normalized compressive load for G2 and G3 mixes were less as compared to the G1 mix. Figure 4.24 (b) displayed that FCR curves of G2M5 and G3M5 were similar to the control mix. However, G1M5 significantly behave differently due to more surface area. In Figure 4.24 (b) a small vertical drop was observed for G2M5 mix and the vertical shift was noted for the G1M5 specimen. For G2M5 specimen vertical drop in FCR curve may be attributed to the occurrence of some compressive elastic crack due to which an instinct in FCR value was noted. After that, the material behaves uniformly. For G1M5 specimen vertical shift in the FCR curve was related to removal of some small portion of the specimen due to tensile crack. As the material broke it creates the gap due to which electrical resistivity values increase and the vertical upward shift was found in the FCR curve.

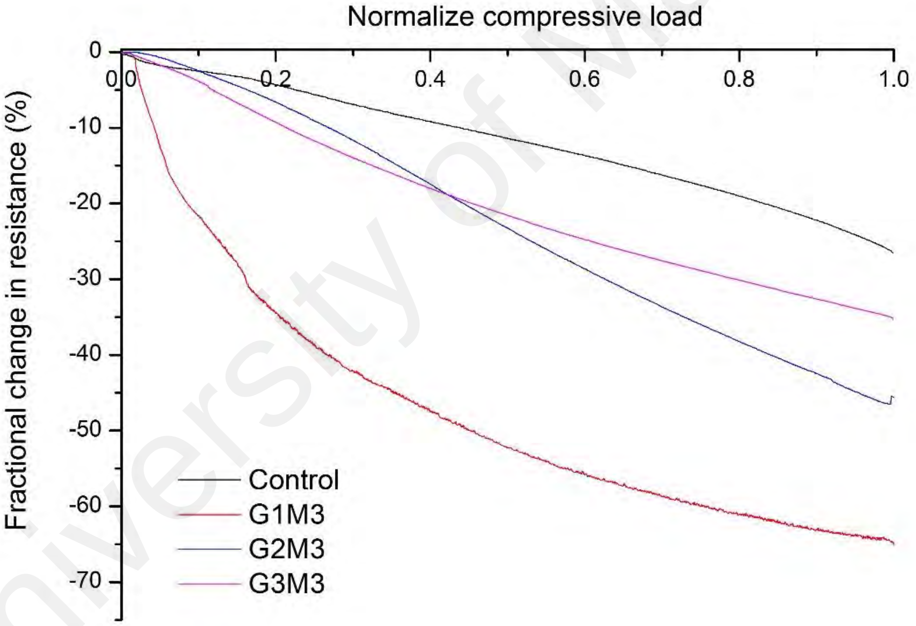

(a) M3 mixes

**Figure 4.24: Continued**

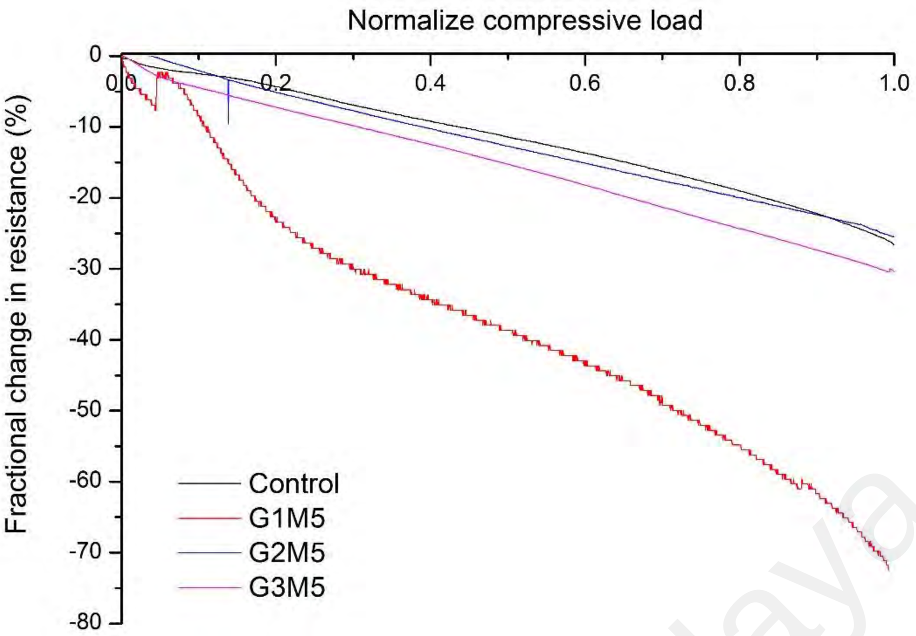

(b) M5 mixes

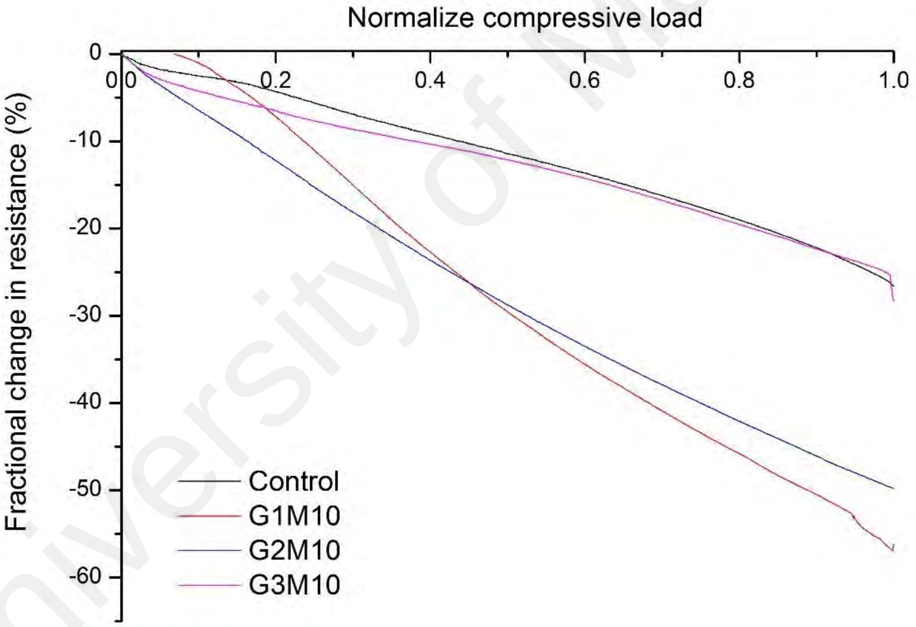

(c) M10 mixes

**Figure 4.24: Influence of graphene type on fractional change in resistance against the normalized compressive loading.**

To elaborate and emphasize the significance of graphene mix, G1M3 results were further compared to the results of two literature studies (Li et al., 2004a, 2006a). Li et al. (2004a) investigated the self-monitoring capability of cement mortar containing nano $Fe_2O_3$. They observed that fractional change in resistance is the key factor for self-sensing instead of resistivity itself. Li et al. (2006a) investigated the strain sensing characteristics of carbon black filled cement composite. They observed the linear relationship between the fractional change in resistivity and compressive strain. It is important to mention here that FCR curve was considered after 20% of normalizing compressive loading. It was done primarily to avoid the response of shrinkage, tensile and elastic cracks. As it can be seen in Figure 4.25 that the control cement mix as determined by Li et al. (2004a) showed a very low fractional change in resistance. However, the addition of 3% nano $Fe_2O_3$ and 15% of Carbon Black (CB) provided a more fractional change in resistance i.e. strain sensing characteristics. It can be seen that due to high electrical transport characteristics of graphene, G1M3 sample in a better way correlates the FCR values with NCL at each point.

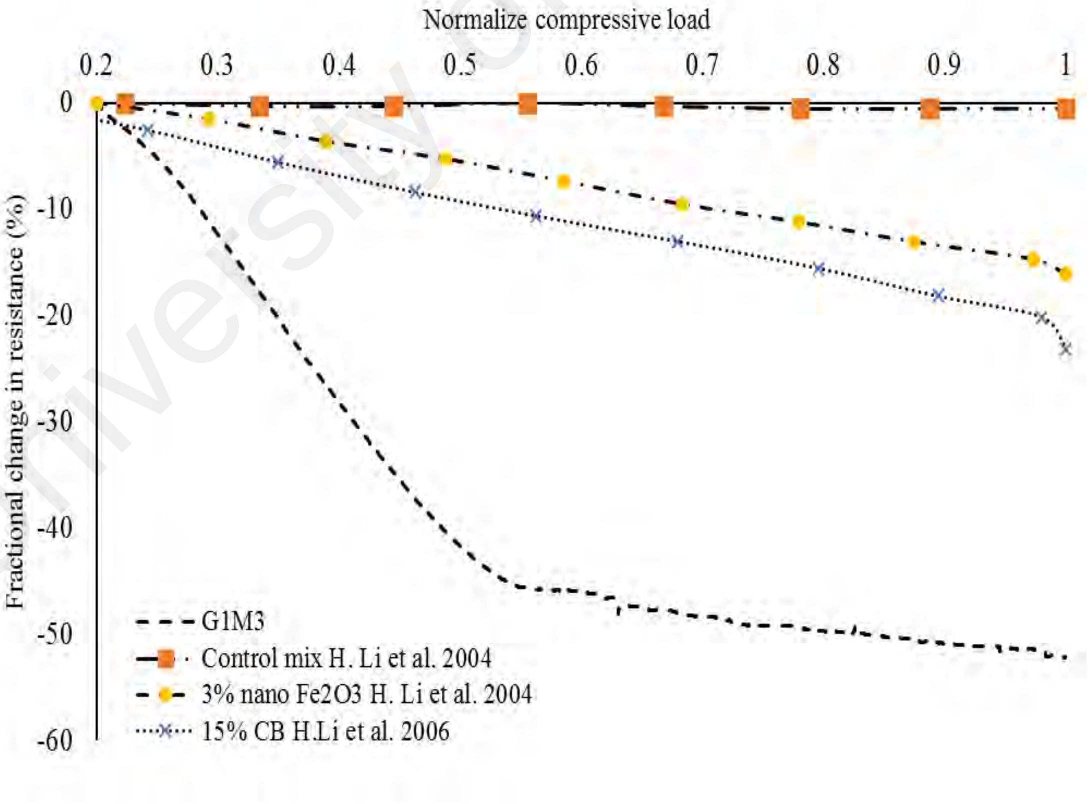

**Figure 4.25: Fractional change in resistance against normalized compression load for various samples.**

## 4.9 Application of Graphene Cement Composite in Laboratory

As graphene is very costly material, therefore, it is very difficult to use the graphene-cement composite material in mega projects instead of plain cement material. However, self-sensing properties of graphene cement composite can be used to provide a sustainable health monitoring of the concrete structures. For this purpose, samples of the graphene-cement composite with dimension 40 x 40 x 160 mm were placed in the real concrete structures. As G1M3 mix outshine the electrical resistivity and fractional change in resistance values therefore, only G1M3 mix was used to evaluate the practical application and self-sensing characteristics of the graphene-cement composites in real structures.

### 4.9.1 Reinforced Beam Subjected to Flexural Loading

In order to strengthen this viewpoint and show its practical application, full-length RC beam was tested in the laboratory by placing G1M3 specimen at the time of casting. This beam was subjected to flexural loading and due to applied loading cracks were generated in the region of the maximum bending moment. Figure 4.26 shows the fractional change in resistance of G1M3 specimen in RC beam. It can be seen that FCR values varied with increase in the applied loading on the beam and a sharp response was noted at the time of beam failure. As the beam was subjected to the flexural loading, therefore, resistance values were positive. The inset figure (enlarged view) in Figure 4.26 showed that with the increase in flexural loading, the fractional change in resistance values were also increasing. It is important to mention here that this response is not linear, however, due to the occurrence of damage and propagation of cracks, the FCR values varied as shown in inset figure (enlarged view of Figure 4.26). It was observed that at 22kN load, a sudden drop in electrical resistivity value occurred. The possible reason is the presence of tensile cracks in RC beam. Initially, tensile cracks started to occur and electrical resistivity values increased linearly. Thereafter, the steel reinforcement started to carry stresses and the significant variation in resistance values was noted in the G1M3 specimen (Figure 4.26). This effect was more significant as the specimen (GNP cement based composite) was placed in the tensile region i.e. just above the reinforcement bars. Finally, at the failure stage abrupt increase in FCR values was observed, which showed the widening and irreversible crack opening inside the beam. Hence, the structural member is not capable of carrying the additional load.

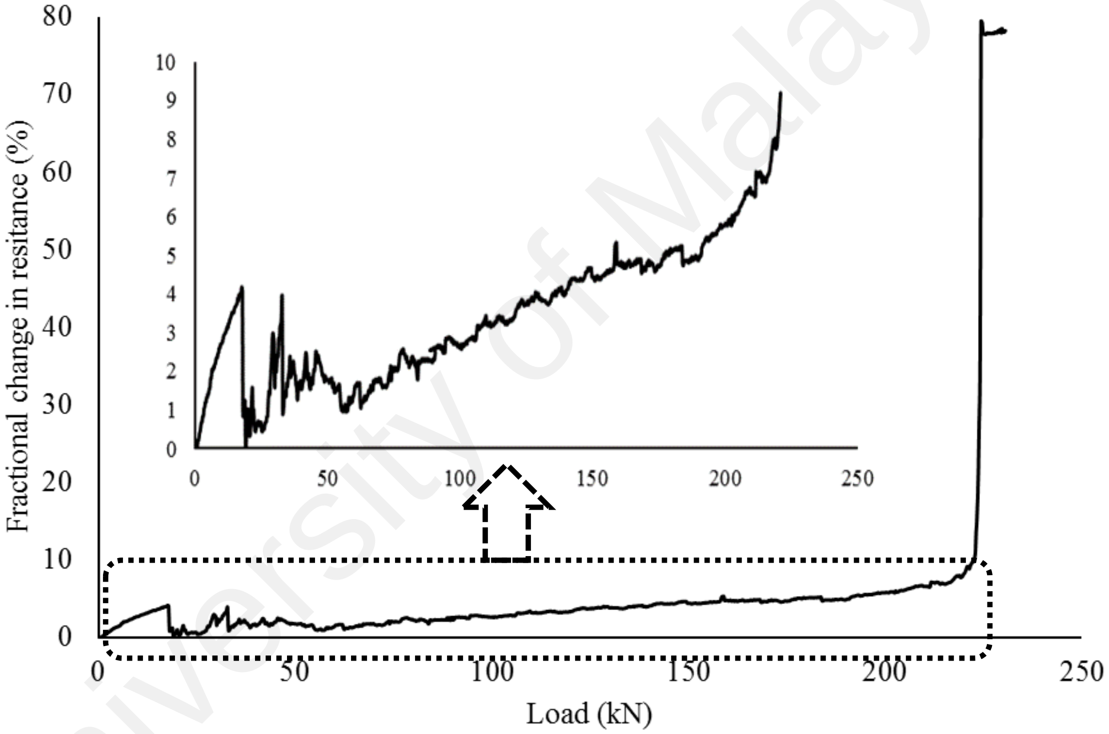

**Figure 4.26: Fractional change in resistance of G1M3 specimen against applied flexural loading on the RC beam.**

A comparison of produced strain against the applied load in reinforcement bars and graphene-cement composite i.e. G1M3 sample was shown in Figure 4.27. In reinforcement bars, the strain produced was linear and slight variation was observed from 60 kN to 100 kN load as shown in Figure 4.27 (a). This variation is very minute and can be neglected for the reinforcement as steel bar was in the linear and elastic region. The

G1M3 sample also showed variation in strain from 60 kN to 100 kN load as marked in Figure 4.27 (b). However, in comparison to reinforcement bar, the variation was large and the strain values for the G1M3 sample decreased significantly. This may be related to the redistribution of stresses in the RC concrete beam. Similarly, when the applied loading exceeded 200 kN, the reinforcement bar showed significant variance in strain values. At the same point, an increase in strain values in graphene cement composite sample was noted. It may be related to crushing of concrete in RC concrete beam.

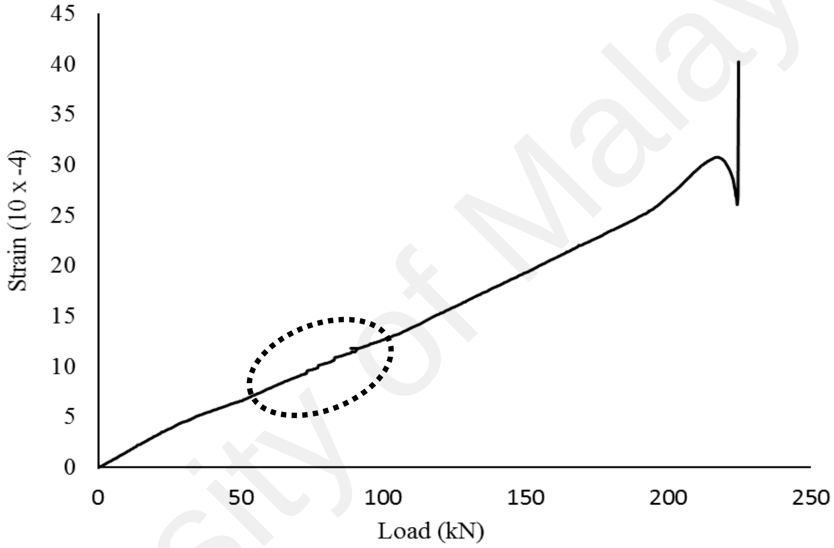

(a) Reinforcement bar

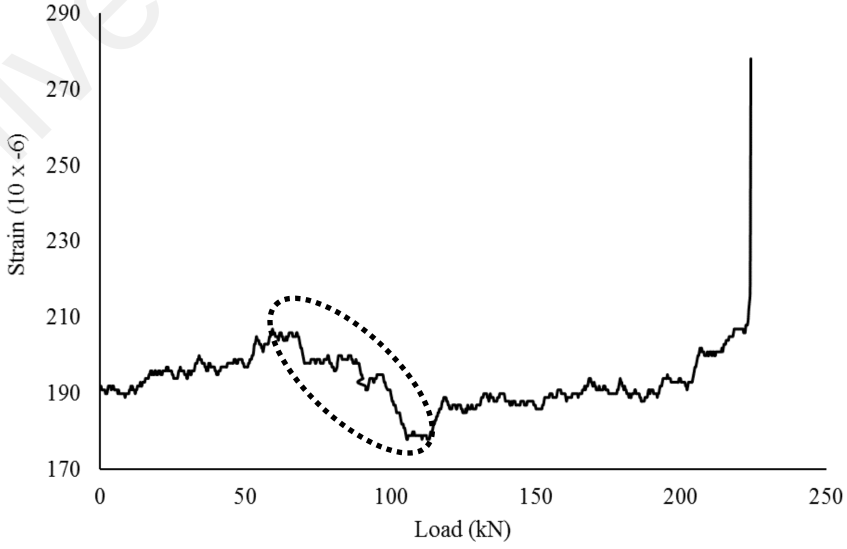

(b) Graphene-cement composite specimen (G1M3)

**Figure 4.27: Strain produced by applied flexural load.**

### 4.9.2 Reinforced Concrete Beam Subjected to Various Damage Levels

Figure 4.28 showed the response of G1M3 specimen against various damage levels. These damage levels were induced intentionally in the RC beam. At different controlled damage levels, cracks propagation was highlighted and electrical resistivity (ER) values of graphene cement composite specimen were noted. The purpose of inducing these controlled damage levels in RC beam was to monitor the characteristics of graphene cement composite specimen for damage memorization and damage-sensing. Damage-sensing is better and realistic approach as compared to stress or strain sensing. Damage generation is irreversible on unloading however, strain can be reversible on unloading provided that specimen is within elastic range. Therefore, real-time and continuous monitoring is not required in case of damage-sensing.

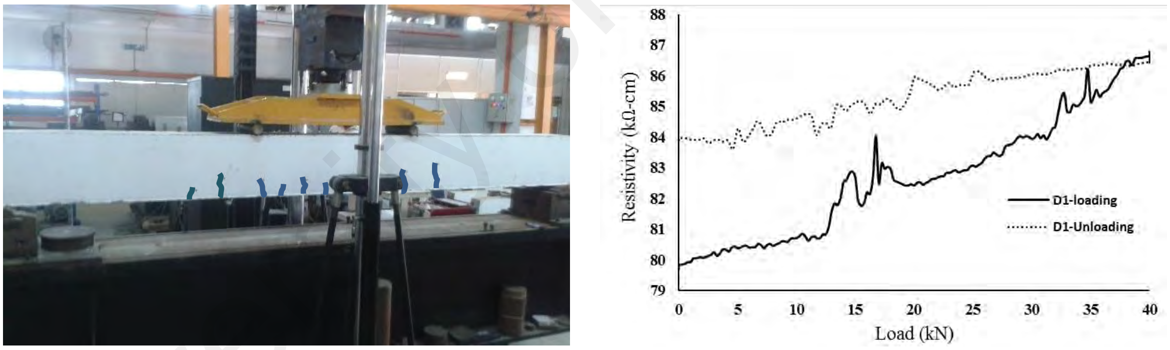

(a) Damage level 1

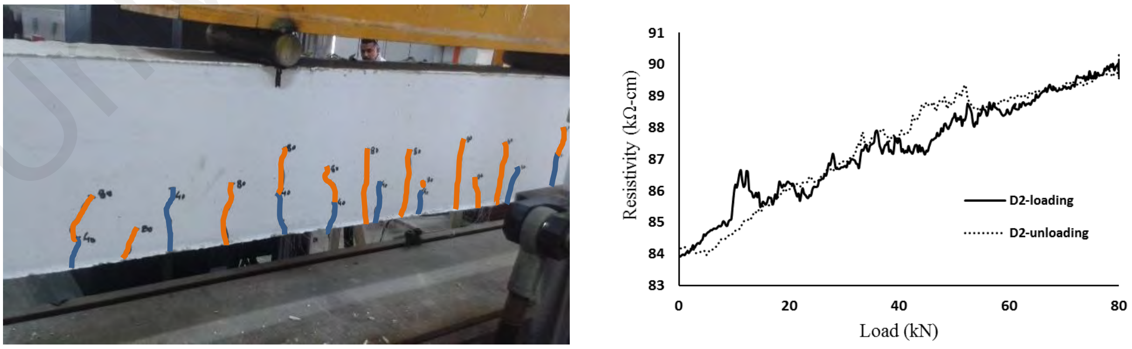

(b) Damage level 2

**Figure 4.28: Continued**

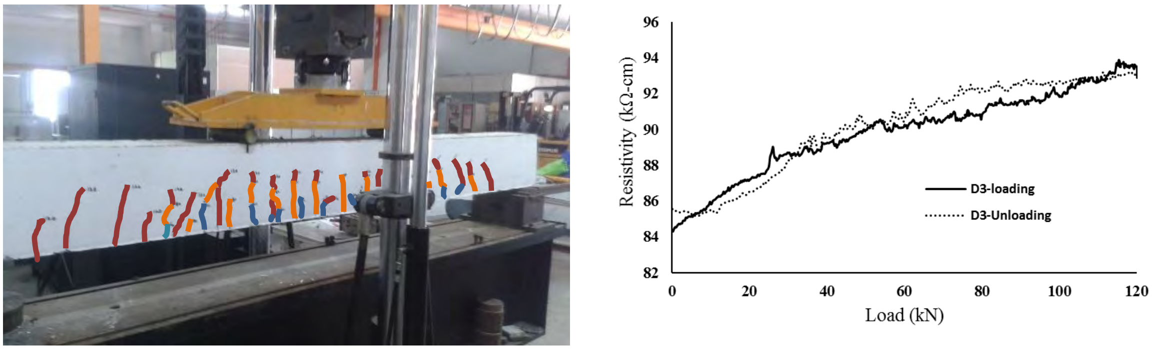

(c) Damage level 3

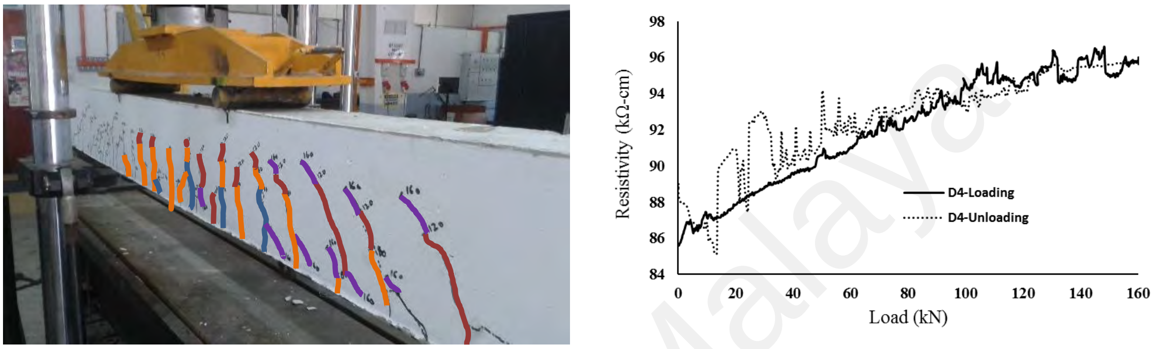

(d) Damage level 4

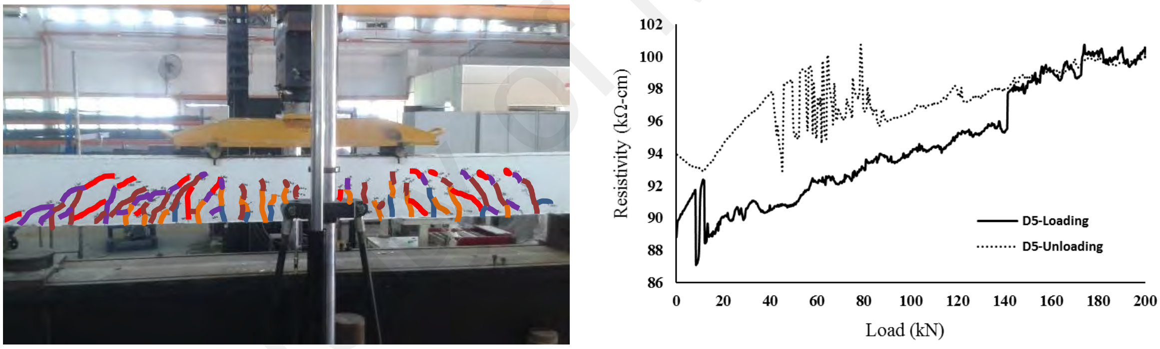

(e) Damage level 5

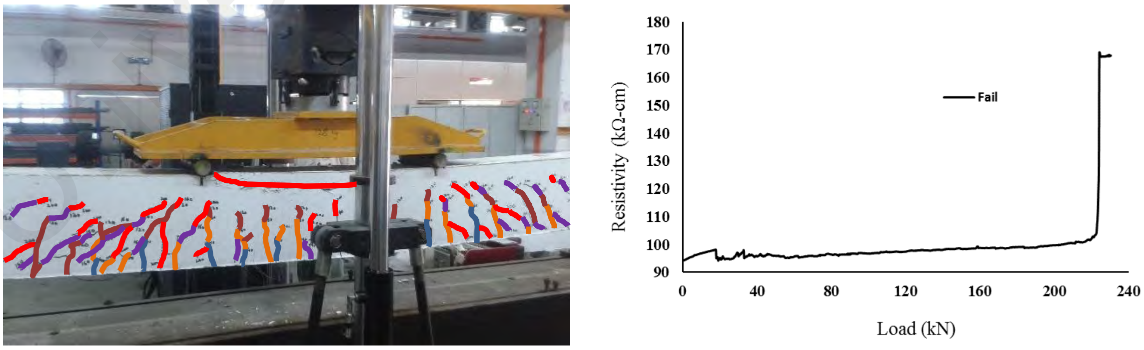

(f) Failure stage

**Figure 4.28: Resistivity values corresponding to different damage levels.**

Electrical resistivity values were plotted against the loading and unloading cycles of the beam in Figure 4.28. Figure 4.28 (a) showed the ER values for damage level 1.

Hairline cracks were generating in the RC beam as marked in Figure 4.28 (a). It was clearly observed that ER values at zero load are different for both loading and unloading curves. Furthermore, in damage level 2 crack length and width was increased as marked in Figure 4.28 (b). ER values were overlapping for both loading and unloading cycles. However, for decreasing load curve the values of ER were higher as compared to increasing loading cycle. For damage level 3, diagonal shear cracks generated in RC beam as shown in Figure 4.28 (c). Moreover, length, width and depth of existing cracks also enhanced. For damage level 4 the crack length progressed in reverse direction as well as highlighted in Figure 4.28 (d). During unloading cycle, the loading rate was 66.67% high as compared to increasing loading rate. Due to this reason, the values of ER for unloading curve fluctuate excessively. Furthermore, this fluctuation also highlights that internally damages are generating in RC beam, and bong matrix between hydrated cement products is breaking. For damage level 5 the density of cracks also increased and new diagonal cracks near the supports were also observed as shown in Figure 4.28 (e). Additionally, cracks are also converging and forming the bigger and widen cracks, therefore, ER pattern for both loading and unloading curve is significantly different as compared to other damage levels. After applying 100 % design loading, the RC beam was further subjected to flexural loading until failure stage. Failure load was higher as compared to design load due to various factors of safety. An abrupt increase in ER pattern was noted at failure stage due to the presence of widened cracks in both beam and G1M3 specimen as seen in Figure 4.28 (f). Thus, it was concluded that after every damage level electrical resistivity values were increased and can be used to identify the structural health of the RC beam.

### 4.10 Advantage of Graphene Cement Specimen

In this section, compatibility and comparison of graphene-cement (GC) specimen with the well-known non-destructive test (NDT) methods has been made. Selection of any methods based on available time, budget, simplicity and reliability therefore, some methods are preferred over others. Ideally, the adaptable method should capable to observe and detect all important defects and anomalies in the concrete structures. Therefore, preference of any method is based on the yielding of the information. Reporting and observing the damages is one of the major problems. For this purpose, damages based on periodic inspection has been classified. The detailed description of damage levels is given in terms of numbering system which provide better information and less dependence on inspector judgement. Elaboration of each damage level based on crack lengths, spalling of concrete cover, applied loading as a percentage of design load, support settlement, titling of foundation (due to the settlement of subsoil or erosion of soil) and reinforcement of corrosion is given in Table 4.26.

**Table 4.26: Detailed description of damage levels.**

| Level | Crack lengths | Spalling | Support settlement | Loading (% of design loading) | Tilting of foundation | Reinforcement corrosion |
|---|---|---|---|---|---|---|
| 0 | None / 1 µm | None | 100 µm | 20% | 0° | None |
| 1 | Partial / 100 µm | None | 1mm | 40% | 0.05° | Some stains on surface |
| 2 | Some/ ≤ 1mm (NDT limit) (Vasudevan et al., 2001) | Partial bulge outward | 50 mm | 60% | 0.1°(Realized) (Deroeck et al., 2000) | Partially stains |
| 3 | Fair amount / ≤10 mm | Partial spalling | 95 mm (Realized) | 80% | 0.3° | Fair amount of stains |
| 4 | Large amount / ≤100 mm | Fair amount of bulge and spalling | 200 mm (Maximum Allowable) (Deroeck et al., 2000) | 100% | 0.5° (Max Allowable) | Fair amount of rusts |
| 5 | Large / ≤1m | Large amount of bulge and spalling | ≥ 200 mm | >100% | ≥ 0.5° | Large amount of rusts |

Furthermore, a flow chart has been proposed for the health monitoring of concrete structures (Figure 4.29). After classifying the damage levels in Table 4.26, several suitable non-destructive test methods were suggested for detailed investigation of the concrete structures. Since maintenance activities are the routine interventions which are applied to the structure to preserve the structural performance and health. Therefore, subsequently, corrective measures are also proposed to recover the lost strength. It is worth important to mention here that GC specimen successfully determined and identified the response of structural member at each damage level. One of the major advantages of GC specimen is its compatibility with concrete materials. It is placed in the concrete member at the time of casting of concrete and remains intact for the whole life of the structure. However, other methods are lacking in this respect. GC specimen also has the advantage over the other methods in terms of the financial aspect. The cost of 5 g of GNPs as per Graphene Laboratories, Inc. USA is 50 USD and 25 samples can be casted of the G1M3 specimen using 5 grams of GNP.  Hence, this G1M3 specimen can be used in an efficient and economical way to predict the damages in concrete structures.

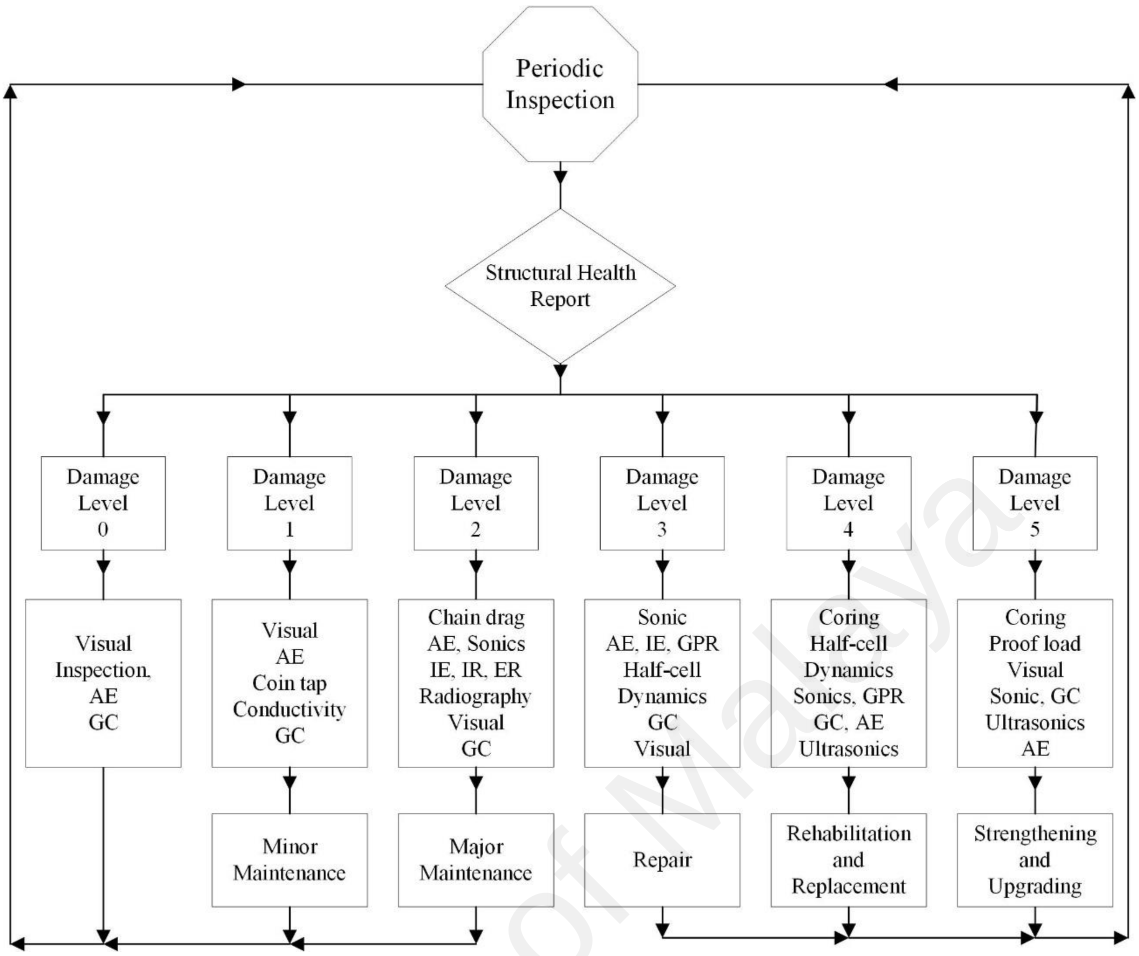

**Figure 4.29: Schematic layout of structural health monitoring procedure, selection of method and potential remedial measure.**

One of the common misperception about the usage of nanomaterials is hazardous nature. For this purpose, material safety data sheets were obtained. Physically and environmentally it is not classified as hazards as per Globally Harmonized System (GHS) of classification. However, it may be harmful if swallowed and can cause eye irritation and respiratory irritation. Therefore, Personal Protective Equipment (PPE) and the usual precautionary measures for handling chemicals should be followed. Furthermore, contact with eyes, skin, food-stuff during practice should be avoided and wash hands after usage.

## 4.11 Conclusion

Three (3) types of graphene have been used in this research which were based on surface area, flake thickness and lateral size were used in this research. It was found that flake thickness and surface area have an important role in the dispersion of graphene flakes in aqueous solution. G1 type with high surface area and least flake thickness showed the highest absorption values in UV-vis spectroscopy results. It was also noted that dispersion efficiency was greatly enhanced by using ultrasonication, superplasticizer and magnetic stirring. Experimental results concluded that magnetic stirring of 40 min in combination with ultrasonication gave the optimum results for all graphene types. Furthermore, TGA results determined that more amount of CSH gel was found followed by portlandite amount. Moreover, hydrated products were found more for G2 type graphene having a high surface area as well as more lateral size. It was observed from TGA data that graphene flakes significantly enhanced the growth of hydrated cement product at an early age. From FESEM images, it was determined that hydrated cement product grows over the graphene flakes, and found compact and durable due to the ordered growth. As a result, mechanical properties of graphene cement composite material enhanced as compared to plain cement specimen.

It was also found that graphene increased the yield stress values of the graphene cement composite paste. Due to the high surface area and average thickness of graphene flakes, overall water demand of the system was increased. Furthermore, graphene flakes formed the agglomerates in the cement paste and entrapped some water molecules inside it. Hence, the free available water content was reduced, which provoked the yield stress values for composite materials. Maximum yield stress values were found for G3 type graphene having more flake thickness. Moreover, the plastic viscosities were found in correlation with yield stress. In Herschel-Bulkley model, the power rate index values were found less than 1 indicating the shear thinning flow behaviour, however, for G3 type with higher content shear thickening behaviour was recorded. Power rate index values were found increasing with the increase in graphene content. It was found that Bingham model determined the lowest standard error values and provided the best fitted mathematical model to the flow curve of graphene cement composite. Furthermore, the dependence of several factors on the rheological properties of cement paste was determined as well. Yield stress values were enhanced with the increase in shear rate cycle range and resting time, however, reduced with superplasticizer. Likewise, parallel plates estimated the higher yield stress values due to less gap and more spread diameter, however, provided the results with realistic approach. Plastic viscosity was found to be dependent on various variables. It increases with the increase of graphene content, resting time and reduces with superplasticizer and high shear rate cycle range. Due to the settlement of suspended particles in cement paste sample, the parallel plates estimated the higher values of plastic viscosities as compared to concentric cylinders due to the settlement of suspended particles in cement paste sample.

Mechanical properties were investigated for graphene cement mortar. For one-day specimen, maximum increment was found as 79% in compressive strength. High surface area of graphene contributed towards the growth of hydration products in an ordered way, while thickness of graphene plays its role in cracks bridging action and blocking the propagation of cracks. Overall 38.1 % increment was noted for flexural strength at 28-day of casting for the G2M10-M mix. Furthermore, overall workability of the cement paste was reduced by addition of graphene in the cement paste and maximum of 9.3 % reduction was noted for flow diameter values of graphene cement paste samples. 30.5 % increase in compressive strength values of graphene cement paste was noted. Hardened density decreased with the incorporation of graphene and 5.4% reduction was noted for

G2M10 mix design. The compressive strain was intensely increased and 113.5% increment was found as compared to control mix. Graphene cement composite showed the ductile behaviour due to the influence of graphene. It was related to blockage of cracks at micro level by the graphene flakes. Graphene flakes influenced the electrical resistivity values of the composites. At maximum compressive load, electrical resistivity values were calculated using four-probe method and 67.8% reduction was found in graphene cement composite specimen. Lastly, the application of graphene cement composite as a smart sensor was evaluated in reinforced concrete. The reinforced concrete beam was subjected to flexural loading and various damage levels were introduced in a concrete beam using profile loading. It was found that graphene cement composite successfully predicted the propagation of damages in RC beam.

# CHAPTER 5: CONCLUSIONS AND RECOMMENDATIONS

## 5.1 Introduction

This chapter relates the findings of the results and discussion chapter with the objectives of this research thesis. This research was performed to explore and evaluate the multifunctional properties of graphene based cement composites. The extraordinary properties of graphene flakes opened the new dimension for development of smart materials and overcoming the weaknesses of existing construction materials. Moreover, investigation of multifunctional properties provided an overview of the problems and issues related to utilization of graphene in cement based applications. In the end, recommendations and suggestions for the future research are also included.

## 5.2 Conclusions

1. Graphene flakes with the high surface area and less flake thickness have better dispersion. G1 type flakes obtained the stable and high absorbance values as compared to G2 and G3. Superplasticizer made the dispersion stable and uniform over long duration due to electrostatic repulsion, however, for thick graphene flakes (G3 type) its effect was limited. Moreover, magnetic stirring in combination with ultrasonication breaks the flocculated and agglomerated structures of graphene flakes. However, excessive magnetic stirring has negative effect on the dispersion and physical properties of graphene flakes, especially for high surface area graphene type. The optimum duration of magnetic stirring time was found to be 40 min. The results of microanalytical characterization of graphene-cement composite indicated that hydrated products in graphene cement composite were in abundance. Thermogravimetric analysis revealed the higher hydration reaction degree and percentage of calcium hydroxide in the graphene-cement composite. TGA results further found that graphene plays its role in early stage hydration. FTIR spectra

exhibited that, due to hydrated products, intensities peaks of various bands were increased and shifting of these bands suggests the chemical interaction. XRD spectra showed that more amount of calcium hydroxide was found by incorporating graphene in cement composite. The FESEM images demonstrated that hydrated cement products grow in an ordered way over the graphene flakes. Furthermore, graphene flakes with more flake thickness (G3) restrained the growth of cracks, filled up the pores at nanoscale and provide an obstacle in the continuity of cracks.

2. Rheological characteristics of the graphene cement paste samples were determined from the flow curves using a variety of rheological models i.e. Bingham model, Modified Bingham model, Herschel–Bulkley (HB) model and Casson model using parallel plate geometry. Generally, Casson model estimated the lowest yield stress values whereas, Modified Bingham models obtained the highest yield stress values. Flake thickness have strong impact on yield stress values and G3 type cement paste estimated the higher values of yield stress as compared to G1 and G2. Maximum yield stress was recorded for G3M10 mix followed by G3M5 and G3M3 which was 182%, 136% and 85% respectively more as compared to M0 mix estimated by Herschel-Bulkley model. Plastic viscosity values significantly increase with the addition of graphene. Bingham model determined the maximum plastic viscosity values followed by Modified Bingham model and Casson model. Approximately 50-107% increase in the plastic viscosity values were observed. Maximum plastic viscosity value was noted for G3M10 mix as compared to M0 mix. Power rate index values estimated by HB model were less than 1 except for G3M10 mix. Bingham model determined the lowest standard error and standard deviation values, whereas Casson model obtained the highest values. Furthermore, effect of graphene/cement ratio, shear rate range, superplasticizer, resting time and test geometries were investigated. For this purpose, G1 based cement composites were selected as it estimated the lowest standard error

values. Addition of graphene flakes results in the formation of flocculated suspension in the paste, which mainly alters the flow properties of the paste. Yield stress values increased by the addition of graphene, shear rate range and resting time, however, decreased with the addition of superplasticizer. Normally, parallel plates determined the higher values for the yield stress and plastic viscosities as compared to the concentric cylinders. Plastic viscosity values were found more for Modified Bingham model in both test geometries. Concentric cylinders estimated the lower values of power rate index as compared to parallel plate. Generally, concentric cylinders estimated the low standard error values for rheological models as compared to parallel plates. Herschel-Bulkley and modified Bingham models were found to be the best-fitted model with lowest standard error values for the concentric cylinders and parallel plates respectively. Moreover, G2 type mortar mixes obtained the maximum values in mechanical properties whereas, G3 type mixes possessed more ductile behaviour. Flow diameter of G1M10 mix was reduced by 9.3%, load carrying capacity was increased by 30% for G2M5 and G3M5 mixes and overall failure strain was increased by 113% for G3M3 mix. Flexural strength of G2M10-M mix was obtained maximum with 38 % increment. Graphene plays a significant role in early age hydration and 79% increment in compressive strength was recorded for G2M5-M specimen after 1-day of casting. Lateral size and thickness of graphene flakes significantly contributes to early age strength while, surface area of graphene flakes is prominent for both early and later age strength.

3. Four-probe method was used to determine the piezo-resistive characteristics of the graphene based cement composites specimen. At maximum compressive load, the electrical resistivity value of G1M3 specimen was reduced by 67.8%. The overall reduction in electrical resistivity values at maximum compressive load was recorded for G1, G2 and G3 mixes as 60%, 33% and 24% respectively in comparison to control

sample. The surface area of graphene flakes has a substantial effect on piezoresistive characteristics of composite specimens. Agglomeration of graphene flakes has an adverse effect on the electrical properties of graphene cement composites. Piezoresistive properties depend on the surface area and uniform dispersion of graphene flakes whereas, thickness and lateral size of graphene flakes have very minute effect. Fractional change in resistance is the key factor for investigating the self-sensing characteristics instead of electrical resistance. Furthermore, maximum FCR values were observed for G1M5 and G1M3 mixes at maximum normalized compressive load as 2.72 and 2.44 times of control specimen respectively. G1M3 sample behaved in a better way to correlate the FCR and NCL values due to high electrical transport characteristics. Moreover, G1M3 specimens estimated the FCR values more accurately and precisely.

4. G1M3 specimen was selected for the practical application of graphene cement composite specimen in concrete structures. Practical application of G1M3 specimen was investigated on the reinforced concrete beam and concrete-filled steel tube beam. It was found that fractional change in resistance values varied with the increase in the applied flexural load on the reinforced concrete beam. A sudden drop in FCR values of G1M3 specimen was noted at 22 kN load in RC beam, which is related to generation and growth of tensile cracks. Afterwards, strain values were successfully found in correlation with the G1M3 specimen and main reinforcement bar in RC beam. Furthermore, reinforced concrete beam was subjected to various controlled damage levels. Various damages were induced in graphene cement specimen to test the damage sensing and damage memorization characteristics. Damage memorization is better and realistic approach. Moreover, the graphene–cement composite specimen successfully predicted the response against crack propagation at various damage levels. At the end of every damage level and loading-unloading cycle, electrical

resistivity values increased. These electrical resistivity values can be used to identify the structural health of RC beam. Therefore, real-time and continuous monitoring is not required in case of damage-memorization. Moreover, for better understanding and simplicity of results electrical resistivity values may be recorded after 20% of normalized loading. The development cost of the G1M3 specimen is very less and have no potential hazardous characteristics.

Based on above findings, graphene cement composites provide an economical and efficient solution for monitoring the structural health of the concrete members throughout their lifespan.

## 5.3 Recommendations

Following are some of the recommendations on the basis of research findings.

1. Further research is recommended on dispersion of graphene flakes using various chemical admixtures and techniques without effecting its chemical structure.
2. Construction materials consume earth natural resources and further studies are required for development of ultra-super strong and smart material using advance nanotechnology.
3. An in-depth investigation is recommended for regulating mechanism of graphene on hydrated cement crystals at atomic level.
4. Research is further needed to investigate the response of graphene-cement smart sensor subjected to cyclic, dynamic and seismic loadings.
5. Piezoresistive characteristics of graphene-cement smart sensor at elevated temperature can further be investigated.

6. Response of GC smart sensor on the existing infrastructure can be determined. For this purpose, further work is required on the strong connection between the surfaces of GC smart sensor and existing building.

# REFERENCES

Abrishami, M. E., & Zahabi, V. (2016). Reinforcing graphene oxide/cement composite with NH2 functionalizing group. *Bulletin of Materials Science, 39*(4), 1073-1078.

Afshari, A., Frazer, D., & Creese, R. (1996). *Ultrasonic techniques for the bonding of rebar in concrete structures.* Paper presented at the Structural Materials Technology—An NDT Conference, San Diego, USA.

Agrawal, S., Raghuveer, M. S., Ramprasad, R., & Ramanath, G. (2007). Multishell Carrier Transport in Multiwalled Carbon Nanotubes. *Nanotechnology, IEEE Transactions on, 6*(6), 722-726. doi: 10.1109/TNANO.2007.907798

Alarcon, R. L., Platret, G., Massieu, E., & Ehrlacher, A. (2005). The use of thermal analysis in assessing the effect of temperature on a cement paste. *Cement and Concrete Research, 35*(3), 609-613.

Alkhateb, H., Alostaz, A., Cheng, A. H. D., & Li, X. (2013). Materials genome for graphene-cement nanocomposites. *Journal of Nanomechanics and Micromechanics, 3*(3), 67-77.

AlMuhit, B. A. (2015). Investigation on the Mechanical, Microstructural, and Electrical Properties of Graphene Oxide-Cement Composite. *PhD Dissertation*.

ASTM C 109. (1999). Standard Test Method for Compressive Strength of Hydraulic Cement Mortars (using 2-in. or [50-mm] Cube Specimens). *ASTM International, West Conshohocken, PA, 2016,.*

ASTM C 348. (2014). Standard Test Method for Flexural Strength of Hydraulic-Cement Mortars. *ASTM International, West Conshohocken, PA, 2016,.*

ASTM C 469. (2014). Standard test method for static modulus of elasticity and Poisson's ratio of concrete in compression. *ASTM International, West Conshohocken, PA, 2016,.*

ASTM C 1437. (2015). Standard Test Method for Flow of Hydraulic Cement Mortar. *ASTM International, West Conshohocken, PA, 2016,.*

Aunkor, M., Mahbubul, I., Saidur, R., & Metselaar, H. (2015). Deoxygenation of graphene oxide using household baking soda as a reducing agent: a green approach. *RSC Advances, 5*(86), 70461-70472.

Balandin, A. A., Ghosh, S., Bao, W., Calizo, I., Teweldebrhan, D., Miao, F., & Lau, C. N. (2008). Superior thermal conductivity of single-layer graphene. *Nano Letters, 8*(3), 902-907.

Barcelo, L., Kline, J., Walenta, G., & Gartner, E. (2014). Cement and carbon emissions. *Materials and Structures, 47*(6), 1055-1065. doi: 10.1617/s11527-013-0114-5

Barnes, H. (2000). A handbook of elementary rheology, University of Wales Institute of Non-Newtonian Fluid Mechanics, Aberystwyth, First published 2000: ISBN 0-9538032-0-1.[75] AC Thomas, analyse du comportement des élastomères, Thèse de doctorat.

Barnes, H., & Walters, K. (1985). The yield stress myth? *Rheologica Acta, 24*(4), 323-326.

Bensted, J., & Varma, S. P. (1974). Some applications of infrared and Raman spectroscopy in cement chemistry. Part 3-hydration of Portland cement and its constituents. *Cement Technology, 5*(5), 440-445 448-450.

Bernal, S. A., Juenger, M. C. G., Ke, X., Matthes, W., Lothenbach, B., De Belie, N., & Provis, J. L. (2016). Characterization of supplementary cementitious materials by thermal analysis. *Materials and Structures, 50*(1), 26. doi: 10.1617/s11527-016-0909-2

Bessaies, B. H., Baumann, R., Schmitz, M., Radler, M., & Roussel, N. (2016). Organic admixtures and cement particles: Competitive adsorption and its macroscopic rheological consequences. *Cement and Concrete Research, 80*, 1-9.

Bingham, E. C. (1922). *Fluidity and plasticity* (Vol. 2): McGraw-Hill Book Compny, Incorporated.

Birchall, J., Howard, A., & Kendall, K. (1981). Flexural strength and porosity of cements.

Boehm, H., Clauss, A., Fischer, G., & Hofmann, U. (1962). *Surface properties of extremely thin graphite lamellae.* Paper presented at the Proceedings of the Fifth Conference on Carbon.

Bose, S., Kuila, T., Mishra, A. K., Kim, N. H., & Lee, J. H. (2012). Dual role of glycine as a chemical functionalizer and a reducing agent in the preparation of graphene: an environmentally friendly method. *Journal of Materials Chemistry, 22*(19), 9696-9703.

BS EN12350-2. (2009). Testing fresh concrete-Part 2: Slump test. *British Standards Institution, London,16*.

BS EN 1015-10. (1999). Methods of test for mortar for masonry-Determination of dry bulk density of hardened mortar. *British Standards Institution, London,16*.

BS EN 5075-1. (1985). Concrete admixtures. Specification for accelerating admixtures, retarding admixtures and water reducing admixtures. *British Standards Institution, London,16*.

BS EN 5168-05. (2005). Glossary of rheological terms. *British Standards Institution, London,16*.

BS EN 12390-3. (2000). Testing Hardened Concrete: Compressive Strength of Test Specimens. *British Standard Institution, London,16*.

Cao, M. l., ZHan, H. x., & ZHan, C. (2016). Effect of graphene on mechanical properties of cement mortars. *Journal of Central South University, 23*(4), 919-925.

Casson, N. (1959). *A flow equation for pigment-oil suspensions of the printing ink type*: Pergamon press.

Chen, D., Li, L., & Guo, L. (2011). An environment-friendly preparation of reduced graphene oxide nanosheets via aminoacid. *Nanotechnology, 22*(32), 325601.

Chong, K. P., Carino, N. J., & Washer, G. (2003). Health monitoring of civil infrastructures. *Smart Materials and Structures, 12*(3), 483.

Chuah, S., Pan, Z., Sanjayan, J. G., Wang, C. M., & Duan, W. H. (2014). Nano reinforced cement and concrete composites and new perspective from graphene oxide. *Construction and Building Materials, 73*, 113-124. doi: http://dx.doi.org/10.1016/j.conbuildmat.2014.09.040

Chung, D. D. L. (2001). Comparison of submicron-diameter carbon filaments and conventional carbon fibers as fillers in composite materials. *Carbon, 39*(8), 1119-1125. doi: http://dx.doi.org/10.1016/S0008-6223(00)00314-6

Chung, D. D. L. (2002). Piezoresistive cement-based materials for strain sensing. *Journal of Intelligent Material Systems and Structures, 13*(9), 599-609.

Collins, F., Lambert, J., & Duan, W. H. (2012). The influences of admixtures on the dispersion, workability, and strength of carbon nanotube–OPC paste mixtures. *Cement and Concrete Composites, 34*(2), 201-207. doi: http://dx.doi.org/10.1016/j.cemconcomp.2011.09.013

Cooper, D. R., D'Anjou, B., Ghattamaneni, N., Harack, B., Hilke, M., Horth, A., Majlis, N., Massicotte, M., Vandsburger, L., & Whiteway, E. (2012). Experimental review of graphene. *ISRN Condensed Matter Physics, 2012*.

Cui, H., Yan, X., Tang, L., & Xing, F. (2017). Possible pitfall in sample preparation for SEM analysis - A discussion of the paper "Fabrication of polycarboxylate/graphene oxide nanosheet composites by copolymerization for reinforcing and toughening cement composites" by Lv et al. *Cement and Concrete Composites, 77*(Supplement C), 81-85. doi: https://doi.org/10.1016/j.cemconcomp.2016.12.007

Cwirzen. (2010). *Controlling physical properties of cementitious matrixes by nanomaterials.* Paper presented at the Advanced Materials Research.

Cwirzen, Habermehl, C. K., Nasibulin, A. G., Kaupinen, E. I., Mudimela, P. R., & Penttala, V. (2009). SEM/AFM studies of cementitious binder modified by MWCNT and nano-sized Fe needles. *Materials Characterization, 60*(7), 735-740.

Dai, P. S., Gao, H. J., Xu, C., Quek, S. T., & Du, H. (2014). *Strain and damage self-sensing cement composites with conductive graphene nanoplatelet.* Paper presented at the SPIE Smart Structures and Materials + Nondestructive Evaluation and Health Monitoring.

Dawood, E. T., & Ramli, M. (2011). High strength characteristics of cement mortar reinforced with hybrid fibres. *Construction and Building Materials, 25*(5), 2240-2247. doi: http://dx.doi.org/10.1016/j.conbuildmat.2010.11.008

Deroeck, G., Peeters, B., & Maeck, J. (2000). Dynamic monitoring of civil engineering structures. *Proceedings of IASS-IACM 2000, Computational Methods for Shell and Spatial Structures, Chania, Greece*.

Devasena, M., & Karthikeyan, J. (2015). Investigation on strength properties of graphene oxide concrete. *International Journal of Engineering Science Invention Research & Development, 1*(8).

Du, H., Quek, S. T., & Dai Pang, S. (2013). *Smart multifunctional cement mortar containing graphite nanoplatelet.* Paper presented at the SPIE Smart Structures and Materials.

Elsener, B., Andrade, C., Gulikers, J., Polder, R., & Raupach, M. (2003). Half-cell potential measurements—Potential mapping on reinforced concrete structures. *Materials and Structures, 36*(7), 461-471.

Ferrari, A. C., Meyer, J. C., Scardaci, V., Casiraghi, C., Lazzeri, M., Mauri, F., Piscanec, S., Jiang, D., Novoselov, K. S., Roth, S., & Geim, A. K. (2006). Raman Spectrum of Graphene and Graphene Layers. *Physical Review Letters, 97*(18), 187401.

Ferraris, C. F. (1999). *Measurement of the rheological properties of cement paste: a new approach.* Paper presented at the Int. RILEM Conf.“The role of admixtures in high performance concrete.

Feys, D., Verhoeven, R., & De Schutter, G. (2007). Evaluation of time independent rheological models applicable to fresh self-compacting concrete. *Applied Rheology, 17*(5), 56244-57190.

Feys, D., Wallevik, J. E., Yahia, A., Khayat, K. H., & Wallevik, O. H. (2013). Extension of the Reiner–Riwlin equation to determine modified Bingham parameters measured in coaxial cylinders rheometers. *Materials and Structures, 46*(1-2), 289-311.

Flatt, R. J., & Houst, Y. F. (2001). A simplified view on chemical effects perturbing the action of superplasticizers. *Cement and Concrete Research, 31*(8), 1169-1176. doi: http://dx.doi.org/10.1016/S0008-8846(01)00534-8

Garboczi, E. J., & Bentz, D. P. (1997). Analytical formulas for interfacial transition zone properties. *Advanced Cement Based Materials, 6*(3-4), 99-108.

Geim, A. K., & Novoselov, K. S. (2007). The rise of graphene. *Nature Materials, 6*(3), 183-191.

Geng, Y., Wang, S. J., & Kim.-K. (2009). Preparation of graphite nanoplatelets and graphene sheets. *Journal of Colloid and Interface Science, 336*(2), 592-598.

Gong, K., Pan, Z., Korayem, A. H., Qiu, L., Li, D., Collins, F., Wang, C. M., & Duan, W. H. (2014). Reinforcing effects of graphene oxide on portland cement paste. *Journal of Materials in Civil Engineering, 27*(2), A4014010.

Gopalakrishnan, K., Birgisson, B., Taylor, P., & Attoh-Okine, N. O. (2011). *Nanotechnology in civil infrastructure*: Springer.

Govin, A., Bartholin, M.-C., Biasotti, B., Giudici, M., Langella, V., & Grosseau, P. (2016). Modification of water retention and rheological properties of fresh state cement-based mortars by guar gum derivatives. *Construction and Building Materials, 122*, 772-780.

Grobert (2007). Carbon nanotubes - becomng clean. *Materialstoday, Volume. 10(1-2)*, 28-35.

Gurunathan, S., Han, J., & Kim. H. (2013). Humanin: a novel functional molecule for the green synthesis of graphene. *Colloids and Surfaces B: Biointerfaces, 111*, 376-383.

Hamann, H., & Clemens, D. (1973). Suspension polymerization of uniform polymer beads: Google Patents.

Han., Guan, X., & Ou, J. (2007). Electrode design, measuring method and data acquisition system of carbon fiber cement paste piezoresistive sensors. *Sensors and Actuators A: Physical, 135*(2), 360-369. doi: https://doi.org/10.1016/j.sna.2006.08.003

Han., Sun, S., Ding, S., ZHan, L., Yu, X., & Ou, J. (2015). Review of nanocarbon-engineered multifunctional cementitious composites. *Composites Part A: Applied Science and Manufacturing, 70*, 69-81.

Han., Zheng, Q., Sun, S., Dong, S., ZHan, L., Yu, X., & Ou, J. (2017). Enhancing mechanisms of multi-layer graphenes to cementitious composites. *Composites Part A: Applied Science and Manufacturing*.

Han. G., Han. Z., & Ou, J. P. (2009). Experimental study on use of nickel powder-filled Portland cement-based composite for fabrication of piezoresistive sensors with high sensitivity. *Sensors and Actuators A: Physical, 149*(1), 51-55. doi: https://doi.org/10.1016/j.sna.2008.10.001

Hanehara, S., & Yamada, K. (1999). Interaction between cement and chemical admixture from the point of cement hydration, absorption behaviour of admixture, and paste rheology. *Cement and Concrete Research, 29*(8), 1159-1165. doi: http://dx.doi.org/10.1016/S0008-8846(99)00004-6

Hemphill, T., Campos, W., & Pilehvari, A. (1993). Yield-power law model more accurately predicts mud rheology. *Oil and Gas Journal;(United States), 91*(34).

Herschel, W., & Bulkley, R. (1926). *Measurement of consistency as applied to rubber-benzene solutions.* Paper presented at the Am. Soc. Test Proc.

Hevin, G., Abraham, O., Pedersen, H., & Campillo, M. (1998). Characterization of surface cracks with Rayleigh waves: a numerical model. *NDT & E International, 31*(4), 289-297.

Horgnies, M., Chen, J., & Bouillon, C. (2013). Overview about the use of Fourier Transform Infrared spectroscopy to study cementitious materials. *WIT Transactions on Engineering Sciences, 77*, 251-262.

Hung, S. S., Farshidi, F., Jones, D., & Harvey, J. T. (2015). Comparison of Concentric Cylinder and Parallel Plate Geometries for Asphalt Binder Testing with a Dynamic Shear Rheometer. *Transportation Research Record: Journal of the Transportation Research Board*(2505), 108-114.

Jadhav, R., & Debnath, N. (2011). Computation of X-ray powder diffractograms of cement components and its application to phase analysis and hydration performance of OPC cement. *Bulletin of Materials Science, 34*(5), 1137-1150.

Jäger, C., Henning, T., Schlögl, R., & Spillecke, O. (1999). Spectral properties of carbon black. *Journal of Non-Crystalline Solids, 258*(1), 161-179.

Jiang, L., Gao, L., & Sun, J. (2003). Production of aqueous colloidal dispersions of carbon nanotubes. *Journal of colloid and interface science, 260*(1), 89-94. doi: http://dx.doi.org/10.1016/S0021-9797(02)00176-5

Jo, B. W., Kim, C. H., Tae, G.-h., & Park, J.-B. (2007). Characteristics of cement mortar with nano-SiO2 particles. *Construction and Building Materials, 21*(6), 1351-1355.

Juárez, C., Valdez, P., Durán, A., & Sobolev, K. (2007). The diagonal tension behavior of fiber reinforced concrete beams. *Cement and Concrete Composites, 29*(5), 402-408. doi: http://dx.doi.org/10.1016/j.cemconcomp.2006.12.009

Kakali, G., Tsivilis, S., Aggeli, E., & Bati, M. (2000). Hydration products of C3A, C3S and Portland cement in the presence of CaCO3. *Cement and Concrete Research, 30*(7), 1073-1077.

Karim, M. R., Hashim, H., & Abdul Razak, H. (2016). Thermal activation effect on palm oil clinker properties and their influence on strength development in cement mortar. *Construction and Building Materials, 125*, 670-678. doi: http://dx.doi.org/10.1016/j.conbuildmat.2016.08.092

Katsnelson, M. I., Guinea, F., & Geim, A. K. (2009). Scattering of electrons in graphene by clusters of impurities. *Physical Review B, 79*(19), 195426.

Kawashima, S., Hou, P., Corr, D. J., & Shah, S. P. (2013). Modification of cement-based materials with nanoparticles. *Cement and Concrete Composites, 36*, 8-15. doi: http://dx.doi.org/10.1016/j.cemconcomp.2012.06.012

Khai, T. V., Kwak, D. S., Kwon, Y. J., Cho, H. Y., Huan, T. N., Chung, H., Ham, H., Lee, C., Dan, N. V., & Tung, N. T. (2013). Direct production of highly conductive graphene with a low oxygen content by a microwave-assisted solvothermal method. *Chemical Engineering Journal, 232*, 346-355.

Khanra, P., Kuila, T., Kim, N. H., Bae, S. H., Yu, D. S., & Lee, J. H. (2012). Simultaneous bio-functionalization and reduction of graphene oxide by baker's yeast. *Chemical Engineering Journal, 183*, 526-533.

Khoury, G. A. (1992). Compressive strength of concrete at high temperatures: a reassessment. *Magazine of Concrete Research, 44*(161), 291-309.

Kim., Miura, Y., & Macosko, C. W. (2010). Graphene/Polyurethane Nanocomposites for Improved Gas Barrier and Electrical Conductivity. *Chemistry of Materials, 22*(11), 3441-3450. doi: 10.1021/cm100477v

Kim., Cote, L. J., Kim, F., Yuan, W., Shull, K. R., & Huang, J. (2010). Graphene Oxide Sheets at Interfaces. *Journal of the American Chemical Society, 132*(23), 8180-8186. doi: 10.1021/ja102777p

Kodur, V. K. R., & Sultan, M. A. (2003). Effect of temperature on thermal properties of high-strength concrete. *Journal of Materials in Civil Engineering, 15*(2), 101-107.

Konsta, G. M. S., Metaxa, Z. S., & Shah, S. P. (2010). Highly dispersed carbon nanotube reinforced cement based materials. *Cement and Concrete Research, 40*(7), 1052-1059.

Konsta, G. M. S., Metaxa, Z. S., & Shah, S. P. (2010). Multi-scale mechanical and fracture characteristics and early-age strain capacity of high performance carbon nanotube/cement nanocomposites. *Cement and Concrete Composites, 32*(2), 110-115.

Kothiyal, N. C., Sharma, S., Mahajan, S., & Sethi, S. (2016). Characterization of reactive graphene oxide synthesized from ball–milled graphite: its enhanced reinforcing effects on cement nanocomposites. *Journal of adhesion science and Technology, 30*(9), 915-933.

Kowald, T., & Trettin, R. (2004). *Influence of surface-modified carbon nanotubes on ultrahigh performance concrete.* Paper presented at the Proceedings of International Symposium on Ultra High Performance Concrete.

Krause, M., Milmann, B., Mielentz, F., Streicher, D., Redmer, B., Mayer, K., Langenberg, K.-J., & Schickert, M. (2008). Ultrasonic imaging methods for investigation of post-tensioned concrete structures: a study of interfaces at artificial grouting faults and its verification. *Journal of Nondestructive Evaluation, 27*(1-3), 67-82.

Kuilla, T., Bhadra, S., Yao, D., Kim, N. H., Bose, S., & Lee, J. H. (2010). Recent advances in graphene based polymer composites. *Progress in Polymer Science, 35*(11), 1350-1375.

Le, J. L., Du, H., & Dai Pang, S. (2014). Use of 2D Graphene Nanoplatelets (GNP) in cement composites for structural health evaluation. *Composites Part B: Engineering, 67*, 555-563.

Lee, C., Wei, X., Kysar, J. W., & Hone, J. (2008). Measurement of the elastic properties and intrinsic strength of monolayer graphene. *Science, 321*(5887), 385-388.

Lee, C., Wei, X., Li, Q., Carpick, R., Kysar, J. W., & Hone, J. (2009). Elastic and frictional properties of graphene. *Physica Status Solidi (b), 246*(11-12), 2562-2567.

Lei, Y., Tang, Z., Liao, R., & Guo, B. (2011). Hydrolysable tannin as environmentally friendly reducer and stabilizer for graphene oxide. *Green Chemistry, 13*(7), 1655-1658.

Leng, Y. (2009). *Materials characterization: introduction to microscopic and spectroscopic methods*: John Wiley & Sons.

Li, G. Y., Wang, P. M., & Zhao, X. (2005). Mechanical behavior and microstructure of cement composites incorporating surface-treated multi-walled carbon nanotubes. *Carbon, 43*(6), 1239-1245. doi: https://doi.org/10.1016/j.carbon.2004.12.017

Li, G. Y., Wang, P. M., & Zhao, X. (2007). Pressure-sensitive properties and microstructure of carbon nanotube reinforced cement composites. *Cement and Concrete Composites, 29*(5), 377-382. doi: https://doi.org/10.1016/j.cemconcomp.2006.12.011

Li., Xiao, H.-g., & Ou, J.-p. (2004a). A study on mechanical and pressure-sensitive properties of cement mortar with nanophase materials. *Cement and Concrete Research, 34*(3), 435-438. doi: http://dx.doi.org/10.1016/j.cemconres.2003.08.025

Li., Xiao, H.-g., & Ou, J.-p. (2006a). Effect of compressive strain on electrical resistivity of carbon black-filled cement-based composites. *Cement and Concrete Composites, 28*(9), 824-828.

Li., Xiao, H.-g., Yuan, J., & Ou, J. (2004b). Microstructure of cement mortar with nano-particles. *Composites Part B: Engineering, 35*(2), 185-189. doi: http://dx.doi.org/10.1016/S1359-8368(03)00052-0

Li., ZHan, M. h., & Ou, J. p. (2006b). Abrasion resistance of concrete containing nano-particles for pavement. *Wear, 260*(11–12), 1262-1266.

Li., Sham, M. L., Kim. K., & Marom, G. (2007). Morphology and properties of UV/ozone treated graphite nanoplatelet/epoxy nanocomposites. *Composites Science and Technology, 67*(2), 296-305.

Li., Xiao, G., Chen, C., Li, R., & Yan, D. (2013). Superior dispersions of reduced graphene oxide synthesized by using gallic acid as a reductant and stabilizer. *Journal of Materials Chemistry A, 1*(4), 1481-1487.

Li, P., Yao, H., Wong, M., Sugiyama, H., ZHan, X., & Sue, H. J. (2014). Thermally stable and highly conductive free-standing hybrid films based on reduced graphene oxide. *Journal of Materials Science, 49*(1), 380-391.

Li., Li, X., Chen, S. J., Liu, Y. M., Duan, W. H., & Shah, S. P. (2017). Effects of graphene oxide on early-age hydration and electrical resistivity of Portland cement paste. *Construction and Building Materials, 136*, 506-514.

Li, Z., Wang, H., He, S., Lu, Y., & Wang. (2006). Investigations on the preparation and mechanical properties of the nano-alumina reinforced cement composite. *Materials Letters, 60*(3), 356-359. doi: http://dx.doi.org/10.1016/j.matlet.2005.08.061

Lin, J., Teweldebrhan, D., Ashraf, K., Liu, G., Jing, X., Yan, Z., Li, R., Ozkan, M., Lake, R. K., & Balandin, A. A. (2010). Gating of Single-Layer Graphene with Single-Stranded Deoxyribonucleic Acids. *Small, 6*(10), 1150-1155.

Liu, C. X., & Choi, J. W. (2012). Improved dispersion of carbon nanotubes in polymers at high concentrations. *Nanomaterials, 2*(4), 329-347.

Liu., & Horrocks, A. R. (2002). Effect of carbon black on UV stability of LLDPE films under artificial weathering conditions. *Polymer Degradation and Stability, 75*(3), 485-499.

Liu., Tian, J., Wang, L., & Sun. (2011). A method for the production of reduced graphene oxide using benzylamine as a reducing and stabilizing agent and its subsequent decoration with Ag nanoparticles for enzymeless hydrogen peroxide detection. *Carbon, 49*(10), 3158-3164.

Lothenbach, B., Scrivener, K., & Hooton, R. D. (2011). Supplementary cementitious materials. *Cement and Concrete Research, 41*(12), 1244-1256. doi: http://dx.doi.org/10.1016/j.cemconres.2010.12.001

Lu., Do, I., Fukushima, H., Lee, I., & Drzal, L. T. (2010). Stable aqueous suspension and self-assembly of graphite nanoplatelets coated with various polyelectrolytes. *Journal of Nanomaterials, 2010*, 2.

Lu., Hou, D., Meng, L., Sun, G., Lu, C., & Li, Z. (2015). Mechanism of cement paste reinforced by graphene oxide/carbon nanotubes composites with enhanced mechanical properties. *RSC Advances, 5*(122), 100598-100605.

Lv, S., Deng, L., Yang, W., Zhou., & Cui, Y. (2016). Fabrication of polycarboxylate/graphene oxide nanosheet composites by copolymerization for reinforcing and toughening cement composites. *Cement and Concrete Composites, 66*, 1-9.

Lv, S., Liu, J., Sun, T., Ma, Y., & Zhou. (2014a). Effect of GO nanosheets on shapes of cement hydration crystals and their formation process. *Construction and Building Materials, 64*, 231-239.

Lv, S., Ma, Y., Qiu, C., Sun, T., Liu, J., & Zhou. (2013a). Effect of graphene oxide nanosheets of microstructure and mechanical properties of cement composites. *Construction and Building Materials, 49*, 121-127.

Lv, S., Ma, Y., Qiu, C., & Zhou. (2013b). Regulation of GO on cement hydration crystals and its toughening effect. *Magazine of Concrete Research, 65*(20), 1246-1254.

Lv, S., Ting, S., Liu, J., & Zhou. (2014b). Use of graphene oxide nanosheets to regulate the microstructure of hardened cement paste to increase its strength and toughness. *CrystEngComm, 16*(36), 8508-8516.

Ma, P. C., Siddiqui, N. A., Marom, G., & Kim. K. (2010). Dispersion and functionalization of carbon nanotubes for polymer-based nanocomposites: A review. *Composites Part A: Applied Science and Manufacturing, 41*(10), 1345-1367.

Mak, K. F., Lee, C., Hone, J., Shan, J., & Heinz, T. F. (2010). Atomically thin MoS 2: a new direct-gap semiconductor. *Physical Review Letters, 105*(13), 136805.

Materazzi, A. L., Ubertini, F., & D'Alessandro, A. (2013). Carbon nanotube cement-based transducers for dynamic sensing of strain. *Cement and Concrete Composites, 37*, 2-11.

Mehrali, M., Sadeghinezhad, E., Latibari, S. T., Kazi, S. N., Mehrali, M., Zubir, M. N. B. M., & Metselaar, H. S. C. (2014). Investigation of thermal conductivity and rheological properties of nanofluids containing graphene nanoplatelets. *Nanoscale Research Letters, 9*(1), 15.

Mei, X., & Ouyang, J. (2011). Ultrasonication-assisted ultrafast reduction of graphene oxide by zinc powder at room temperature. *Carbon, 49*(15), 5389-5397.

Metaxa, Z. S. (2016). Exfoliated graphene nanoplatelet cement-based nanocomposites as piezoresistive sensors: Influence of nanoreinforcement lateral size on monitoring capability. *Ciência & Tecnologia dos Materiais, 28*(1), 73-79.

Midgley, H. G. (1978). The use of thermal analysis methods in assessing the quality of high alumina cement concrete. *Journal of Thermal Analysis, 13*(3), 515-524.

Mitsoulis, E. (2007). Flows of viscoplastic materials: models and computations. *Rheology Reviews, 2007*, 135-178.

Mohammed, A., Sanjayan, J., Duan, W., & Nazari, A. (2016). Graphene Oxide Impact on Hardened Cement Expressed in Enhanced Freeze–Thaw Resistance. *Journal of Materials in Civil Engineering, 28*(9), 04016072.

Mokhtar, M. M., Abo, E., S A, Hassaan, M. Y., Morsy, M. S., & Khalil, M. H. (2017). Mechanical performance, pore structure and micro-structural characteristics of graphene oxide nano platelets reinforced cement. *Construction and Building Materials, 138*, 333-339.

Mollah, M. Y. A., Yu, W., Schennach, R., & Cocke, D. L. (2000). A Fourier transform infrared spectroscopic investigation of the early hydration of Portland cement and the influence of sodium lignosulfonate. *Cement and Concrete Research, 30*(2), 267-273. doi: https://doi.org/10.1016/S0008-8846(99)00243-4

MS-522: Part 1. (2003). Specification for Portland cement (ordinary and rapid hardening). *Part 1: Standard specification (second revision). Department of Standards Malaysia (SIRIM); Malaysia:* .

Munz, M., Giusca, C. E., Myers, W., Rachael L, Gaskill, D. K., & Kazakova, O. (2015). Thickness-dependent hydrophobicity of epitaxial graphene. *Acs Nano, 9*(8), 8401-8411.

Murugan, M., Santhanam, M., Gupta, S. S., Pradeep, T., & Shah, S. P. (2016). Influence of 2D rGO nanosheets on the properties of OPC paste. *Cement and Concrete Composites, 70*, 48-59.

Naeimi, H., & Golestanzadeh, M. (2015). Microwave-assisted synthesis of 6, 6′-(aryl (alkyl) methylene) bis (2, 4-dialkylphenol) antioxidants catalyzed by multi-sulfonated reduced graphene oxide nanosheets in water. *New Journal of Chemistry, 39*(4), 2697-2710.

Nehdi, M., & Rahman, M. A. (2004). Estimating rheological properties of cement pastes using various rheological models for different test geometry, gap and surface friction. *Cement and Concrete Research, 34*(11), 1993-2007. doi: http://dx.doi.org/10.1016/j.cemconres.2004.02.020

Neville, A. M., & Brooks, J. J. (1987). *Concrete technology*.

Nonnet, E., Lequeux, N., & Boch, P. (1999). Elastic properties of high alumina cement castables from room temperature to 1600 C. *Journal of the European Ceramic Society, 19*(8), 1575-1583.

Novoselov, K., Fal, V., Colombo, L., Gellert, P., Schwab, M., & Kim, K. (2012). A roadmap for graphene. *Nature, 490*(7419), 192-200.

Novoselov, K., Geim, A. K., Morozov, S. V., Jiang, D., ZHan, Y., Dubonos, S. V., Grigorieva, I. V., & Firsov, A. A. (2004). Electric field effect in atomically thin carbon films. *Science, 306*(5696), 666-669.

Ormsby, R., McNally, T., Mitchell, C., Halley, P., Martin, D., Nicholson, T., & Dunne, N. (2011). Effect of MWCNT addition on the thermal and rheological properties of polymethyl methacrylate bone cement. *Carbon, 49*(9), 2893-2904. doi: http://dx.doi.org/10.1016/j.carbon.2011.02.063

Ortego, J. D., Jackson, S., Yu, G. S., McWhinney, H., & Cocke, D. L. (1989). Solidification of hazardous substances-a TGA and FTIR study of Portland cement containing metal nitrates. *Journal of Environmental Science & Health Part A, 24*(6), 589-602.

Pan, Z., He, L., Qiu, L., Korayem, A. H., Li, G., Zhu, J. W., Collins, F., Li, D., Duan, W. H., & Wang. C. (2015). Mechanical properties and microstructure of a graphene oxide–cement composite. *Cement and Concrete Composites, 58*, 140-147. doi: http://dx.doi.org/10.1016/j.cemconcomp.2015.02.001

Papo, A. (1988). Rheological models for cement pastes. *Materials and Structures, 21*(1), 41-46.

Peng, H., Meng, L., Niu, L., & Lu, Q. (2012). Simultaneous reduction and surface functionalization of graphene oxide by natural cellulose with the assistance of the ionic liquid. *The Journal of Physical Chemistry C, 116*(30), 16294-16299.

Peyvandi, A., Soroushian, P., Abdol, N., & Balachandra, A. M. (2013). Surface-modified graphite nanomaterials for improved reinforcement efficiency in cementitious paste. *Carbon, 63*, 175-186.

Pham, V. H., Pham, H. D., Dang, T. T., Hur, S. H., Kim, E. J., Kong, B. S., Kim, S., & Chung, J. S. (2012). Chemical reduction of an aqueous suspension of graphene oxide by nascent hydrogen. *Journal of Materials Chemistry, 22*(21), 10530-10536.

Qian, Y., Abdallah, M. Y., & Kawashima, S. (2015). Characterization of Cement-Based Materials Modified with Graphene-Oxide *Nanotechnology in Construction* (pp. 259-264): Springer.

Qu, J., & Han. (2008). Piezoresistive cement-based strain sensors and self-sensing concrete components. *Journal of Intelligent Material Systems and Structures*.

Rafiee, M. A., Lu, W., Thomas, A. V., Zandiatashbar, A., Rafiee, J., Tour, J. M., & Koratkar, N. A. (2010). Graphene nanoribbon composites. *Acs Nano, 4*(12), 7415-7420.

Raki, L., Beaudoin, J., Alizadeh, R., Makar, J., & Sato, T. (2010). Cement and concrete nanoscience and nanotechnology. *Materials, 3*, 918-942.

Ramanathan, T., Abdala, A. A., StankovichS, Dikin, D. A., Herrera Alonso, M., Piner, R. D., Adamson, D. H., Schniepp, H. C., ChenX, Ruoff, R. S., Nguyen, S. T., Aksay, I. A., Prud'Homme, R. K., & Brinson, L. C. (2008). Functionalized graphene sheets for polymer nanocomposites. *Nat Nano, 3*(6), 327-331. doi: http://www.nature.com/nnano/journal/v3/n6/suppinfo/nnano.2008.96_S1.html

Rao, M. A. (2014). Flow and functional models for rheological properties of fluid foods *Rheology of Fluid, Semisolid, and Solid Foods* (pp. 27-61): Springer.

Rhee, I., Kim, Y. A., Shin, G. O., Kim. H., & Muramatsu, H. (2015). Compressive strength sensitivity of cement mortar using rice husk-derived graphene with a high specific surface area. *Construction and Building Materials, 96*, 189-197.

Rhee, I., Lee, J. S., Kim, Y. A., Kim. H., & Kim. H. (2016). Electrically conductive cement mortar: Incorporating rice husk-derived high-surface-area graphene. *Construction and Building Materials, 125*, 632-642.

Richardson, I. G., & Groves, G. W. (1997). The structure of the calcium silicate hydrate phases present in hardened pastes of white Portland cement/blast-furnace slag blends. *Journal of Materials Science, 32*(18), 4793-4802.

Roussel, N. (2006). A thixotropy model for fresh fluid concretes: Theory, validation and applications. *Cement and Concrete Research, 36*(10), 1797-1806. doi: http://dx.doi.org/10.1016/j.cemconres.2006.05.025

Roussel, N., Ovarlez, G., Garrault, S., & Brumaud, C. (2012). The origins of thixotropy of fresh cement pastes. *Cement and Concrete Research, 42*(1), 148-157.

Saak, A. W., Jennings, H. M., & Shah, S. P. (1999). *Characterization of the rheological properties of cement paste for use in self-compacting concrete.* Paper presented at the Proceeding of the First International RILEM Symposium on "Self-Compacting Concrete", Eds. A. Skarendahl & O. Petersson, Stockholm, Sweden.

Sanchez, F., & Sobolev, K. (2010). Nanotechnology in concrete – A review. *Construction and Building Materials, 24*(11), 2060-2071. doi: http://dx.doi.org/10.1016/j.conbuildmat.2010.03.014

Scott, B. G. W. (1966). The success of Casson's equation. *Rheologica Acta, 5*(3), 184-187.

Sedaghat, A., Ram, Manoj K ,Zayed, A, Kamal, Rajeev, Shanahan, Natallia. (2014). Investigation of physical properties of graphene-cement composite for structural applications. *Open Journal of Composite Materials, 2014*.

Segal, M. (2009). Selling graphene by the ton. *Nat Nano, 4*(10), 612-614.

Senff, L., Labrincha, J. A., Ferreira, V. M., Hotza, D., & Repette, W. L. (2009). Effect of nano-silica on rheology and fresh properties of cement pastes and mortars. *Construction and Building Materials, 23*(7), 2487-2491. doi: http://dx.doi.org/10.1016/j.conbuildmat.2009.02.005

Shah, M. S., Fard, F. G., Khatibi, E., & Sarpoolaky, H. (2009). Dispersion and stability of carbon black nanoparticles, studied by ultraviolet–visible spectroscopy. *Journal of the Taiwan Institute of chemical Engineers, 40*(5), 524-527.

Shah, S. P., & Ouyang, C. (1991). Mechanical Behavior of Fiber-Reinforced Cement-Based Composites. *Journal of the American Ceramic Society, 74*(11), 2727-2953.

SHan, Y., ZHan, D., Yang, C., Liu, Y., & Liu, Y. (2015). Effect of graphene oxide on the rheological properties of cement pastes. *Construction and Building Materials, 96*, 20-28. doi: http://dx.doi.org/10.1016/j.conbuildmat.2015.07.181

Sharma, S., & Kothiyal, N. C. (2015). Influence of graphene oxide as dispersed phase in cement mortar matrix in defining the crystal patterns of cement hydrates and its effect on mechanical, microstructural and crystallization properties. *RSC Advances, 5*(65), 52642-52657.

Sharma, S., & Kothiyal, N. C. (2016). Comparative effects of pristine and ball-milled graphene oxide on physico-chemical characteristics of cement mortar nanocomposites. *Construction and Building Materials, 115*, 256-268.

Shaughnessy, R., & Clark, P. E. (1988). The rheological behavior of fresh cement pastes. *Cement and Concrete Research, 18*(3), 327-341.

Shi, C., & Qian, J. (2000). High performance cementing materials from industrial slags — a review. *Resources, Conservation and Recycling, 29*(3), 195-207. doi: http://dx.doi.org/10.1016/S0921-3449(99)00060-9

Silva, R. A., de Castro Guetti, P., da Luz, M. S., Rouxinol, F., & Gelamo, R. V. (2017). Enhanced properties of cement mortars with multilayer graphene nanoparticles. *Construction and Building Materials, 149*, 378-385.

Sixuan, H. (2012). *Multifunctional Graphite Nanoplatelets (GNP) Reinforced Cementitious Composites (Doctoral dissertation).*

Smith, B. C. (2011). *Fundamentals of Fourier transform infrared spectroscopy*: CRC press.

Stankovich, S., Piner, R. D., Chen, X., Wu, N., Nguyen, S. T., & Ruoff, R. S. (2006). Stable aqueous dispersions of graphitic nanoplatelets via the reduction of exfoliated graphite oxide in the presence of poly (sodium 4-styrenesulfonate). *Journal of Materials Chemistry, 16*(2), 155-158.

Sun, S., Yu, X., Han., & Ou, J. (2013). In situ growth of carbon nanotubes/carbon nanofibers on cement/mineral admixture particles: A review. *Construction and Building Materials, 49*, 835-840. doi: http://dx.doi.org/10.1016/j.conbuildmat.2013.09.011

Sun., Wu, Q., ZHan., Qing, Y., Wu, Y., & Lee, S. (2017). Rheology, curing temperature and mechanical performance of oil well cement: Combined effect of cellulose nanofibers and graphene nano-platelets. *Materials & Design, 114*, 92-101.

Taffe, A., & Wiggenhauser, H. (2006). *Validation for thickness measurement in civil engineering with ultrasonic echo.* Paper presented at the Proceedings of the 9th European Conference on NDT.

Thakur, S., & Karak, N. (2012). Green reduction of graphene oxide by aqueous phytoextracts. *Carbon, 50*(14), 5331-5339.

Tong, T., Fan, Z., Liu, Q., Wang, S., Tan, S., & Yu, Q. (2016). Investigation of the effects of graphene and graphene oxide nanoplatelets on the micro-and macro-properties of cementitious materials. *Construction and Building Materials, 106*, 102-114.

Topçu, İ. B., & Canbaz, M. (2007). Effect of different fibers on the mechanical properties of concrete containing fly ash. *Construction and Building Materials, 21*(7), 1486-1491. doi: http://dx.doi.org/10.1016/j.conbuildmat.2006.06.026

Tran, D. N., Kabiri, S., & Losic, D. (2014). A green approach for the reduction of graphene oxide nanosheets using non-aromatic amino acids. *Carbon*.

Trezza, M. A. (2007). Hydration study of ordinary portland cement in the presence of zinc ions. *Materials Research, 10*, 331-334.

Tyson, B. M. (2010). *Carbon nanotube and nanofiber reinforcement for improving the flexural strength and fracture toughness of Portland cement paste.* Texas A&M University.

Ubertini, F., Laflamme, S., Ceylan, H., Materazzi, A. L., Cerni, G., Saleem, H., D'Alessandro, A., & Corradini, A. (2014). Novel nanocomposite technologies for dynamic monitoring of structures: a comparison between cement-based embeddable and soft elastomeric surface sensors. *Smart Materials and Structures, 23*(4), 045023.

Valdes, L. B. (1954). Resistivity measurements on germanium for transistors. *Proceedings of the IRE, 42*(2), 420-427.

Vasudevan, A. K., Sadananda, K., & Glinka, G. (2001). Critical parameters for fatigue damage. *International Journal of Fatigue, 23*, 39-53.

Vikan, H., Justnes, H., Winnefeld, F., & Figi, R. (2007). Correlating cement characteristics with rheology of paste. *Cement and Concrete Research, 37*(11), 1502-1511.

Wallevik, J. E. (2009). Rheological properties of cement paste: thixotropic behavior and structural breakdown. *Cement and Concrete Research, 39*(1), 14-29.

Wang., Jiang, R., & Wu, Z. (2016). Investigation of the mechanical properties and microstructure of graphene nanoplatelet-cement composite. *Nanomaterials, 6*(11), 200.

Wang, J. Y., Banthia, N., & ZHan, M. H. (2012). Effect of shrinkage reducing admixture on flexural behaviors of fiber reinforced cementitious composites. *Cement and Concrete Composites, 34*(4), 443-450.

Wang., Wang, R., Yao, H., Farhan, S., Zheng, S., & Du, C. (2016). Study on the three dimensional mechanism of graphene oxide nanosheets modified cement. *Construction and Building Materials, 126*, 730-739.

Wang., Cui, X., Wang, J., Li, S., Lv, C., & Dong, Y. (2017). Effect of fly ash on rheological properties of graphene oxide cement paste. *Construction and Building Materials, 138*, 35-44.

Wang., Wang, J., Lu, C. X., Liu, B. W., ZHan, K., & Li, C. Z. (2015). Influence of graphene oxide additions on the microstructure and mechanical strength of cement. *New Carbon Materials, 30*(4), 349-356.

Wang., Wang, J., Lv, C. X., Cui, X. Y., Li, S. Y., & Wang, X. (2016). Rheological behavior of fresh cement pastes with a graphene oxide additive. *New Carbon Materials, 31*(6), 574-584.

Wang., Shi, Z., & Yin, J. (2011). Facile synthesis of soluble graphene via a green reduction of graphene oxide in tea solution and its biocomposites. *ACS Applied Materials & Interfaces, 3*(4), 1127-1133.

Wilson, N. R., Pandey, P. A., Beanland, R., Young, R. J., Kinloch, I. A., Gong, L., Liu, Z., Suenaga, K., Rourke, J. P., & York, S. J. (2009). Graphene oxide: structural analysis and application as a highly transparent support for electron microscopy. *Acs Nano, 3*(9), 2547-2556.

Wotring, E. (2014). *Dispersion of graphene nanoplatelets in water with surfactant and reinforcement of mortar with graphene nanoplatelets.* University of Illinois at Urbana-Champaign.

Xu, L. Q., Yang, W. J., Neoh, K. G., Kang, E. T., & Fu, G. D. (2010). Dopamine-induced reduction and functionalization of graphene oxide nanosheets. *Macromolecules, 43*(20), 8336-8339.

Xu., Lo, Y. T., Ouyang, D., Memon, S. A., Xing, F., Wang, W., & Yuan, X. (2015). Corrigendum to ‘‘Effect of rice husk ash fineness on porosity and hydration reaction of blended cement’’[Constr. Build. Mater. 89 (2015) 90–101]. *Construction and Building Materials, 93*, 1249.

Yahia, A., & Khayat, K. (2001). Analytical models for estimating yield stress of high-performance pseudoplastic grout. *Cement and Concrete Research, 31*(5), 731-738. doi: https://doi.org/10.1016/S0008-8846(01)00476-8

Yahia, A., & Khayat, K. (2003). Applicability of rheological models to high-performance grouts containing supplementary cementitious materials and viscosity enhancing admixture. *Materials and Structures, 36*(6), 402-412.

Yakovlev, G., Kerienė, J., Gailius, A., & Girnienė, I. (2006). Cement based foam concrete reinforced by carbon nanotubes. *Materials Science [Medžiagotyra], 12*(2), 147-151.

Yang, H., Cui, H., Tang, W., Li, Z., Han, N., & Xing, F. (2017). A critical review on research progress of graphene/cement based composites. *Composites Part A:*

*Applied Science and Manufacturing, 102*(Supplement C), 273-296. doi: https://doi.org/10.1016/j.compositesa.2017.07.019

Yu, X., & Kwon, E. (2009). A carbon nanotube/cement composite with piezoresistive properties. *Smart Materials and Structures, 18*(5), 055010.

Zhan., Yang, H., Shen, G., Cheng, P., ZHan., & Guo, S. (2010). Reduction of graphene oxide via L-ascorbic acid. *Chemical Communications, 46*(7), 1112-1114.

Zhan, M. H., Sisomphon, K., Ng, T. S., & Sun, D. J. (2010). Effect of superplasticizers on workability retention and initial setting time of cement pastes. *Construction and Building Materials, 24*(9), 1700-1707.

Zhan, Y., Kong, X., Gao, L., Lu., Zhou, S., Dong, B., & Xing, F. (2016). In-situ measurement of viscoelastic properties of fresh cement paste by a microrheology analyzer. *Cement and Concrete Research, 79*, 291-300.

Zhan, Y., Tan, Y. W., Stormer, H. L., & Kim, P. (2005). Experimental observation of the quantum Hall effect and Berry's phase in graphene. *Nature, 438*(7065), 201-204.

Zhao., & Bai, J. (2015). Highly sensitive piezo-resistive graphite nanoplatelet–carbon nanotube hybrids/polydimethylsilicone composites with improved conductive network construction. *ACS Applied Materials & Interfaces, 7*(18), 9652-9659.

Zhao., Guo, X., Ge, C., Li, Q., Guo, L., Shu, X., & Liu, J. (2016). Investigation of the effectiveness of PCat GO on the reinforcement for cement composites. *Construction and Building Materials, 113*, 470-478.

Zhao., Guo, X., Ge, C., Li, Q., Guo, L., Shu, X., & Liu, J. (2017a). Mechanical behavior and toughening mechanism of polycarboxylate superplasticizer modified graphene oxide reinforced cement composites. *Composites Part B: Engineering, 113*, 308-316.

Zhao., Guo, X., Liu, Y., Ge, C., Guo, L., Shu, X., & Liu, J. (2017b). Synergistic effects of silica nanoparticles/polycarboxylate superplasticizer modified graphene oxide on mechanical behavior and hydration process of cement composites. *RSC Advances, 7*(27), 16688-16702.

Zhou, C., Li, F., Hu, J., Ren, M., Wei, J., & Yu, Q. (2017). Enhanced mechanical properties of cement paste by hybrid graphene oxide/carbon nanotubes. *Construction and Building Materials, 134*, 336-345.

Zhou., & Glasser, F. P. (2001). Thermal stability and decomposition mechanisms of ettringite at <120°C. *Cement and Concrete Research, 31*(9), 1333-1339. doi: http://dx.doi.org/10.1016/S0008-8846(01)00558-0

Zhu., Guo, S., Fang, Y., & Dong, S. (2010). Reducing sugar: new functional molecules for the green synthesis of graphene nanosheets. *Acs Nano, 4*(4), 2429-2437.

Zhu., Murali, S., Cai, W., Li, X., Suk, J. W., Potts, J. R., & Ruoff, R. S. (2010). Graphene and graphene oxide: synthesis, properties, and applications. *Advanced materials, 22*(35), 3906-3924.

# LIST OF PUBLICATIONS

## Accepted Articles

## ISI Indexed

1. **Rehman, S. K. U.,** Ibrahim, Z., Memon, S. A., Javed, M. F., & Khushnood, R. A. (2017). A Sustainable Graphene Based Cement Composite. Sustainability, 9(7), 1229. **(ISI Indexed, Q2, IF: 1.789)**
2. **Rehman**, S. K. U., Ibrahim, Z., Memon, S. A., Aunkor, M., Hossain, T., Javed, M. F., Mehmood, K. & Shah, S. M. A. (2018). Influence of Graphene Nanosheets on Rheology, Microstructure, Strength Development and Self-Sensing Properties of Cement Based Composites. *Sustainability*, *10*(3), 822 **(ISI Indexed, Q2, IF: 1.789)**.
3. **Rehman, S.K.U.,** Ibrahim, Z., Memon, S.A. and Jameel, M., (2016). Nondestructive test methods for concrete bridges: A review. Construction and Building Materials, 107, pp.58-86. (**ISI Indexed, Q1, IF: 2.421**)

## Refereed Conference Papers

4. **Rehman, S. K.U,** Ibrahim, Z., Javed, M. F., Hanif, M. U., M., (2017) Piezo-resistive characteristics of Graphene based cement mWallevik, 2009aterials. 24th International Congress on Sound and Vibration (ICSV 24). July 23-27, London.
5. **Rehman, S. K.U.,** Ibrahim, Z., Javed, M. F., Hanif, M. U., M., Ghaedi, K., (2017). Self-Sensing Carbon Based Cement Composite Material. Conference

Proceedings 2nd International Conference on Advances in Engineering and Technology 2017 (RTET-2017). Feb. 9-10, 2017, Penang, Malaysia.

6. **Rehman, S. K.U.,** Ibrahim, Z., Jameel, M., Hanif, M. U., M., Ghaedi, K., Javed, M. F., Tababalan, V., (2016). Influence of Graphene Oxide Nanosheets on Properties of Cement Based Materials. Conference Proceedings 13th International Conference on Concrete Engineering and Technology 2016 CONCET2016. May 31-June 2, 2016, Universiti Teknologi Mara, Shah Alam, Selangor, Malaysia.

## In progress/Under review Articles

7. **Rehman, S. K. U.,** Ibrahim, Z., Memon, S. A., Jameel, M., & Javed, M. F. Recent research on graphene based cement composite: A review (Construction and Building Materials, **ISI Indexed, Q1, IF: 3.169**)
8. **Rehman, S. K. U.,** Ibrahim, Z., Memon, S. A., Jameel, M., & Javed, M. F. Assessment of rheological properties of graphene cement paste using various models and geometries (International Journal of Concrete Structures and Materials, **ISI Indexed, Q2, IF: 2.031**)